

(NASA-CP-2431) THIRTEENTH INTERNATIONAL
LASER RADAR CONFERENCE (NASA) 335 p
CSCL 20B

N87-10263
THRU
N87-10375
Unclas
44014

G3/35

Thirteenth International Laser Radar Conference

Abstracts of papers presented at the
conference sponsored by the Atmospheric
Environment Service and York University, Toronto,
Ontario, Canada, and by NASA Langley Research
Center, Hampton, Virginia, U.S.A., and held in
Toronto, Ontario, Canada
August 11-15, 1986

NASA
National Aeronautics
and Space Administration
Scientific and Technical
Information Branch

1986

This conference was held under the auspices of the International Coordination group for Laser Atmospheric Studies (ICLAS) of the International Radiation Commission of the International Association of Meteorology and Atmospheric Physics of IUGG and the Committee on Laser Atmospheric Studies (CLAS) of the American Meteorological Society. It was sponsored by the Atmospheric Environment Service, York University, and NASA. The conference chairman, ICLAS members, and CLAS members are listed below.

Conference Chairman: A.I. CARSWELL, York University, North York, Canada.

ICLAS Members:	M.P. MCCORMICK Chairman, NASA Langley Research Center, Hampton, USA. A.I. CARSWELL York University, North York, Canada. B.M. HERMAN University of Arizona, Tucson, USA. G. MEGIE Service d'Aeronomie du CNRS, France. R. REITER Fraunhofer Institute, Garmish Partenkirchen, FRG.
----------------	--

CLAS Members:	H. MELFI Chairman, NASA Goddard Space Flight Center, Greenbelt, USA. A.I. CARSWELL York University, North York, Canada. M. FUJIWARA Kyushu University, Fukuoka, Japan. E.V. BROWELL NASA Langley Research Center, Hampton, USA. L. THOMAS University College of Wales, Aberystwyth, U.K. E.W. ELORANTA University of Wisconsin, Madison, USA R.M. HUFFAKER Coherent Technologies, Boulder, USA. R. MENZIES Jet Propulsion Laboratory, Pasadena, USA. P. FLAMANT Ecole Polytechnique, France.
---------------	---

PREFACE

This publication contains abstracts of papers presented at the Thirteenth International Laser Radar Conference (ILRC), held at the Ramada Hotel in Toronto, Canada, August 11-15, 1986. The conference was hosted by York University and the Atmospheric Environment Service, Canada. Eighty papers and 35 posters were presented during 9 sessions. These conferences have historically provided lidar researchers from throughout the world with a forum to present their latest achievements and to discuss problems of mutual concern. The conferences have addressed subjects from lidar-based atmospheric investigations to the development of new lidar systems and techniques.

This thirteenth conference again portrays a maturing field with many examples of lidar atmospheric investigations. The abstracts discuss laser radar measurements of properties from the Earth's surface to the mesosphere, made with techniques ranging from elastic and inelastic scattering to Doppler shifts and differential absorption. The first session begins with spaceborne measurements describing a recommitment to make lidar measurements from space.

The conference was held under the auspices of the International Coordination group for Laser Atmospheric Studies (ICLAS) of the International Radiation Commission, International Association of Meteorology and Atmospheric Physics, and the Committee on Laser Atmospheric Studies of the American Meteorological Society. ICLAS is the parent organization for these ILRC's which are held during even years. Through the cooperation of many societies and organizations, national lidar conferences and conferences/workshops associated with specific or related aspects of lidar research are held during odd years. The 13th ILRC was organized under the leadership of Allan Carswell of York University and Ray Hoff of the Atmospheric Environment Service with assistance from Shiv Pal and Doug Houston. The Program Committee and Professor Carswell, who chaired the committee, are to be commended for the excellent selection of scientific papers.

This volume was prepared for publication through the efforts of the staff of the Research Information and Applications Division, NASA Langley Research Center, and the staff of York University Physics Department. Special thanks go to Bea Frith and Pat Pearson for attending to the diverse tasks required for the success of this conference.

The use of trade names or manufacturers' names in this publication does not constitute endorsement, either expressed or implied, by the National Aeronautics and Space Administration.

M. Patrick McCormick
Chairman, International Coordination
Group for Laser Atmospheric Studies
International Radiation Commission

CONTENTS

PREFACE

iii

SESSION A: SPACEBORNE LIDAR/NEW APPLICATIONS

Monday, August 11, 1986

Chairperson: S.G. Tilford

08:30 a.m. - 12:00 noon

- | | |
|--|----|
| A1. ESA ACTIVITIES IN SPACE LASER SOUNDING AND RANGING
H. Lutz. (Invited Paper) | 1 |
| A2. LIDAR REMOTE SENSING FROM SPACE: NASA'S PLANS IN THE EARTH SCIENCES
R.J. Curran (Invited Paper) | 2 |
| A3. TUNABLE SOLID-STATE LASER TECHNOLOGY FOR APPLICATIONS TO SCIENTIFIC
AND TECHNOLOGICAL EXPERIMENTS FROM SPACE
F. Allario, L.V. Taylor (Invited Paper) | 3 |
| A4. COHERENT LIDAR TECHNOLOGY FOR GLOBAL WIND PROFILING
R.M. Huffaker | 4 |
| A5. DEVELOPMENT OF A HIGH-ALTITUDE AIRBORNE DIAL SYSTEM--THE LIDAR
ATMOSPHERIC SENSING EXPERIMENT (LASE)
E.V. Browell, W.R. Vaughan, W.M. Hall, J.J. Degnan, R.D. Averill,
J.G. Wells, D.E. Hinton, J.H. Goad | 6 |
| A6. MIE LIDAR PROPOSED FOR THE GERMAN SPACE SHUTTLE MISSION D2
W. Renger, M. Endemann, H. Quenzel, Ch. Werner | 10 |
| A7. THE LIDAR IN-SPACE TECHNOLOGY EXPERIMENT (LITE)
M.P. McCormick | 14 |

SESSION B: EXTINCTION/ VISIBILITY

Monday August 11, 1986

Chairperson: R.M. Hoff

1:30 p.m. - 5:00 p.m.

Co-Chairperson: A.I. Carswell

- | | |
|---|----|
| B1. ADVANCES IN LIDAR ATMOSPHERIC STUDIES IN THE USSR
V.E. Zuev (Invited Paper) | 15 |
| B2. AEROSOL STUDIES IN MID-LATITUDE COASTAL ENVIRONMENTS IN AUSTRALIA
S.A. Young, D. Cutten, M.J. Lynch, J.E. Davies | 16 |
| B3. VISIBILITY RELATED TO BACKSCATTER AT 1.54 μ m
T.L. Barber, D.R. Larson | 20 |
| B4. INVERSION OF TWO WAVELENGTH LIDAR DATA FOR CLOUD PROPERTIES
S.R. Pal, A.I. Carswell | 22 |
| B5. THE USEFULNESS OF KLETT'S INVERSION ALGORITHMS TO SIMULATED SATELLITE
LIDAR RETURNS
M. Kästner, H. Quenzel | 24 |

B6.	WAVELENGTH DEPENDENCE OF AEROSOL BACKSCATTER COEFFICIENTS OBTAINED BY MULTIPLE WAVELENGTH LIDAR MEASUREMENTS Y. Sasano, E.V. Browell	28
B7.	EXTINCTION AND VISIBILITY MEASUREMENTS IN THE LOWER ATMOSPHERE WITH UV-YAG-LIDAR A. Hagård	32
B8.	SENSITIVITY OF THE LIDAR RATIO TO CHANGES IN SIZE DISTRIBUTION AND INDEX OF REFRACTION B.T.N. Evans	34
B9.	LIDAR MEASUREMENTS OF SLANT VISUAL RANGE Yu. S. Balin, S.I. Kavkyanov, G.M. Krekov, I.A. Razenkov	38
B10.	VISIBILITY AND AEROSOL MEASUREMENT BY DIODE-LASER RANDOM-MODULATION CW LIDAR N. Takeuchi, H. Baba, K. Sakurai, T. Ueno, N. Ishikawa	41
B11.	CORRECTION FUNCTION IN THE LIDAR EQUATION AND THE SOLUTION TECHNIQUES FOR CO ₂ LIDAR DATA REDUCTION Y. Zhao, T.K. Lea, R.M. Schotland	45

SESSION C: DIAL

Chairperson: G. Megie
Co-Chairperson: P.T. Woods

Tuesday August 12, 1986
8:30 a.m. - 12 Noon

C1.	ASSESSMENT OF DIAL DATA COLLECTION AND ANALYSIS TECHNIQUES E.V. Browell, P.T. Woods (Invited Paper)	49
C2.	AIRBORNE LIDAR MEASUREMENTS OF THE ATMOSPHERIC PRESSURE PROFILE WITH TUNABLE ALEXANDRITE LASERS C.L. Korb, G.K. Schwemmer, M. Dombrowski, J. Milrod, H. Walden	52
C3.	MEASUREMENTS OF THE EFFECT OF HORIZONTAL VARIABILITY OF ATMOSPHERIC BACKSCATTER ON DIAL MEASUREMENTS G.K. Schwemmer, C.L. Korb, M. Dombrowski, C.Y. Weng	55
C4.	FLIGHT TESTS OF A RANGE-RESOLVED AIRBORNE DIAL WITH TWO MINI-TEA CO ₂ LASERS T. Itabe, M. Ishizu, T. Aruga, T. Igarashi, K. Asai	57
C5.	Nd: GLASS-RAMAN LASER FOR WATER VAPOR DIAL R.H. Kagann, J.C. Petheram, A. Rosenberg	59
C6.	A METEOROLOGICAL (HUMIDITY, TEMPERATURE, AEROSOLS) MOBILE DIAL SYSTEM: CONCEPTS AND DESIGN Cl. Cahen, J.L. Lesne, J. Benard, P. Ponsardin	61

C7.	INFLUENCE OF RAYLEIGH-DOPPLER BROADENING ON THE SELECTION OF H ₂ O DIAL SYSTEM PARAMETERS S. Ismail, E.V. Browell	65
C8.	CORRECTION OF DOPPLER-BROADENED RAYLEIGH-BACKSCATTERING EFFECTS IN H ₂ O DIAL MEASUREMENTS A. Ansmann, J. Bösenberg	70
C9.	ATMOSPHERIC CONTRIBUTIONS TO THE COLUMN VARIANCE IN DIRECT-DETECTION DIAL M.J.T. Milton, P.T. Woods	73
C10.	HIGH SPECTRAL PURITY, NARROW LINEWIDTH LASER TRANSMITTER FOR DIAL MEASUREMENTS U.N. Singh, P.H. Flamant	76
C11.	ON THE MEASUREMENT OF ATMOSPHERIC DENSITY USING DIAL IN THE O ₂ A-BAND (770 nm) T.D. Wilkerson, G.K. Schwemmer, L.J. Cotnoir, U.N. Singh	80

SESSION D: POSTER PARTY

Chairperson: J.D. Lawrence Jr.

Co-Chairperson: J. Cooney

Tuesday August 12, 1986
7:00 p.m.

D1.	USING A LASER AUREOLE TO INVERT LIDAR RETURN W.P. Hooper, H. Gerber	84
D2.	DETERMINATION OF CLOUD MICROPHYSICAL PROPERTIES BY LASER BACKSCATTERING AND EXTINCTION MEASUREMENTS R.N. Dubinsky, A.I. Carswell, S.R. Pal	85
D3.	EFFECT OF BACKSCATTER-TO-EXTINCTION RATIO ON LIDAR INVERSIONS E.M. Measure	86
D4.	LABORATORY MEASUREMENTS OF FORWARD AND BACKWARD SCATTERING OF LASER BEAMS IN WATER DROPLET CLOUDS R.B. Smith, J.D. Houston, A. Ulitsky, A.I. Carswell	92
D5.	REAL-TIME ATMOSPHERIC ABSORPTION SPECTRA FOR IN-FLIGHT TUNING OF AN AIRBORNE DIAL SYSTEM M. Dombrowski, H. Walden, G.K. Schwemmer, J. Milrod, C.L. Korb	94
D6.	OBSERVATION OF ATMOSPHERIC OZONE BY DIAL WITH RAMAN LASERS PUMPED BY A KrF LASER M. Maeda, T. Shibata	95
D7.	STRENGTH, WIDTH, AND PRESSURE SHIFT MEASUREMENTS OF 54 LINES IN THE OXYGEN A-BAND K. J. Ritter, T.D. Wilkerson	98
D8.	AN ALL-PURPOSE COMPUTER PROGRAM FOR LIDAR SIMULATIONS AND REDUCTION OF LIDAR DATA C. Braun	102

D9. CONVECTIVE STRUCTURE OF THE PLANETARY BOUNDARY LAYER OVER THE OCEAN DURING GALE S.H. Melfi, R. Boers	104
D10. METHODS FOR ESTIMATING THE OPTICAL CONSTANTS OF ATMOSPHERIC HAZES BASED ON COMPLEX OPTICAL MEASUREMENTS V.E. Zuev, B.S. Kostin, I.E. Naats	105
D11. MULTIFREQUENCY DIAL SENSING OF THE ATMOSPHERIC GASEOUS CONSTITUENTS USING THE FIRST AND SECOND HARMONICS OF A TUNABLE CO ₂ LASER RADIATION V.E. Zuev, Yu.M. Andreev, V.G. Voevodin, A.I. Gribenyukov, V.A. Kapitanov, A.V. Sosnin, G.A. Stuchebrov, G.S. Khmel'nitskii	108
D12. REMOTE EXPRESS ANALYSIS OF GROUND-LAYER AEROSOL BASED ON LASER-INDUCED SPARK SPECTRA V.E. Zuev, Yu.D. Kopytin, V.A. Korol'kov, M.E. Levitskii, M.F. Nebol'sin, B.G. Sidorov, N.P. Soldatkin	111
D13. LASER SOUNDING OF INSTANTANEOUS AND MEAN SPEED OF WIND USING CORRELATION METHOD V.E. Zuev, I.V. Samokhvalov, G.G. Matvienko, I.N. Kolev, O.P. P'rvanov	113
D14. OPTIMAL FILTRATION OF THE ATMOSPHERIC PARAMETERS PROFILES V.E. Zuev, G.N. Glaznov, G.M. Igonin	117
D15. OPTICAL MODELS OF THE MOLECULAR ATMOSPHERE V.E. Zuev, Yu.S. Makushkin, A.A. Mitsel, Yu.N. Ponomarev, V.P. Rudenko,, K.M. Firsov	119
D16. THE INFLUENCE OF AN OPTICAL RECEIVING SYSTEM ON STATISTICAL CHARACTERISTICS OF A LIDAR SIGNAL V.E. Zuev, V.A. Banakh, V.L. Mironov	122
D17. COHERENT LIDARS BASED ON INTRACAVITY HETERODYNING OF ECHO SIGNALS V.E. Zuev, S.D. Burakov, A.P. Godlevskii, Yu.D. Kopytin, S.V. Lazarev, S.A. Ostanin, P.P. Sharin	125
D18. THE INFLUENCE OF SCATTERING PARTICLES MORPHOLOGY ON THE CHARACTERISTICS OF LIDAR SIGNALS V.E. Zuev, I.E. Naats, A.A. Popov	126
D19. IMPROVED SOLUTION OF THE LIDAR EQUATION UTILIZING PARTICLE COUNTER MEASUREMENTS H. Jäger, M. Littfass, D.J. Hofmann, J.M. Rosen	129
D20. IMPROVEMENTS IN THE GODDARD BALLOON-BORNE LIDAR W.S. Heaps	131
D21. FEATURES OF STRATOSPHERIC AEROSOL LIDAR OBSERVATIONS AT MAUNA LOA, 1974-1985 J.J. DeLuisi, T. DeFoor, D.U. Longenecker	132

D22. EL CHICHON AEROSOLS IN THE STRATOSPHERE: ANALYSES OF LIDAR DATA AND CALCULATIONS OF RADIATION BUDGET M. Fujiwara, H. Akiyoshi, N. Otsuka	133
D23. LIDAR OBSERVATIONS OF STRATOSPHERIC AEROSOL AFTER MT. EL CHICHON ERUPTION Sun Jinhui, Qiu Jinhuan, Xia Qilin, Zhang Jindin	134
D24. LIDAR MEASUREMENT OF STRATOSPHERIC AEROSOL AT SYOWA STATION, ANTARTICA Y. Iwasaka, T. Hirasawa, H. Fukunishi, T. Ono, A. Nomura	135
D25. MULTIPLE SCATTERING MEASUREMENTS IN LABORATORY AND FOGGY ATMOSPHERE P. Bruscaiglioni, E. Battistelli, P. Pili, G. Zaccanti	139
D26. MULTIPLE SCATTERING OF LASER BEAMS IN DENSE HYDROSOLS A. Zardecki, S.A.W. Gerstl, W.P. Unruh, G.H. Stokes, D.M. Stupin, N.E. Elliott, J.A. Weinman	143
D27. TIME-RESOLVED LIDAR FLUOROSENSOR FOR SEA POLLUTION DETECTION A. Ferrario, P.L. Pizzolati, E. Zanzottera	146
D28. VARIATION OF THE URBAN NO ₂ CONCENTRATION DURING A GROUND INVERSION SITUATION A. Sunesson, W. Wendt, B. Galle	148
D29. AN INTENSITY-MODULATED DUAL-WAVELENGTH He-Ne LASER FOR REMOTE SENSING OF METHANE K. Uehara, F. Taguchi	151
D30. LIDAR MAPPING OF A MIXTURE OF AEROSOL CONCENTRATIONS IN A VARYING ATMOSPHERE M. Kleiman, S. Egert, A. Cohen	155
D31. THREE ATMOSPHERIC DISPERSION EXPERIMENTS INVOLVING OIL FOG PLUMES MEASURED BY LIDAR W.L. Eberhard, G.T. McNice, S.W. Troxel	158
D32. FEASIBILITY EXPERIMENTS ON TIME-RESOLVED FLUOROSENSING APPLIED TO OIL SLICKS P. Camagni, G. Colombo, G. Koechler, A. Pedrini, N. Omenetto, G. Rossi	162
D33. ROTATIONALLY RESOLVED COLLISIONAL TRANSFER RATES IN OH T. J. McGee, J. Butler, J. Burris, W. Heaps	167
D34. TIME-DOMAIN SENSITIVITY ENHANCEMENT IN PULSED Pb-TDL GAS MONITORS R. Koga, M. Kosaka, H. Sano	168
D35. PERFORMANCE TESTING OF LIDAR RECEIVERS M.Y. Shams	172

SESSION E: WINDS AND TROPOSPHERIC STUDIES

Chairperson: W. Renger

Co-Chairperson: R.M. Schotland

Wednesday August 13, 1986

8:30 a.m. - 12 noon

- | | |
|--|-----|
| E1. PROGRESS IN COHERENT LASER RADAR
J.M. Vaughan (Invited Paper) | 174 |
| E2. DOPPLER LIDAR STUDIES OF ATMOSPHERIC WIND FIELD DYNAMICS
R.M. Hardesty, M.J. Post, T.R. Lawrence, F.F. Hall, Jr. | 176 |
| E3. THE EFFECT OF TURBULENCE ON LIDAR BACKSCATTERED SIGNAL FLUCTUATIONS
S. Fastig, A. Choen | 180 |
| E4. REMOTE SENSING OF ATMOSPHERIC WINDS USING A COHERENT, CW LIDAR AND
SPECKLE-TURBULENCE INTERACTION
J.F. Holmes, F. Amzajerdian, V.S.R. Gudimetia, J.M. Hunt | 181 |
| E5. EXPERIMENTAL AND THEORETICAL DOPPLER-LIDAR SIGNATURES OF AIRCRAFT
WAKE VORTICES
F. Koepp, W.A. Krichbaumer | 185 |
| E6. LOWER ATMOSPHERIC TEMPERATURE PROFILE MEASUREMENTS USING A RAMAN
LIDAR
S.H. Melfi, D. Whiteman | 188 |
| E7. A COMBINED RAMAN LIDAR FOR LOW TROPOSPHERIC STUDIES
Yu.F. Arshinov, S.M. Bobrovnikov, V.E. Zuev, A.I. Nadeev,
K. D. Shelevoy | 189 |
| E8. INTERCOMPARISONS OF HIGH-RESOLUTION SOLAR BLIND RAMAN LIDAR
ATMOSPHERIC PROFILES OF WATER VAPOR WITH RADIOSONDES AND KYTOON
K. Petri, A. Salik, J. Cooney | 192 |
| E9. LIDAR METHOD OF MEASUREMENT OF ATMOSPHERIC EXTINCTION AND OZONE
PROFILES
J.A. Cooney | 193 |
| E10. VERTICAL STRUCTURE OF ARCTIC HAZE OBSERVED BY LIDAR
R.M. Hoff | 194 |
| E11. LIDAR OBSERVATIONS AND MODELING OF COLD AIR OUTBREAKS DURING MASEX
AND GALE
R. Boers, S.H. Melfi | 197 |

SESSION F: MIDDLE ATMOSPHERE

Chairperson: L. Thomas

Co-Chairperson: M. Fujiwara

Wednesday August 13, 1986

1:30 p.m. - 5:00 p.m.

- | | |
|---|-----|
| F1. THE APPLICATION OF LIDAR TO STRATOSPHERIC AEROSOL STUDIES
M.P. McCormick (Invited Paper) | 201 |
|---|-----|

F2.	VOLCANIC ERUPTIONS AND THE INCREASES IN THE STRATOSPHERIC AEROSOL CONTENT - LIDAR MEASUREMENTS FROM 1982 TO 1986 S. Hayashida, Y. Iikura, H. Shimizu, Y. Sasano, H. Nakane, N. Sugimoto, I. Matsui, N. Takeuchi	203
F3.	OBSERVATIONS OF STRATOSPHERIC AEROSOLS ASSOCIATED WITH THE EL CHICHON ERUPTION L. Thomas, G. Vaughan, D.B. Jenkins, D.P. Wareing, M. Farrington	207
F4.	LIDAR OBSERVATIONS OF THE DECLINE OF THE EL CHICHON STRATOSPHERIC LOAD H. Jäger, W. Carnuth	208
F5.	AIRBORNE LIDAR OBSERVATIONS OF ARCTIC POLAR STRATOSPHERIC CLOUDS L.R. Poole, G.S. Kent	210
F6.	XeF LIDAR MEASUREMENTS OF DENSITY AND TEMPERATURE IN THE MIDDLE ATMOSPHERE T. Shibata, M. Maeda	211
F7.	LIDAR MEASUREMENTS OF THERMAL STRUCTURE D.B. Jenkins, D.P. Wareing, L. Thomas, G. Vaughan	214
F8.	LIDAR STRATOSPHERIC OZONE MEASUREMENTS AT THE OBSERVATOIRE DE HAUTE PROVENCE (FRANCE) S. Godin, J. Pelon, G. Mégie	215
F9.	LIDAR OBSERVATION OF THE MESOSPHERIC SODIUM LAYER IN ANTARCTICA A. Nomura, Y. Iwasaka, H. Fukunishi, T. Hirasawa, S. Kawaguchi, T. Kano	219
F10.	LIDAR DETECTION OF METALLIC SPECIES AT THE MESOPAUSE LEVEL C. Granier, J.P. Jegou, G. Megie	222
F11.	DAYTIME LIDAR MEASUREMENTS OF TIDAL WINDS IN THE MESOSPHERIC SODIUM LAYER AT URBANA, ILLINOIS K.H. Kwon, D.C. Senft, C.S. Gardner, D.G. Voelz, C.F. Sechrist, Jr. F.L. Roesler	226

SESSION G: CLOUDS AND MULTIPLE SCATTERING

Chairperson: E. Eloranta

Co-Chairperson: J. Weinman

Thursday August 14, 1986

8:30 a.m. - 10:00 a.m.

G1.	LIDAR STUDY OF STORM TOPS J.D. Spinhirne, W.D. Hart	230
G2.	INVESTIGATION OF CLOUDS SPATIAL DISTRIBUTION USING GROUND-BASED LIDAR I.N. Kolev, O.P. Parvanov, B.K. Kaprielov, I.K. Ilev	233
G3.	MULTIPLE SCATTERING DEPOLARIZATION IN MARINE STRATUS CLOUDS: LIDAR EXPERIMENTS K. Sassen, R.L. Petrilla	237

G4. NEAR-IR EXTINCTION AND BACKSCATTER COEFFICIENT MEASUREMENTS IN LOW- AND MID-ALTITUDE CLOUDS Z.G. Sztankay	238
G5. BACKSCATTER AND EXTINCTION MEASUREMENTS IN CLOUD AND DRIZZLE AT CO ₂ LASER WAVELENGTHS S.G. Jennings	244
G6. CLOUD DETECTION BY LIDAR EXTINCTION CALCULATIONS W.J. Lentz	248

SESSION H: POLLUTION STUDIES
Chairperson: N. Takeuchi
Co-Chairperson: H. Inaba

Thursday August 14, 1986
10:30 a.m.- 12:30 noon

H1. WIDE-AREA REMOTE-SENSING SYSTEM OF POLLUTION AND GAS DISPERSAL BY NEAR-INFRARED ABSORPTION BASED ON LOW-LOSS OPTICAL FIBER NETWORK H. Inaba	251
H2. A MOBILE SYSTEM FOR ACTIVE OPTICAL POLLUTION MONITORING A. Sunesson, H. Edner, S. Svanberg, L. Unéus, W. Wendt, K. Fredriksson	255
H3. GAS CORRELATION LIDAR FOR METHANE DETECTION E. Galletti, E. Zanzottera, S. Draghi, M. Garbi, R. Petroni	258
H4. DETECTION OF NO _x , C ₂ H ₄ CONCENTRATIONS BY USING CO AND CO ₂ LASERS W. Gengchen, K. Qinxin	259
H5. MAPM: A COHERENT DUAL CO ₂ LASER DIAL SYSTEM W.B. Grant, J.R. Bogan	263
H6. LASER HETERODYNE SYSTEM FOR OBTAINING HEIGHT PROFILES OF MINOR SPECIES IN THE ATMOSPHERE S.L. Jain, A.K. Saha	264
H7. A CORRELATION LIDAR WITH IMAGE RECEIVER V.K. Beljaev, K.S. Gochelashvily, N.N. Denisov, A.A. Manenkov, V.L. Mitev, TS.A. Mitsev, A.M. Prochorov, E.V. Stoikova, E. Ferdinandov, V.K. Chevokin, M. JA. Schelev (Invited Paper)	265

SESSION I: NEW SYSTEMS
Chairperson: M. Vaughan
Co-Chairperson: M. Huffaker

Friday August 15, 1986
8:30 a.m.- 1:00 p.m.

I1. COHERENT LIDAR SIGNAL FLUCTUATION REDUCTION BY MEANS OF FREQUENCY DIVERSITY TECHNIQUE R.M. Schotland, P. V. Cvijin, Yan-Zeng Zhao	266
--	-----

I2.	WAVELENGTH DEPENDENCE OF COHERENT AND INCOHERENT SATELLITE-BASED LIDAR MEASUREMENTS OF WIND VELOCITY AND AEROSOL BACKSCATTER M.J. Kavaya, R.M. Huffaker	269
I3.	THE NCAR AIRBORNE INFRARED LIDAR SYSTEM (NAILS) R.L. Schwiesow, P.A. Lightsey	273
I4.	ATMOSPHERIC CORRELATION TIME MEASUREMENTS USING COHERENT CO ₂ LIDAR G.M. Ancellet, R.T. Menzies	276
I5.	PULSED MONONODE DYE LASER DEVELOPED FOR A GEOPHYSICAL APPLICATION J.P. Jegou, T. Pain, G. Mégie	280
I6.	CALIBRATION AND ANALYSIS FOR A 0.53 μ m INCOHERENT DOPPLER LIDAR J. Sroga, A. Rosenberg	283
I7.	CO ₂ LIDAR SYSTEM FOR ATMOSPHERIC STUDIES R. Barbini, A. Ghigo, M. Giorgi, K.N. Iyer, A. Palucci, S. Ribezzo	287
I8.	GENERATION OF ATTENUATION CORRECTED IMAGES FROM LIDAR DATA E. W. Eloranta, D.K. Forrest	291
I9.	GAS DISPERSION MEASUREMENTS USING A MOBILE RAMAN LIDAR SYSTEM J.D. Houston, D.R. Brown	295
I10	SPECTROSCOPIC ASPECTS OF DIFFERENTIAL METHOD FOR SOUNDING GAS COMPOSITION OF THE ATMOSPHERE V.V. Zuev, I.I. Ippolitov, Yu.N. Ponomarev	298
I11.	LINEWIDTH CHARACTERISTICS OF RAMAN-SHIFTED DYE LASER OUTPUT AT 720 AND 940 nm B.E. Grossmann, U.N. Singh, N.S. Higdon, L.J. Cotnoir, T.D. Wilkerson E.V. Browell	300
I12.	THE GSFC GROUND-BASED LIDAR FOR THE MEASUREMENT OF STRATOSPHERIC OZONE T.J. McGee	305
I13.	DEVELOPMENT OF A SIMULTANEOUS MULTI-WAVELENGTH DYE LASER FOR DIFFERENTIAL ABSORPTION TECHNIQUE Y. Saito, A. Nomura, T. Kano	306
I14.	ALEXANDRITE LASER SOURCE FOR ATMOSPHERIC LIDAR MEASUREMENTS J. Pelon, C. Loth, P.H. Flamant, G. Mégie	310
I15.	THE TFP AND A PULSED LD: NEW LIDAR COMPONENTS H. Shimizu, I. Matsui, K. Asai	314
I16.	CHEMICAL CONTAMINATION REMOTE SENSING J.P. Carrico, K.R. Phelps, E.N. Webb, R.A. MacKay, E.R. Murray	318
	AUTHOR INDEX	319

N87

10264

UNCLAS

ESA ACTIVITIES IN SPACE LASER SOUNDING AND RANGING

H. Lutz
European Space Agency, ESA/ESTEC
Keplerlaan 1 - Postbus 299
2200 AG Noordwijk, The Netherlands

Laser remote sensing from space is undoubtedly one of the most promising means to obtain essential atmospheric and geophysical parameters on a global scale. Efforts including feasibility assessments, technology developments and mission definition studies are in progress at the European Space Agency (ESA) to prepare for the prospective use of laser remote sensing systems in space. This paper will present an overview of the programs under way and discuss the perspectives of laser remote sensing in the context of ESA's Long-Term European Space Plan.

ESA technological preparation in the field of laser remote sensing is directed towards lidar technology for atmospheric sounding and laser ranging systems for use in solid-earth geophysics. Development efforts in spaceborne laser ranging concentrate on CO₂ laser Doppler systems for precise geoid mapping using satellite-to-satellite tracking, and on dual-wavelength picosecond pulse ranging for accurate distance measurements to ground. Activities in the lidar area focus on the development and early deployment of a direct-detection backscatter lidar which, when combined with passive sensors, can provide valuable data for weather forecasting and climate prediction.

Following the recommendations of an ESA Workshop on Space Laser Applications and Technology (SPLAT), held in March 1984, a Technology Working Group on Space Laser Sounding and Ranging has now been established. The group is composed of scientists, users and laser instrumentation specialists, and its task is to advise ESA on requirements and development priorities in the area of laser remote sensing. The group's charter also includes the elaboration of an implementation plan for spaceborne laser monitoring systems, together with the identification and examination of flight opportunities. Preliminary conclusions of the working group will be presented.

In January 1985, the governments of the ESA member states endorsed the proposal for a Long-Term European Space Plan, opening up new perspectives for satellite-borne laser remote sensing, particularly for what concerns flight opportunities, platform capabilities and funding of relevant development work. An In-Orbit Technology Demonstration Program (TDP) has been approved, providing a suitable framework for the in-orbit verification of laser remote sensing instruments. Using the European Retrievable Carrier (EURECA), demonstration flights of up to 6 months duration will be possible, with adequate platform mass and power resources available. Similarly, the European contribution (COLUMBUS) to the US Space Station might offer a serviceable polar platform which would open up further opportunities for experimental missions involving lidars or other laser remote sensing instruments.

N87

10265

UNCLAS

LIDAR REMOTE SENSING FROM SPACE: NASA'S PLANS IN THE EARTH SCIENCES

Robert J. Curran
Earth Sciences and Applications Division
Office of Space Sciences and Applications
National Aeronautics and Space Administration
Washington, DC 20546

NASA, in collaboration with the Earth Sciences community, is developing a multidisciplinary study of the Earth System to provide a better understanding of the complex interrelated processes involved in that system. The name given to this NASA program is the Earth Observing System (Eos). Capabilities of the Space Station, both the polar orbiting platform and the lower inclination platforms, will be used to accommodate a number of large active and/or passive sensors. These platforms are well matched to the requirements of anticipated lidar instruments. Two lidar instruments being considered as part of the Eos payload are the Lidar Atmospheric Sounder and Altimeter (LASA) and the Laser Atmospheric Wind Sounder (LAWS). For each of these lidar instruments, a panel composed of earth scientists as well as laser technologists has been assembled to describe the science objectives and instrument characteristics.

The LASA instrument is separable into two portions: the atmospheric sounder component and the retroranging component. The LASA atmospheric sounder will sample the spatial distribution of several atmospheric parameters. Most significant in terms of improved understanding of the global hydrological cycle is atmospheric water vapor. Characteristic of a lidar instrument, LASA will provide high spatial resolution observations of water vapor and other atmospheric parameters, with limited coverage. These characteristics make LASA observations a strong contributor to synergistic studies utilizing observations from a number of other Eos sensors. The primary objective of the retroranging component of LASA will be to determine the precise three-dimensional position of specifically placed retro-reflectors and to sense how these retro-reflectors change position over monthly to yearly time periods.

The instrument concept for LAWS utilizes a lidar system capable of measuring the Doppler shift in the backscattered intensity to determine the wind velocity profile. The ability to directly measure atmospheric motions is a scientific goal crucial to future progress in the atmospheric sciences. Early testing of the LAWS concept is being considered for both the Shuttle and Space Station platforms. The current concept of the NASA Eos LASA and LAWS lidar systems will be described including their measurement objectives and evolution for follow-on flights.

N87

10266

UNCLAS

TUNABLE SOLID-STATE LASER TECHNOLOGY FOR
APPLICATIONS TO SCIENTIFIC AND TECHNOLOGICAL
EXPERIMENTS FROM SPACE

F. Allario and L. V. Taylor
NASA Langley Research Center, Flight Electronics Division
Hampton, VA 23665 U.S.A.

Current Agency plans for the NASA Earth Observing System (Eos) include development of a lidar facility to conduct scientific experiments from a polar orbiting platform. A recommended set of experiments to meet the Eos scientific investigations has been scoped by the Laser Atmospheric Sounder and Altimetry (LASA) panel, which includes techniques of atmospheric backscatter (Lidar), Differential Absorption Lidar (DIAL), altimetry, and retroranging. For the DIAL experiments, which include measurements of the vertical profiles of water vapor, pressure, temperature and ozone, tunable lasers are required with fairly stringent performance requirements on average power, spectral purity, stability and tunability over a broad range of the electromagnetic spectrum. These requirements have been scoped by the LASA panel members.

Additionally, preliminary assessments of the resources (power, weight, volume) required by the Eos Lidar Facility have been conducted. These assessments included trade-off studies between various telescope diameters, laser transmitter technologies and optical receiver systems. An obvious approach to reduce the weight, power and volume required from the Eos space platform is to incorporate elements of the newly emerging tunable solid state laser technology.

In response to Eos and other technological needs, a research program in tunable solid state laser technology has been developed at the NASA Langley Research Center. This research program includes laser materials development, modeling and experiments on the physics of solid state laser materials, and development of solid state laser transmitters with a strong focus on Eos scientific investigations. In this paper, we will discuss some of the system studies that have been conducted which highlight the payoff of solid state laser technology for the Eos scientific investigations. Additionally, a summary of some promising research results which have recently emerged from our research program will be presented, and will be used to project the future research and development program required to bring this promising technology to fruition for the Eos era.

Although an important goal of the solid state laser research program is for the development of tunable laser technology for the Eos lidar facility, there are other important applications, including the NASA Global Tropospheric Research Program and interesting technological experiments from the Space Shuttle and NASA high flying aircraft. Comments will be offered in this presentation on some future possibilities in technological experiments that can be conducted on these platforms.

N87

10267

UNCLAS

COHERENT LIDAR TECHNOLOGY FOR GLOBAL WIND PROFILING

R. Milton Huffaker

Coherent Technologies, Inc.
P.O. Box 7488
Boulder, Colorado 80306-7488
USA

INTRODUCTION

Coherent lidar systems are proven sensors for atmospheric wind measurement. Ground-based and airborne CW and pulsed CO₂ systems have been developed and applied to several wind measuring applications. Analytical and hardware feasibility studies[†] indicate the feasibility of measuring the global wind field from a space platform. Global wind profiles are a needed input to global circulation models for improved weather forecast accuracy. A recent workshop sponsored by NASA on "Global Wind Measurements," in August, 1985 recommended the development of a space-based global wind profiling system.

GLOBAL AEROSOL BACKSCATTER

The most critical unknown in the design of a Global Wind Profiling System is the aerosol backscatter cross section for the selected laser wavelengths. For the CO₂ laser a wavelength of 9.11 microns was recommended. A Global Backscatter Experiment (GLOBE) is planned by NASA to develop a global model of aerosol backscatter. Several existing lidar systems have been and can be utilized to obtain this data base.

NOAA has obtained a 3-year set of aerosol backscatter profiles at 10.6 microns in the Boulder, Colorado area, using a 100 mJ/pulse coherent CO₂ TEA lidar.* The 95% backscatter value was found to be 5E-11 1/m 1/sr for an 8-km altitude.

JPL has measured aerosol backscatter profiles at 9.25 and 10.6 micron wavelengths in the Los Angeles area for approximately 2 years.[‡] These data indicate a significant increase in backscatter at 9.25 microns in the upper troposphere. The 95% backscatter values at 5-km altitude were found to be 4E-11 and 4E-12 1/m 1/sr at 9.25 and 10.6 microns, respectively.

The Royal Signals and Radar Establishment lidar group has obtained aerosol backscatter profile data at 10.6 microns using an airborne CO₂ CW lidar. Considerable data have been taken over the British Isles and the North Atlantic for the past 3 years.

Ground-based and airborne CW and pulsed CO₂ lidar systems have been used by NASA-MBFC to obtain aerosol backscatter data.

[†] R.M. HUFFAKER, NOAA TECH. MEMO. ERL WPL-37 SEPT 1978

* M.J. POST, APPLIED OPTICS, VOL. 23, NO. 15, AUG 1984

[‡] R.T. MENZIES, M.J. KAVAYA, F.H. FLAMANT, D.A. HANER, APPLIED OPTICS, VOL. 23, NO. 15, AUG 1984

A joint experiment between NASA and CSIRO, to measure aerosol backscatter in the Southern Hemisphere, is under way in Melbourne, Australia using a NASA-MSFC CW coherent CO₂ lidar operating on a CSIRO aircraft. Ground-based aerosol backscatter profiles will also be obtained using a ruby and a pulsed CO₂ lidar. The CSIRO aircraft will be equipped with aerosol sampling instruments such as optical particle counters and cascade impacters.

Aerosol backscatter data are needed in the Southern Hemisphere where aerosol concentrations are expected to be minimal. The current aerosol backscatter data set is primarily in the mid-latitude northern hemisphere. The NASA GLOBE program should answer this critical design parameter for a global wind profiling system.

COHERENT LIDAR HARDWARE TECHNOLOGY

The NOAA 2 J/pulse CO₂ injection-locked TEA lidar is the most engineered coherent TEA lidar presently in operation. This lidar is being used for meteorological research and includes a hardware processor and real-time color displays.

The JPL 2 J/pulse injection-locked CO₂ TEA lidar has been used primarily for aerosol backscatter measurement but is now capable of wind observation.

The Air Force Geophysics Laboratory is developing an e-beam excited 2 J/pulse CO₂ TEA lidar for wind and aerosol backscatter measurement.

The recommended laser power for a global wind profiling system is 10 J/pulse. Current CO₂ lidar systems are demonstrating 2 J/pulse capability. Scaling to 10 J/pulse should not be a major consideration. The required life-time in space is now the critical hardware issue.

It now seems possible to develop a Nd:YAG coherent lidar. Components have been stabilized at Stanford University. A solid-state laser source, the most critical element in a solid-state coherent lidar, is now possible for coherent Doppler measurements. The system problems that need to be solved are significant but should be solvable. Coherent Technologies, Inc. has plans to develop a 0.5 J/pulse coherent Nd:YAG lidar for wind and aerosol backscatter measurement. Eyesafe wavelength solid-state coherent lidar systems also appear to be feasible.

Coherent lidar technology continues to advance rapidly. Current systems are certainly scalable to satellite conditions. Technology assessments continue to indicate the feasibility of measuring the global wind field from a space platform.

N87

10268

UNCLAS

DEVELOPMENT OF A HIGH-ALTITUDE AIRBORNE DIAL SYSTEM--THE
LIDAR ATMOSPHERIC SENSING EXPERIMENT (LASE)

E. V. Browell, W. R. Vaughan, W. M. Hall, J. J. Degnan^a,
R. D. Averill, J. G. Wells, D. E. Hinton, and J. H. Goad

NASA Langley Research Center
Hampton, Virginia, 23665-5225, USA

The ability of a Differential Absorption Lidar (DIAL) system to measure vertical profiles of H₂O in the lower atmosphere has been demonstrated both in ground-based¹⁻³ and airborne^{4,5} experiments. In these experiments, tunable lasers were used that required real-time experimenter control to locate and lock onto the atmospheric H₂O absorption line for the DIAL measurements. The Lidar Atmospheric Sensing Experiment (LASE) is the first step in a long-range effort to develop and demonstrate an autonomous DIAL system for airborne and spaceborne flight experiments. The LASE instrument is being developed to measure H₂O, aerosol, and cloud profiles from a high-altitude ER-2 (extended range U-2) aircraft. This paper presents the science of the LASE program, describes the LASE system design, and discusses the expected measurement capability of the system.

The measurement of tropospheric H₂O profiles and column content with the LASE system can be used in various atmospheric investigations, including studies of air mass modification, latent heat flux, the water vapor component of the hydrological cycle, and atmospheric transport using H₂O as a tracer of atmospheric motions. The simultaneous measurement of aerosol and cloud distributions can provide important information on atmospheric structure and transport, and many meteorological parameters can also be inferred from these data. In addition, the impact of subvisible and visible aerosol/cloud layers on passive satellite measurements and radiation budgets can be assessed. The atmospheric science investigations that can be conducted with LASE are greatly enhanced because measurements of H₂O profiles and column content are made simultaneously with aerosol and cloud distributions. The LASE measurement objectives are given in Table 1. These objectives are consistent with the measurement requirements needed to conduct atmospheric investigations on the spatial scales indicated.

A block diagram of the LASE system is shown in Figure 1, and the LASE system parameters are given in Table 2. The transmitter consists of two Alexandrite lasers that are independently tunable over the wavelength range from 726.5 to 732.0 nm. With the assistance of a wavemeter, one of the Alexandrite lasers is tuned to the center of the selected H₂O absorption line, and the second laser is tuned off the absorption line but within 70 pm of the first laser. The laser

^a NASA Goddard Space Flight Center, Greenbelt, Maryland,
20771, USA

pulses are sequentially transmitted with about 400 μ s separation. This permits the use of the same avalanche photodiodes (APD) for detecting the lidar returns. The use of low and high light level APD's are used to provide linear response to atmospheric and cloud/ground returns, respectively. Lidar returns are digitized and recorded at 5 Hz, and when possible, the data are telemetered to the LASE ground station for real-time processing and experiment control. Operation with either of two preselected H₂O lines can be made during the mission to optimize the measurement of H₂O in different altitude regions. A detailed description of the LASE system is presented in this paper.

Extensive simulations have been conducted to establish performance requirements for the various LASE subsystems. A simulation of the combined H₂O measurement errors for the LASE system is shown in Figure 2. The errors considered include those from systematic and random sources. With atmospheric modeling and analysis of the off-line lidar return for aerosol scattering distributions, the LASE measurement uncertainties can be reduced to less than 10 percent over about an 8 km altitude range. If the LASE system performance exceeds the minimum requirements, as expected, the measurement error can be further reduced. The capability of the LASE system to measure H₂O profiles and column content is discussed in this paper.

References

1. Schotland, R. M.: Some Observations of the Vertical Profile of Water Vapor by Means of a Laser Optical Radar. Proc. of the Fourth Symposium on Remote Sensing of the Environment, Ann Arbor, Michigan, April 12-14, 1966, pp. 273-283.
2. Browell, E. V., T. D. Wilkerson, and T. J. McIlrath: Water Vapor Differential Absorption Lidar Development and Evaluation. Appl. Opt., 18, 2474-3483 (1979).
3. Cahen, C., G. Megie, and P. Flamant: Lidar Monitoring of the Water Vapor Cycle in the Troposphere. J. Appl. Meteor., 21, 1506-1515 (1982).
4. Browell, E. V.: Remote Sensing of Tropospheric Gases and Aerosols with an Airborne DIAL System. In Optical and Laser Remote Sensing, D. K. Killinger and A. Mooradian, eds., Springer-Verlag (1983), pp. 138-146.
5. Browell, E. V., A. K. Goroch, T. D. Wilkerson, S. Ismail, and R. Markson: Airborne DIAL Water Vapor Measurements Over the Gulf Stream. Proc. of the Twelfth International Laser Radar Conference, Aix en Provence, France, August 13-17, 1984, pp. 151-155.

Table 1. LASE Measurement Objectives

ATMOSPHERIC PARAMETER	INVESTIGATION REGION	ALTITUDE RANGE, km	SPATIAL RESOLUTION		MEASUREMENT UNCERTAINTY, %	
			HORIZONTAL, km	VERTICAL, m	NIGHT	DAY*
H ₂ O PROFILE	MESOSCALE	0-3	10	200	10	15
	CLOUD CLUSTER	0-3	100	200	8	12
		3-17	100	500	8(5**)	10
	LARGE SCALE	0-17	250	500	8(5**)	10
H ₂ O COLUMN CONTENT**	SUB-CUMULUS SCALE	---	200 m	---	8	10
ATMOSPHERIC BACKSCATTER	AEROSOL AND CLOUDS (SUB-CUMULUS CLOUDS)	0-17	40 m	50	3	5

* OCEAN ALBEDO

** WITH EXPECTED SPECTRAL PURITY IMPROVEMENT

Table 2. LASE H₂O DIAL Parameters

<u>Transmitter</u>	
Energy per Pulse	150 mJ (on & off)
Linewidth	1.1 pm
Rep. Rate	5 Hz
Wavelength	726.5 - 732.0 nm
Beam Divergence	0.73 mrad
Pulse Width	300 ns
Aircraft Altitude	16 - 21 km
Aircraft Velocity	200 m/s
<u>Receiver</u>	
Area (Effective)	0.11 m ²
Field of View	1.23 mrad
Filter Bandwidth	0.3 nm (Day) 20 nm (Night)
Optical Transmittance (Total)	23% (Day) 70% (Night)
Detector Efficiency	80% APD (Si)
Noise Eq. Power	7.5×10^{-15} W/Hz ^{1/2} (-20°C for Si APD)
Excess Noise Factor (APD)	1.5
Amplifier Noise (for APD)	710 Photoelectrons/μs

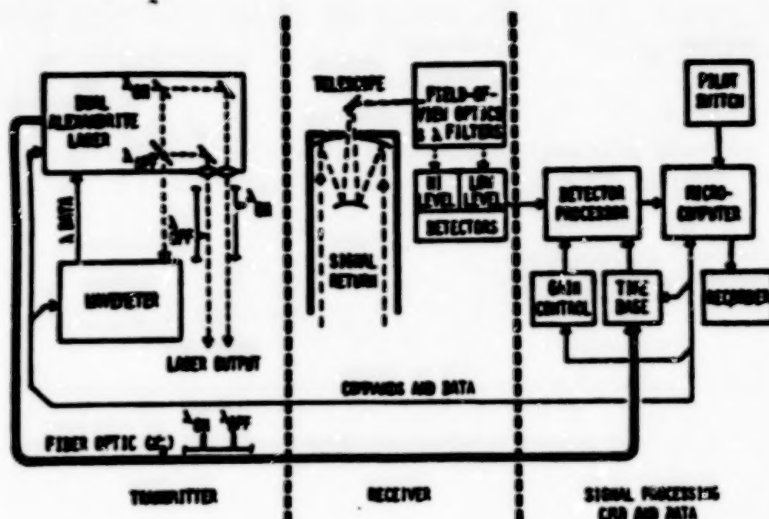


Figure 1. LASE system block diagram.

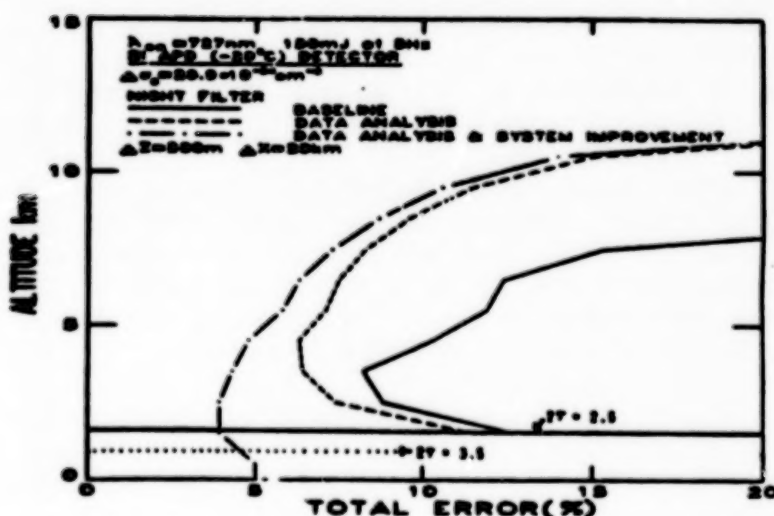


Figure 2. LASE H₂O DIAL combined measurement errors from all sources. Calculations assume aircraft altitude of 16 km and mid-latitude summer H₂O profile. Baseline curve assumes system performs to minimum requirements and no corrections made for systematic errors. Data Analysis line reflects correction for systematic errors, and System Improvements curve represents measurement improvement that would occur if the system performs beyond minimum requirements as expected.

N87

10269

UNCLAS

**MIE LIDAR PROPOSED FOR THE GERMAN SPACE SHUTTLE
MISSION D2**

W. Renger
DFVLR, Institute for Atmospheric Physics
Muenchner Str. 20, D-8031 Wessling, FRG

M. Endemann
Battelle-Institut
Am Roemerhof 35, D-6000 Frankfurt 90, FRG

H. Quenzel
Meteorologisches Institut der Universität München
Theresienstr., D-8000 Muenchen 2, FRG

Ch. Werner
DFVLR, Institute of Optoelectronics
Muenchner Str. 20, D-8031 Wessling, FRG

For more than 15 years now, proposals for spaceborne lidars have been discussed by many research groups. Technical feasibility studies for different lidar designs were performed in the US as well as in Europe, and scientific working groups from NASA and ESA were and still are elaborating new applications of lidar technique, weighing the benefit against competitive methods and in combination with passive sensors.

There are firm plans for a second German spacelab mission (D2- mission) originally scheduled for late 1988 which will be basically a zero-g mission, but will also include earth observation experiments. Encouraged by our experience with airborne lidar systems and the results from theoretical studies, we have proposed a backscatter lidar for this mission.

Since the lidar is only a "parasitic" instrument on the D2- mission, and since the available time to construct the experiment is extremely short, we are deriving the following guidelines:

- Use presently available techniques
- Use available space proofed pressurized containers for housing the various critical subcomponents (e.g. laser, power supplies) to minimize qualification testing
- Demonstrate the expected benefit of active technique in combination with passive sensors
- Validate lidar data by independent measurements

With these limitations, we are aiming at the following experiment parameters:

- Nd-YAG Laser, 10 Hz (700 m horizontal resolution)
400 mJ at 1064 nm, 120 mJ at 532 nm
- Cassegranian Telescope, 50 cm diam., FOV 0.2... 1 mrad
- Receiver: APD (1.06 μ m), PMT (0.53 μ m)
- 12 bit digitization at 3 MHz (50 m vertical resolution)
Photon counting for nighttime measurements
- optional experiment equipment is a 10 μ m radiometer

The laser with power supply and alignment control mechanism will be mounted in a Getaway-Special (GAS) container to avoid time-consuming qualification procedures. The receiving telescope with signal and alignment detectors will either be mounted in a second GAS container with lid or externally. The structures are fixed onto the Unique Support Structure (USS) of the spacelab facility and utilize the standard interface to spacelab. The lidar can be reflown on later shuttle missions without major modifications.

The D2-lidar facility will allow us to perform a number of different measurements with the goal to obtain performance data for the design of future operational spaceborne lidar instruments:

- Cloud top heights

Accurate knowledge of cloud top height together with data from passive sounders promises to increase the accuracy of the height assignment from wind-, temperature- and humidity measurements. Data from spaceborne lidar are required to answer the questions about the required horizontal resolution for useful average values, optimum vertical resolution, the influence of the spot size on the measurement accuracy, etc.

- Height of planetary boundary layer

The height of the PBL is not only an important climate parameter, but also the major parameter for pollutant transport. The data from the D2-lidar will allow us to assess the feasibility to extract the PBL-height from the backscatter data.

- Optical thickness and cloud base height of thin and medium thick clouds

The source of incorrect temperature soundings at cloud top levels is often the unknown emissivity of clouds which is coupled to their optical depth. In addition even subvisible thin cirrus clouds which are not detectable by present passive methods are masking any measurements of passive optical sensors. By the D2-lidar these thin clouds can easily be detected and the lidar derived optical quantities could help for corrections.

- Ice-/water phase discrimination for clouds

This information can be yielded by cross polarization measurements and is of importance for heat budget studies and weather forecast.

- Tropopause height

Lidar measurements performed in the past show in many cases a distinct change in the lidar return at tropopause level due to the blocking effect of this temperature inversion. Spaceborne lidar data are needed to verify this measurement capability of lidar.

- Tropospheric aerosols

Lidar profiles can help to determine the extent of distributed aerosol layers, their transport and the change of optical properties of the atmosphere by changing aerosol loads.

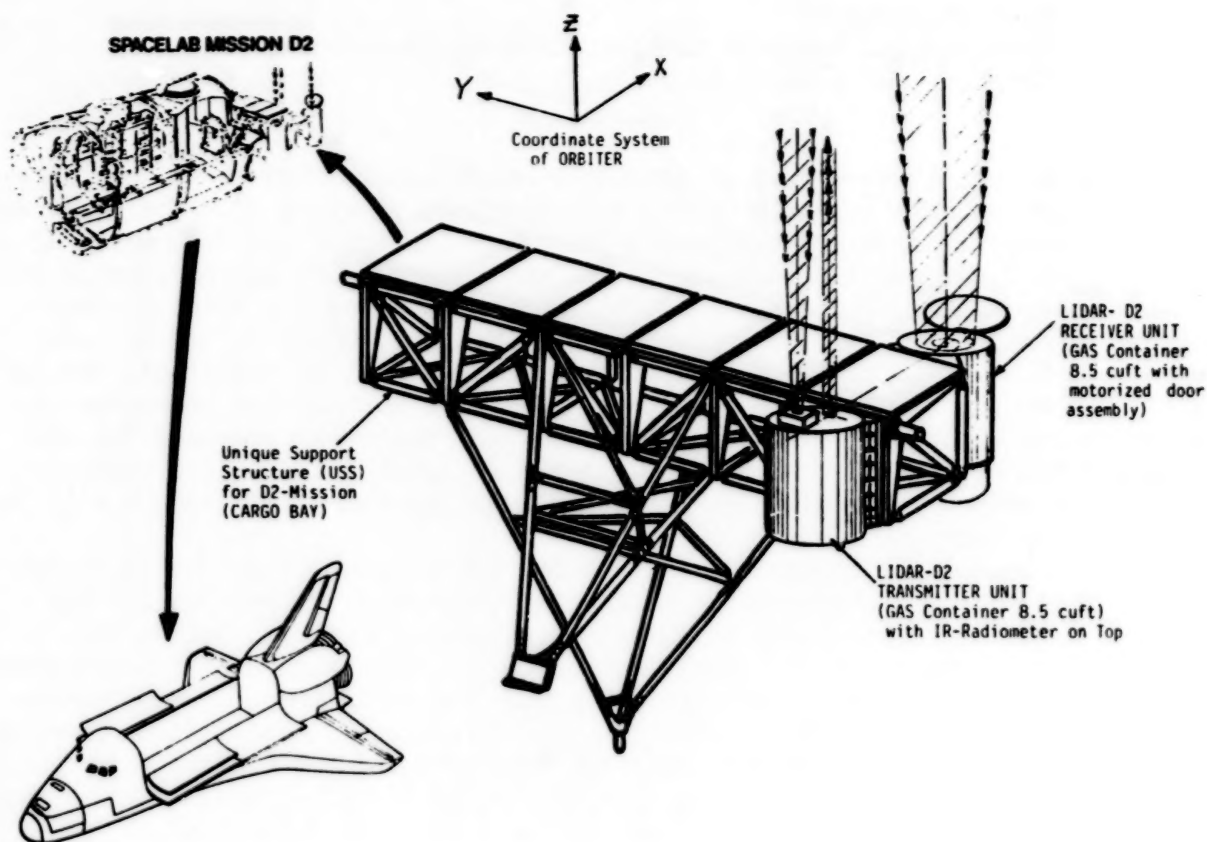
- Stratospheric aerosols

Stratospheric aerosol model assumptions are by now well established to derive aerosol mass loading from lidar data and to calculate effects on the stratosphere (climate, optics).

To validate data gathered by the D2 lidar, a limited ground truth campaign at areas with good probability for adequate weather conditions (like in North Africa) is planned.

BIBLIOGRAPHY

Experiment Proposal for D2 Facilities
 Meteorologisches Institut München, DFVLR-NE-OE, DFVLR-NE-PA,
 Battelle-Institut e. V.
 November 1985.



EXAMPLE FOR LIDAR-D2 ACCOMMODATION ON THE UNIQUE SUPPORT STRUCTURE

N87

10270

UNCLAS

THE LIDAR IN-SPACE TECHNOLOGY EXPERIMENT (LITE)

M. P. McCormick*

NASA Langley Research Center, Atmospheric Sciences Division
Hampton, VA 23665 U.S.A.

A spaceborne lidar system is presently being constructed for flight aboard the U.S. space shuttle in early 1991. The experiment, called LITE for Lidar In-Space Technology Experiment, utilizes a neodymium:YAG laser and 0.85-meter effective diameter Cassegranian-configured telescope receiver for making elastic backscatter measurements. The laser will be frequency doubled and tripled simultaneously producing at a 10-Hz rate 200 mJ at 1064 nm, 400 mJ at 532 nm, and 150 mJ at 355 nm. The field of view of the receiver will be adjustable with a nominal 3.4 mr for nighttime measurements and 1.7 mr for daytime measurements. A turning mirror with quad-detector in the receiver system will be used for the 355-nm and 532-nm channels and a silicon avalanche photodiode will probably be used for the 1064-nm channel. The backscatter at all three wavelengths will be simultaneously recorded.

The technological objectives of LITE are to evaluate lidar system operations in space, lidar techniques in space, and to provide a test bed for new lidar techniques in later flights. The measurement objectives include the determination of cloud top and planetary boundary layer heights, the measurement of tropospheric and stratospheric aerosols, and the measurement of temperature and density between 10 to 40 km altitude. Detailed simulations will be presented showing the errors associated with each of these measurement objectives. In addition, the experiment scenario will be described including measurement times, data flow, processing and archival, and initial plans for validation of the LITE data set with correlative measurements.

*Project scientist for LITE. Many others have contributed to the material to be presented in this talk. These include but are not limited to the Project Manager, Mr. Richard Nelms, the Instrument Manager, Mr. Harold Poole, and the following engineering group leaders: Messrs. Leonard Kopia, John Cox, Richard Couch, Anthony Jalink, and William Fuller.

17801-78W

ADVANCES IN LIDAR ATMOSPHERIC STUDIES IN THE USSR

V.E. Zuev

Institute of Atmospheric Optics SB

USSR Acad. Sci. Tomsk, USSR

This paper presents an analysis of advances in technique developments and lidar creation for atmospheric monitoring. Based on aerosol and molecular scattering, absorption, Raman scattering, and fluorescence methods for the solution of inverse problems of laser sounding are given. Results of complex investigations of the atmosphere are discussed.

N87

10271

UNCLAS

AEROSOL STUDIES IN MID-LATITUDE COASTAL ENVIRONMENTS IN AUSTRALIA

S.A. YOUNG, D. CUTTEN⁺, M.J. LYNCH and J.E. DAVIES

School of Physics and Geosciences

W.A. Institute of Technology, Perth, Western Australia

⁺Electronics Research Laboratory

Department of Defence

Defence Science and Technology Organisation

GPO Box 2151, Adelaide, South Australia

INTRODUCTION

LIDAR is capable of remotely measuring range - resolved aerosol and molecular backscattering with good spatial and temporal resolution over significant ranges. Under certain atmospheric conditions, extinction coefficients can be derived from the backscattered signal through a β/σ relationship. Under conditions of horizontal homogeneity and moderate levels of atmospheric extinction, it should be possible to establish useful β/σ relationships for each of the particular air masses studied. Hence, the potential capability exists for LIDAR to measure and characterise aerosol extinction height profiles which are representative of temperate and tropical maritime environments around Australia that include both seasonal and diurnal variations. The long term aim is to establish a database and to use the data in the LOWTRAN atmospheric computer model¹ to make it more representative of the Australian environment.

This paper will present the results of the evaluation of several inversion procedures that were used to select one which provides the most accurate atmospheric extinction profiles for small aerosol extinction coefficients (that often predominate in the maritime airmass). Height profiles of atmospheric extinction calculated by a two component atmosphere solution

to the LIDAR equation will be compared with corresponding in situ extinction profiles based on the size distribution profiles obtained in Western Australia. Values of the aerosol backscatter to extinction ratio obtained from multi-angle LIDAR measurements will be used in this solution.

INSTRUMENTATION

A LIDAR from WAIT was employed for determining the aerosol backscattered signal. The instrument, which is of a standard configuration, employs a Quanta Ray DCR 2A Nd:YAG frequency-doubled laser as the source. A 25 cm diameter telescope, a 1 nm bandwidth interference filter centred on 0.53 μm and an EMI model 9816B comprise the receiver. Linearly or logarithmically amplified signals are sampled at up to 20 MHz using an 8-bit digitiser based on the TRW 1007J ADC. Data are stored on floppy discs by a PDP11/23 processor. Other data including laser output pulse energy, azimuth and elevation angles, signal sampling interval etc., also are stored. The laser has a plane polarized output beam enabling total backscatter or the parallel and depolarised components to be measured.

Ground based meteorological measurements consisted of air temperature, relative humidity, wind speed and direction. An integrating nephelometer operating at an effective wavelength of 0.5 μm and a condensation nuclear particle counter provided data on aerosol scattering and total particle concentrations, respectively: such data helped classify the air mass.

Slow ascent radiosonde data provided air temperature and relative humidity profiles to about 7 km with a resolution of 150-200 m. Balloons were released at the lidar site with a minimum of one for each measurement period and an extra flight if conditions changed sufficiently to warrant it.

The instrumentation in the CSIRO F27 aircraft consisted of three instruments which could size aerosol particles over the size range 0.2-100 μm diameter plus total particle counter, air temperature and dew point meter units.

FIELD STUDIES

Four field studies have been undertaken at a coastal site (Garden Island, lat.32S, long.116E), 40 km SSW of Perth, Western Australia. The study periods were selected to allow the seasonal variability of aerosols to be investigated.

Typically winter is dominated by low pressure systems of polar origin

which bring easterly moving cold fronts and winter rains to the coastal region. The airmass in these circumstances is expected to be representative of very clean maritime air.

Summer is dominated by slow moving sub-tropical high pressure systems which, when located over the continent, can bring strong easterly flows of 3-6 days persistence. In a typical weather pattern the coastal region experiences warm easterly flows during night and mornings and a strong sea breeze from mid-morning to the evening.

In order to study aerosol variability, not just seasonally, but also over the diurnal cycle, measurements were taken during morning, afternoon and evening periods. Slant path measurements were normally recorded at 5° increments in elevation angle, although occasionally 1° increments were used to study events of interest. The October 1984 study was supported on 3 days by an instrumented Fokker F27 aircraft operated by the CSIRO Division of Atmospheric Research. Aerosol and meteorological parameters were obtained in a series of spiral descents from 6000 m to the surface through the same airmass sampled by the LIDAR.

The investigation of aerosol scattering close to the sea surface was supported by separate measurements with the LIDAR beam horizontal and as close to the surface (~4 m) as the site permitted. Typically, sequences of 20 shots at 2 Hz were recorded with this configuration.

Over 1986-1987 three further field studies are planned in tropical maritime air at Cowley Beach (lat.17.4S, long.146E) 30 km south of Innisfail on the North Queensland Coast.

DATA ANALYSIS PROCEDURES

The maritime atmospheres at Garden Island studied by the LIDAR are usually very clear with high visibilities and low aerosol scattering coefficients. For this reason we were concerned that analysis procedures that assumed a single-component atmosphere with backscatter and extinction related by an expression of the form $\beta = C\sigma^k$ would be inappropriate. Extinction profile solutions, even if performed in the backward direction as recommended by Klett², and Ferguson and Stephens³ were expected to converge very slowly if an incorrect boundary value was assumed. As the extinction by air molecules was considered to be significant this should be included in the analysis (cf. Fernald⁴ and Klett⁵).

Accordingly different analysis schemes were compared. A scheme that assumed an atmosphere containing both aerosols (A) and air molecules (M) with backscatter (β) and extinctions (σ) related by the expression

$$\beta_T = \frac{1}{4\pi} (P_A \sigma_A + P_M \sigma_M)$$
 was compared with the single-component atmosphere

solution. The sensitivity of the solutions to the assumed value of the aerosol phase function for backscatter (P_A) was also tested.

RESULTS

In that the project is not scheduled for completion until December 1987 we will present a review of data analysed to date.

Initially, we present a review of the relative performance of the LIDAR data analysis procedures which have been tested on synthetic atmospheric and aerosol profiles. This will be followed by examples of analysed field data for selected cases.

REFERENCES

1. Kneizys, F.X. et al, "Atmospheric Transmittance/Radiance: Computer Code LOWTRAN6".
AFGL-TR-83-0187, August 1983.
2. Klett, J.D., "Stable Analytical Inversion Solutions for Processing Lidar Returns".
Appl.Opt. 20, p211, 1981.
3. Ferguson, J.D. and Stephens, D.H., "Algorithm for Inverting Lidar Returns".
Appl.Opt. 22, p3673, 1983.
4. Fernald, F.G., "Analysis of Atmospheric LIDAR Observations : Some Comments".
Appl.Opt. 23, p652, 1984.
5. Klett, J.D., "LIDAR Inversion with Variable Backscatter/Extinction Ratios".
Appl.Opt. 24, 1638 1985.

N87

10272

UNCLEAR

VISIBILITY RELATED TO BACKSCATTER AT $1.54\mu\text{m}$

T. L. Barber
Atmospheric Sciences Laboratory
White Sands Missile Range, NM 88002
D. R. Larson
Physical Science Laboratory
New Mexico State University
Las Cruces, NM 88003

ABSTRACT

A need for a remote measurement of visibility is becoming more evident around such facilities as airports, particularly in adverse weather. The lidar process has been shown to have the necessary potential to fulfill this measurement need. From a lidar return optical extinction, hence visibility, can be inferred. The wavelength $1.54\mu\text{m}$ was chosen, being near the visible wavelength region and having a high eye safety threshold, 200,000 times higher than $1.06\mu\text{m}$; $1.54\mu\text{m}$ is the erbium laser wavelength.

This research utilized 105 measured height profiles of natural droplet size distributions data, taken in clouds, fog and haze. These profiles were examined to determine the completeness of the droplet counting data. It was found that the particle spectrometer data were incomplete in the very light fog and haze so this portion of the data was eliminated.

Utilizing the Mie theory, these droplet size distribution profiles were converted to backscatter at $1.54\mu\text{m}$ and extinction in the visible region, $.55\mu\text{m}$. Using Koschmeider's relationship, the extinction profiles were converted to visibility. The visibility and backscatter profiles were compared to develop a relationship between visibility and backscatter at $1.54\mu\text{m}$.

The relationship clearly falls into two areas. The first is a hyperbolic portion, covering conditions found in clouds and heavy fog, for visibility extending from 300m to 700m,

$$v = .23/b$$

The remainder of the data, in light fog (visibility more than 700m), falls along a well defined curve:

$$v = 3.912/\ln(a+cb)$$

67501-78W

where v is visibility, b = backscatter and a , c and p are constants.

We conclude that a lidar of wavelength $1.54\mu\text{m}$ has great potential as a remote visibility measurement system.

N87

10273

UNCLAS

INVERSION OF TWO WAVELENGTH LIDAR DATA FOR CLOUD PROPERTIES

S. R. Pal and A.I. Carswell
 Dept. of Physics and CRESS
 York University

4700 Keele St. Downsview, Ont. M3J 1P3

The inversion of the lidar equation to derive quantitative properties of the atmosphere has continued to present considerable difficulty. Even when the lidar system parameters are known, one is still confronted with a single equation having two unknowns; namely the attenuation coefficient σ (m^{-1}) and the backscatter coefficient β ($\text{m}^{-1} \text{sr}^{-1}$). To perform the inversion it is necessary to have additional information. Even for non-absorbing scattering media where the volume scattering coefficient σ_s equals σ one would have to know a priori the backscatter phase function $P_\pi/4\pi$ since $\beta = \sigma_s (P_\pi/4\pi)$. Lacking this information the solution can be obtained by assuming a relationship between β and σ . The relation, $\beta = c \sigma^k$, (1) where c and k are constants, has been widely used.

With this approach the inversion of the lidar equation has been carried out in a variety of ways of which the backward inversion^{1,2} provides a more stable solution. This method recently brought to the forefront by Klett has been widely discussed in the literature and extensions related to the contribution due to molecular scattering and the spatial dependence of the parameters have been undertaken with some success^{3,4}. Klett's procedure is found to give better results for media with medium to high σ . For media with very low σ and very high σ with considerable multiple scattering, such as in clouds, the accuracy of this procedure is more in doubt. However, very few quantitative experimental evaluations of this inversion procedure have appeared in the literature.

In this paper we wish to report on the results of a study in which we have utilized Klett's procedure for analysis of cloud backscatter measurements made simultaneously at two ruby lidar wavelengths (694 nm, 347 nm). With one lidar system a cloud is probed at the two wavelengths and the backscatter measured simultaneously by separate receivers. As a result we can obtain two σ profiles which should differ only because of the wavelength dependence of the scattering.

The two wavelength measurements can provide better insight into the applicability of the inversion procedure. We have observed that the values of σ of the clouds (to be used is the initial input into the inversion at the two wavelengths) differ considerably for most clouds with the shorter wavelength having larger σ . The match between the inverted σ profiles at the two wavelengths is better in the lower parts

of the profiles while the divergence between them with pulse penetration is a real feature unresolved by the inversion technique.

This divergence, however, may be attributable to the differential multiple scattering at two wavelengths which is not taken into account in the inversion procedure.

Since the beam replenishment in multiple scattering builds up with pulse penetration depth, this causes the effective cloud σ to be reduced from the initial single-scattering value. In the relationship (1) between σ and β the above effect can be included by increasing the value of k used in the inversion. The σ profile inversions with different k values have been investigated in our analysis.

Another limitation of the inversion method has been observed. For a significant number of clouds the backscatter profiles at the two wavelengths had significantly different range dependence and as a result the inverted σ profiles were very different. Changes in the boundary values of σ or in k values used in the inversion were not able to provide a satisfactory match between the two σ profiles. Such behaviour would indicate that the size distributions in the clouds were significantly varying in space and as a result the application of the inversion procedure was inaccurate.

Experimental data will be presented to demonstrate the effects and the implications on the applications of the inversion method will be discussed.

References:

1. J.D. Klett, Appl. Opt. 20, 211, 1981.
2. W. Mitschfeld and J. Borden, J. Meteorol., 11, 58, 1959.
3. F.G. Fernald, Appl. Opt. 23, 652, 1984.
4. Y. Sasano, E.V. Browell and S. Ismail, Appl. Opt. 24, 3929, 1985.

N87

10274

UNCLAS

THE USEFULNESS OF KLETT'S INVERSION ALGORITHMS TO SIMULATED SATELLITE LIDAR RETURNS

M. Kästner, H. Quenzel
University of Munich, Meteorological Institute
Munich, Fed. Rep. of Germany

1. Introduction

The lidar equation is a special form of the radiative transport equation in single scattering approximation and describes the return signal of a lidar. Based on this lidar equation satellite backscatter lidar returns P have been simulated¹ using realistic optical parameters of the atmosphere (β = total backscatter coefficient, σ = total extinction coefficient). The lidar equation reads

$$P(r) = C_G \cdot \frac{1}{r^2} \cdot \beta(r) \cdot \exp\left(-2 \int_{r_0}^r \sigma(\tau) d\tau\right) \quad (1)$$

where r is the range from the lidar to the scattering volume, and C_G is the instrumental constant including the pulse energy. Because of the viewing mode vertically down to the earth surface the range r_0 is at that range where the return signal is detectable and the maximum range r_m is the satellite altitude.

The simulated lidar signal shows the bounds of atmospheric layers with different optical density with a height resolution of about 100 m. It is even possible to detect the upper bound of the planetary boundary layer (PBL) through a thin cirrus cloud. 'Subvisible' clouds not detectable with passive remote sensing techniques will be recognized with satellite lidar.

The inversion of satellite lidar data to the profile of the extinction coefficient and so to the optical depth of each atmospheric layer and the transmission of the atmosphere contributes e.g. to studies on the radiation flux and the radiation budget, from which heating/cooling rates can be derived.

2. Sensitivity study on Klett's algorithm

Klett's² algorithm for retrieving the total extinction coefficient profile has been developed for application to ground-based lidar returns by a backward integration from the far end r_m to the near end r_0 , the range where the incident and backscattered pulse overlap totally. Our study results in an assessment of the applicability of Klett's algorithm to satellite backscatter lidar returns. We used the simulated data¹ of a 1 J Alexandrite laser operated at about $0.7 \mu\text{m}$ and at a satellite flight level of 840 km. Klett assumes a power law for the β - σ -relation ($\beta = c \cdot \sigma^k$), the exponent k has been chosen to be 0.7 according to Fenn³. Klett's solution with backward integration mode reads

$$\sigma(r) = \frac{\exp((S(r) - S(r_m))/k)}{(\sigma(r_m))^{-1} + \frac{2}{k} \int_r^{r_m} \exp((S(\tau) - S(r_m))/k) d\tau} \quad (2)$$

with $S(r) = \ln(P(r) \cdot r^2)$

while the forward integration mode reads

$$\sigma(r) = \frac{\exp((S(r) - S(r_0))/k)}{(\sigma(r_0))^{-1} - \frac{2}{k} \int_{r_0}^r \exp((S(\tau) - S(r_0))/k) d\tau} \quad (3)$$

where $\sigma(r_m)$ is the total extinction coefficient at the far end bound (just above the earth surface) and $\sigma(r_0)$ is the near end bound value (top of the atmosphere) for a satellite lidar system.

Variations of these boundary values result in a parallel shift of the retrieved extinction profile (lin-log-scale) to greater values for greater $\sigma(r_m)$ or $\sigma(r_0)$. Higher values of the exponent k makes the retrieved profile steeper. The stability of both solutions is moderate, because in the forward integration mode the nominator increases and the denominator decreases, while the reverse is true in the backward integration mode.

3. Results

In Fig. 1 the vertical profiles of the total extinction coefficient σ (log-scale) versus the height (lin-scale) are shown resulting from Eqs. (2) and (3) with correct boundary values of $\sigma(r_m)$ and $\sigma(r_0)$, respectively. The solid lines are the known input σ_{in} -profiles of two atmospheric models. In an atmosphere with low turbidity (Fig. 1a) the forward integration mode leads to a better σ_{out} -profile (dashed) than the backward integration mode (dashed-dotted σ_{out} -profile). On the other hand in an atmosphere with high turbidity (Fig. 1b) the backward integration leads to better results. But these two examples give exceptionally good inversion results.

Both modes have been applied to a large number of simulated satellite signals of multiply layered atmospheres, which differ by the aerosol type or the optical depth of each layer. Typical results of the inversions are given in Fig. 2. Fig. 2a) shows the σ_{in} - and two σ_{out} -profiles for a clear atmosphere with a cirrus layer (optical depth = 0.3) between 7.5 and 9.5 km height, Fig. 2b) shows the set of extinction profiles for an atmosphere with low turbidity in the stratosphere and troposphere but very high turbidity in the PBL (desert dust), and Fig. 2c) shows the set of profiles for a turbid stratosphere (volcanic aerosol) and a clear troposphere. All examples demonstrate that both inversion algorithms are unsatisfying for satellite lidar signals, because the inverted profiles are incorrect to about one order of magnitude. A reason for these unsatisfying results is that the values of the pair (c, k) of the power law are different for different aerosol types and that c is assumed to be constant in the derivation of Eqs. (2) and (3) and only one value of k is used in the inversion algorithm.

Recently Klett⁴ proposed an improved algorithm distinguishing between air molecules (subscript R) and aerosol particles (subscript M). The lidar equation for these two scatterers reads

$$P(r) = C_0 \cdot \frac{1}{r^2} \cdot (\beta_R(r) + \beta_M(r)) \cdot \exp\left(-2 \int_{r_0}^r (\sigma_R(\tau) + \sigma_M(\tau)) d\tau\right) \quad (4)$$

A linear law for the β - σ -relation, the aerosol lidar ratio $S_M(r) = \sigma_M(r)/\beta_M(r)$ is assumed in the solution to the aerosol extinction coeffi-

cient. The lidar ratio may change from layer to layer according to the aerosol type. The aerosol extinction coefficient profiles

$$\sigma_M(r) = -A(r) + \frac{X(r) \cdot \exp\left(\int_r^{r_m} (A(\tau) - \sigma_R(\tau)) d\tau\right)}{\frac{X(r_m)}{A(r_m) + \sigma_M(r_m)} + 2 \cdot \int_r^{r_m} X(\tau) \cdot \exp\left(\int_\tau^{r_m} (A(\tau) - \sigma_R(\tau)) d\tau\right) d\tau} \quad (5)$$

with $A(r) = S_M(r) \cdot \beta_R(r)$ and $X(r) = S_M(r) \cdot P(r) \cdot r^2$ and

$$\sigma_M(r) = -A(r) + \frac{X(r) \cdot \exp\left(-\int_r^{r_0} (A(\tau) - \sigma_R(\tau)) d\tau\right)}{\frac{X(r_0)}{A(r_0) + \sigma_M(r_0)} - 2 \cdot \int_r^{r_0} X(\tau) \cdot \exp\left(-\int_\tau^{r_0} (A(\tau) - \sigma_R(\tau)) d\tau\right) d\tau} \quad (6)$$

are the solutions of the backward and forward integration modes of the lidar equation (4).

Above the PBL the values of $A(r)$ and the second term (called $B(r)$) are at least one order of magnitude greater than the value of $\sigma_M(r)$. Slight errors in both terms lead to great errors in σ_M . If $B(r)$ is less than $A(r)$, negative values of $\sigma_M(r)$ are gained, which is more likely with the backward integration mode. Fig. 3 gives the σ_M -profiles according to Eq.(5) (dashed-dotted) and according to Eq.(6) (dashed) and the correct σ_M input profile (solid), the simulated $P(r)$ profile is without noise, the boundary values are the correct ones, the lidar ratio $S_M(r)$ used is by a factor 0.5 too little. The figure shows a relative deviation of the retrieved profile from the input profile to about 0.43 at the surface for the forward and to about 6.7 at the top of the atmosphere for the backward integration mode. The problem how to get the correct values of the lidar ratio has not been solved up to now; perhaps it can be estimated from the lidar signal itself, where the increased information of a multiple wavelength lidar would certainly help.

It is not always advantageous, as Fernald⁵ states, to apply the last calculated $\sigma_M(r)$ as a new boundary value $\sigma_M(r_m)$ or $\sigma_M(r_0)$ because, if this σ_M -value is wrong, this error will propagate through the whole inversion.

In fact, the problem of inverting the lidar returns may be even more complex because there is some evidence⁶ that even in optically rather thin atmospheres the second order scattering cannot be ignored, so that an extended version of the lidar equation must be used. Then there is certainly no chance anymore to get an analytical solution of the inversion problem.

So we try to solve the lidar equation to the aerosol extinction coefficient with an iterative method, which seems to be more stable with respect to inaccuracies in the input data.

- 1 Quenzel, H., E. Thomalla and K. Nodop: Performance Simulations of Backscatter Lidar. In: Vol. 1 of M. Endemann: Orbiting Lidars for Atmospheric Sounding, Battelle-Institut e.V., Frankfurt a.M., December 1984, 107-197.
- 2 Klett, J.D., 1981, Appl. Opt. 20, 211-220.
- 3 Fenn, R.W., 1966, Appl. Opt. 5, 293-295.
- 4 Fernald, F.G., 1984, Appl. Opt. 23, 652-653.
- 5 Klett, J.D., 1985, Appl. Opt. 24, 1638-1643.
- 6 Ricklefs, U., 1985, Doctorate-Thesis, Univ. Karlsruhe, 153 p.

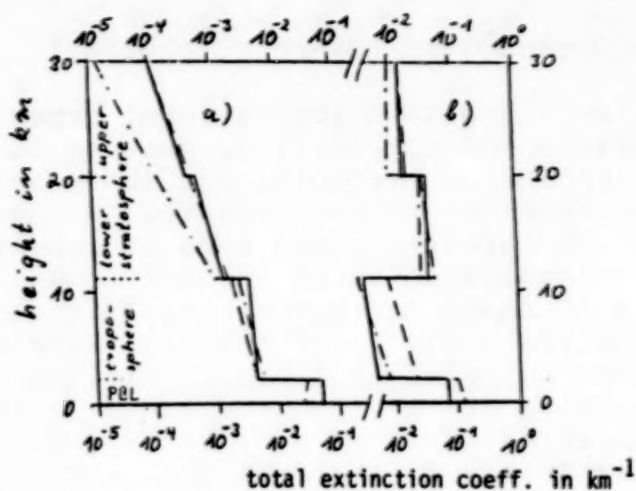


Figure 1

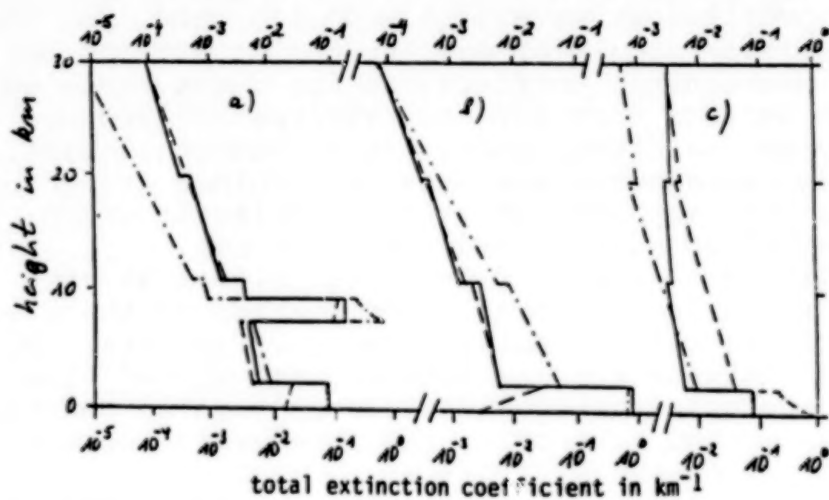


Figure 2

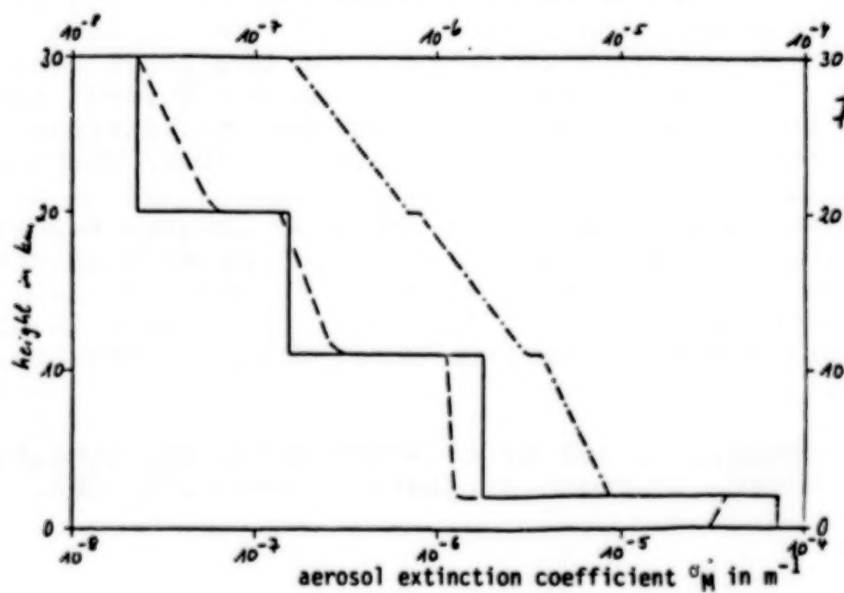


Figure 3

N87

10275

UNCLAS

WAVELENGTH DEPENDENCE OF AEROSOL BACKSCATTER
COEFFICIENTS OBTAINED BY MULTIPLE WAVELENGTH
LIDAR MEASUREMENTSYasuhiro Sasano^a and Edward V. Browell^b

Aerosols are often classified into several general types according to their origin and composition, such as maritime, continental, and stratospheric aerosols, and these aerosol types generally have different characteristics in chemical and physical properties. The present study aims at demonstrating the potential for distinguishing these aerosol types by the wavelength dependence of their backscatter coefficients obtained from quantitative analyses of multiple wavelength lidar signals. Information on aerosol types obtained by this technique would contribute greatly to understanding transport and radiative effects of aerosols on a global scale.

The present study utilized data from the NASA Airborne DIAL System (Browell et al., 1983), which can measure aerosol backscatter profiles at wavelengths of 300, 600, and 1064 nm and ozone profiles from DIAL wavelengths at 286 and 300 nm. Profiles of backscatter coefficients for these three wavelengths were derived from the observations of aerosols of different types (maritime, continental, Saharan desert, rain forest, and stratospheric aerosols in a folded tropopause). Observations were carried out over the Atlantic Ocean, the Southwestern United States, and French Guyana.

Quantitative analysis of the lidar signal at each wavelength is required to obtain information on the wavelength dependence of the aerosol backscatter coefficients. Difficulties in this analysis are, in general, associated with calibrating the total optical efficiency (system constant) of the lidar system and correcting the attenuation of the laser light due to extinction by aerosols.

The solution of the two-component (aerosols and air molecules) lidar equation (Fernald, 1984) was applied in the present data analysis to correct for the laser beam attenuation. This analysis assumes that the aerosol extinction coefficient is proportional to the aerosol backscatter coefficient and that the proportionality factor, which is often

^a This research was conducted at the NASA Langley Research Center while Dr. Sasano was a visiting research scientist at the Old Dominion University Research Foundation, P.O. Box 6369, Norfolk, Virginia, 23508, USA. Dr. Sasano is with the National Institute for Environmental Studies, Tsukuba, Ibaraki 305, Japan.

^b National Aeronautics and Space Administration, Langley Research Center, Hampton, Virginia, 23665-5225, USA.

called an extinction to backscatter ratio, is constant with range. The solution is written as

$$\begin{aligned} & \beta_1(R) + \beta_2(R) \\ & \quad X(R) \exp\{-2(S_1 - S_2) \int_{R_0}^R \beta_2(r) dr\} \\ = & \frac{X(R_0)}{\beta_1(R_0) + \beta_2(R_0)} - 2S_1 \int_{R_0}^R X(r) \exp\{-2(S_1 - S_2) \int_{R_0}^r \beta_2(r') dr'\} dr \end{aligned} \quad (1)$$

where: β and S_1 are the backscatter coefficient and extinction to backscatter ratio, respectively; the subscripts 1 and 2 represent the values for aerosols and air molecules, respectively; R is the range from the lidar; $X(R)$ is the lidar signal corrected for range-squared dependence; and R_0 is the range where a boundary condition is assigned as described below.

Calibration of the system constant was done by giving a boundary condition at a certain range $R=R_0$ in the solution. In practice, the so-called matching method was applied to the lidar signal--an aerosol free layer was assumed at $R=R_0$.

Backscatter coefficient profiles derived from lidar signals through Eq. (1) depend on the extinction to backscatter ratio S_1 as well as on the optical thickness and aerosol distribution. The extinction to backscatter ratio is considered to have a value between about 10 and 90. The solution profile may sometimes be quite different from the true profile when an erroneous extinction to backscatter ratio is assumed.

New methods were proposed and applied to the multiple wavelength lidar signals to reduce uncertainties in the derived backscatter profiles. In the first step of the analysis, the extreme values of the extinction to backscatter ratio (e.g., 10 and 90) are assumed to get possible ranges in the derived backscatter coefficients. The profiles thus obtained sometimes show negative values for the aerosol backscatter coefficient and sometimes diverge. This results from an assumed extinction to backscatter ratio that is unrealistic. The second step restricts the solution by requiring that the backscatter coefficient never takes a negative value and that the solution never diverges. The third step is based on the assumption that the solution profiles obtained from the lidar signals for three wavelengths should have similar shapes. In general, the backscatter coefficient profile for the longer wavelength has less dependence on the extinction to backscatter ratio S_1 , because the optical depth for longer wavelength is smaller than that for shorter wavelengths. Therefore, the profiles solved with $S_1=10$ and 90 for the lidar signal at 1064 nm can be used as references, although they do not necessarily coincide with each other. Solution profiles for the other two wavelengths can be obtained with appropriate extinction to backscatter ratios which give profiles similar to the standards.

Lidar signals were analyzed by combining the three steps above to get quantitative profiles for aerosol backscatter coefficients with the minimum uncertainty. The wavelength dependence of the backscatter coefficient was evaluated assuming a power-law relationship. The following equation gives the exponent of the wavelength dependence:

$$\delta(\lambda, \lambda_0) = - \frac{\ln\{\beta_1(\lambda) / \beta_1(\lambda_0)\}}{\ln(\lambda/\lambda_0)} \quad (2)$$

where λ and λ_0 are the measurement wavelengths.

Fig. 1 summarizes the results of the analyses, showing a two-dimensional diagram of wavelength dependence parameter δ derived from combinations of lidar returns at wavelengths of 300 and 600 nm and 600 and 1064 nm. Uncertainties in δ are represented by rectangles for maritime, continental and tropopause fold aerosols, while uncertainties were too small to draw for the Saharan and the rain forest aerosols. Characteristic features found in the figure are that $\delta(300, 600)$ for the Saharan aerosol show negative values and that $\delta(300, 600)$ and $\delta(600, 1064)$ for the folded tropopause aerosols have higher values than the others studied. In addition, Fig. 1 shows that each aerosol type investigated occupies a unique location on the δ diagram. This suggests that it may be possible to distinguish between major aerosols types by observing backscatter coefficients at multiple wavelengths. Further studies are planned to provide additional data sets for further evaluation of this technique.

References

- Browell, E. V., et al. (1983): The NASA Multipurpose Airborne DIAL System and Measurements of Ozone and Aerosol Profiles. Appl. Opt., 22, 522.
- Fernald, F. G. (1984): Analysis of Atmospheric Lidar Observations: Some Comments. Appl. Opt., 23, 652.

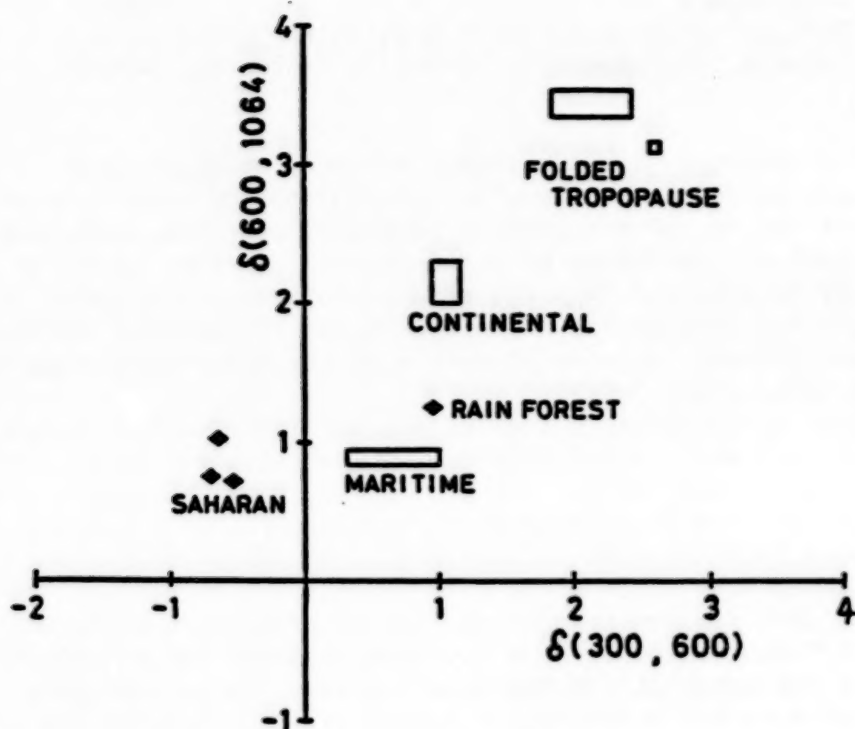


Fig.1 Diagram which shows the relationship between $\delta(300 \text{ nm and } 600 \text{ nm})$ and $\delta(600 \text{ nm and } 1064 \text{ nm})$ determined from the lidar observations for various kinds of aerosol types.

N87

10276

UNCLAS

EXTINCTION AND VISIBILITY MEASUREMENTS IN THE LOWER ATMOSPHERE WITH UV-YAG-LIDAR

Arne Hågård

National Defence Research Institute

Department 3, Box 1165, S-581 11 Linköping, Sweden

With the intention to investigate methods for slant path visibility measurements and to develop information for modelling of extinction profiles in the atmospheric boundary layer, we performed measurements with a lidar based on a YAG-laser. The third harmonic at 355 nm in UV is used and thus eye safety problems are avoided. At this wavelength the lens of the human eye is not transparent and the safety distance for our laser is 50 meters as compared to several km for a corresponding green laser.

The lidar is a coaxial system with a turntable mirror system for beam steering. Laser output data are: pulse rep. rate 10 Hz, pulse energy at 355 nm: 125 mJ, pulse length 15 ns and beam divergence 0,6 mrad. The receiver is a Cassegrainian telescope with 30 cm aperture diam. and 1 mrad field of view. A double grating monochromator is used for spectral background suppression with a bandwidth of 0,5 nm. The system is also used for Raman sounding. The detector is a photomultiplier with Rubidium cathode. By a waveform recorder the signal is digitized to 8 bit words at 100 MHz sampling rate. In an averaging unit controlled by a microprocessor a number of lidar returns are added and stored as 20 bit words for analysis and presentation.

A laser nephelometer is part of the lidar system. A part of the laser pulse energy is used in the nephelometer to measure the extinction coefficient at the lidar site. Green light from the second harmonic can also be used in the nephelometer. Thus the extinction coefficient at both 355 nm and 532 nm can be measured and their ratio determined. Provided that the wavelength dependence of the aerosol extinction is range independent, the measured extinction profile at 355 nm can be converted to a corresponding profile at 532 nm, which is more relevant for visibility determination.

In order to calculate the extinction profile the lidar equation is inverted by a method, which is based on Klett's (1) method. A reference return obtained in clear homogeneous conditions is used to correct for the lidar system function, which accounts for geometric optic functions. The backscattering coefficient β and the extinction coefficient α are the sum of parts due to aerosol (A) and Rayleigh (R) scattering

$$\beta(r) = \beta_A(r) + \beta_R(r)$$

(1)

$$\alpha(r) = \alpha_A(r) + \alpha_R(r)$$

53501-584

where r is range. We assume that the ratio β/α for aerosols is known either as a constant or a function of range. According to Fernald (2) we can then define an extinction coefficient α_L (which we may call the equivalent lidar extinction coefficient).

$$\alpha_L = \alpha_A + b\alpha_R \quad (2)$$

where b is $\beta_R\alpha_A/\beta_A\alpha_R$

Thus the lidar equation can be written in a form which can be inverted. A recorded lidar return $P(r)$ is divided with the reference return $P_0(r)$ and multiplied with a known attenuation function (due to Rayleigh scattering and attenuation of the reference return) to get

$$q(r) \cdot \alpha_{L0} = \alpha_L(r) \exp(-2 \int_0^r \alpha_L(x) dx) \quad (3)$$

where $q(r)$ is the normalized lidar return and α_{L0} is obtained from the nephelometer.

The solution can now be written:

$$\alpha_L(r) = \alpha_L(r_m) \frac{q(r)/q(r_m)}{1 + 2\alpha_L(r_m) \int_r^{r_m} [q(x)/q(r_m)] dx} \quad (4)$$

where r_m is the range to a distant point and $\alpha_L(r_m)$ is the estimated extinction coefficient at that point. The real α value is then obtained from equations 1 and 2.

Measurements have so far been performed along a horizontal path with a calibration target at 2.5 km distance. Transmission values obtained from the aerosol return can thus be compared to values obtained from the target returns. Contrast transmission has been measured simultaneously with a CCD camera looking at a calibrated contrast screen. In planned experiments lidar measurements along slant paths will be compared to observations from aircraft.

References:

- (1) Klett J.D., Appl. Optics, Vol. 24, No 11, 1 June, 1985.
- (2) Fernald F.G., Appl. Optics, Vol. 23, No 5, 1 March, 1984.

N87

10277

UNCLAS

SENSITIVITY OF THE LIDAR RATIO TO CHANGES IN SIZE DISTRIBUTION AND INDEX OF REFRACTION

B.T.N. EVANS

Defence Research Establishment Valcartier
2459, Pie XI Blvd., North (P.O. Box 8800)
Courcelette, Quebec, CANADA G0A 1R0

In order to invert lidar signals to obtain reliable extinction coefficients σ , a relationship between σ and the backscatter coefficient β must be given. These two coefficients are linearly related if the complex index of refraction m , particle shape and particle size distribution N does not change along the path illuminated by the laser beam. This, however, is generally not the case. Thus significant deviations from this linear relationship must sometimes be expected.

The relationship between β and σ has been investigated since 1953¹ and intensively in recent years.²⁻⁴ However, theoretical and experimental work to date has been very limited in terms of size distributions and refractive indices covered. Because of this lack of data it is difficult to know, in a typical lidar situation, if a good relationship between β and σ exists.

This study involves an extensive Mie computation of the lidar ratio $R = \beta/\sigma$ and the sensitivity of R to the changes in a parametric space defined by N and m . The real part of m was varied from 0 to 2, the imaginary part from 0 to ∞ , the mode particle size parameter X_m of N was varied from .03 to 3000 and the geometric standard deviation σ_g or width of N was varied from .03 to 1. The log-normal distribution was used the most; however, calculations have been done on many other types, including experimental distributions. For a given m , an average value of R , \bar{R} , was calculated over a set of N . In this set both the mode X_m and width σ_g were varied over a small range. Also the deviation of R over this set, σ_R , was computed. Thus σ_R gives a indication of relative sensitivity of R in a particular region of this parametric space.

The results of the study indicate that there are large volumes of the parametric space in which significant changes in N have little or no effect on R , that is that $\beta \propto \sigma$ in regions difficult to predict theoretically. For example, Fig. 1a shows 4 size distributions, with the same m corresponding to water in the visible, for which $R = .054$. Clearly R is insensitive to changes in N for this set of distributions. Fig. 1b shows other size distributions, again with the same m , for which small changes in N will change R dramatically. The difference between the distributions in Fig. 1a and Fig. 1b is that in Fig. 1b the X_m are small and/or σ_g are small relative to those in Fig. 1a. Thus there is less averaging of the efficiency factors. Figure 2a shows \bar{R}

plotted as a function of the real part of m ; n with the imaginary part $k = 0$. X_m is varied as indicated. Note that there is a general trend for \bar{R} to increase with particle size and that \bar{R} is increasingly sensitive to changes in n with increasing X_m . Very large values of R are obtained for $n = 1.8 - 2.0$ and large X_m . Also note that for pure water in the visible, where $n = 1.33$, \bar{R} changes little. Figure 2b is a plot of σ_g or deviation of R over the set of N versus n . Note that there is extreme sensitivity of R for $n \approx 1.1$ and $n = 1.8 - 2.0$. It is clear that for $n = 1.33$, R is insensitive to changes in N , especially for X_m varying from 12 - 30. Figures 3a and 3b are the same as 2a and 2b except that \bar{R} and σ_g are now plotted against k or absorption. In Fig 3a, \bar{R} initially decreases with increasing absorption, reaching very small values and then rapidly rises with very large values of k . Fig. 3b shows that the sensitivity of R initially stays constant, or decreases, followed by a maximum, and finally R becomes relatively insensitive at large values of k . The maximums of the curves in Fig. 3b are obviously related to the approach of the minimum values in Fig. 3a. This is caused by the fact that distributions with absorption in this region have the large particles absorbing all of the radiation while the small particles still let significant amounts of the radiation scatter or pass through. The maximums occur when $5kX_m \approx 1$.

Since Mie scattering is exact for spheres and thus includes many resonant effects, it is possible that slight deviations from a sphere may have a large effect on R and the sensitivity of R to changes in N . It is known that the most significant resonant effects come from edge-effect rays or rays that just graze the surface of the particles.⁵ These rays may then travel as surface waves and/or enter the particle with further possible scattering. Thus a calculation was performed that neglected these rays and the results compared with the full Mie theory calculation and experimental values taken from the literature.⁶⁻⁸ Figure 4 shows the results. One can see that, without the edge-rays, \bar{R} is considerably less than that predicted by the full Mie theory. Since the 23 experimental points cluster about the full Mie theory, it can be concluded that, in these experiments, the edge-rays contribute the most to R and thus sensitivity of R to changes in N .

Although only a very small portion of the calculation can be presented here, they are indicative of the general behaviour of R and σ_g .

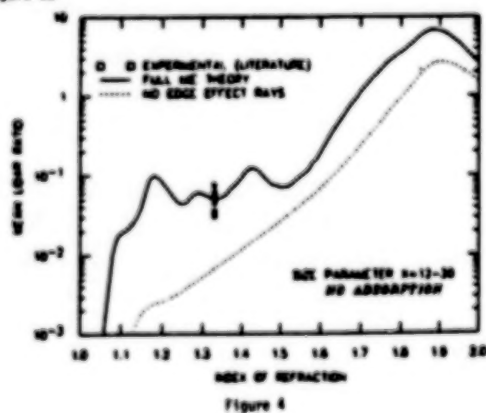
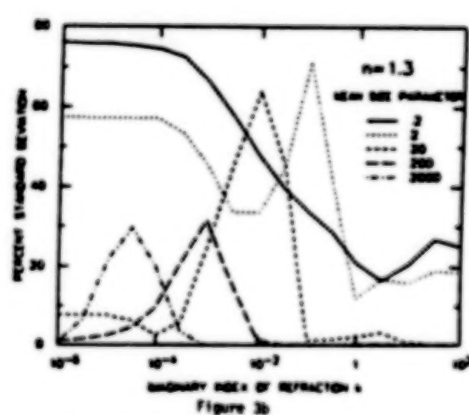
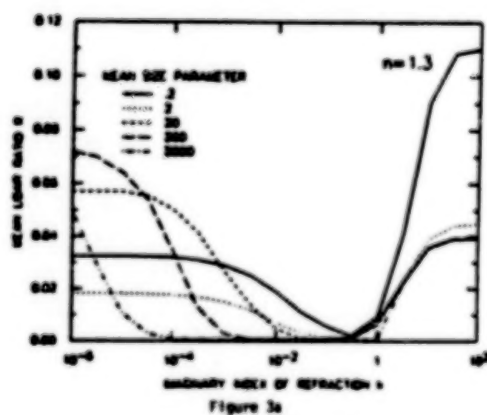
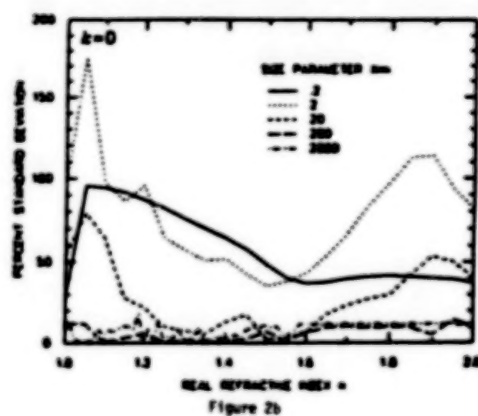
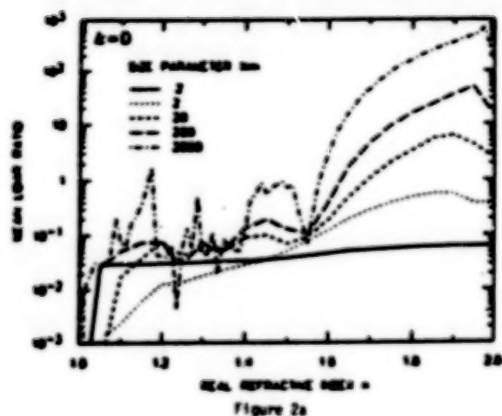
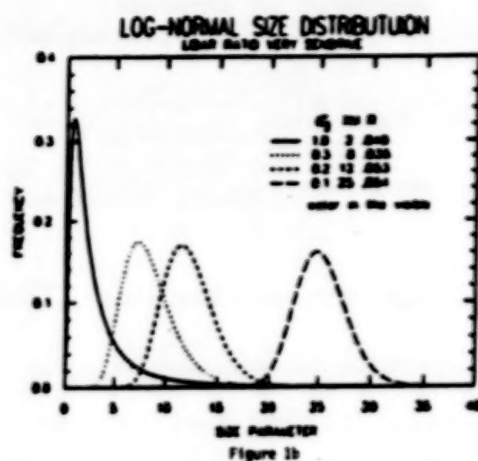
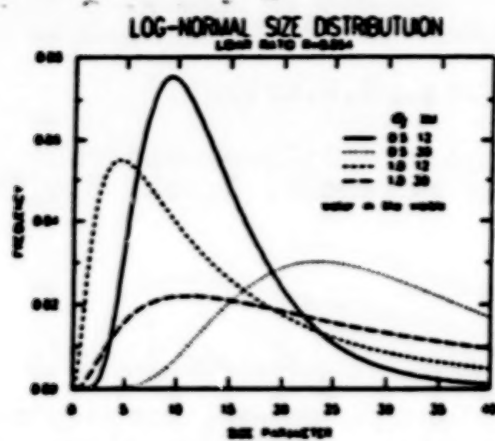
A few of the many conclusions from this study are:

- R is insensitive to changes in N when
 - a) all the particles are non-absorbing and small compared to the wavelength (Rayleigh scattering region)
 - b) for water in the visible and near-infrared, the modal particle size is greater than $1\mu m$
 - c) for water and with wavelengths 6 - $12\mu m$, the modal particle size is greater than $10\mu m$
 - d) $n = 1.5$ and $k \leq 10^{-4}$ and the modal size parameter $X_m \geq 6$
 - e) $2kX_m \geq 1$

- R is sensitive to changes in N when
 - a) for water and with wavelengths $.2 - 12\mu\text{m}$, the modal size parameter $X_m \leq 2$
 - b) the aerosols are of the rural or maritime type⁹ for any wavelength in the visible and infrared
 - c) for water and with the wavelength in the far-infrared, the particle sizes are of the order of several microns (in particular R is many more times more sensitive to size changes at $10.6\mu\text{m}$ than at $1.06\mu\text{m}$ ³)
 - d) $X_m \approx 1$
 - e) relative humidity increases above 70% in hygroscopic aerosols

References

- [1] L. Foitzik and H. Zschaek, "Measuring the spectral scatter function of ground-level air in good visibility, haze and fog," *Z. Meteor.* **7** (1953), 1-19.
- [2] J. D. Klett, "Stable Analytical Inversion Solution for Processing Lidar Returns," *Appl. Opt.* **20** (1981), 211-220.
- [3] R. G. Pinnick, S. G. Jennings, P. Chylek, C. Ham, and W. T. Grandy, Jr., "Backscatter and Extinction in Water Clouds," *Geophys. Res.* **88** (1983), 6787-6796.
- [4] G. deLeeuw, "Mie calculations on Particle Size Distributions," *TNO report PHL 1982-50* National Defense Research Organization, Netherlands (1982).
- [5] H. M. Nussenzweig, "Complex Angular Momentum Theory of the Rainbow and the Glory," *J. Opt. Soc. Am.* **69** (1969), 1068-1079.
- [6] D. A. Giglio, B. J. Rod and H. M. Smalley, "Nephelometer for Mapping of Backscatter and Attenuation Coefficients of Clouds," *HDL TR-1660*, Harry Diamond Labs., Washington, Md. (1974).
- [7] R. B. Smith, A. I. Carswell, J. D. Houston, S. R. Pal, B. C. Greiner, "Multiple Scattering Effects on Backscattering and Propagation of Infrared Laser Beams in Dense Military Screening Clouds," *DREV contract report 8SD81-00084* (1983).
- [8] S. R. Pal, J. S. Ryan and A. I. Carswell, "Cloud Reflectance with Laser Beam Illumination," *Appl. Opt.* **17** (1978), 2257-2259.
- [9] E. P. Shettle and R. W. Fenn, "Models for the Aerosols of the Lower Atmosphere and the Effects of Humidity Variations on Their Optical Properties," *AFGL-TR-79-0214*, Air Force Geophysics Lab., Hanscom AFB, Mass. (1979).



N87

10278

UNCLAS

LIDAR MEASUREMENTS OF SLANT VISUAL RANGE

Yu.S.Balin, S.I.Kavkyanov, G.M.Krekov,
I.A.Razenzov
The Institute of Atmospheric Optics, Siberian
Branch, USSR Academy of Sciences, Tomsk, 634055
U S S R

When converting the lidar equation

$$P_z = A_z z^2 \beta_z T_{oz}^2 = A_z z^2 \beta_z \exp \left\{ -2 \int_0^z \epsilon_z dz' \right\} \quad (1)$$

relative to the extinction coefficient ϵ_z and, correspondingly, the visual range, one encounters the instability of solution at the increase of the optical density of the sounding path (P_z is the lidar signal from the distance z , T_{oz} is the transmittance of the layer $[0, z]$, β_z is the backscattering coefficient, A_z is the calibration function). The search for a stable solution has resulted in the appearance of a set of inversion algorithms differing mainly in the manner of assigning the a priori information on the profile sought [1]. The paper suggests a stable algorithm of inversion and gives a comparative analysis and experimental verification of some methods of processing the signals at sounding the optically dense atmospheric formations.

The solution of Eq.(1), relative to ϵ_z , has, as known, the form

$$\epsilon_z = \psi_z \left(\frac{\psi_{z_k}}{\epsilon_{z_k}} - 2 \int_{z_k}^z \psi_{z'} dz' \right)^{-1} \quad \psi_z = \frac{P_z z^2}{A_z g_z T_{oz}^2} \quad (2)$$

$g_z = \beta_z / \epsilon_z$ is the lidar ratio, z_k is the reference (calibration) point, which can be chosen randomly along the sounding path $[z_s, z_m]$. The theoretical analysis and model calculations showed that the choice of a reference point z_k determines, in many respects, the stability of the solutions obtained. That is, the stability is the higher, the farther z_k is from the lidar. For $z_k = z_m$ the solution of the form

$$\epsilon_z = \psi_z \left(\frac{\psi_{z_m}}{\epsilon_{z_m}} - 2 \int_{z_m}^z \psi_{z'} dz' \right)^{-1} = \psi_z \left(\frac{\psi_{z_m}}{\epsilon_{z_m}} + 2 \int_z^{z_m} \psi_{z'} dz' \right)^{-1} \quad (3)$$

is most stable [1]. The similar conclusion has been arrived at by Klett [2]. His algorithm does not in fact differ from (3).

The main difficulty encountered when utilizing Eq.(3) is the necessity of measuring ϵ_{z_m} by an independent technique. The use, in this case, of logarithmic derivative (determination of ϵ_{z_m} based on the lidar-signal logarithm slope in the vicinity of z_m) is problematical due to the instability of the method to random variations of the signal. The most admissible is the processing of li-

dar signals with the use of integral calibration when transmittance of a sufficiently large segment $[\tau_0, \tau_m]$ is considered to be known. When $\tau = \tau_m$ the solution has the form

$$\epsilon_{\tau} = \frac{\psi_{\tau}}{2} \left(\epsilon \int_{\tau_0}^{\tau_m} \psi_{\tau'} d\tau' + \int_{\tau}^{\tau_m} \psi_{\tau'} d\tau' \right)^{-1} \quad \epsilon = (T_{\tau_0 \tau_m}^{-2} - 1)^{-1} \quad (4)$$

and is absolutely stable [1].

For approximately evaluating the parameter ϵ , one should use in Eq. (4) the lidar data together with different qualitative assumptions on the optical properties of the atmosphere along the path [1]. The simplest estimate $T_{\tau_0 \tau_m}^2$ can be obtained by using the least-square method assuming the statistical homogeneity along the path

$$T_{\tau_0 \tau_m}^2 = \exp \left\{ -\frac{3}{(\tau_m - \tau_0)^2} \int_{\tau_0}^{\tau_m} (\tau - \tau_0) \ln \frac{\psi_{\tau}}{\psi_{\tau_0}} d\tau \right\} \quad (5)$$

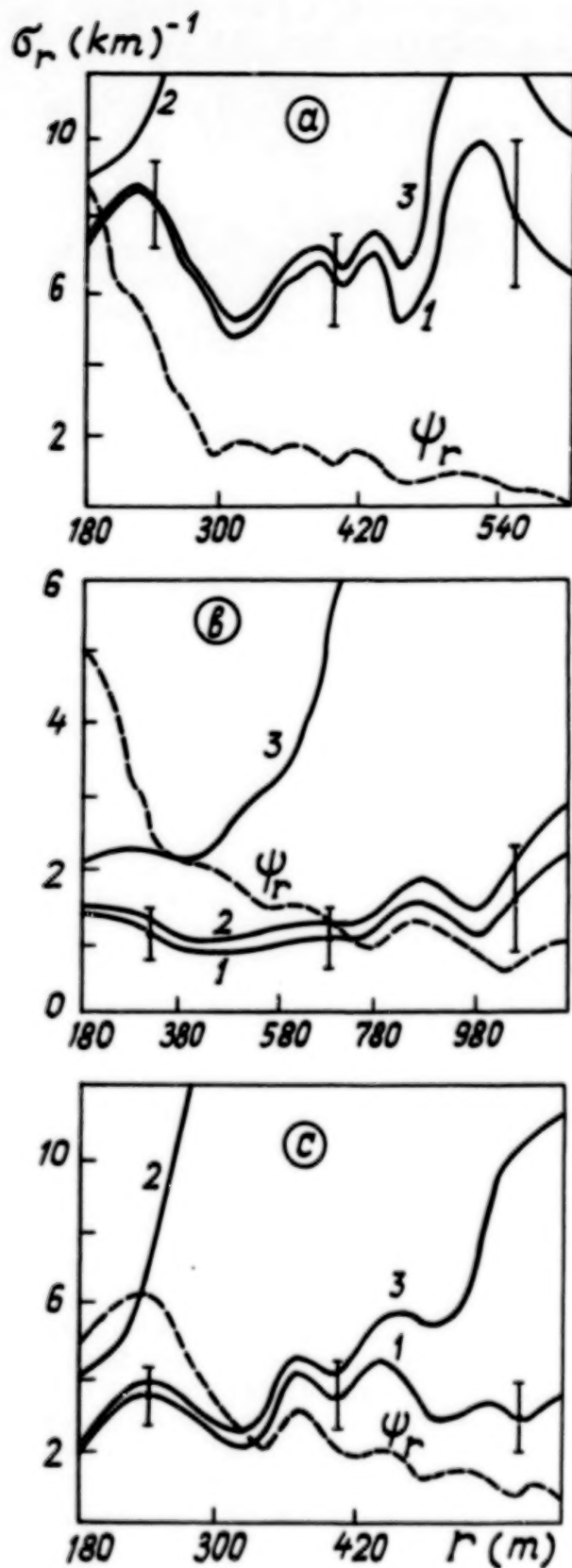
Such an approximation is sufficient for the sounding paths close to horizontal.

The data on sounding fogs obtained with the use of lidar "LOZA-3" developed at the Institute of Atmospheric Optics was used to experimentally verify the algorithms (4,5). The sounding at $\lambda = 0.53 \mu\text{m}$ was carried out in the horizontal direction with simultaneous monitoring for the optical state of the atmosphere with the photometer placed at the beginning of the path. Some results of these measurements are given in figures where the signals ψ_{τ} and the profiles ϵ_{τ} restituted with the use of the algorithm described (curves 1) are shown in relative units. The profiles ϵ_{τ} restituted using Eq.(2) with the photometer calibration at the beginning of the path (curves 2) and using Eq.(3) in which ϵ_{τ_m} value is determined using the method of logarithmic derivative (curves 3) are presented for comparison

$$\epsilon_{\tau_m} = \frac{1}{2(\tau^* - \tau_m)} \ln \frac{\psi_{\tau_m}}{\psi_{\tau^*}} \quad (6)$$

In many cases the use of photometer calibration at the beginning of the path resulted, as it should be expected, in the solution divergence (Figs. a-c). The use of the value

ϵ_{τ_m} from (6) for calibration does not allow one to carry out stable processing, since in this case ϵ_{τ_m} strongly depends on choice of the point τ^* corresponding to the assumption on homogeneity ϵ_{τ} at the segment $[\tau^*, \tau_m]$. If in Figs. a, c the value ϵ_{τ_m} obtained from (6) can be considered valid, then the inhomogeneity at the end of the path for the case b leads to a negative value ϵ_{τ_m} and divergence of the profile ϵ_{τ} . The necessity in choosing a homogeneous segment of the path makes the automated processing of the results difficult. It should be noted that the use of some model value ϵ_{τ_m} for calibration, as the calibrations showed, gives sufficient accuracy for large optical depths of the path $\tau \geq 2$ only. In the range $0.5 \leq \tau \leq 2$, the most probable



at sounding fogs, the solution is quite critical to the accuracy of evaluation σ_r . The algorithms (4,5) gave stable results for all signal ψ_r realizations. Thus, the use of functional limitations to the type of the solution sought (in this case, the assumption on statistical homogeneity of the path) allows one to construct stable algorithms for processing the results. The use of the more detailed information on solution and noises [1] gives the possibility of obtaining optimal algorithms with wider application limits than those of algorithms (4,5).

References

1. V.E.Zuev, S.I.Kavkya-nov, G.M.Krekov, *Izv. Akad.Nauk SSSR, Fizika atm. i okeana*, **19**, 255 (1983).
2. J.D.Klett, *Appl.Opt.*, **20**, 211 (1981)

N87

10279

UNCLAS

Visibility and Aerosol Measurement by Diode-Laser Random-Modulation CW Lidar

N. TAKEUCHI, H. BABA,^{*} K. SAKURAI,^{*} T. UENO^{**}
and N. ISHIKAWA

National Institute for Environmental Studies
Yatabe, Tsukuba, Ibaraki 305 Japan

^{*} The University of Tokyo, Komaba, Tokyo 153 Japan

^{**} Chiba University, Yayoi-cho, Chiba 260 Japan

^{***} Meisei Electric Co. Ltd., Moriya, Ibaraki 302-01

1. Introduction. In recent years, the diode laser (DL) has shown a large development in the lasing power, the mode quality, and reliability. Lidar systems using DL were reported in the application, to the slant visibility measurement¹⁾ and the ceilometer²⁾. However, the DL power is usually limited by the catastrophic optical damage at the cavity surface. Therefore, the peak power of the pulsed operation is within the range of only a few orders of magnitude larger than the cw power, and single mode operation is difficult and the excellent features of the DL are not sufficiently utilized in pulsed operation. In this situation, random-modulation cw (RM-CW) lidar³⁾ is suitable for the efficient use of the small DL power. We designed a portable DL RM-CW lidar with the detection ability of the aerosol profile up to 1⁴⁾ km in distance, reported the construction at the 12th ILRC⁴⁾, and published the preliminary results⁵⁾. Here we report the further development of the DL RM-CW lidar and its application to the field use.

2. System. The principle of the RM-CW lidar is based on the δ -function-like feature of the autocorrelation of pseudo-random code (we use M-sequence in this system), and the details are described in Ref. 3).

The DL RM-CW lidar was constructed as a compact, portable and easy-handling system. It consists of three parts: lidar head, processor, and personal computer. The whole system can be carried by a small van and operated by one person. The details of the purposes of construction and the original specifications are described in Ref. 5). The present specification is shown in Table

1. The items of improvement are

- 1) the power-up of the DL from 15 to 36 mW
- 2) improvement of the receiving optics (smaller aberration with larger aperture)
- 3) change of photomultiplier to the one with a large dynamic range

3. Outdoor measurements. Different from the laboratory measurement, outdoor operation has the severe conditions such as the variation of the power supply voltage and the large changes in environmental temperature and humidity. Sometimes the temperature

of DL is necessary to be kept in a certain range for stable operation in single-mode. Otherwise a ghost may appear in lidar data. After the above improvement, we obtained a nighttime aerosol profile over a 1 km distance. In the following, we introduce some examples of the outdoor measurements.

(1) Visibility. Visibility is the important meteorological parameter for the aviation safety as well as an index of comfortableness. Especially slant visibility is an important parameter for the landing of the airplanes. Visibility is inversely proportional to a distance averaged value of the extinction coefficient of the light passing through the atmosphere. Therefore the accurate profile of aerosol is not required. Werner et al¹⁾ monitored the visibility at Munich Airport for a long time using a pulsed DL lidar system. We derived the visibility based on the slope method and compared it with the data from a transmissometer (Meisei TZE-3T) set on the same site. An example for fast visibility change is shown in Fig. 1. The lidar shows smaller value than the transmissometer due to the inhomogeneous distribution of the aerosol. For spatially varied aerosol distribution, the exact visibility value should be obtained⁶⁾ by resolving the lidar equation according to the Klett method⁶⁾.

(2) Aerosol vertical profile. Range-corrected aerosol profile (linear plot) with the elevation angle of 10 deg is shown in Fig. 2. This was taken automatically with the time interval of 20 min. The integration time was 80 sec. The cross-over function becomes 1 at about 200 m. In a case of DL, the beam divergence is very small so that a small size of the laser beam cross section is small enough to use a mirror for bending the direction of the laser. Therefore if we set a mirror along the ground surface so that the crossover function is unity beyond the mirror, we obtain the vertical aerosol profile from the ground surface.

(3) Cloud movement. When the thickness of the cloud is not thick enough, the structure of the cloud is easily measured by the lidar. In Fig. 3, the rapid change of the cloud is shown. The data are taken every 30 sec with integration time of 10 sec. A cloud is shown at the height of 1000 m. The signal near the ground is the aerosol.

4. Summary. We report some examples of the DL RM-CW lidar measurement. They demonstrate the ability for the measurement of the visibility, vertical aerosol profile, and the cloud ceiling height. Although the data shown here were all measured at nighttime, the daytime measurement is of course possible. For that purpose, accurate control of the laser frequency to the center frequency of a narrow band filter is required. Now a new system with a frequency control is under construction.

References

- 1) Ch. Werner et al: Application to an eye-safe laser slant visual range measuring device at Munich Airport, 12th ILRC, B5 (1984).
- 2) Ceilometer model TXK-3, Meisei Electric Co., Ltd.
- 3) N. Takeuchi et al: Random modulation cw lidar, Appl. Optics 22, 1382(1983).
- 4) N. Takeuchi et al: Construction of compact RM-CW lidar systems, 12th ILRC, E9(1984).
- 5) N. Takeuchi et al: Diode-laser random-modulation cw lidar, Appl. Optics 25, 63(1986).
- 6) J.D. Klett: Stable analytical inversion solution for processing lidar returns, Appl. Optics 20, 211(1981).

Table 1. Specifications of a DL RM-CW Lidar

LASER: GaAlAs-DL(Sharp)	
Wavelength	780 nm
Output	36 mW
Driving current	160 mA(bias) + 100 mA(mod)
Operating Temp.	-5~10°C
Beam Divergence	<0.1 mrad (after collimation)
MODULATION: M-seq. random code	
Clock time	60 ns
Number of elements	4095 ($=2^{12}-1$)
Period	240 μ sec
Range resolution	9 m
RECEIVING OPTICS	
Telescope	Schmidt-Cassegrain (reflection)
Aperture	150 mm
Focal length	1500 mm (eff.)
FOV	0.5~3.0 mrad
Opt. filter bandwidth	1.2 nm
DETECTOR: PMT Hamamatsu R928	
Quantum efficiency	0.1
Amplific. factor	1×10^7
SIGNAL PROCESSOR	
ADC	3 bit (clock time 60 ns)
Accumulation	up to 2^{16}

1985.12.9-10

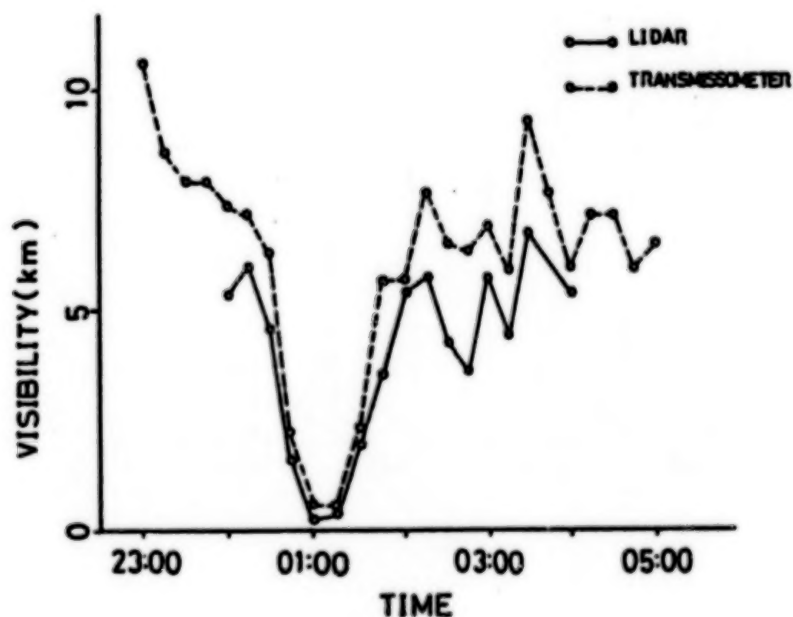


Fig. 1 Comparison of visibility data between a DL RM-CW lidar and a transmissometer.

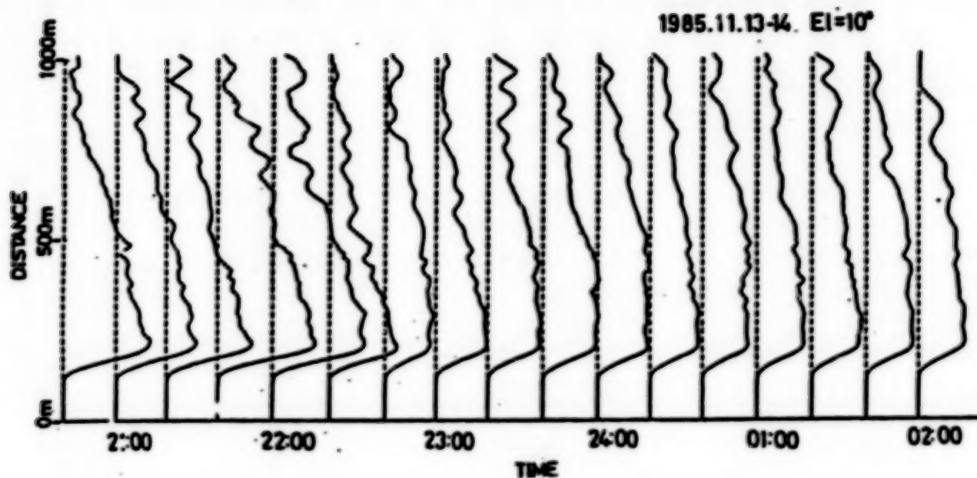


Fig. 2 Sequential measurement of aerosol profile. Elevation angle: 10 deg, integration time 80 sec.

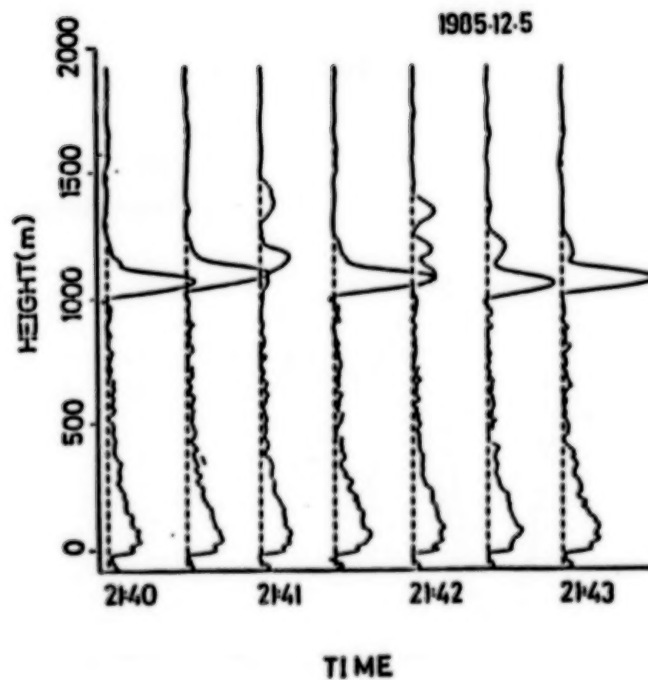


Fig. 3 Temporal variation of the cloud thickness. Accumulation time: 5 sec, no range correction.

N87

10280

UNCLAS

CORRECTION FUNCTION IN THE LIDAR EQUATION AND THE SOLUTION
TECHNIQUES FOR CO₂ LIDAR DATA REDUCTION

YANZENG ZHAO*, TING KAUNG LEA AND RICHARD M. SCHOTLAND

Institute of Atmospheric Physics, University of Arizona,
Tucson, Arizona, USA

For lidar systems with long laser pulses the unusual behavior of the near-range signals causes serious difficulties and large errors in data reduction. The commonly used lidar equation is no longer applicable since the convolution of the laser pulse with the atmospheric parameter distributions should be taken into account. It is the purpose of this paper to give more insight into this problem and find solution techniques.

Starting from the original equation, the authors suggest a general form for the single-scattering lidar equation where a correction function Cr is introduced:

$$V(R) = CA \beta_{\pi}(R) T^2(R) Cr(R) / R^2 \quad (1)$$

where

$V(R)$ = lidar return signal at range R
 $\beta_{\pi}(R)$ = atmospheric backscattering coefficient
 $T^2(R)$ = two-way transmittance of the atmosphere

The correction function $Cr(R)$ derived from the original equation indicates the departure from the normal lidar equation:

$$Cr(R) = \int_0^{2R/c} P(t') Y(R, t') S(R, t') B(R, t') Tr(R, t') dt' / E \quad (2)$$

where $P(t')$ = laser power as a function of time
 $Y(R, t')$ = near-range receiving efficiency of the system
 $\quad = \eta(R - ct'/2)$
 $S(R, t') = (1 - ct'/2R)^2$
 $B(R, t') = \beta_{\pi}(R - ct'/2) / \beta_{\pi}(R)$
 $Tr(R, t') = T^2(R - ct'/2) / T^2(R)$
 E = energy of the laser pulse

EQ.(1) is very similar to the normal lidar equation except for the correction function Cr . It is therefore more convenient to use the lidar equation (1) than to use the original one because it is easier to compare the lidar signals of long laser pulse with those of the short pulses and discuss the changing of the signals by analyzing the features of correction function Cr . It is

* On leave from The Institute of Atmospheric Physics, Chinese Academy of Sciences

also easier to find a solution to the equation under certain circumstances.

EQ.(2) shows that Cr is a normalized, weighted, range dependent laser energy with weighting functions $Y(R,t')$, $S(R,t')$, $B(R,t')$ and $Tr(R,t')$. The weighting functions modify the laser pulse shape in the following ways:

1. As t' increases, the inverse range square factor $S(R,t')$ increases rapidly and strongly amplifies the contribution of the tail of laser pulse
2. Since atmospheric transmittance always decreases with range, $Tr(R,t')$ increases with t' and also amplifies the laser tail
3. If $\beta_{\pi}(R)$ decreases with R , as usually happens in the vertical direction, $B(R,t')$ increases with t' and amplifies the laser tail, otherwise it suppresses the tail
4. $Y(R)$ increases rapidly and approaches 1 within a few hundred meters, $Y(R,t')$ decreases with t' and more or less cancels the effect of $S(R,t')$ and $Tr(R,t')$

Because of the properties of the weighting functions, the tail of the laser pulse has significant contributions to the magnitude of $Cr(R)$, even when the tail is two to three orders of magnitude lower than the peak.

Numerical simulation shows that the general features of $Cr(R)$ are as follows:

1. In most cases and for most of the range concerned, $Cr(R) > 1$, and there is always a big "hump" in the near range. The peak of the hump can be as large as 3.5 in horizontal observation for CO_2 lidar in long pulse operation at weak absorption wavelengths.
2. $Cr(R)$ depends on laser pulse shape, particularly the length and form of the tail. The $Cr(R)$ also depends on the configuration of the lidar.
3. The $Cr(R)$ is sensitive to atmospheric transmittance and is very different for the on-line and off-line wavelengths, causing big errors in DIAL measurement if it is not considered.
4. The $Cr(R)$ is sensitive to backscattering distribution.

Examples of $Cr(R)$ for a coaxial CO_2 lidar system are shown in Fig.1. DIAL errors caused by the differences of $Cr(R)$ for H_2O measurements are plotted against height in Fig.2.

Numerical analyses also show that $Cr(R)$ at weak H_2O absorption wavelengths is not sensitive to the amount of water vapor, while the ratio of $Cr(R)$ at $R(18)$ and $R(20)$ lines of CO_2 lidar is not sensitive to backscattering coefficient distribution. In addition, at CO_2 wavelengths the atmospheric transmittance is primarily independent of the backscattering coefficient. These facts lead to solution techniques for atmospheric backscattering distri-

bution and water vapor content from CO_2 lidar signals. Iteration procedures are suggested and the convergence of the iteration has been proved by numerical tests.

BIBLIOGRAPHY

1. P.W.Baker, APPLIED OPTICS, VOL.22, NO. 15, 2257(1983).
2. M.J. Kavaya, R.T. Menzies, ABSTRACTS OF PAPERS, 12TH ILRC, 1984, AIX en PROVENCE, FRANCE.

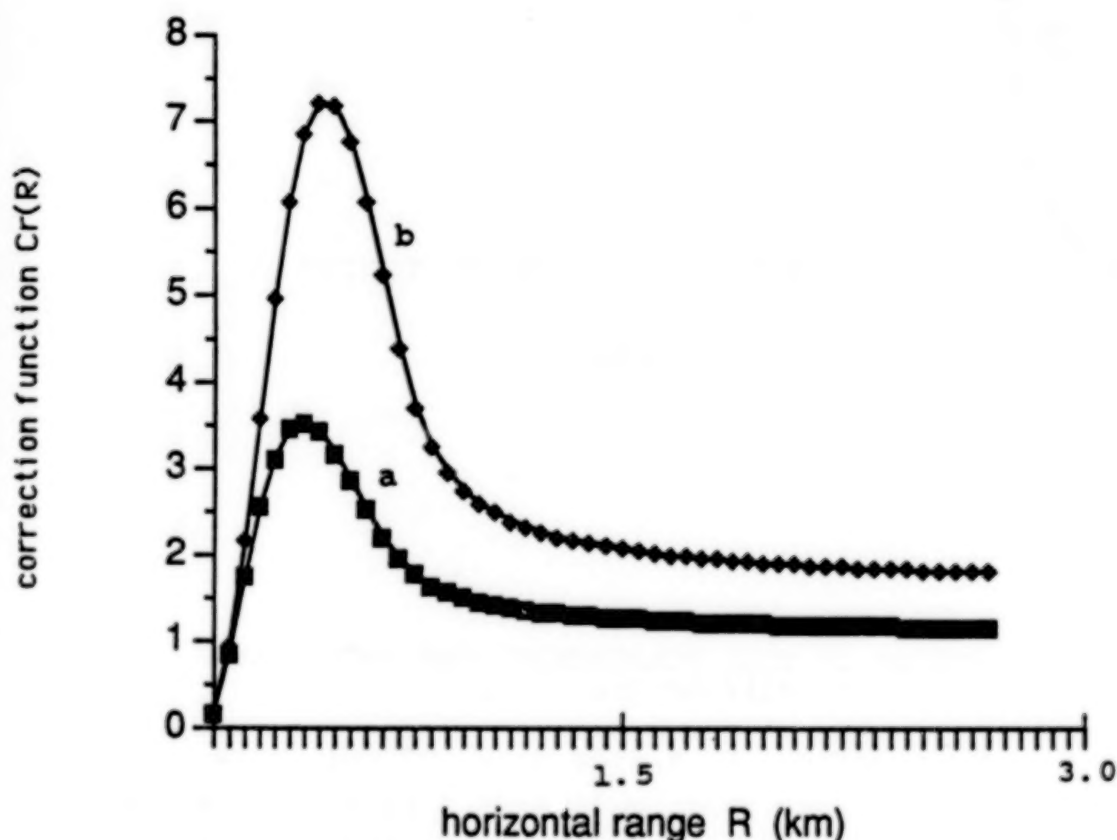


FIG.1 $Cr(R)$ IN HORIZONTAL CASE
(a) atmospheric extinction coefficient = $0.2/\text{KM}$
(b) atmospheric extinction coefficient = $1.5/\text{KM}$

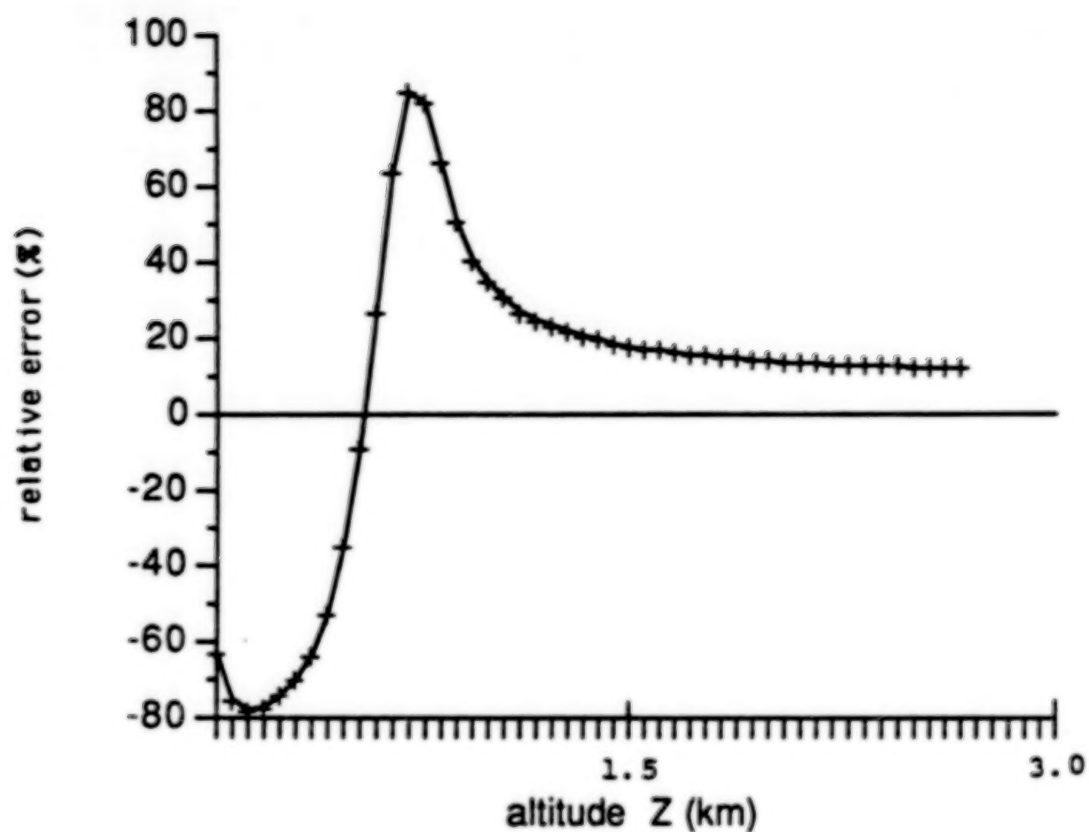


FIG. 2 ERRORS OF DIAL MEASUREMENT FOR WATER VAPOR
CAUSED BY DIFFERENCES OF C_r

wavelengths: R(18) and R(20) of CO_2 laser

water vapor pressure follows a negative exponential
distribution with scale height = 2000 meter and
surface value = 20 mb

N87

10281

UNCLAS

ASSESSMENT OF DIAL DATA COLLECTION AND
ANALYSIS TECHNIQUESE. V. Browell^a and P. T. Woods^b

The First International DIAL Data Collection and Analysis Workshop was held in Virginia Beach, Virginia, on November 18-21, 1985. The objectives of the Workshop were to assemble representatives from most of the leading DIAL groups into a limited and focused working group and to address the details of current and future DIAL data collection and analysis techniques. The emphasis of the Workshop was on direct detection DIAL methods and on an assessment of current techniques used in DIAL measurements throughout the 0.2 - 11 μ m spectral range. A total of 38 researchers from 22 DIAL groups contributed to the Workshop. A list of the DIAL participants in this Workshop is given by country and organization in Table 1. A NASA report is being prepared to communicate the Workshop results to the entire DIAL community. This paper discusses the Workshop and summarizes the Workshop's assessment of DIAL data collection and analysis techniques.

The Workshop was organized to examine the key issues in all areas of DIAL data collection and analysis techniques. This included consideration of the practical and theoretical limitations of DIAL and the range of possible DIAL measurements. Table 2 lists the main topics discussed at the Workshop and examples of issues addressed in each area. Each of the DIAL groups represented at the Workshop presented a current status of their DIAL research as it pertained to the topics of the Workshop. A written summary of each report is found in the appendix of Reference 1. During the Workshop, each of the topics identified in Table 2 was discussed initially by a panel comprised of several of the DIAL participants and later by the entire Workshop. Each panel chairman had the responsibility of leading the Workshop discussion on a particular DIAL topic and of drafting a section of the Workshop report. Each panel report defined the issues to be considered, the various approaches used to address each issue, and, where possible, quantitatively compared competing techniques. The report from this Workshop presents a comprehensive assessment of the major DIAL techniques, and this paper summarizes the results of this Workshop in each of the major topic areas.

-
1. Browell, E. V., and P. T. Woods, eds.: Assessment of DIAL Data Collection and Analysis Techniques. NASA Langley, work in preparation.

^a National Aeronautics and Space Administration, Langley Research Center, Hampton, Virginia 23665, U.S.A.

^b National Physical Laboratory, Teddington; Middlesex TW11 0LW, U.K.

Table 1. DIAL Participants in the First International DIAL
Data Collection and Analysis Workshop

Sweden: Lund Inst. of Tech. - K. Fredrikson

Japan: Kyushu Univ. - O. Uchino
NIES - N. Sugimoto

France: CNRS/Serv. Aeronomy - G. Megie/J. Pelon
CNRS/Dynam. Meteor. - P. Flamant
Elect. Du. France - C. Cahen/B. Grossmann

U.K.: NPL - P. T. Woods/B. W. Jolliffe/M. Milton
Univ. of Hull - B. J. Rye
CERL - R. H. Varey

F.R.G.: Inst. for Physik - A. Breinig/W. Staehr
MPI fur Meteor. - J. Boesenberg
DFVLR - W. Renger

Italy: ENEL and CISE - A. Marzorati/E. Zanzottera

Canada: AES - R. M. Hoff/F. A. Froude

U.S.: NOAA/WPL - R. M. Hardesty
EPA Las Vegas - M. Bristow/D. Bundy
SRI Inter. - R. E. Warren/J. G. Hawley
NASA GSFC - C. L. Korb/G. K. Schwemmer
RCA Astro. - A. Rosenberg/J. C. Petheram
JPL - W. B. Grant/S. McDermid
Univ. of MD - T. D. Wilkerson/C. Braun
NASA LaRC - E. V. Browell/S. Ismail/A. F.
Carter/R. J. Allen

Table 2. DIAL Workshop Topics

	<u>EXAMPLES OF ISSUES</u>
I. Data Collection Techniques	
Transmitting Systems	Laser Requirements; Simultaneous Versus Non- simultaneous Outputs; Laser Output Characterization; Spectral Data
Atmospheric Effects	Speckle; Turbulence; Wavelength-Dependent Propagation Effects
Receiving Systems	Telescope Design; Coaxial; Collinear
Detection Systems	Linearity; Gain Modulation; Noise Effects; Wavelength Separation Techniques
Post-detection Electronics	Amplifier Saturation; Dynamic Range Compression, Digitiza- tion Speed; Accuracy Limitations
New Concepts	
II. Data Analysis	
Signal Processing	Averaging Techniques; Smoothing; Differentiation
Data Handling	Parallel Processing; Computa- tional Techniques
Correction to Results	Wavelength Dependence of Scattering; Correction for Atmospheric Density; Absorption Cross Sections; Deconvolution of Laser Spectral Properties
Error Analysis	Contributions to Total Error Budget

N87

10282

UNCLAS

AIRBORNE LIDAR MEASUREMENTS OF THE ATMOSPHERIC PRESSURE PROFILE WITH TUNABLE ALEXANDRITE LASERS

C. L. Korb, G. K. Schwemmer, M. Dombrowski, J. Milrod, and H. Walden, NASA Goddard Space Flight Center, Laboratory for Atmospheres, Greenbelt, Maryland, U.S.A

This paper describes the first remote measurements of the atmospheric pressure profile made from an airborne platform. The measurements utilize a differential absorption lidar and tunable solid state Alexandrite lasers. The pressure measurement technique¹ uses a high resolution measurement of the integrated path absorption in the wings of lines in the oxygen A band where the absorption is highly pressure sensitive due to collision broadening. We use absorption troughs, regions of minimum absorption between pairs of strongly absorbing lines, for these measurements. The trough technique allows the measurements to be greatly desensitized to the effects of laser frequency instabilities.

Our aircraft lidar system incorporates two Alexandrite lasers which are continuously tunable from 725 to 790 nm and have a bandwidth of 0.02 cm^{-1} using a birefringent filter and two etalons. We have measured the short-term frequency stability of the lasers to be better than 0.005 cm^{-1} and the Q-switched pulse length to be 100-130 nsec. One laser has a 100 mm x 5 mm diameter Alexandrite rod and a 150 mJ output energy. The tuning elements are electronically controlled and have a 3 cm^{-1} spectral scanning capability. The second Alexandrite laser has a 75 mm x 5 mm rod and a 100 mJ output energy. Its tuning elements are manually controlled and it is typically used for the off-line measurement. Both lasers operate at repetition rates up to 10 Hz and have a multi-mode spatial intensity distribution. The output of each laser consists of three axial modes with overall widths of 0.016 and 0.026 cm^{-1} for the two lasers, respectively. We have measured the spectral purity of the Alexandrite lasers to be greater than 99.99%.

The energy backscattered from the atmosphere is collected with a 40 cm telescope and detected with a multialkali photomultiplier tube. The receiver field of view was set at 8 mrad for the nighttime measurements and a 720 nm long pass filter was used for spectral background rejection. A 200 μsec time delay between the laser pulses was introduced to separate the on- and off-line laser signals. A single detector channel is used to observe both on- and off-line signal returns. The signals from the photomultiplier are digitized with 10 (flight 1) or 12 bit (flight 2) transient digitizers at 5 MHz. An LSI-11/23 microprocessor controls system functions, monitors operator inputs, and displays system status and data in real time.

The airborne measurements of the atmospheric pressure profile were made using the Goddard lidar facility on the Wallops Lockheed Electra aircraft. Flights were made on November 20 and December 9, 1985. Data for the first flight were taken along the flight line extending from Sea Isle, Delaware ($39^{\circ}05'N/74^{\circ}45'W$) to Point Lynus ($38^{\circ}01'N/72^{\circ}39'W$), approximately 220 km off the coast of Delaware. Data for the second flight were taken along the line between Sea Isle, Delaware, and Bowie, Maryland ($39^{\circ}00'N/76^{\circ}44'W$).

Figure 1 shows data from the November 20 flight taken near Point Lynus. The lidar system was set up to measure pressure with the on-line laser tuned to the absorption trough at 13147.3 cm^{-1} and with the reference laser tuned to a non-absorbing frequency near 13170.0 cm^{-1} . The lidar signal returns were sampled with a 200 nsec range gate (30 m vertical resolution) and

averaged over 100 shots. The integrated absorption coefficient between the lidar at the aircraft altitude of 2790 m and each altitude was calculated from these data. The pressure profile was then determined by relating the measured integrated absorption coefficient to the difference in the squares of the pressures at the measurement altitude and laser altitude.¹ Uncertainties in the oxygen line parameters were corrected for by a single constant calibration fit of the measured data to ground truth. Figure 1 shows a comparison of the lidar measured pressure profile in the vicinity of Point Lynus to radiosonde data taken two hours earlier at Wallops Island, Virginia (37°51'N/75°28'W). The average deviation of the lidar pressure profile data from the radiosonde data is less than 2.0 mb. As shown, the deviation between the lidar and radiosonde profiles tends to be systematic. We note that the noise level of the raw lidar data was close to the theoretical limits.

Reference

1. Korb, C. Laurence and Chi Y. Weng, "Differential Absorption Lidar Techniques for Measurement of the Atmospheric Pressure Profile," Applied Optics, 22, 3759-3770, 1983.

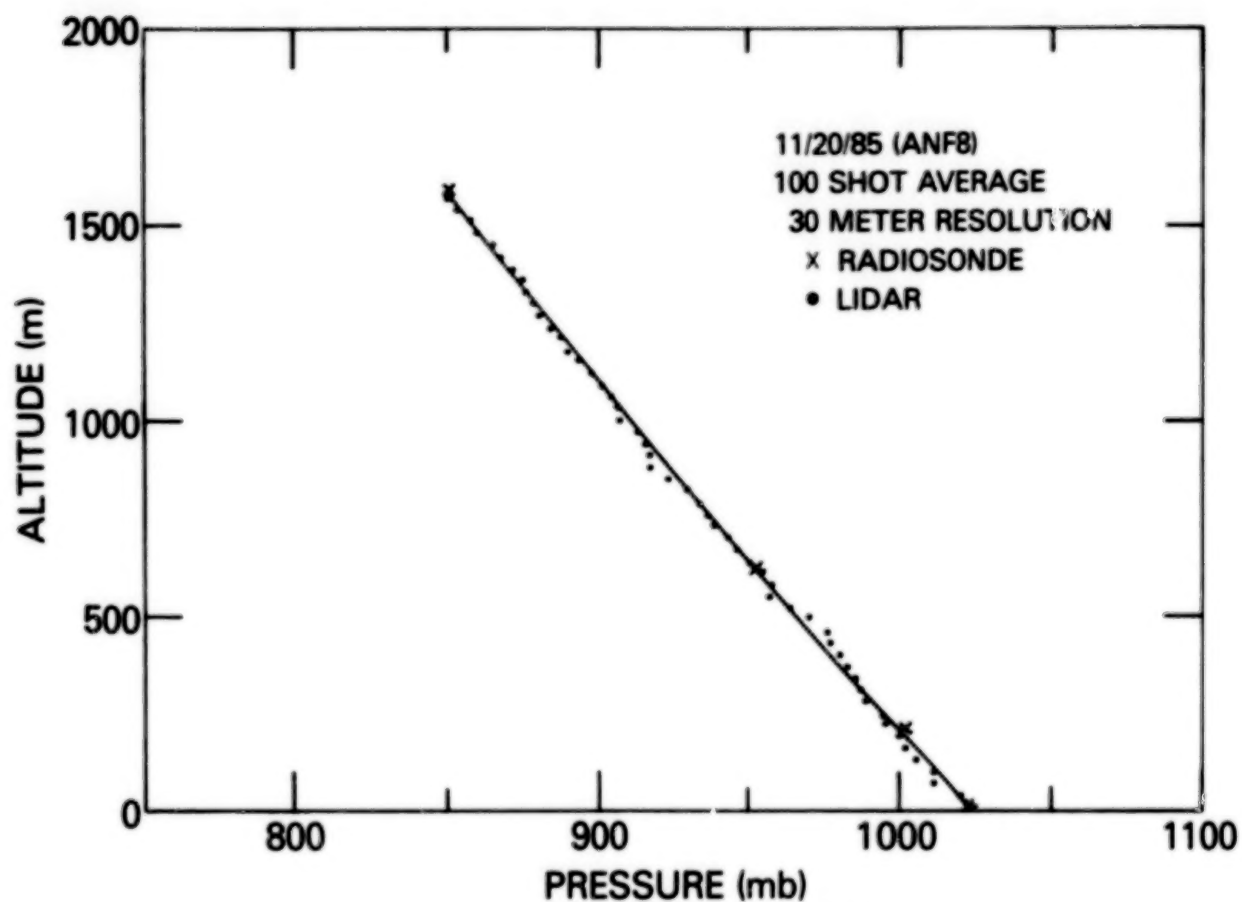


Figure 1 – Lidar pressure profile measured from aircraft at 2790m compared with radiosonde data.

N87

10283

UNCLAS

MEASUREMENTS OF THE EFFECT OF HORIZONTAL VARIABILITY OF ATMOSPHERIC BACKSCATTER ON DIAL MEASUREMENTS

G. K. Schwemmer, C. L. Korb, M. Dombrowski, and C. Y. Weng¹
 NASA Goddard Space Flight Center, Laboratory for Atmospheres
 Greenbelt, Maryland U.S.A.

¹Science Systems and Applications, Inc., Seabrook, Maryland U.S.A.

The horizontal variability of atmospheric backscatter may have a substantial effect on how Differential Absorption Lidar (DIAL) data must be taken and analyzed. To minimize errors, lidar pulse pairs must be taken with time separations which are short compared to the time scales associated with variations in atmospheric backscatter. These time scales have typically been considered to be on the order of hundreds of microseconds. We have found low levels of variability in the atmospheric backscatter for time scales on the order of ten seconds which correspond to spatial distances of 1 km for data taken from an aircraft in clear nighttime conditions.

To assess the atmospheric variability for time scales which are long compared to the lidar pulse repetition rate, one can compute the variance of the lidar return signal in a given channel. The variance in a given signal, $\sigma^2(S_j)$, has contributions from both instrumental, σ^2_I , and atmospheric, σ^2_A , effects:

$$\sigma^2(S_j) = \sigma^2_I(S_j) + \sigma^2_A(S_j) \quad (1)$$

where j represents either the on- or off-line signal. In general, the instrumental and atmospheric terms cannot be easily separated. However, if we take data in two channels with sufficiently short temporal separation, then the atmospheric effects are essentially the same in the two channels. Thus, a ratio of the two channels yields a quantity which is essentially free of atmospheric backscatter variability. The variance in this ratio is given as:

$$\sigma^2(S_1/S_2) = \sigma^2_I(S_1) + \sigma^2_I(S_2) \quad (2)$$

It follows from equations (1) and (2) that the atmospheric variance is given as:

$$\sigma^2_A = \frac{\sigma^2(S_1) + \sigma^2(S_2) - \sigma^2(S_1/S_2)}{2} \quad (3)$$

We calculated the variances (as the square of the standard deviation in percent) of the on-line, off-line, and ratio of the on- to off-line signals at given altitudes obtained with our dual solid-state Alexandrite laser system. We have made these evaluations for both down-looking aircraft and up-looking ground-based lidar data. Data were taken with 200 μ sec separation between on- and off-line laser pulses, 30 m altitude resolution, 5 Hz repetition rate, and the signals are normalized for outgoing laser energy. Figure 1 shows the horizontal atmospheric variability versus altitude for a 50 shot (10 sec) average of data taken from aircraft. This averaging time corresponds to a 1 km horizontal spatial scale. It is seen that very low levels of atmospheric variability occur for these clear, nighttime conditions. This shows that if the atmospheric transmission at a given altitude is calculated using on- and off-line signals that are separated by as much as 1 km in space or 10 sec in time, then the errors in the transmission are between 1 and 2 percent.

88901-584

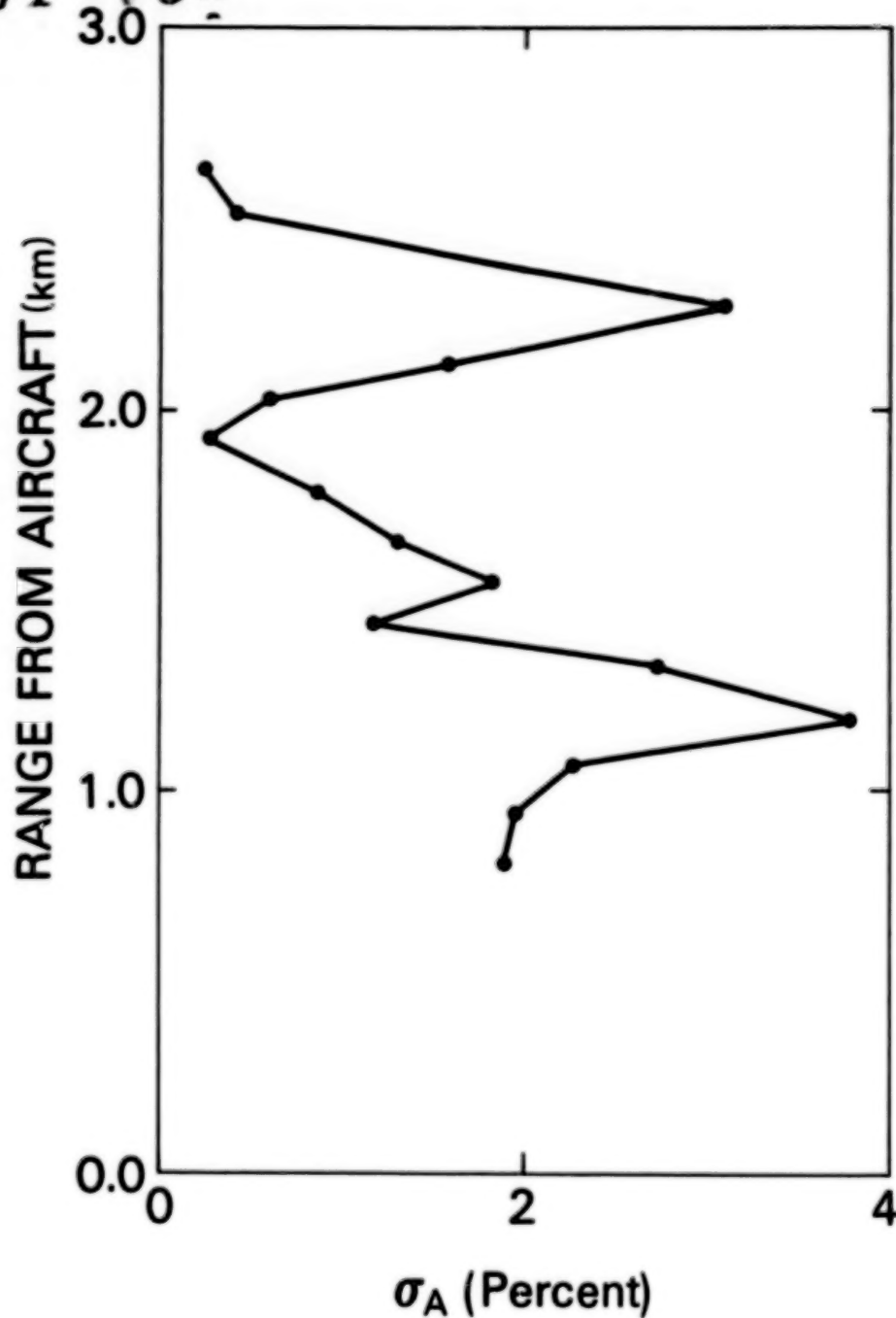


Figure 1 – Horizontal atmospheric variability for various altitudes for a 50 shot (10 sec.) average of data taken from aircraft (1 km spatial average) at 2790m altitude.

N87

10284

UNCLAS

FLIGHT TESTS OF A RANGE-RESOLVED AIRBORNE DIAL WITH TWO MINI-TEA CO₂ LASERS

T.Itabe, M.Ishizu, T.Aruga, T.Igarashi
Radio Research Laboratory
Ministry of Posts and Telecommunications
Koganei,Tokyo, Japan

K.Asai
Tohoku Institute of Technology
Sendai,Miyagi,Japan

It is important to measure regional distributions of ozone concentrations in a short time for understanding a mechanism of photo-chemical smog development. Several ways of airborne laser remote sensing should be featured as a powerful technique for this purpose. One of the best ways is an airborne CO₂ DIAL (Differential Absorption Lidar) since this is active and sensitive.

An airborne DIAL system with two low-power mini-TEA CO₂ lasers has been developed for measuring three-dimensional distributions of ozone in the lower troposphere. The CO₂ DIAL is a nadir-looking system and is designed to measure ozone profiles between ground and airplane by using atmospheric aerosols as a distributed radar target. A twin-engine aero-commander, which can carry 8 passengers, is selected to carry the DIAL System. Characteristics of the system are shown in Table 1. The transmitter of the DIAL is composed of two mini-TEA CO₂ lasers and a telescope. The discharge section of the flowing-type CO₂ laser has an electrode of Chang's profile, a metal mesh and a SiC ceramics preionizer. Output of the laser in flight tests is 200mJ. A receiving telescope has an almost diffraction-limited primary mirror with a diameter of 300mm and a F-number of 2 to efficiently collect photons backscattered from aerosols. One laser is triggered 100μsec after the other to provide a near-simultaneous dual-wavelength operation with only one 1mm square HgCdTe detector by means of the direct detection.

First flight tests with a single laser have been conducted in February 1985 over the Tokyo area. The system was operated at an altitude of 5000ft(1.7 km). All flight path lines of the flight mission on Feb. 23, 1985 are shown in Fig.1. Receiving power (P_r) of the laser₂ radar is given by

$$P_r = K B^r \exp(-\int \sigma_t dR) / R^2$$

where K = system efficiency

B = aerosol backscattering coefficient

R = range from the system

σ_t = atmospheric extinction coefficient

The receiving power corrected by R^2 vs. height is shown in Fig.2. The corrected receiving power is given by

$$P_r R^2 = K B \exp(-\int \sigma_z dR).$$

The number r at the top of Fig.2 indicates the flight path line. Note that results of the first flight tests show that the height profiles of the received power in the boundary layer were different between over land and ocean. The received power has to be inverted to an expression of a single optical parameter to see real aerosol distributions. Inversion of the lidar signal to the aerosol extinction has been performed by using Klett's solution. We will discuss the inversion of the lidar signal at the meeting.

Second flight tests with two lasers will be made soon.

We hope to report results of the second flight tests to measure ozone at the meeting.

Table I: CHARACTERISTICS OF AIRBORNE DIAL

Transmitting telescope	
Diameter	100mm
Type	Galilei
Objective	off-axis mirror
Laser	
Type	mini TEA CO ₂ laser
Output	300mJ
Receiving telescope	
Diameter	300mm
Focal length	600mm
Type	Newton
Detector	
Material	HgCdTe
Size	1mmSquare
D*	$10^{10} \text{ W}^{-1} \text{ Hz}^{1/2} \text{ cm}$

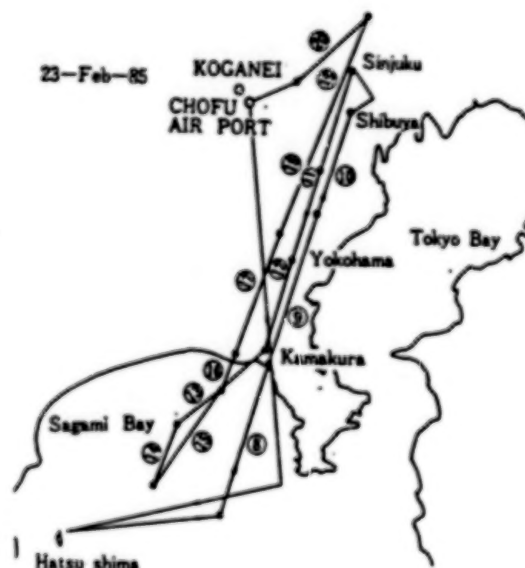


Fig. 1

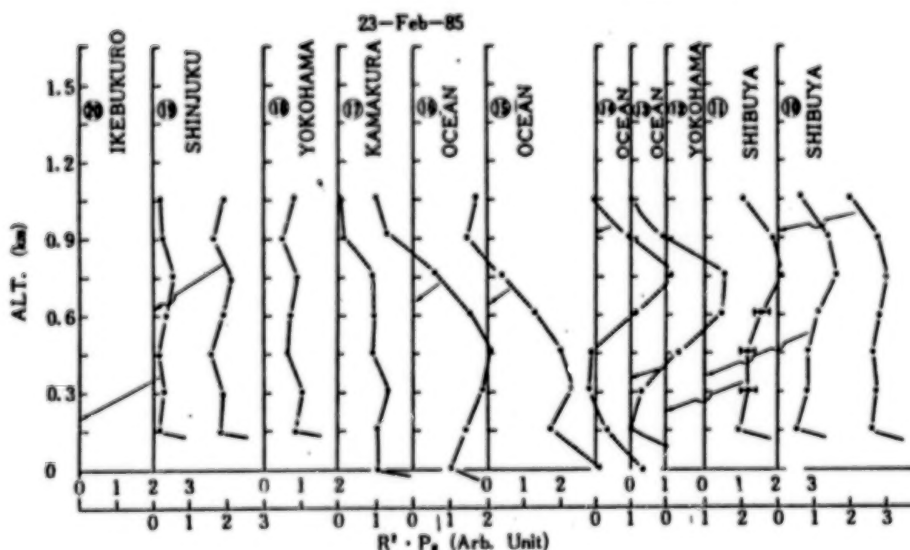


Fig. 2

N87

10285

UNCLAS

Nd:GLASS-RAMAN LASER FOR WATER VAPOR DIAL

R. H. Kagam, J. C. Petheram, and A. Rosenberg

RCA Astro-Electronics, P.O. Box 800, Princeton, N.J. 08543-0800

In this paper we describe a tunable solid-state Raman shifted laser which we use in a water vapor DIAL system at 9400 Å. The DIAL transmitter is based on a tunable glass laser operating at 1.06 μm , a hydrogen Raman cell to shift the radiation to 1.88 μm , and a frequency doubling crystal. We report the results of measurements which characterize the output of the laser with respect to optimization of optical configuration and of Raman parameters. We also describe the DIAL system and show preliminary atmospheric returns.

These experiments are a part of an ongoing DIAL research program at RCA Astro-Electronics to develop and demonstrate techniques for measuring atmospheric water vapor, pressure, and temperature profiles which will lead to the development of spaceborne sensors. The space environment requirements (i.e. long lifetime and high electrical efficiency) led us to choose the Nd:glass-Raman gas cell configuration. The Nd:glass laser is a tunable solid state laser with a long research history and since its absorption band occurs at 8000 Å (which coincides with the emission band of the AlGaAs diode), it has the potential to be pumped by 2D diode arrays. The diode array pump has two strong advantages over flashlamps — much greater operational lifetimes, and efficiencies of up to ten percent. Furthermore, since hydrogen is the candidate gas for achieving 9400 Å radiation, we benefit by using the gas which exhibits the largest efficiency (~80%) of all Raman gases. Second harmonic generation is a mature technology with which efficiencies of 40 to 50 percent can be achieved. Thus, with diode pumping, Nd:glass - H₂ Raman lasers can achieve overall efficiencies of ~2%.

Since 2D diode arrays are not yet available, we are using flashlamps to demonstrate the water vapor DIAL technique. A block diagram of the flashlamp pumped DIAL system laser transmitter is shown in Fig. 1. The oscillator contains a birefringent filter (BRF), and two etalons, 0.1 cm and 1.0 cm thick. These three components are used for wavelength selection. Tuning is achieved by tilting the 1.0 cm etalon. The other etalon is tilted and the BRF is rotated to maintain the laser cavity at the center of the respective modes. The cavity is Q-switched with a Pockels cell. The Q-switched output of the cavity is 50 mJ with a pulse duration of 60 nsec and a linewidth of $<0.04 \text{ cm}^{-1}$. This output is then passed through Nd:glass amplifiers, which include up to three flashlamp pumped Nd:glass rods, one of which may be, if necessary, double passed. We maintain the amplifier gain to obtain ~1 Joule pulses.

28901-78N

The output of the amplifiers is Raman shifted in hydrogen gas. To achieve a high conversion efficiency of the Raman shift, we use a Raman oscillator-amplifier configuration. Here, a pump beam is divided into two beams. A low energy tightly focused beam enters the Raman oscillator to provide a low energy Stokes beam to seed the Raman amplifier. In the Raman amplifier, the main part of the pump beam is spatially and temporally overlapped with the seed and amplification occurs, with consequent depletion of the pump. The Raman shifted radiation ($1.88 \mu\text{m}$) is passed into a frequency doubling crystal (LiIO_3) where 9400 \AA radiation then emerges.

The receiver of the DIAL system is a $f/4.5$, 45 cm Newtonian telescope. A field stop (1 to 10 mm) is placed at the focal plane of the telescope, a lens images the field stop on a RCA C30950E Silicon Avalanche Photodiode detector. In a preliminary test of the system a 1 to 2 mJ per pulse, 9400 \AA beam was transmitted vertically on a clear evening and aerosol backscatter was observed up to 3.5 km .

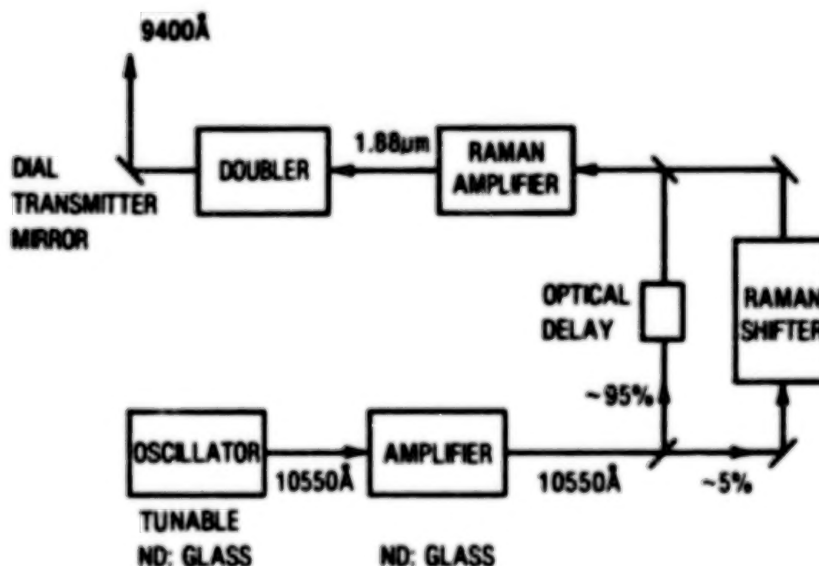


FIG. 1. BLOCK DIAGRAM OF ND: GLASS-RAMAN LASER

N87

10286

UNCLAS

A METEOROLOGICAL (HUMIDITY, TEMPERATURE, AEROSOLS) MOBILE DIAL SYSTEM: CONCEPTS AND DESIGN

Cl. CAHEN, J.L. LESNE, J. BENARD, P. PONSARDIN

Électricité de France, Direction des Etudes et Recherches, 6
quai Watier, 78400 CHATOU, FRANCE

1-Introduction

Since 1982 we have conducted a program to develop a mobile meteorological (humidity, temperature, aerosols) DIAL system devoted to the studies of the nuclear power plant atmospheric surroundings.

Though different papers have already addressed specific points of this development^(1,2), hereafter we take the opportunity of the conference to present a global overview of this system.

On the next table are defined the measurement objectives according to the user's needs and the lidar feasibility.

	range m	resolution m	accuracy	acq.time mn
humidity	30-3000	100	5%	10'
temperature	30-3000	100	5/10°C	10'
aerosols	30-3000	50	1%	10'

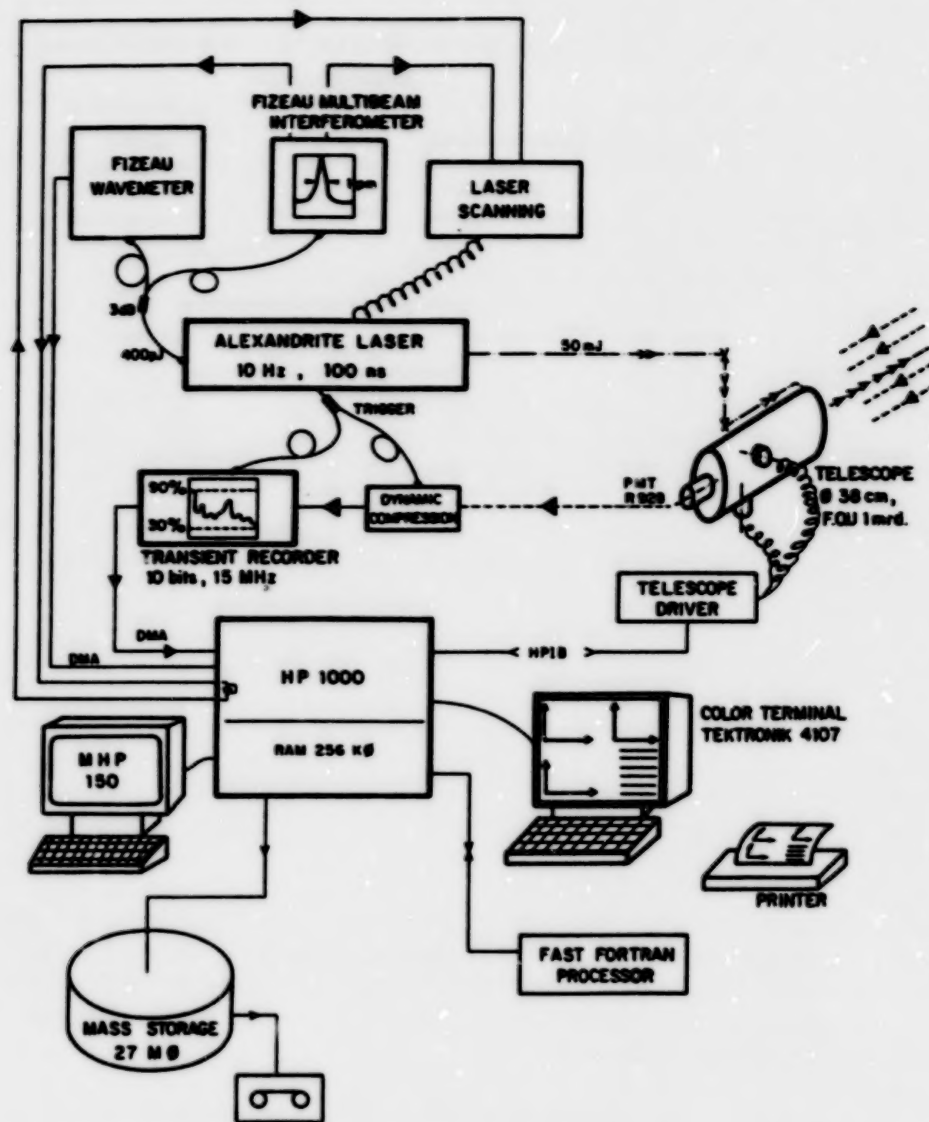
User's needs can be summarized as follows: automatic, flexible, quasi-realtime measurement displays. The methodological requirements are the commonly adopted issues: overall acquisition accuracy (10^{-3}), signal dynamic (10^4), spectrally narrow laser (1 pm), frequency stable laser (± 0.2 pm).

In this paper, we describe the concepts and design adopted to meet both the requirements and the measurement objectives. Each sub-system will be sequentially addressed: transmitting system, receiving system, detection system, post detection electronics, but a general synoptic of the system is given on the figure.

2-Transmitting system

a) laser source

An Alexandrite laser source is selected to be part of the mobile lidar system to be installed in a small van. The broad tunability capability of this source makes possible the



SYNOPTIC OF THE METEOROLOGICAL DIAL SYSTEM

measurements of humidity and temperature with only one active laser medium by changing the tuning elements positioning. The laser is commercially available but deeply modified to get the necessary operationality.

b) laser output characterization

The automatically tunable narrow line output emission is simultaneously controlled by a high accuracy wavemeter and a high finesse interferometer: a two beam Fizeau wavemeter for absolute wavelength determination and a multi-beam Fizeau interferometer for linewidth measurement.

The light routine is made by using multimode optical fibers (core 50 μ m + Selfoc coupling).

A calibration procedure of the wavemeter has been derived to take into account a spatial filtering effect on the absolute wavelength determination. Also improved was the algorithm already available. A statistical evaluation of the expected wavelength is performed to prevent from erroneous corrections due to integer handling associated with an equivalent mode jump in the interferometer. The ultimate resolution in the pulse regime is a few parts in 10^7 .

The Fizeau interferometer is microprocessor controlled to compute on a shot to shot basis the number of observed components associated to an uncorrect tuning of the intracavity etalons.

In addition to linewidth and absolute wavelength positioning requirements we paid a special attention to the evaluation of the possible residual amplified spontaneous emission (ASE). A precise simulation of the ASE effect on the wavelength determination enables us to estimate the residual ASE of the Alexandrite laser to be less than 0.5%

c) spectral data

For both water vapor and temperature measurements accurate spectral data (absorption cross section, line shape) are required to limit the systematic error.

We have performed the determination of cross sections and linewidths of selected water vapor and oxygen lines using a cw ring dye laser and an open White cell at atmospheric pressure. Comparison and results are reported in a recent paper⁽³⁾.

3-Receiving system

For daytime measurements in the 0.7 μ m range the spectral width of the receiving optics associated to the telescope is limited to 0.1 nm by a combination of a broadband filter plus a Fabry-Perot etalon. The transmission of this system has been calibrated using actual lidar echos and is found to be $\sim 40\%$ which is higher than the value obtained with a single narrow band interferential filter ($\sim 20\%$).

4-Detection system

Specialized experiments have been run to study the impulse response of a R 928 Hamamatsu PMT. A modified load circuitry has been tested and preserved a 1% linearity over 4 decades.

5-Post-detection electronics

As already mentioned the overall accuracy should be close to 0.1% to be compatible with temperature measurement accuracy of 0.2%.

We developed a two stage digitizer to ensure a true 10 bits digitization:

1) a signal recognition is performed using an A-D multiplier and a 68000 microprocessor to set a correct gain table for the adjustable input amplifier. It ensures that the signal level remains within 30-90% of the 10 bits digitizer full scale. A possible saturation of the electronics is prevented on a shot to shot basis and a change of the gain table leads to only one laser shot lost.

2) the analog signal is digitized using a 10 bit 15 MHz AD converter. The performances have been tested using both FFT and statistical missing code analysis: no missing code has been found and the noise is - 80 dB lower than the input signal.

Conclusion

At the very moment we write this paper, we are running the whole system in the laboratory before assembling into the van. We hope to be able to present the first measurements of humidity using an Alexandrite laser source at the Conference.

References:

(1) Cahen Cl., Mégie G., Flamant P., Bourdet M., et al. "Overview of recent developments in France for DIAL-LIDAR technique applications", 1985, 1st Intl. DIAL Data Collection and Analysis Workshop, Virginia Beach, U.S.A, Nov. 18-21.

(2) Cahen Cl., Lesne J-L., "Active remote sensing in France: laser developments for meteorological applications", 1985, OPTO 85, Paris, France, May 18, p. 147

(3) Grossmann B., Cahen Cl., Lesne J-L., Benard J., Leboudec G., "Intensities and atmospheric broadening coefficients measured for O₂ and H₂O absorption lines selected for DIAL monitoring of both temperature and humidity", 1986, to appear in Applied Optics.

N87

10287

UNCLAS

INFLUENCE OF RAYLEIGH-DOPPLER BROADENING ON THE SELECTION OF H₂O DIAL SYSTEM PARAMETERS

Syed Ismail
SASC Technologies
17 Research Drive
Hampton, VA 23666

Edward V. Browell
Atmospheric Sciences Division
NASA Langley Research Center
Hampton, VA 23665

INTRODUCTION

Rayleigh Doppler broadening is a process that causes spectral spreading of backscattered laser energy due to the random motion of air molecules. Early lidar measurements¹ showed that, due to their lower mass, air molecules are more effective in Doppler broadening of the laser energy than aerosol particles. Assuming that the molecular velocity distribution is given, approximately, by the Maxwellian function, the Doppler broadening width $d\lambda$ (HWHM) is given by

$$d\lambda = \frac{2\lambda}{c} \sqrt{\frac{2kT(\ln 2)}{m}} \quad (1)$$

where k is the Boltzman constant, T is the atmospheric temperature, m is the mean molecular mass, λ is the wavelength of the laser, and c is the velocity of light. The magnitude of $d\lambda$ defined in Equation (1), which arises due to the backscattering processes, is twice the normal Doppler broadening observed in absorption or emission. For $\lambda = 728$ nm, $T = 300^\circ\text{K}$ and $m = 28.9$ amu, $d\lambda \sim 1.7$ pm, which is similar to the H₂O absorption linewidth² at ~ 12 km altitude. Previous studies have shown that Doppler broadening has a significant influence on DIAL measurements²⁻⁴. Doppler broadening reduces the effective absorption cross section in H₂O DIAL measurements; however, this systematic effect is predictable and can be removed to first order. This aspect of the Doppler broadening effect has been well documented, but the influence of Doppler broadening on DIAL sensitivities to errors in other parameters has not been previously reported. Doppler broadening reduces the sensitivity of DIAL H₂O measurement errors due to the finite laser linewidth, laser position uncertainty and laser spectral resolution measured by a wavemeter. This effect also reduces errors due to an uncorrected pressure shift of the H₂O absorption line with altitude. Examples of these effects will be discussed after a description of the modeling assumptions.

MODELING

Computer simulations have enabled us to study the performance of a H₂O DIAL system by spectrally analyzing the forward propagating and backscattered laser energy. The assumed atmospheric, aerosol and H₂O

model profiles reflect an average mid-latitude summer-time condition⁵ without clouds. Strong gradients in aerosol and H₂O profiles have been avoided so that the altitude variations of the DIAL parameters could be studied without interference due to gradient terms⁴. The simulations were done for a high altitude (21 km) DIAL system operating in a nadir-viewing mode. These results are directly applicable to the National Aeronautics and Space Administration's H₂O DIAL system currently under development⁶, and they are also relevant to a spaceborne DIAL system. The laser spectral output is assumed to be composed of 3 equal-amplitude equally spaced modes over a 1 pm interval, which is typical of recently developed Alexandrite lasers operating in the 728 nm region. Unless otherwise stated, a nominal value for the H₂O absorption cross section of $\sigma_0 = 20.9 \times 10^{-24} \text{ cm}^2$ at ground level is assumed.

SIMULATION RESULTS

The Rayleigh Doppler broadening effect on the measurements of H₂O concentrations can cause systematic underestimates² greater than 10% at altitudes $> 10 \text{ km}$. While these errors are large, this systematic offset error can be calculated with the help of a model temperature profile and an aerosol scattering ratio profile (retrievable from the off-line DIAL signal). Our calculations show that with a 10% temperature error and 50% error in the aerosol scattering ratio, the worst case error in the calculated absorption cross section leads to only about a $\pm 1.5\%$ error in the H₂O measurements in regions free of large aerosol gradients. Therefore, in effect, the Doppler broadening causes only about a 1.5% error in H₂O DIAL measurement and we will show that the Doppler broadening, at least in clean atmospheric regions, reduces sensitivity to measurement uncertainty caused by finite laser linewidth, laser position uncertainty, system spectral resolution of laser energy, and H₂O line pressure shift. Examples of these effects are given below.

Figure 1 shows the combined influence of laser spectral width and Rayleigh broadening (uncorrected) on the H₂O DIAL measurement errors. For these simulations we used a strong absorption line ($\sigma_0 = 70.1 \times 10^{-24} \text{ cm}^2$) which is suitable for measurements over the altitude region 2-10 km. The errors caused by the distortion of the laser spectral profile due to H₂O absorption are also included in these error estimates. At altitudes $\sim 6 \text{ km}$ the Rayleigh broadening offset error (indicated by the 0.3 pm curve) decreases as the laser spectral width increases. This is because, in this altitude region, with low aerosols and small H₂O linewidths, the Doppler broadening influence is more effective for smaller laser linewidths. Below 6 km, the Rayleigh broadening influence decreases and the distortion of the laser line shape becomes important. In this altitude region, the 3 pm line suffers from laser line distortion problem more severely (which can perhaps be corrected with an iterative H₂O DIAL solution). The difference in systematic errors between the 1 pm and 0.3 pm DIAL systems is $\lesssim 1\%$. Above 6 km the 0.3 pm line has larger error due to greater Doppler broadening influence and below 6 km the 1 pm linewidth produces larger error due to laser line distortion. Even when the Doppler broadening and laser line distortion effects are corrected, it is expected that the residual error difference between these two will be less than 1%

over the 0-15 km altitude range. These results suggest that H₂O DIAL systems having a total spectral width ~ 1 pm would perform nearly as well as single-mode laser DIAL systems.

Figure 2 shows the sensitivity of laser tuning error with and without Doppler broadening influence. The profiles have been normalized to eliminate laser distortion error and it has been assumed that Doppler broadening is fully correctable. In the lower troposphere (< 5 km), the error due to a 0.5 pm detuning is comparable for the two cases but at high altitudes (> 5), this error is reduced by the Doppler broadening influence. It can be seen that at 15 km, this error is larger by about 45% in the absence of Doppler broadening. In Figure 3, overestimates of the H₂O density measurement due to wavemeter resolutions of 0.5 and 1 pm with and without Doppler broadening are compared. It shows that Doppler broadening when fully corrected reduces the sensitivity of the error due to wavemeter resolution.

Rayleigh Doppler broadening also reduces sensitivity to atmospheric effects. Zuev et al.⁷ have shown that pressure shifts (uncorrected) can cause up to 30% error at 20 km altitude. They did not include the influence of Doppler broadening in their calculations. Figure 4 shows that without Doppler broadening, the errors would be larger by about 45% at 15 km altitude. Therefore, the presence of Rayleigh broadening reduces the sensitivity of error due to pressure shifts when the line positions are not properly selected.

We have evaluated the influence of Rayleigh Doppler broadening on DIAL measurement accuracies and have shown that the Rayleigh broadening influence, which can be corrected to first order in regions free of large aerosol gradients, reduces the sensitivity of DIAL H₂O measurement errors in the upper tropospheric regions (≥ 10 km). We discuss in this paper our ability to correct the Rayleigh broadening and the selection of H₂O DIAL parameters when all the systematic effects are combined.

REFERENCES

1. Fiocco, F. G., G. Benedetti-Michelangeli, K. Maischberger, and E. Madonna, Nature, Phys. Sci., Letters, 229, 78, (1971).
2. Ismail, S., E. V. Browell, G. Megie, P. Flamant, and G. Grew, 12th Int. Laser Radar Conf. Abstracts, p. 431, Aug. 1984.
3. Korb, C. L. and C. Y. Weng, 11th Int. Laser Radar Conf., NASA Ref. Pub. 22288, p. 78, 1982.
4. Ansman, A., Appl. Opt., 24, 3476, (1985).
5. McClatchey, R. A., et al., AFCRL-72-0497, Aug. 1972.
6. Browell, E. V., W. R. Vaughan, W. M. Hall, J. J. Degnan, R. D. Averill, J. G. Wells, D. E. Hinton, and J. H. Goad, 13th Int. Laser Radar Conf. Abstracts, NASA CP-2431, 1986.
7. Zuev, V. V., Yu, N. Ponomarev, A. M. Solodov, B. A. Tikhomirov, and O. A. Romanovsky, Opt. Lett., 10, 318, (1985).

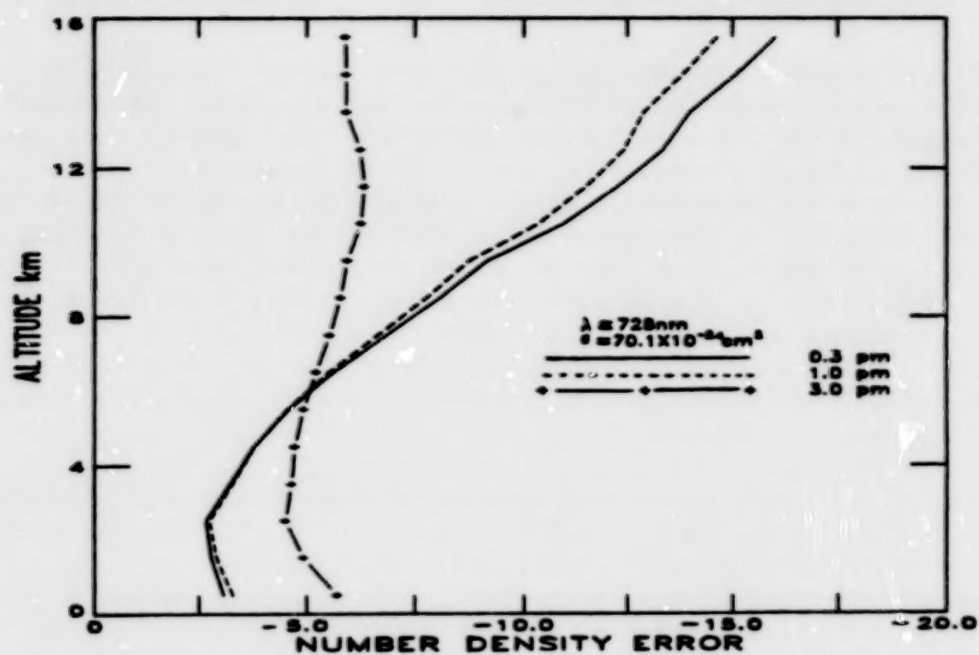


Figure 1. Influence of laser linewidth on Rayleigh Doppler broadening and laser line distortion error.

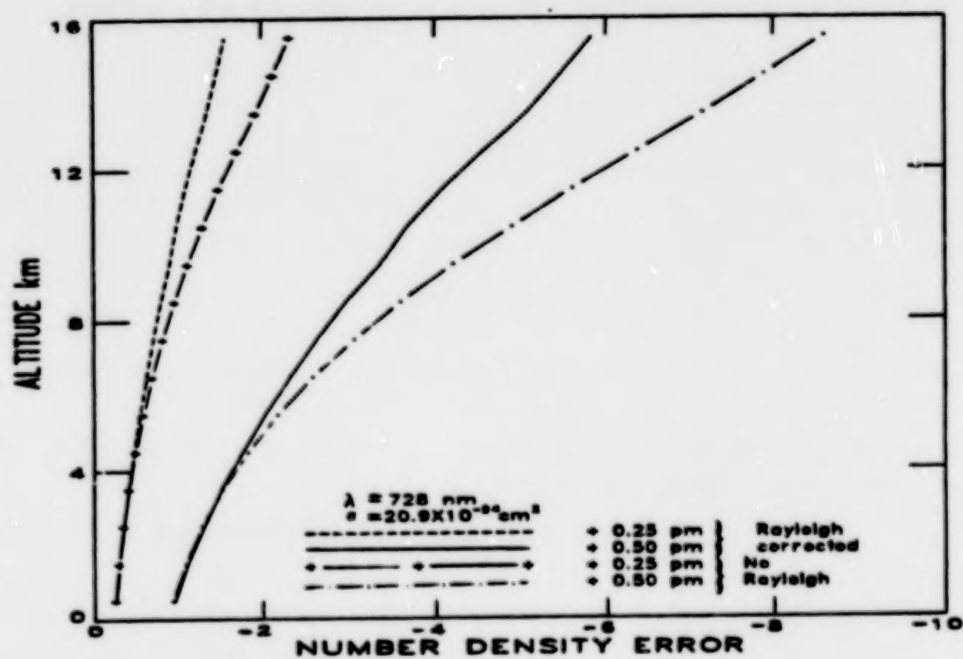


Figure 2. Laser shift (detuning) error with Rayleigh broadening (corrected) and in the absence of Rayleigh broadening influence.

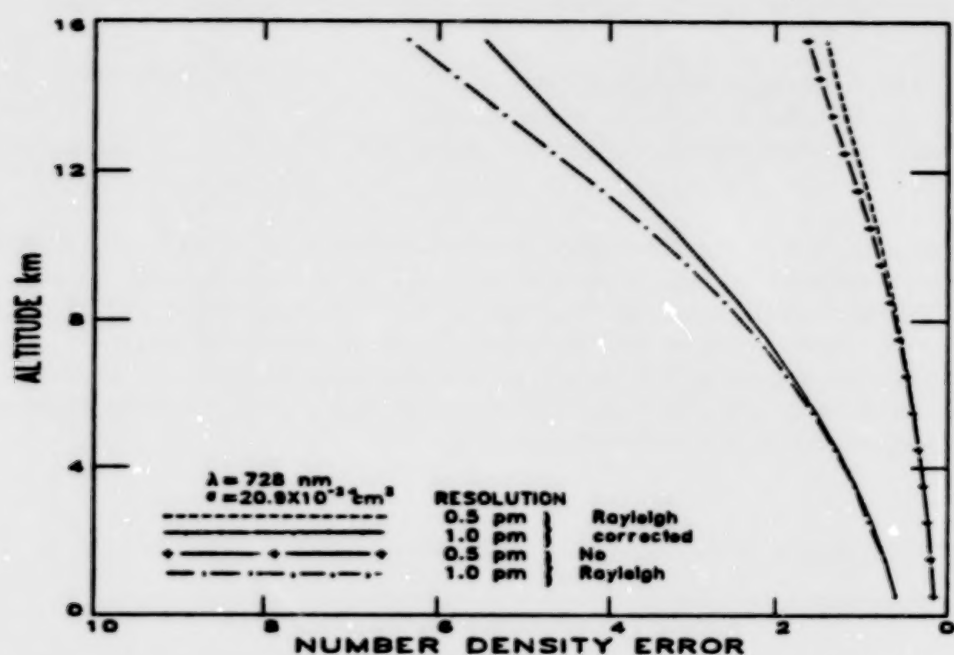


Figure 3. Wavemeter bandwidth errors with and without Rayleigh broadening (corrected).

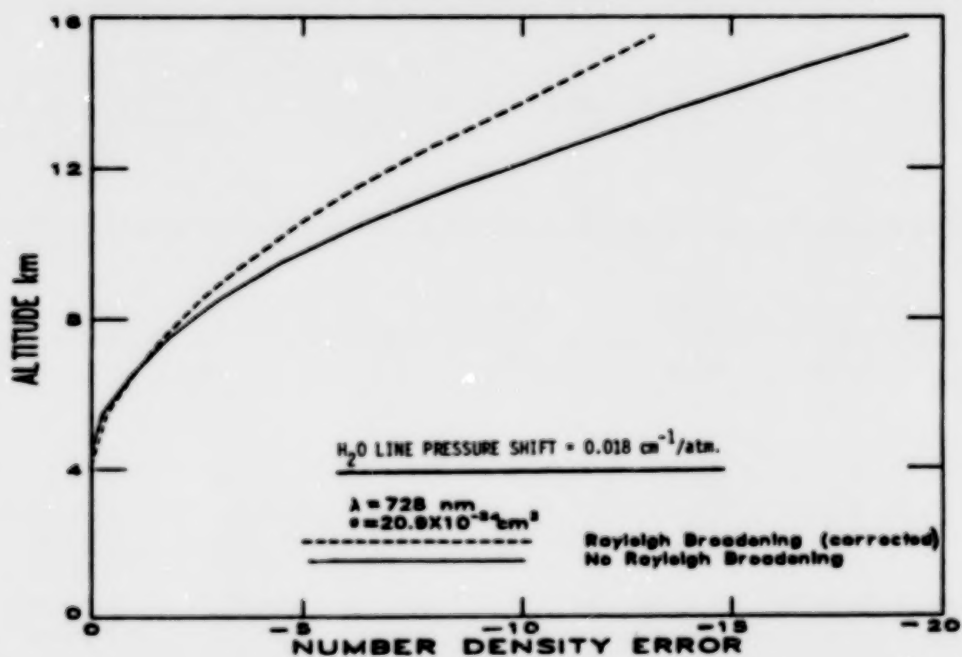


Figure 4. Errors due to pressure shift effects in H_2O absorption lines with and without Rayleigh broadening (corrected). The laser line is assumed to be at the center of the H_2O line at ground altitude.

N87

10288

UNCLAS

CORRECTION OF DOPPLER-BROADENED RAYLEIGH-BACKSCATTERING EFFECTS IN H₂O DIAL MEASUREMENTS

A. Ansmann and J. Bösenberg
Max-Planck-Institut für Meteorologie
Bundesstrasse 55, D-2000 Hamburg 13, FRG

This paper describes and discusses a general method of solutions for treating effects of Doppler-broadened Rayleigh backscattering in H₂O DIAL measurements. Errors in vertical DIAL measurements caused by this laser line broadening effect can be very large (Ansmann, 1) and, therefore, this effect has to be accounted for accurately.

To analyze and correct effects of Doppler-broadened Rayleigh backscattering in DIAL experiments, a generalized DIAL approximation was derived starting from a lidar equation, which includes Doppler broadening:

$$(1) \quad N(\bar{R}) = \frac{1}{2(\sigma_1(\bar{R}) - \sigma_2(\bar{R}))DR} \left\{ \ln \left(\frac{P_1(R_1) \cdot P_2(R_2)}{P_1(R_2) \cdot P_2(R_1)} \right) + D_1(\bar{R}) - D_2(\bar{R}) \right\}$$

where $N(\bar{R})$ is the water vapor number density averaged over the range cell DR centered at $\bar{R} = (R_1 + R_2)/2$ and $P_1(R)$ and $P_2(R)$ are the on- and off-line laser signals backscattered from the range cell at R, respectively. The absorption cross section for wave number ν , ($i = 1$: on-line, $i = 2$: off-line) averaged over the range cell DR centered at \bar{R} is given by

$$(2) \quad \sigma_i(\bar{R}) = \frac{1}{2} \int_{-\infty}^{\infty} \sigma_i(\nu, \bar{R}) \cdot \left(\left(1 + \frac{\beta_M(R_2)}{\beta(R_2)} \right) h_i(\nu) + \frac{\beta_R(R_2)}{\beta(R_2)} g_i(\nu, R_2) \right) d\nu$$

and the Doppler broadening correction term D_i for wave number ν , is given by

$$(3) \quad D_1(\bar{R}) = \ln \left\{ \int_{-\infty}^{\infty} \left(\frac{\beta_M(R_2)}{\beta(R_2)} h_1(\nu) + \frac{\beta_R(R_2)}{\beta(R_2)} g_1(\nu, R_2) \right) \cdot \exp \left(- \int_{R_0}^{R_1} N(r) \cdot \sigma_1(r, \nu) dr \right) d\nu \right\}$$

$$- \ln \left\{ \int_{-\infty}^{\infty} \left(\frac{\beta_M(R_1)}{\beta(R_1)} h_1(\nu) + \frac{\beta_R(R_1)}{\beta(R_1)} g_1(\nu, R_1) \right) \cdot \exp \left(- \int_{R_0}^{R_1} N(r) \cdot \sigma_1(r, \nu) dr \right) d\nu \right\}$$

where $\beta(R_i)$ is the total backscattering coefficient for range R_i , $\beta_M(R_i)$ and $\beta_R(R_i)$ are the Mie and Rayleigh backscattering coefficients for range R_i , $h_i(\nu)$ is the normalized laser line shape for wave number ν , and $g_i(\nu, R_i)$ is the convolution of the incident laser profile $h_i(\nu)$ and the intensity distribution of an incident monochromatic frequency ν , backscattered by air molecules in the range cell at R_i .

The calculation of water vapor density $N(\bar{R})$ with Eqs. (1)-(3) includes the correction of Doppler broadened Rayleigh backscattering effects. For using this calculation scheme, laser and H₂O absorption line parameters, temperature and pressure have to be known as usual for H₂O DIAL retrieval. In addition, for the correction of effects of Doppler broadening, backscattering properties of molecules and aerosols have to be known. The backscattering properties of molecules can be determined from measured temperature and pressure pro-

files or approximated from model atmosphere data. The aerosol backscattering properties can be obtained from range normalized off-line signals $P_2(R) \cdot R^2$ using a numerical integration scheme (Fernald, 2; Sasano et al., 3). Here, in addition, Rayleigh backscattering coefficients, aerosol extinction/backscattering ratio and aerosol backscattering coefficient at calibration range R_c have to be known. To yield generally stable solutions of this integration scheme for $\beta_M(R)$ with respect to uncertainties in the signals and the other input parameters, backward integration mode with boundary value $\beta_M(R_c)$ for maximum range $R_c = R_{max}$ should be used (Klett, 4). For the evaluation of the integral in Eq. (3) giving the water vapor optical thickness up to the range R_1 , values for $N(r)$ calculated in the preceding steps $R_0 < R < R_1$ can be used. The off-line Doppler broadening correction term D_2 can be neglected, if off-line absorption is approximately constant over the transmitted spectrum.

To evaluate the accuracy of H₂O DIAL measurements using Eqs. (1)-(3), computer simulations were performed using Gaussian laser line shape with HWHM of 0.0125 cm⁻¹, Voigt-H₂O absorption lines with Lorentz halfwidth of 0.09 cm⁻¹, profiles of temperature, pressure and H₂O density (5.9 g m⁻³ at ground level) for standard atmospheric conditions, aerosol scattering coefficients for clear atmosphere conditions (McClatchey, 5, ground level visibility of 23 km) with additional layers of enhanced aerosol backscattering, and realistic lidar and receiver parameters. Lidar signals needed for the determination of H₂O and aerosol backscattering were calculated with a lidar equation considering Doppler broadened Rayleigh backscattering. H₂O-DIAL number densities were calculated with Eqs. (1)-(3). To analyze only Doppler broadening effects, no errors in the profile $\ln(P_1(R)/P_2(R))$ used for solving the DIAL approximation (1) were assumed. The difference between the retrieved and the true or input H₂O is shown in the figures.

In Fig. 1 examples of error profiles to be expected in ground based H₂O DIAL experiments due to realistic uncertainties in input parameters for backscattering retrieval are shown. It can be seen that correction of Doppler broadening effects is generally necessary. The accuracy of this correction mainly depends on the accurate determination of aerosol backscattering coefficients. Analysis of the influence of each input parameter for aerosol backscattering retrieval shows that it is especially important to have a proper estimate of the boundary value $\beta_M(R_c)$ at $R_c = R_{max}$ as a starting value for iterative aerosol backscattering retrieval. Error peaks at the upper layer boundaries in Fig. 1 are mainly due to errors in $\beta_M(R_c)$. The influence of errors in backscattering calculation is most important, when Mie and Rayleigh backscattering coefficients are of the same order of magnitude and, in addition, layers with steep gradients of aerosol backscattering are present. This is the case in the figures for the layer regions in the middle and upper troposphere. The relative water vapor error due to uncertainties in Doppler broadening correction is proportional to DR^{-1} so that the shown effects decrease with increasing DR.

In conclusion, correction of Doppler broadened Rayleigh backscattering is possible with good accuracy in most cases of tropospheric H₂O DIAL measurements, but great care has to be taken when layers with steep gradients of Mie backscattering like clouds or inversion layers are present.

References

1. Ansmann, A., "Errors in Ground-Based Water-Vapor DIAL Measurements due to Doppler-Broadened Rayleigh Backscattering", *Appl. Opt.*, **24**, 3476 (1985).
2. Fernald, F.G., "Analysis of Atmospheric Lidar: Some Comments", *Appl. Opt.*, **23**, 652 (1984).
3. Sasano, Y., Browell, E.V., and Ismail, S., "Error Caused by Using a Constant Extinction/Backscattering Ratio in the Lidar Solution", *Appl. Opt.*, **24**, 3929 (1985).
4. Klett, J.D., "Stable Analytical Solution for Processing Lidar Returns", *Appl. Opt.*, **20**, 211 (1981).
5. McClatchey, R.A., Fenn, R.V., Selby, J.E.A., Volz, F.E., and Garing, J.S., "Optical Properties of the Atmosphere", AFCRL-71-0279, Environmental Research Papers, 354 (1971).

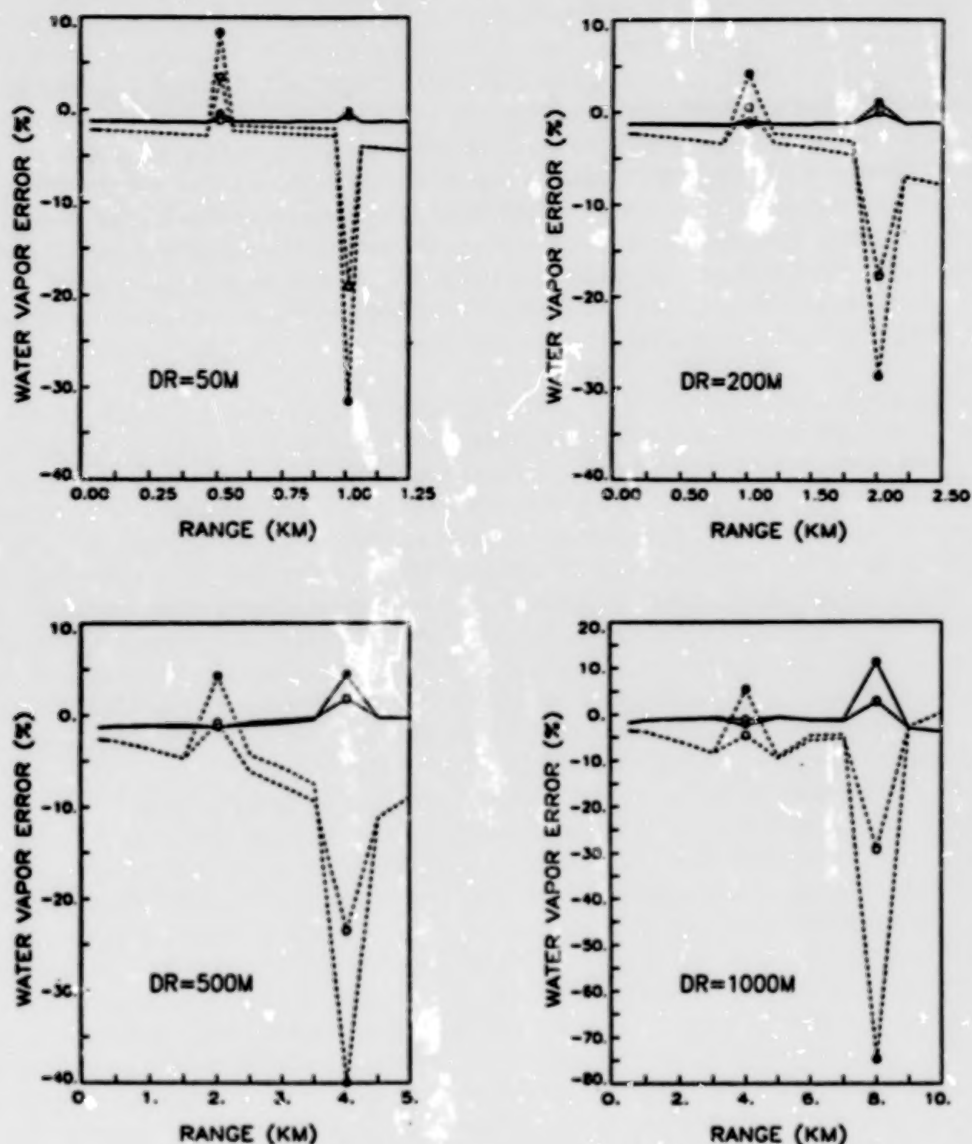


Fig. 1: Errors in H_2O DIAL measurements due to Doppler-broadened Rayleigh backscattering. Dashed lines: without correction of Doppler broadening; solid lines: correction applied. Errors in input parameters assumed for retrieval: 3K in temperature, -10 hPa in pressure; aerosol extinction/backscattering ratio assumed for retrieval: 60 sr, true value: 80 sr; Mie/Rayleigh backscattering ratio at R_{max} assumed for retrieval: 0, true value: 0.18. Aerosol layers with an aerosol concentration a factor 2 (○) and 5 (●) higher than the aerosol concentration of the clear air model between 0.5-1 km (DR = 50 m), 1-2 km (DR = 200 m), 2-4 km (DR = 500 m), and 4-8 km (DR = 1000 m).

N87

10289

UNCL

M J T Milton and P T Woods
Division of Quantum Metrology
National Physical Laboratory
Queens Road, Teddington, Middlesex, TW11 0LW, UK

One of the most important parameters of a DIAL system is the delay time between the on and off-resonant pulses. It is important that this delay time is sufficiently small to ensure that the atmosphere is effectively "frozen" between the pulses. Therefore, most DIAL systems have been designed with two lasers firing alternately less than 1 msec apart (Schotland 1974). Despite the importance of this parameter in the design of DIAL systems and its contribution to the overall error of a column measurement, very little is known about the size of the error for the case of a direct-detection system using atmospheric backscatter.

The UV DIAL system at NPL uses two independent YAG/dye lasers and is therefore suitable for measuring the effects of different pulse delays on the variance of column measurements for a variety of atmospheric conditions. A set of DIAL returns has been acquired with the two lasers tuned to the same wavelength and with a range of pulse delay times between 250 microseconds and several minutes. This data set was recorded in full on a computer and has been used both to test different averaging techniques and also to evaluate atmospheric contributions to DIAL columns.

1 PULSE AVERAGING

In order to produce good measurements of column content, the return-signals from a DIAL system are generally averaged over many pulse pairs. For a system that acquires on and off-resonant pulses alternately, there are three methods (Warren 1986) for performing this average.

$$CL(r) = \frac{1}{2\Delta\alpha} - \frac{1}{N} \sum_{i=1}^N \log \frac{P_i^{ON}(r)}{P_i^{OFF}(r)} \quad (1)$$

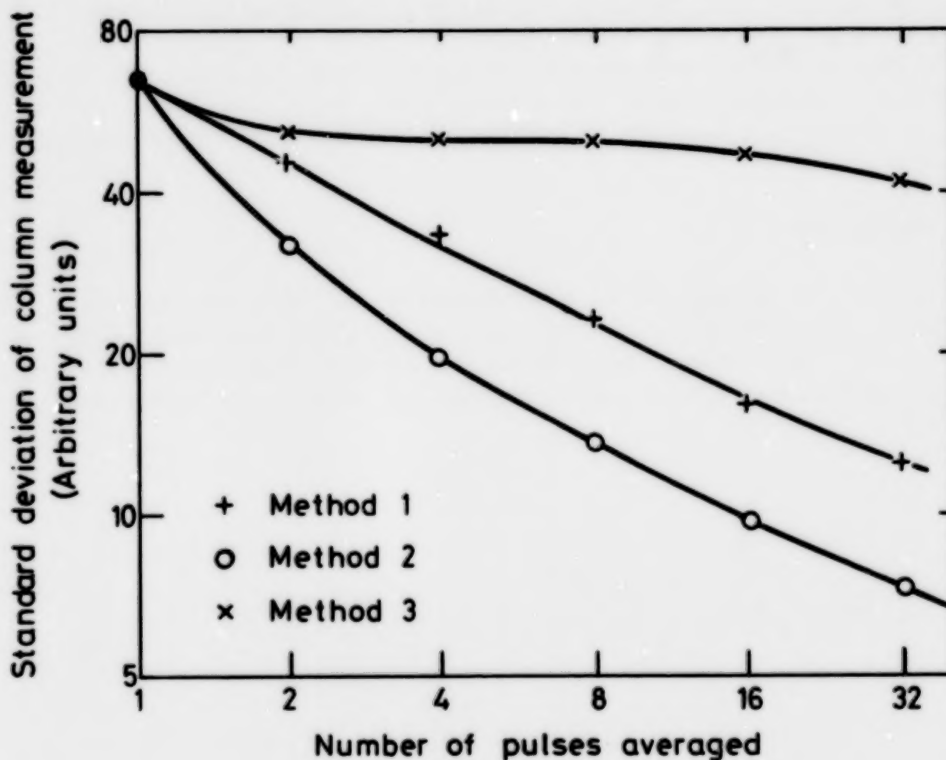
08901-58M

$$CL(r) = \frac{1}{2\Delta\alpha} \log \frac{\sum_i P_i^{ON}(r)}{\sum_i P_i^{OFF}(r)} \quad (2)$$

$$CL(r) = \frac{1}{2\Delta\alpha} \log \frac{1}{N} \sum_{i=1}^N \frac{P_i^{ON}(r)}{P_i^{OFF}(r)} \quad (3)$$

where $P_i^{ON}(r)$ is the power received from a distance r from the on-resonant pulse i , $CL(r)$ is the integrated column content up to the distance r and N is the total number of pulse-pairs averaged.

These three different algorithms have been applied at NPL to the atmospheric backscatter returns produced by a set of 32 pulse pairs. Some typical results are shown below. It can be seen that the standard deviation of the column decreases in proportion to $N^{-1/2}$ for method 1, but not for either method 2 or 3. This kind of behaviour has been observed before (Menyuk 1985), in experiments using a topographic target to provide the return signal.



Pulse averaging for an ensemble of 32 pulses

This technique of calculating standard deviations for various averaging intervals does not produce unambiguous information about the atmospheric contribution to DIAL errors because of the other errors that are involved. Most importantly, the methods used for background subtraction and pulse energy normalisation effect the algorithms in different ways. In addition, the bias introduced (Rye 1978) and the effects of shot noise must also be considered. However, it is a useful pragmatic exercise for selecting an optimum signal averaging method.

2 CROSS CORRELATION

A more direct method for assessing the atmospheric contribution to the column error is by evaluating the cross correlation between two pulses:

$$\rho_{ij}(r) = \frac{\langle (P_i^{\text{ON}}(r) - \overline{P_i^{\text{ON}}}(r))(P_j^{\text{OFF}}(r) - \overline{P_j^{\text{OFF}}}(r)) \rangle}{\sqrt{\langle (P_i^{\text{ON}}(r) - \overline{P_i^{\text{ON}}}(r))^2 \rangle \langle (P_j^{\text{OFF}}(r) - \overline{P_j^{\text{OFF}}}(r))^2 \rangle}}$$

This kind of method has been used before (Sugimoto 1986) for atmospheric backscatter returns and shows that the atmospheric contributions depend upon the exact measurement set-up (eg horizontal or vertical pointing) and the size of the receiver field of view.

REFERENCES

- Schotland, R M (1974), Errors in the Lidar Measurement of Gases by Differential Absorption, *J Appl Met* 13, 1974, 71-77.
- Warren, R E, Pelon, J and Milton, M J T (1986), Dial Signal Processing in Workshop on Dial Data Processing and Collection Techniques. Ed. E V Browell and P T Woods, NASA (to be published).
- Menyuk, N, Killinger, D K and Menyuk, C R (1985), Error Reduction in Laser Remote Sensing: Combined Effects of Cross Correlation and Signal Averaging, *Appl Opts* 24, 1985, 118-131.
- Rye, B J (1983), Power Ratio Estimation in Incoherent Backscatter Lidar: Heterodyne Receiver with Square Law Detector, *J Appl Met* 22, 1983, 1899-1913.
- Sugimoto, N, Matsui, I, Shimizu, H, Takeuchi, N (1986), Experimental Estimation of the Error Due to the Fluctuation of Aerosol Backscattering in DIAL Measurements, in Workshop on Dial Data Processing and Collection Techniques. Ed. E V Browell and P T Woods, NASA (to be published).

N87

10290

UNCLAS

HIGH SPECTRAL PURITY, NARROW LINEWIDTH LASER
TRANSMITTER FOR DIAL MEASUREMENTS

U.N. Singh

University of Maryland, Institute for Physical Science
and Technology, College Park, Maryland 20742, U.S.A.

P.H. Flamant

Laboratoire de Meteorologie Dynamique du CNRS,
Ecole polytechnique, 91128 Palaiseau, France

The use of the pulsed, oscillator-amplifier dye laser as a source of tunable coherent radiation for DIAL measurements is attractive because of its wide tunability, narrow spectral linewidth and high peak power. However, the multi-stage, high gain amplifiers, beside generating radiation within a narrow spectral bandwidth (a few picometers), also generate uncontrolled emission of a broad spectral nature (covering tens of nanometers) called amplified spontaneous emission (ASE). Thus the output radiation has two spectral components: (1) radiation within the required spectral bandwidth called signal radiation, and (2) radiation outside the required bandwidth called noise. The spectral purity can be defined as the percentage of signal radiation in the total output. The presence of ASE along with signal radiation is an unwanted interference in DIAL measurements.^{1,2}

To minimize systematic errors associated with DIAL measurements, a narrow linewidth laser transmitter with a very high degree of spectral purity is needed.

A frequency-doubled Nd:YAG-pumped dye laser (Quintel 180C + Jobin Yvon HPHR) was used as a light source in our experiments. Rhodamine 6G and Carbazine 122 laser dyes were used for the generation of 580 nm and 720 nm wavelengths. A spectrometer (Spex 1800) in combination with an Optical Multichannel Analyzer (OMA) was used for spectral purity measurements. A multipass white cell with a path length of 150 meters was used along with a ratio meter (Lasers Precision, Inc. model Rj 7200) to study the influence of ASE on humidity measurements.

With a Rhodamine 6G concentration of 4.5×10^{-4} M/L for the oscillator and 1.8×10^{-4} M/L for the amplifier, the peak of the frequency doubled Nd:YAG-pumped dye laser gain curve lies near 580 nm. Figure 1 illustrates the dependence of dye laser spectral purity on the oscillator energy, firstly, when emitted radiation is centered at the peak of the gain curve and secondly, when it is detuned.

With a Carbazine 122 concentration of 3.0×10^{-3} M/L and 1.25×10^{-3} M/L for oscillator and amplifier, respectively, Figure 2 shows the dye laser spectral purity dependence on oscillator energy.

Figure 3 shows the water vapor absorption line at 723.4734 nm recorded using a white cell of 150 meter path length. This linewidth was found to be 11.6 pm (FWHM), which is slightly higher than the value of 11.2 pm and 10.6 pm measured, respectively, by Wilkerson et al³ and Grossmann et al⁴.

For small values of optical depth, a simple theoretical calculation predicts a linear variation of the White cell transmission with spectral purity: transmission approaches unity as spectral purity approaches zero, and becomes minimum when the spectral purity is high, i.e. approaches unity.

Figure 4 shows the transmission of the White cell as a function of spectral purity for the laser line centered at the peak of the water vapor absorption line at 723.4734 nm. The spectral purity at this laser output was varied in a known way by changing the orientation of the oscillator dye cell. Figure 4 clearly indicates the error involved in humidity measurements, if the emitted radiation from the laser transmitter does not have a high degree of spectral purity.

CONCLUSIONS

A laser transmission with very high degree of spectral purity has been described. ASE dependence on the oscillator energy and the detuning away from the gain curve center are demonstrated. The effects of both finite laser linewidth and spectral purity on humidity measurements are experimentally demonstrated.

References

1. J. Lefrere, G. Megie, C. Cahen, and P.H. Flamant, Proc. Twelfth International Laser Radar Conference, Aix-en-Provence, France, August 13-17, 1984.
2. U.N. Singh, "Etude d'un nouveau lidar bi-impulsion bi-frequence pour la mesure de la vapeur d'eau dans l'atmosphere", Ph.D. thesis in Physics, l'Universite' Pierre et Marie Curie (February 1985).
3. T.D. Wilkerson, G. Schwemmer, and B. Gentry, J. Quant Spectros. Radiat. Transfer **22**, 315 (1979).
4. B. Grossmann, C. Cahen and J.L. Lesne, Proc Twelfth International Laser Radar Conference, Aix-en-Provence, France, August 13-17, 1984.

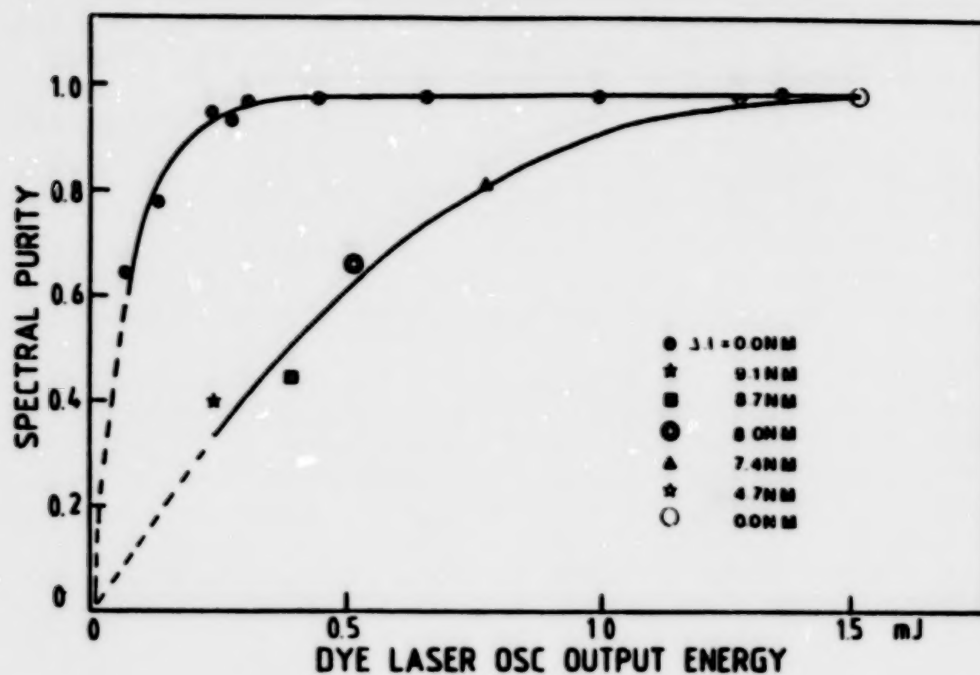


Figure 1 Spectral purity as a function of oscillator output energy and detuning from the center of the gain curve (580 nm).

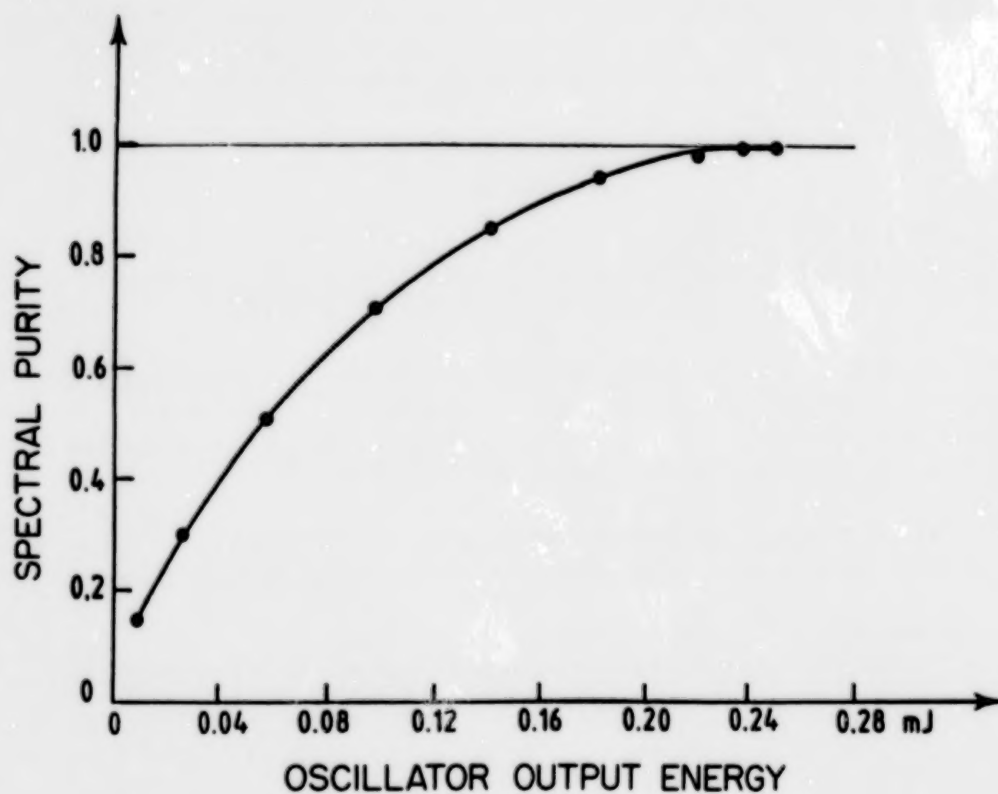


Figure 2 Spectral purity versus oscillator output energy at 724 nm.

18501-784

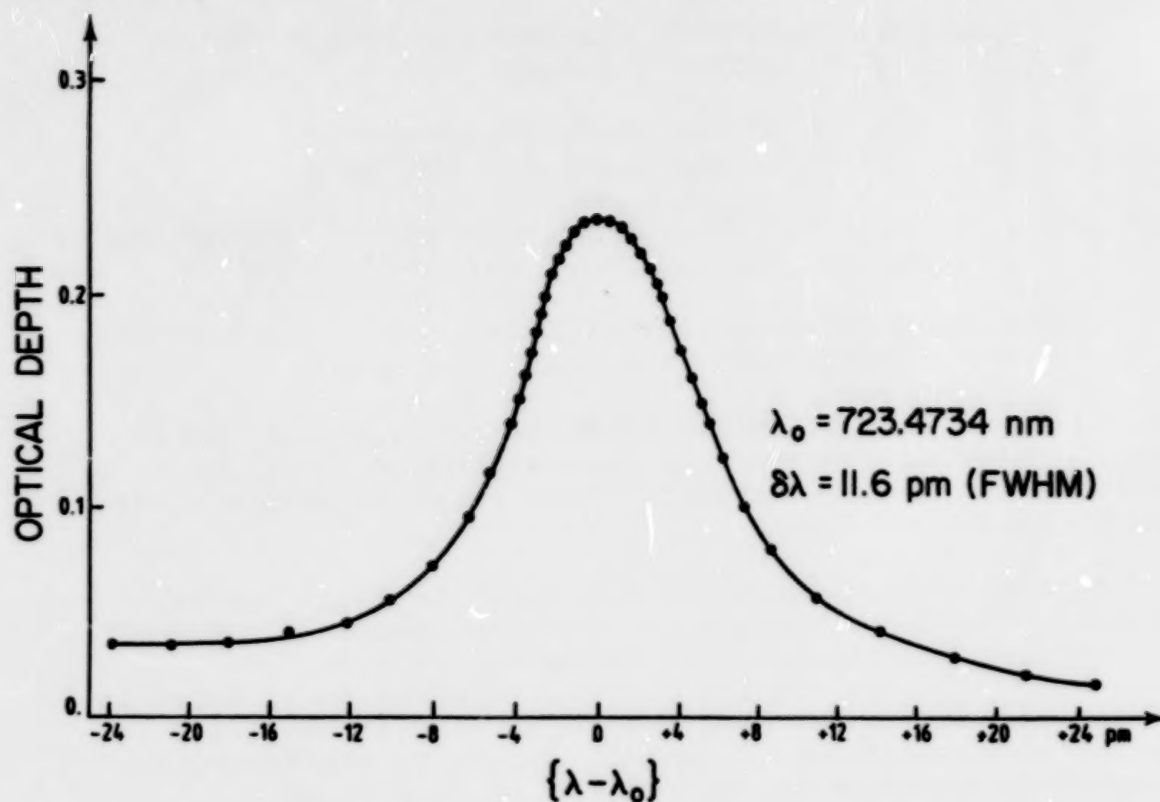


Figure 3 Water vapor absorption spectrum at 723.4734 nm obtained with pulsed dye laser.

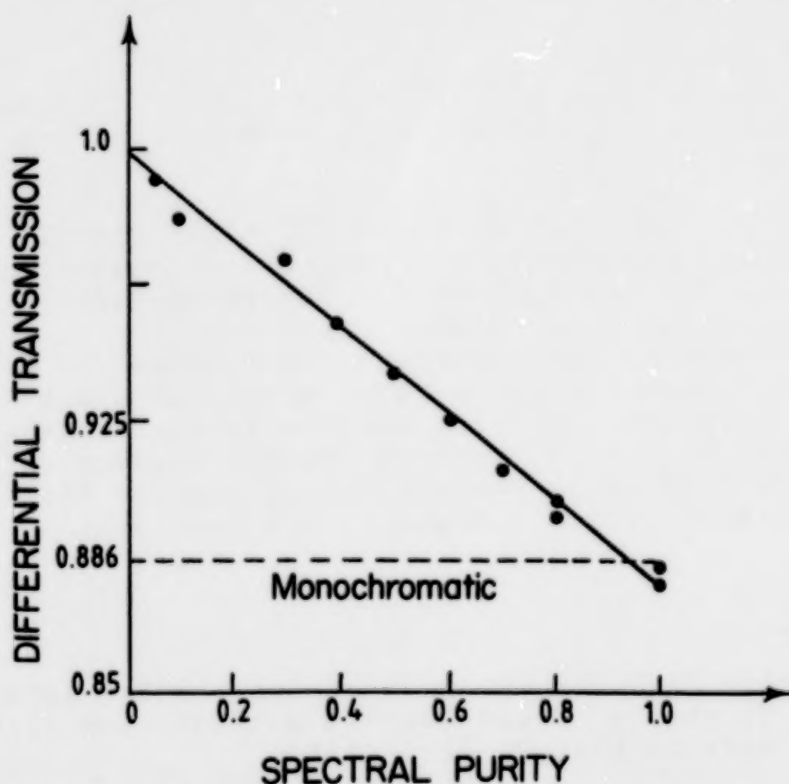


Figure 4 Differential transmission of the white cell at 723.4734 nm versus spectral purity.

N87

10291

UNCLAS

ON THE MEASUREMENT OF ATMOSPHERIC DENSITY USING
DIAL IN THE O₂ A-BAND (770 nm)*

T.D. Wilkerson, G.K. Schwemmer(+),
L.J. Cotnoir, and U.N. Singh

Institute for Physical Science and Technology, University of
Maryland, College Park, Maryland 20742

(+)Laboratory for Atmospheres, NASA Goddard Space Flight
Center, Greenbelt, Maryland 20771

Differential absorption lidar measurements in the A-band of molecular oxygen have been suggested as a means of profiling atmospheric density. This paper reports progress towards this capability.

Figure 1 illustrates the "troughs" in which optical absorption by O₂ is roughly temperature independent for near-ambient conditions. For measuring density (or pressure^{2,3,4}) the "on-line" DIAL transmission is tuned to the appropriate trough, and the off-line laser is tuned to just outside the A-band. Identification of the "density troughs" is based on the far wing line absorption coefficient given by

$$K(\nu) = \frac{Ck^2 b_c^0(T_0)}{\pi P_0 (\nu - \nu_0)^2} \left(\frac{T_0}{T}\right)^n N^2 e^{-E/kT} \{1 - h.o.(3\%)\}$$

where N is particle density, $b_c^0(T_0)$ is the line profile HWHM at reference temperature T_0 , pressure $P_0 = NkT_0$, and the exponent $n=0.7$ for O₂.

We have carried out error analyses for this type of lidar and for related temperature- and pressure-measuring techniques that utilize the O₂ A-band. The parameters assumed are given in Table I. Figure 2 shows a representative example of the numerical simulations for a fixed altitude resolution of 150 meters; elevation angles of 90°, 60°, and 30° are used for time periods in the range 1-4 min. The accuracy of these O₂ density profile measurements is predicted to be 0.3% or better throughout most of the troposphere. Standard lidar instrumentation has been

*Research supported by NASA LaRC through Cooperative Agreement NCC1-25, NOAA-NESDIS through Grant NA83-AA-A-00036, and by U.S. Army ASL through Contract DAAG 29-81-D-0100.

assumed. We have shown that tropospheric density can be profiled with accuracies of order 0.1-0.5%, with good altitude resolution, over a useful range of atmospheric conditions.

Density profiles in the atmosphere may also be measured via Raman scattering by N_2 , but require precise knowledge of the optical form factor for the lidar system. This requirement does not apply to the two-beam O_2 DIAL technique. However, DIAL does require careful monitoring of laser wavelength and linewidth, using spectrometer/wave-meter instrumentation.^{5,6}

Generation of tunable, narrow band, pulsed laser output at 760-770 nm can be done with laser-pumped dye lasers or with a tunable crystal laser such as Alexandrite. As part of a program⁷ described elsewhere at this meeting, we are investigating the alternative of "Raman shifting" in H_2 ($\Delta\nu \sim 4100 \text{ cm}^{-1}$) starting with tunable dye laser output at 585 nm. Due to a special design, the radiation bandwidth can be as low as 0.02 cm^{-1} .

Detailed results on energy and narrow linewidth at 770 nm will be presented for both the straight dye laser and the Raman-shifted dye laser, including high resolution scans of the O_2 absorption spectrum for comparison with quantitative spectroscopic data.^{8,9} This work is part of a general approach to develop a meteorological lidar system for measuring density, pressure, temperature, and humidity - all based on DIAL and the very near infrared absorption lines of H_2O and O_2 (700-1140 nm).

We thank K. Ritter, B. Grossmann, and S. Higdon for assistance in this research.

Table I. Meteorological Lidar Parameters for O_2 A-band

Tunable laser: 100 mJ pulse energy, 10Hz PRF, λ 760-770 nm
Rcvr. area 1.0 m^2 ; Optical efficiency 5% (night), 2.5% (day)
Transmitted beam divergence 0.3 mrad; Rcvr. FOV 0.5 mrad.

References

1. C.L. Korb and C.Y. Weng, "A Two-Wavelength Lidar Technique for the Measurement of Atmospheric Density Profiles," Proc. CLEO, Phoenix, AZ (April 1982).
2. C.L. Korb and C.Y. Weng, Appl. Optics 22, 3759 (1983).
3. G.K. Schwemmer, C.L. Korb, M. Dombrowski and R.M. Kagann, "Atmospheric Pressure Profiles Measured Using an Alexandrite Laser Differential Absorption Lidar," Proc. OSA Topical Meeting on Optical Remote Sensing of the Atmosphere, Incline Village, NV (January 1985).
4. C.L. Korb, G.K. Schwemmer, M. Dombrowski, J. Milrod, and H. Walden, "Airborne Lidar Measurements of the Atmospheric Pressure Profile with Tunable Alexandrite Lasers," Proc. 13th International Laser Radar Conf., Toronto, Canada (August 1986).
5. C. Cahen, J.P. Jegou, J. Pelon, P. Gildwarg, and J. Porteneuve, Rev. Phys. Appl. 16, 353, (1981).
6. L.J. Cotnoir, T.D. Wilkerson, M. Dombrowski, R.H. Kagann, C.L. Korb, G.K. Schwemmer, and H. Walden, "A Wavemeter for Use with a Line-Narrowed Alexandrite Laser in Differential Absorption Lidar," Proc. OSA Topical Meeting on Tunable Solid-State Lasers, Arlington, VA (May 1985).
7. B.E. Grossmann, U.N. Singh, N.S. Higdon, L.J. Cotnoir, T.D. Wilkerson, and E.V. Browell, "Linewidth Characteristics of Raman-Shifted Dye Laser Output at 720 nm and 940 nm," Proc. 13th International Laser Radar Conference, Toronto, Canada (August 1986).
8. B.E. Grossmann, "Etude par spectroscopie d'absorption laser en regime continu et impulsionnel des molecules d'eau et d'oxygene: Applications aux sondage lasers de l'atmosphere," Ph.D. thesis in Physics, l'Universite Pierre et Marie Curie (December 1984).
9. K.J. Ritter and T.D. Wilkerson, "Strengths, Widths, and Pressure Shifts of Fifty Four Oxygen A-band Lines," Proc. 13th International Laser Radar Conference, Toronto, Canada (August 1986).

Temp: 288K
Press: 1013mb
Path: 1000M
Oxygen: 21%

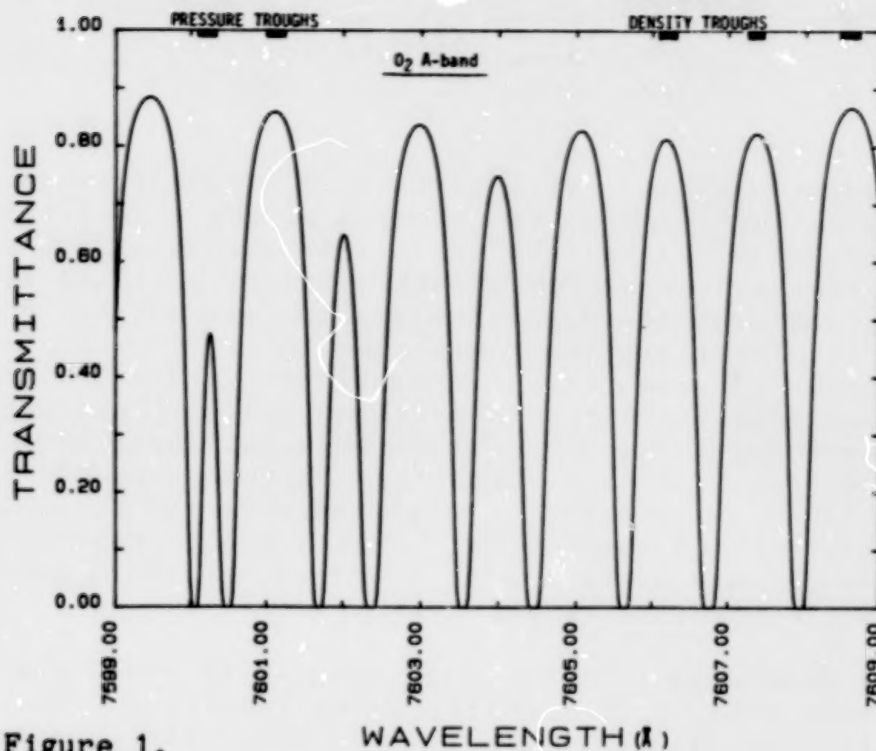


Figure 1.

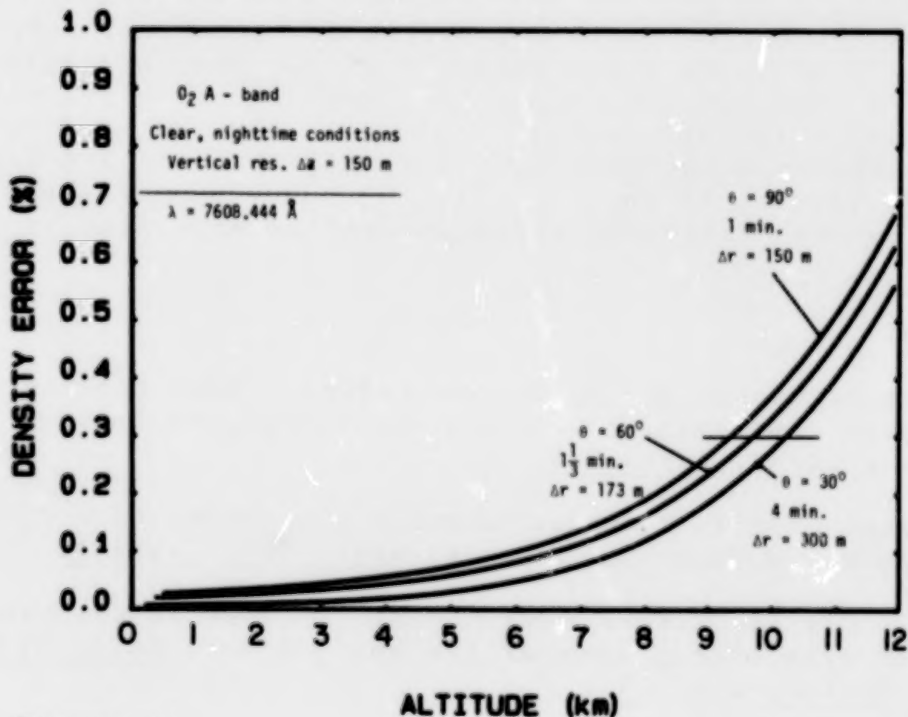


Figure 2.

N87

10292

UNCLAS

USING A LASER AUREOLE TO INVERT LIDAR RETURN

William P. Hooper and H. Gerber
Atmospheric Physics Branch
Naval Research Laboratory
Washington, DC 20375-5000

In a recent article¹, we theoretically studied an aureole generated by a laser beam. The strength of the signal redirected towards a sensor high above the surface by a combination of one scattering event in the marine boundary layer (mbl) and one single reflection event from the ocean surface was estimated. A model of mbl aerosol size distributions² was used to estimate Mie scattering for a wide range of meteorological conditions. The sea surface reflection was determined from a Gaussian model of the wave slopes³. These laser aureoles, which were estimated over the wide range of conditions and were normalized by the reflected laser light, were found to be highly correlated with the optical depth of the boundary layer. By estimating optical depth from the aureole, the Bernoulli-Riccati inversion of lidar return could be constrained and the inversion accuracy improved.

We have developed a Monte Carlo program to study the laser aureole generated by up to 8 orders of reflection and scattering. Initially, this program has been used to model the conditions of the original study; the aureole was generated by a narrow, 10 nsec laser pulse at 1.06 microns and measured by a receiver 10 km above the ocean surface. We found the original theoretical computation compared well with the Monte Carlo results. When multiple scatter effects were included, the normalized aureole was still highly correlated with the mbl optical depth over the range of conditions. In our presentation, we will show more detailed results from our Monte Carlo studies of the aureole. The accuracy of the aureole estimated optical depth and lidar inversions will also be discussed.

References:

1. William P. Hooper and H. Gerber (1986): Down looking lidar inversion constrained by ocean reflection and forward scatter of laser light, Appl. Opt. 5.
2. H. Gerber (1985): Infrared aerosol extinction from visible and near-infrared light scattering, Appl. Opt. 24, 4155.
3. Charles Cox and Walter Munk (1956): Slopes of the sea surface deduced from photographs of the sun glitter, Bull. Scripps Inst. Oceanogr. 6, 401.

N87

10293

UNCL

DETERMINATION OF CLOUD MICROPHYSICAL PROPERTIES
BY LASER BACKSCATTERING AND EXTINCTION MEASUREMENTS

R.N. Dubinsky, A.I. Carswell and S.R. Pal
Department of Physics and CRESS
North York
Ontario, Canada, M3J 1P3

ABSTRACT

The extinction and backscattering of 514nm laser radiation in poly-disperse water droplet clouds has been studied in the laboratory. Three cloud size distributions with modal diameters of 0.02 μ m, 5 μ m and 12 μ m have been investigated. The relationships between the cloud optical parameters (attenuation coefficient, σ and volume backscattering coefficient, β_v) and the cloud water content, C, have been measured for each size distribution. It has been found that a linear relationship exists between σ and C and between β_v and C for cloud water content values up to 3 gm/m³. The linear relationships obtained, however, have slopes which depend on the droplet size distribution. For a given water content both σ and β_v increase as the modal diameter decreases. The measured data are compared with existing theoretical analyses and discussed in terms of their application to lidar measurements of atmospheric clouds. It is concluded that the empirical information obtained can serve as a basis for quantitative lidar measurements.

N87

10294

UNCLAS

EFFECT OF BACKSCATTER-TO-EXTINCTION RATIO ON LIDAR INVERSIONS

Edward M. Measure
Atmospheric Sciences Laboratory
White Sands Missile Range, NM

One way of deriving the atmospheric extinction coefficient from lidar measurements is to start from the single scattering lidar equation, which we will write in the form:

$$(1) \quad P(r) = P_0 A \frac{c\lambda}{2} \frac{\beta(r)}{r^2} \exp \left[-\int_0^r \sigma(r^1) dr^1 \right]$$

This equation cannot be solved directly, since both $\beta(r)$ and $\sigma(r)$ are unknown. In the approach under consideration here, one attempts to solve the equation by postulating a relation between β and σ of the form:

$$(2) \quad \beta(r) = c [\sigma(r)]^k$$

Such a relation cannot hold in general, but may be approximately valid for a wide range of realistic atmospheric conditions. Real atmospheres will deviate from this relation, of course, so it is important to know how large are the errors which we should expect due to such deviations.

In the present study this question has been addressed by conducting simulations of lidar experiments and extinction coefficient calculations and examining the resulting errors. In order to make the simulations realistic, the volume backscatter coefficients and extinction coefficients used in the simulations were based on measured particle distributions, in this case on the particle size distributions measured in Meppen, Germany in the fall of 1980 by J. D. Lindberg and others of the Atmospheric Sciences Laboratory (Lindberg, 1982).

In that experiment particle size distributions were measured with a balloon-borne particle spectrometer (a PMS FSSP 100) during balloon descents from about 600 meters above ground to the surface. Each particle spectrum represents a layer of at most a few meters thickness so an altitude resolved profile of particle size spectra is measured.

T. L. Barber (Barber, 1985) used a Mie code to compute linear extinction coefficient and volume backscatter coefficient profiles from the particle size spectra for each balloon sounding. In these computations it was assumed that the individual droplets consisted purely of water.

Simulated lidar returns were constructed by inserting the computed values of extinction and backscatter coefficients into a discrete version of equation

(1). In order to mimic the range gating characteristics of an actual lidar used by the author (Measure and Rubio, 1982) at the Meppen experiment, the interval in the discrete version of the lidar equation was chosen to be three meters, and the backscatter and extinction coefficient profiles were interpolated at the chosen points. This resulted in a set of values $P(r)$ for $r = 3n$ meters, $n = 1, 2, \dots$ which constituted the simulated lidar return. (For simplicity, the factor $P_0 c \lambda A / 2$ was set to 1).

This simulated lidar return was then used to compute the extinction coefficient by Klett's algorithm (Klett, 1981):

$$(3) \quad \sigma(r) = \frac{\exp[(S(r) - S(r_m))/k]}{\left[\sigma_m(r_m)\right]^{-1} + \frac{2}{k} \int_{r_m}^r \exp[(S(r) - S(r_m))/k] dr}$$

where $S(r) = \ln(r^2 P(r))$. This algorithm requires that the boundary value $\sigma(r_m)$ be specified. In the simulation, the value used was that computed from the particle spectra, so that the simulations were "perfect" at the point r_m and the only error should be that due to the deviation from the backscatter to extinction relation (2).

Figure 1 indicates the data flow in the simulation. Representative results of the simulation are indicated in figures 2 - 4. Note that using a k value other than 1 may result in a significantly smaller error. Note also that no other potential sources of error are considered in the simulation. Absorption, multiple scattering, and instrumental errors all may contribute to error in a real lidar measurement but are not represented here.

References

Barber, T. L., 1985, "Visibility Related to Backscatter at 1.06 μm ," Appl. Opt., (Nov 1, 1985).

Klett, J. D., 1981, "Stable Analytical Inversion Solution for Processing Lidar Returns," Appl. Opt., 20:211 (Jan 15, 1981).

Lindberg, J. D., ed., Early Wintertime European Fog and Haze on Project Meppen 80, ASL Technical Report TR-0108, U.S. Army Atmospheric Sciences Laboratory, WSMR, NM (1982).

Measure, Edward M., and Roberto Rubio, 1982, "Quantitative Lidar Measurement of Extinction Coefficient," in Conference Abstracts of the Eleventh International Laser Radar Conference, NASA Conference Publication 2228, (June 21-25, 1982).

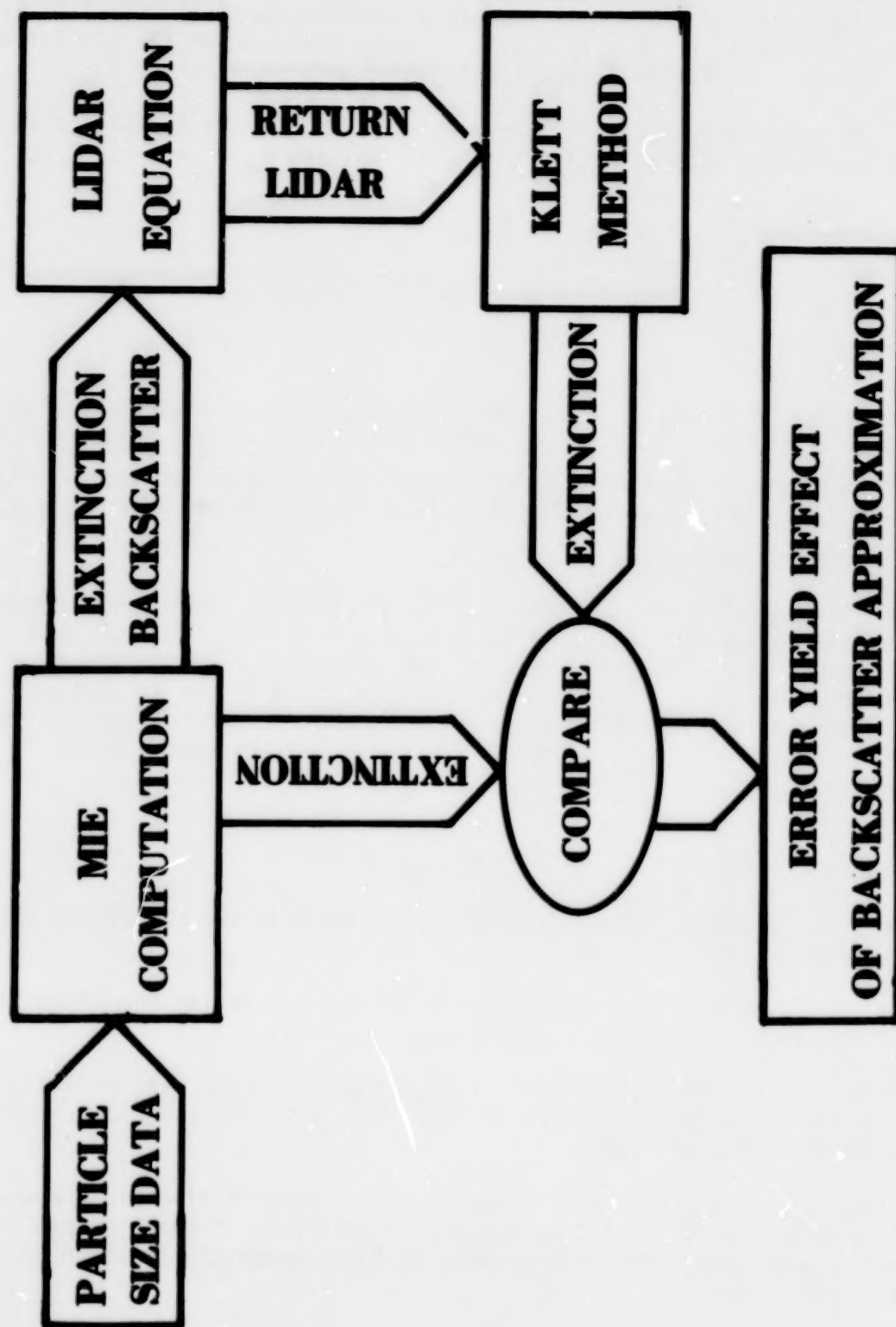


FIG. 1 METHOD

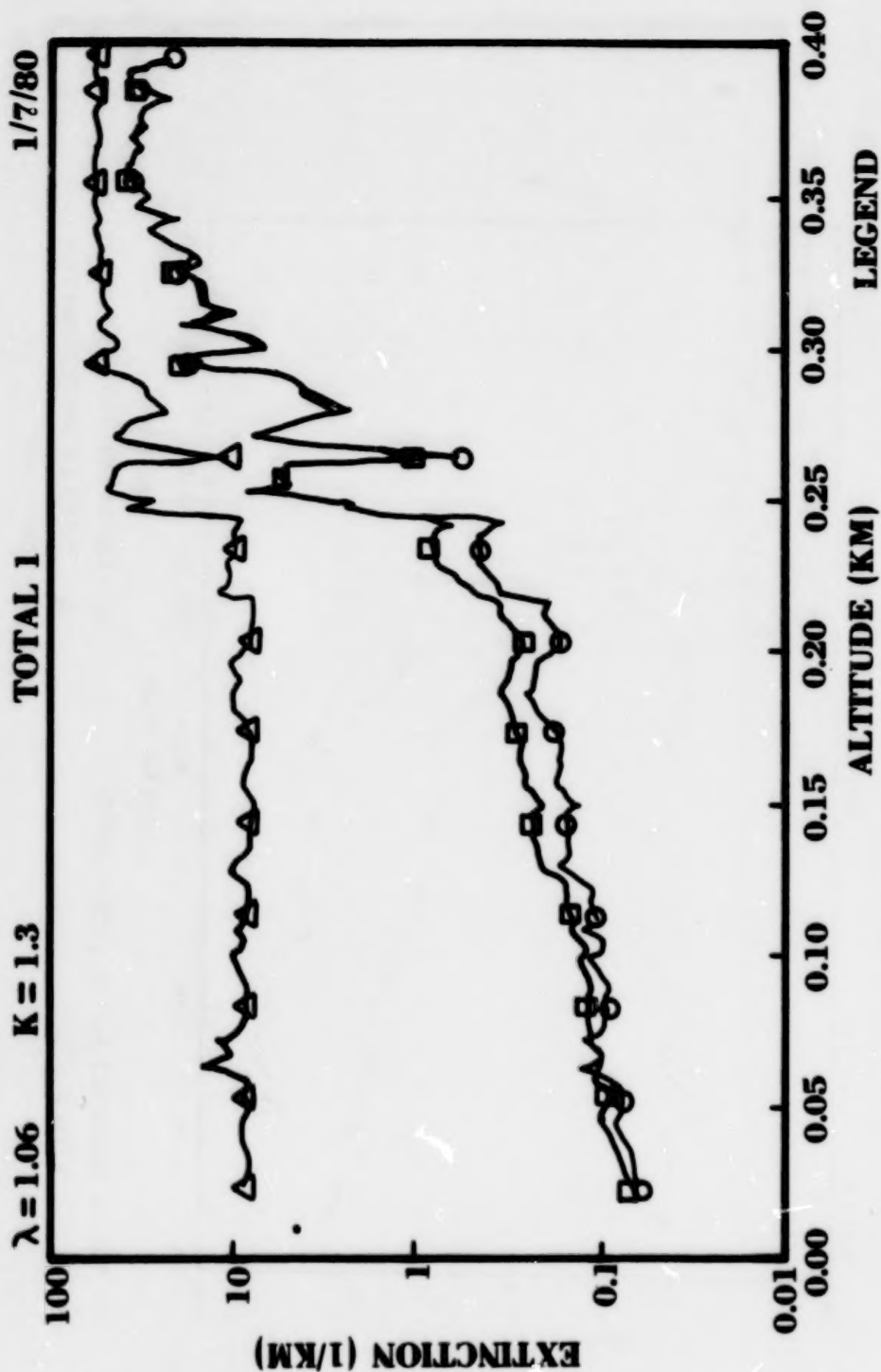


FIG. 2 DATA SET TOTAL 1 PROCESSED
WITH $K = 1.3$

EFFECT OF β/σ RATIO

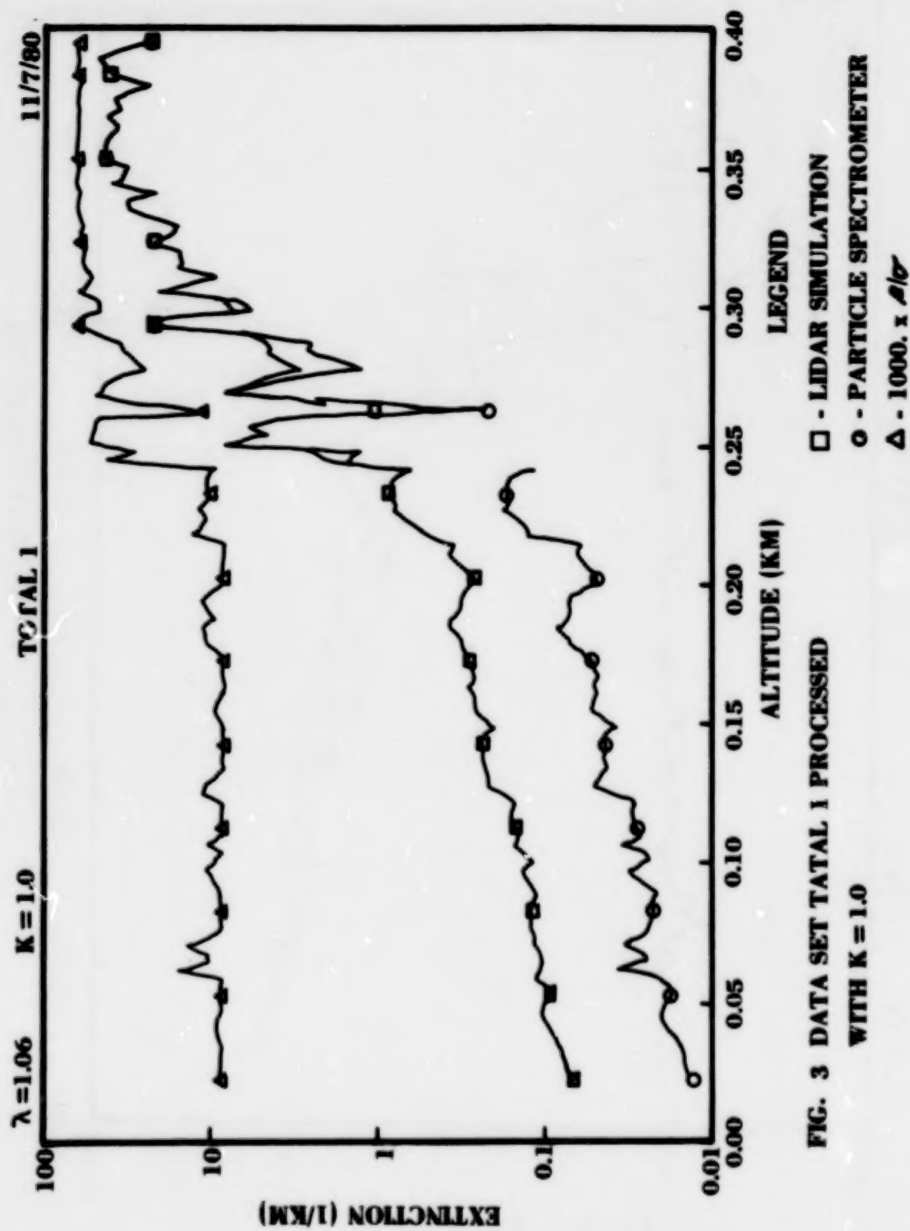


FIG. 3 DATA SET TATAL 1 PROCESSED
WITH $K = 1.0$

EFFECT OF β/σ RATIO

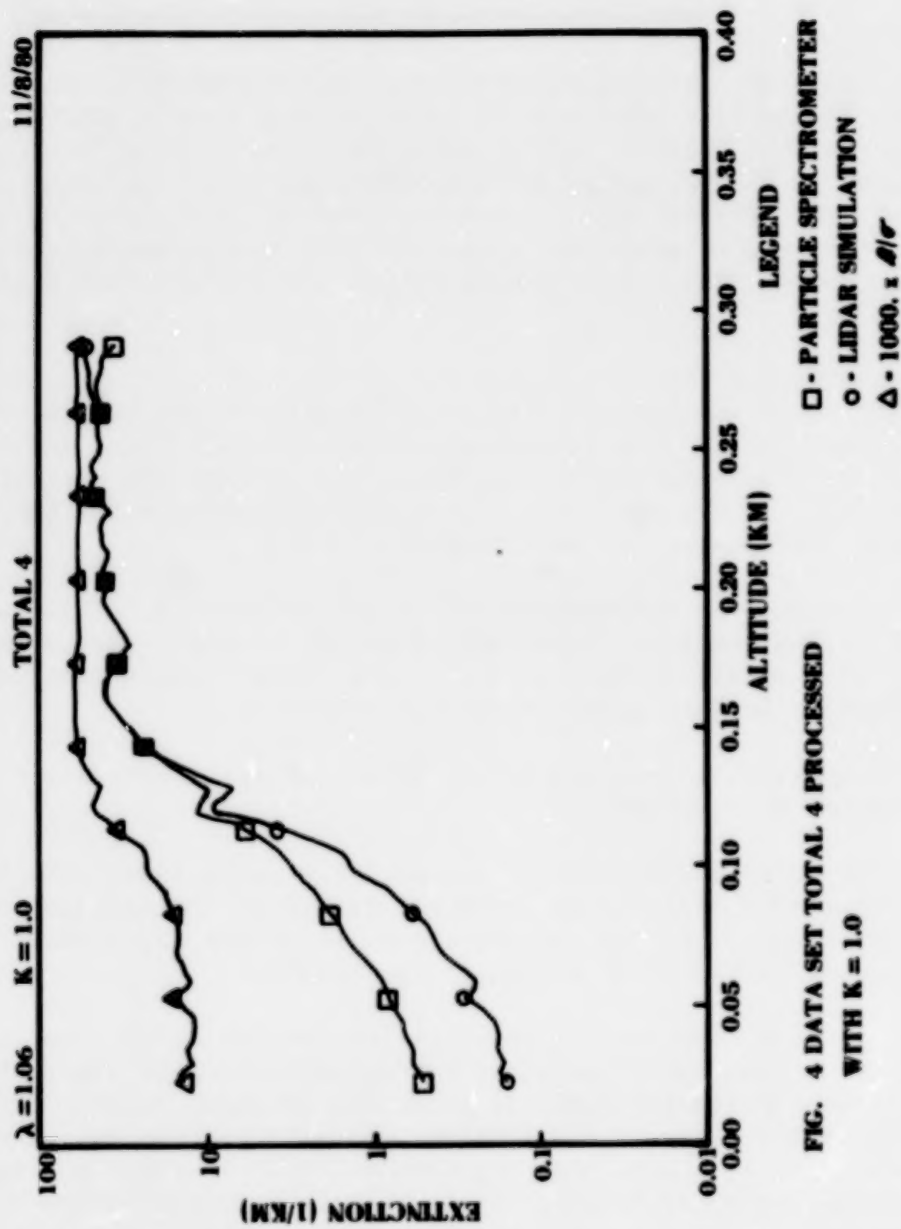


FIG. 4 DATA SET TOTAL 4 PROCESSED
WITH K = 1.0

N87

10295

UNCL

LABORATORY MEASUREMENTS OF FORWARD AND BACKWARD
SCATTERING OF LASER BEAMS IN WATER DROPLET CLOUDS

R.B. Smith, J.D. Houston, and A. Ulitsky
Optech Inc., Downsview, Ontario, Canada M3J 2N6

A.I. Carswell
York University, Downsview, Ontario, Canada M3J 1P3

Many aspects of the forward and backward scattering in dense water droplet clouds have been studied using a laboratory scattering facility. A summary of the results will be presented in this paper. This system is configured in a lidar geometry to facilitate comparison of the laboratory results to current lidar oriented theory and measurements. The backscatter measurements are supported with simultaneous measurements of the optical density, mass concentration and droplet size distribution of the clouds.

Measurements of the extinction and backscatter coefficients at several important laser wavelengths have provided data on the relationship between these quantities for our laboratory clouds at .633, 1.06, and 10.6 μ m. The results of the measurements have been used to test the approximations of Pinnick et al.¹ In addition, the effect of multiple scattering on the measured coefficients has been studied.

The polarization characteristics of the backscatter of 1.06 μ m have been studied using several different types of clouds. These measurements extend the results of Ryan et al.² The linear depolarization ratio has been shown to be very important in two respects:

- 1/ as a qualitative measure of the amount of multiple scattering in the measured backscatter
- 2/ as a sensitive indicator of the particle shape (ie. spherical versus irregular). This is an important result in the application of lidar measurements of the atmosphere where clouds may consist of either spherical droplets or irregular ice crystals

The use of spatial filtering in combination with the polarization measurements has greatly extended our understanding of the distribution of multiple backscattering radially about the incident beam. This has also helped define the polarization characteristics of the multiple backscatter. We have observed a radial distribution of the multiple backscatter which is Gaussian in form. This result agrees with previous observations by Ryan et al.² and Donchenko et al.³ The addition of the polarization characterization to these measurements has helped define the radial dependence of the polarization in the backscatter.

Transmitted beam profile measurements have illustrated the broadening of the propagating laser beam profile due to scattering. This broadening

has been observed to be very strong at 0.633 and 1.06 μ m but virtually non-existent at 10.6 μ m.

More recently, the laboratory facility has been modified to allow range-resolved backscatter measurements at 1.06 μ m. These measurements extend those described by Smith and Carswell.⁴ In this case we can construct clouds made up of 3 layers, each with its own density. This allows the study of the effect of cloud inhomogeneity on the forward and backscatter.

References:

1. R.G. Pinnick, S.G. Jennings, P. Chylek, C. Ham and W.T. Grandy, Jr., J. Geophys. Research 88, 6787, 1984.
2. J.S. Ryan, S.R. Pal and A.I. Carswell, J. Opt. Soc Am., 69, 60, 1979.
3. V.A. Donchenko, I.V. Samokhvalov and G.G. Matviyenko, Izv. Atmospheric and Oceanic Physics, 7, 1183, 1971.
4. R.B. Smith and A.I. Carswell, Appl. Opt., 24, 3546, 1985.

N87

10296

UNCL

REAL-TIME ATMOSPHERIC ABSORPTION SPECTRA FOR IN-FLIGHT TUNING OF AN AIRBORNE DIAL SYSTEM

M. Dombrowski, H. Walden, G. K. Schwemmer, J. Milrod, and
C. L. Korb, NASA Goddard Space Flight Center, Laboratory for
Atmospheres, Greenbelt, Maryland U.S.A.

Real-time measurements of atmospheric absorption spectra are displayed and used to precisely calibrate and fix the frequency of an Alexandrite laser to specific oxygen absorption features for airborne Differential Absorption Lidar (DIAL) measurements of atmospheric pressure and temperature.

The DIAL system used contains two narrowband tunable Alexandrite lasers: one is electronically scanned to tune to oxygen absorption features for on-line signals while the second is used to obtain off-line (non-absorbed) atmospheric return signals. Other system components pertinent to the tuning capabilities are a 0.5 m Czerny-Turner spectrometer with 0.25 cm^{-1} (15 pm) resolution, a microcomputer terminal for display and keyboard input, software to process and output data in real time, and the atmospheric path over which measurements are made. A one meter multipass gas cell can alternatively be used instead of the atmosphere.

In operation, the two lasers are coarsely tuned to within 0.5 cm^{-1} of the desired frequencies utilizing the spectrometer which has an X-Y CRT display of its reticon detector, with a cursor and channel number readout. The laser outputs are transmitted through the atmosphere, and a real-time plot of atmospheric transmission versus time is displayed on the microcomputer's console terminal. The lidar operator may select the number of shots to be averaged, the altitude, and altitude interval over which the signals are averaged using single key stroke commands. The on-line laser is electronically tuned with a constant scan rate while the display is continuously updated. The operator determines exactly which oxygen absorption lines are scanned by comparing the line spacings and relative strengths with known line parameters, thus calibrating the laser wavelength readout. The CRT is either refreshed or overwritten every 512 laser shots, and a hardcopy of the screen may be obtained using a graphics printer.

After determining the wavelength calibration, the on-line laser is manually tuned to the desired absorption feature; either a transmission peak (absorption trough) for pressure measurements or an absorption peak for temperature measurements and recording of data on magnetic tape commences.

The system just described was used successfully to measure the atmospheric pressure profile on the first flights of this lidar, November 20, and December 9, 1985, aboard the NASA Wallops Electra aircraft. It has been used previously in our groundbased laboratory to make upward-looking measurements of pressure and temperature and to measure the spectral purity of the Alexandrite laser.

A system for long-term control of the laser frequency using a stabilized high resolution etalon is currently under development.

N87

10297

UNCLAS

OBSERVATION OF ATMOSPHERIC OZONE BY DIAL WITH RAMAN LASERS PUMPED BY A KrF LASER

M. Maeda and T. Shibata
 Department of Electrical Engineering,
 Kyushu University, Hakozaki, Higashi-ku,
 Fukuoka 812 Japan

Since we first began using the XeCl excimer laser (308 nm) in DIAL for stratospheric ozone detection,¹ the XeCl ozone lidar became a useful tool for^{2,3} the monitoring of the stratospheric ozone concentration.

Shorter wavelength lasers are needed for the observation of ozone in the troposphere where the ozone concentration is about one order of magnitude smaller than in the stratosphere. In 1983, we observed tropospheric ozone with the combination of the second Stokes line (290.4 nm) of stimulated Raman scattering⁴ from methane pumped by a KrF laser and the XeCl laser line.

In this paper, we will report the measurement of the ozone distribution from ground to 30 km, using three Stokes lines of Raman lasers pumped by a KrF laser. The characteristics of our lidar system are shown in Table 1. Fig.1 shows the ozone profile observed by the second Stokes lines of methane (290.4 nm) and hydrogen (313 nm). This system is simpler than that of the previous paper,⁴ because it is based on a single KrF excimer laser. We are now preparing the KrF laser with fast repetition rate (~80 Hz). A set of data will be taken in several minutes with this high-power laser.

At wavelengths shorter than 295 nm, the background solar radiation is effectively suppressed by atmospheric ozone. Such a solar-blind effect can be expected when we use two wavelengths 277 and 290.4 nm for DIAL ozone detection. Fig.2 shows a preliminary measurement of the day time ozone distribution in the troposphere using these wavelengths generated by a KrF laser with a Raman shifter. Analysis using the lidar equation predicts the maximum detectable range is 7 km. In the present experiment, the dominant range limiting factor is the low transmission of the solar-blind filter.

References

1. Uchino, O. et al., Appl. Phys. Lett., Vol. 33, 807 (1978).
2. Werner, J. et al., Appl. Phys., Vol. B32, 113 (1983).
3. Pelon, J. and G. Megie, 12th ILRC (1984).
4. Uchino, O. et al., Opt. Lett., Vol. 8, 347 (1983).

Transmitter			
Laser	KrF-pumped $H_2(S_1)$	KrF-pumped $CH_4(S_2)$	KrF-pumped $H_2(S_2)$
Wavelength (nm)	277.0	290.4	313.0

Receiver	
Telescope	50 cm dia.
Field of view	1 mrad
Filter bandwidth (transmission)	2 nm (10 %)
Photo counter	
vertical resolution	1 sec
channel number	1000

Table 1. Characteristics of Lidar system

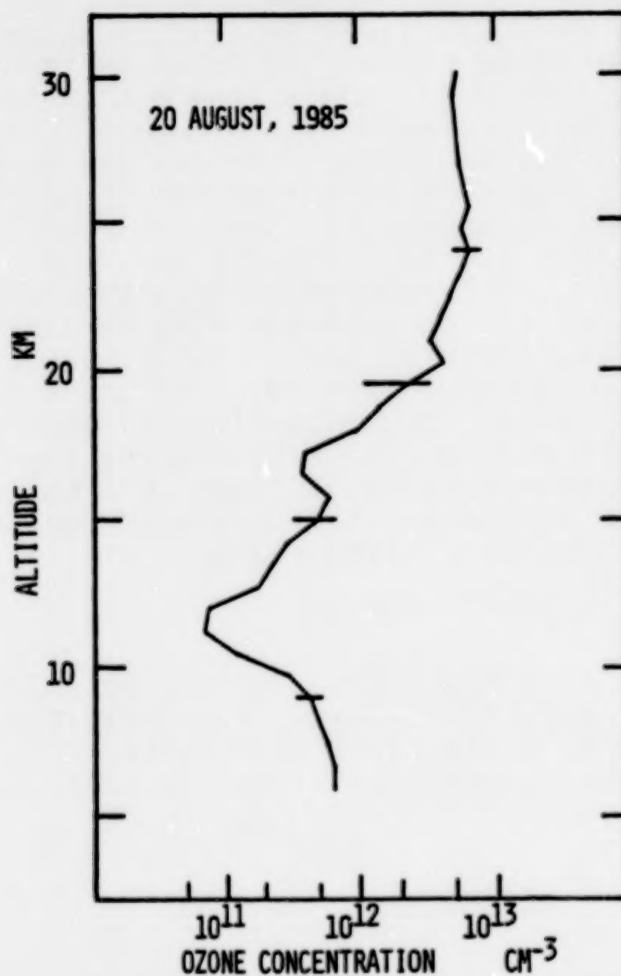


Fig.1 Ozone profile by 290.4 and 313 nm.

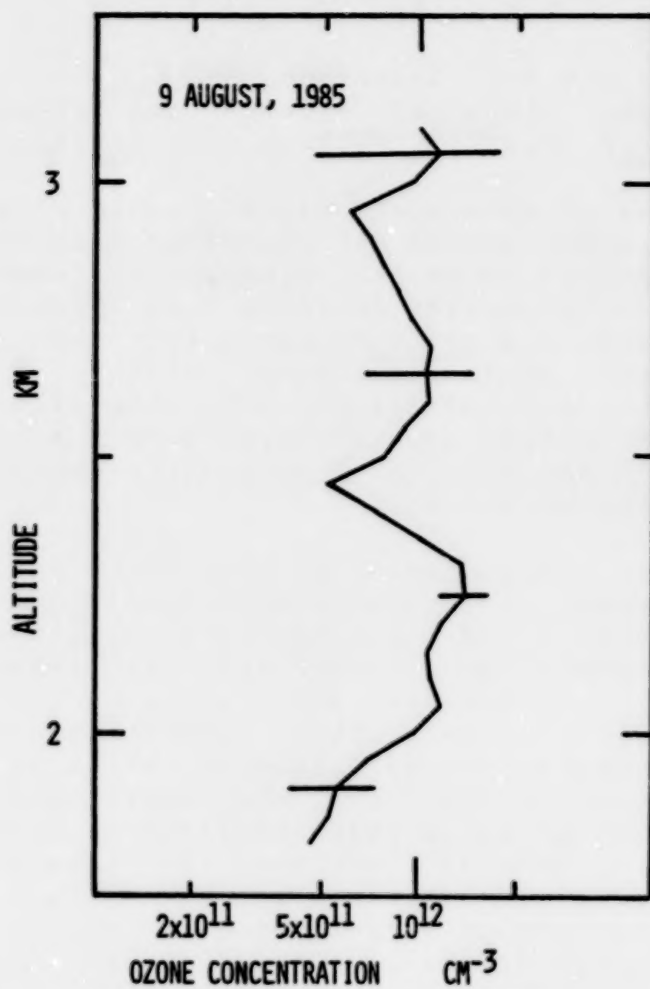


Fig. 2 Ozone profile by 277 and 290.4 nm
in the daytime.

N87

10298

UNCLAS

STRENGTH, WIDTH, AND PRESSURE SHIFT MEASUREMENTS
OF 54 LINES IN THE OXYGEN A-BAND¹

K.J. Ritter and T.D. Wilkerson
Institute for Physical Science and Technology
University of Maryland, College Park Maryland

The absorption band of molecular oxygen, centered at 760nm and known as the oxygen A-band, is the atmospheric absorber for DIAL systems being developed to measure atmospheric temperature, pressure and density. To provide accurate line parameters for such systems, we have made a careful spectroscopic study of the A-band, with measurements of line strengths, widths, pressure-induced frequency shifts, and collisional narrowing effects. The width and shift parameters have been measured over a temperature range of -20°C to 100°C so that the temperature dependence of these parameters can also be determined.

To make accurate measurements of these line parameters, three separate experimental arrangements were used. In each, a cw narrow linewidth tunable dye laser was used to scan over the individual absorption lines. For strength and width measurements at ambient temperature, the laser was used in conjunction with a multi-pass absorption cell to make high resolution absorption spectra. To measure pressure induced frequency shifts at ambient temperature, a photo-acoustic (PA) cell was positioned between the laser and absorption cell, so that simultaneous scans could be made of both cells. This is basically the same technique used by Bösenberg (ref. 1) to measure water vapor shifts. Figure 1 is an example of one of these composite scans, showing simultaneous absorption and PA scans of the PP 15,15 line.

To measure widths and shifts as a function of temperature, we constructed an additional, temperature controllable, PA cell. This cell was used with the ambient temperature PA cell to produce simultaneous PA spectra at different temperatures and pressures.

To analyze the results from the above measurements, we wrote a least-squares fitting routine to fit standard line profiles to the observed profiles. We found that the Galatry collisionally narrowed profile (ref. 2) was better than the standard Voigt profile in fitting the observed profiles, so we used the Galatry function for the data analysis. The fitting

¹From a dissertation to be submitted to the Graduate School, University of Maryland, by Kenneth J. Ritter in partial fulfillment of the requirements for the Ph.D. degree in Physics. Measurements were carried out in the High Resolution Spectroscopy Laboratory, Laboratory for Atmospheres, at the NASA Goddard Space Flight Center.

process produced a set of line parameters for each scan of an individual line; these included: strength (absorption scans only), pressure broadened width, position (relative frequency only), and collisional narrowing parameter.

Using the strengths of the individual lines, we have determined the integrated band strength to be:

$$S_B = 612 \text{ cm}^{-1} \cdot \text{km}^{-1} \cdot \text{amagat}^{-1} \quad (\text{std. dev.} = 1\%)$$

Width and shift results as a function of pressure are shown in figures 2 and 3 respectively. Widths and shifts were also measured in air. Line widths measured in air were found to be only about 3% greater than those measured in pure O_2 . Pressure shifts however, were found to be 30% higher in air as compared to pure O_2 . Results for pressure broadening coefficients and pressure shift coefficients for all the lines measured are shown graphically in figures 4 and 5 respectively.

We believe that these measurements, which include the first observations of pressure shifts and collisional narrowing in this band, will be an important contribution to lidar systems utilizing the A-band.

References

- 1) J. Bösenberg, Appl. Optics 24,3531-3534 (1985).
- 2) L. Galatry, Phys. Rev. 122,1218-1223 (1961).

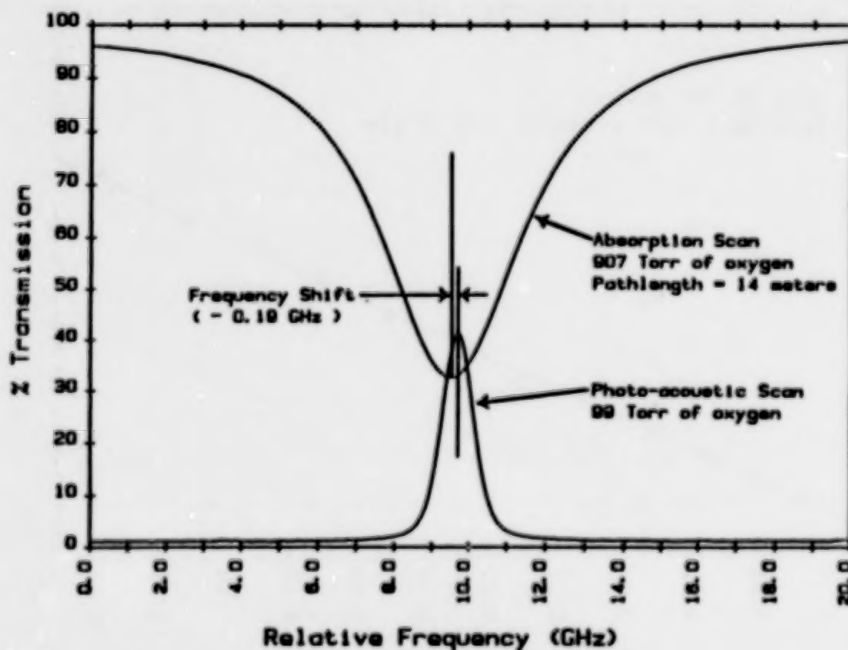


Figure 1.

An example of simultaneous absorption and photo-acoustic scans for the determination of pressure-induced frequency shifts. This set of scans shows the PP 15,15 line.

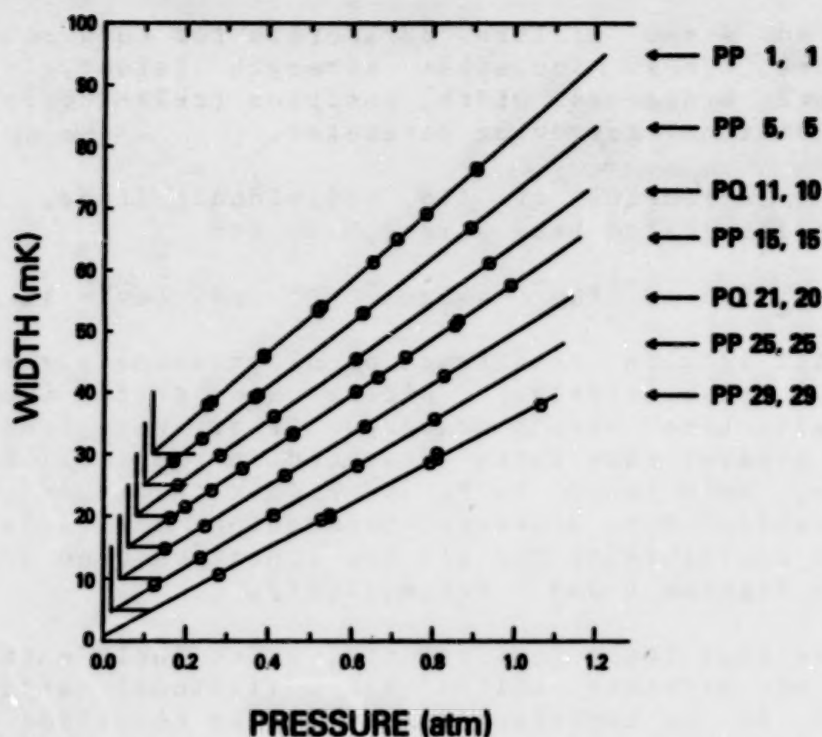


Figure 2.

Measurements of the self-broadened width vs. pressure for 7 P-branch lines. Each point was determined by fitting an observed profile (taken at the indicated pressure) with a Galatry profile. For clarity, widths for each successive line have been offset by 5 milli-Kaisers and 0.02 atm.

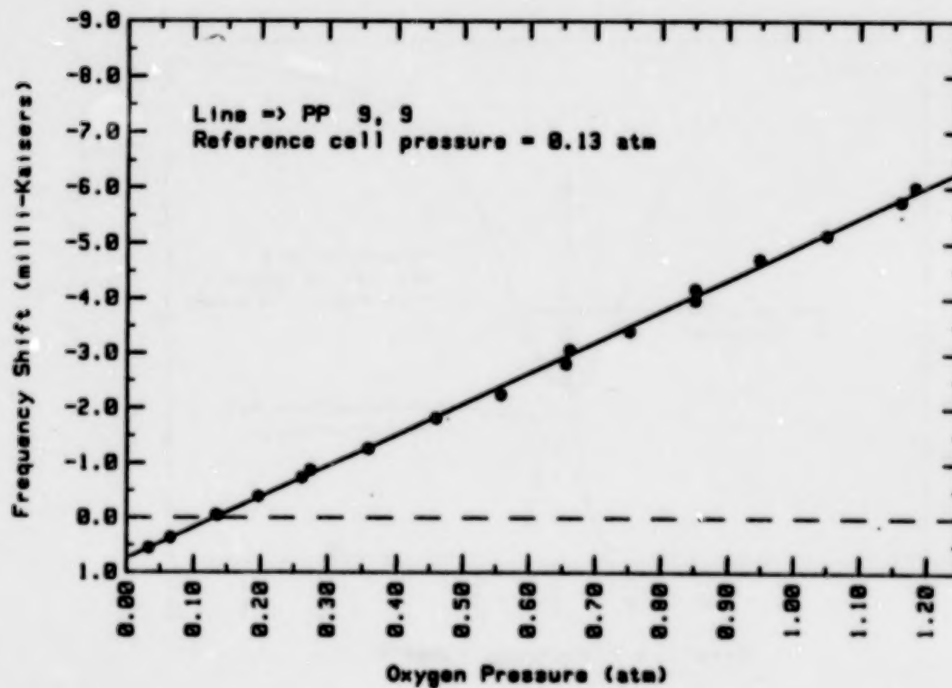


Figure 3.

Pressure induced frequency shifts of the PP 9,9 line. Each point corresponds to a scan similar to that shown in figure 1.

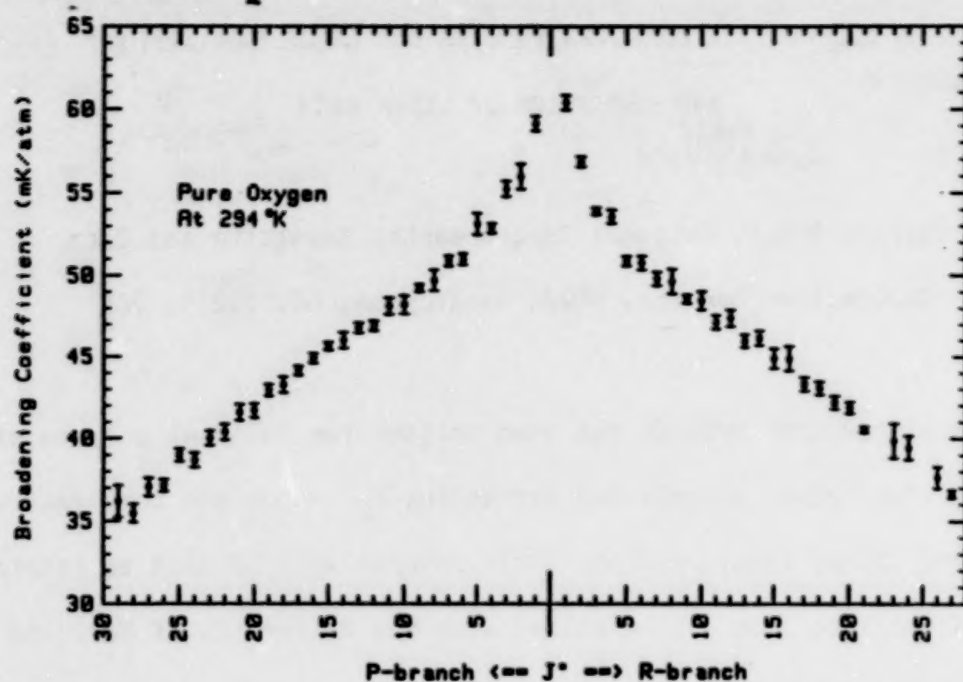


Figure 4.
Self-broadening coefficients of Oxygen A-Band lines.

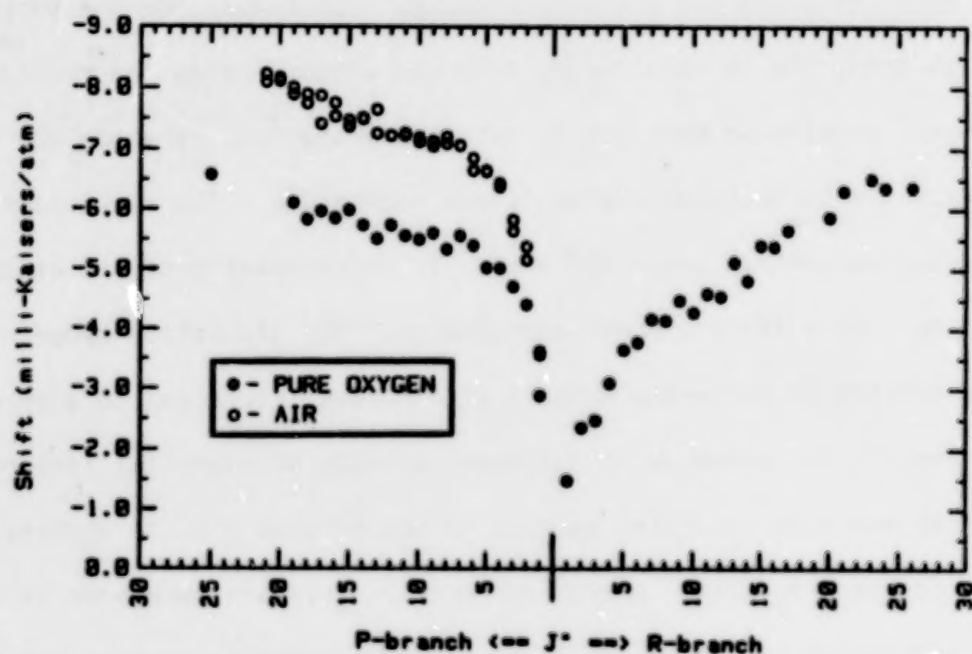


Figure 5.
Pressure shift coefficients for both air-broadening and self-broadening of Oxygen A-Band lines.

N87

10299

UNCL

AN ALL-PURPOSE COMPUTER PROGRAM FOR LIDAR SIMULATIONS
AND REDUCTION OF LIDAR DATA

Charles Braun, National Environmental Satellite and Data
Information Service, NOAA, Washington, DC, 20233, USA¹

A general computer program has been written for the dual purpose of simulating lidar return signals and extracting H₂O vapor and temperature (T) profiles from actual lidar returns. This program will be used to retrieve H₂O vapor and T profiles from data obtained with the University of Maryland ground-based lidar system.

The program is designed to simulate and to analyze lidar returns from a monostatic system for two cases: when the output laser pulse is monochromatic, and when the pulse has a known wavelength spectrum. For the purpose of simulation studies, the backscattering from the atmosphere is assumed to have two components, an elastic part due to backscattering from aerosols and an inelastic part due to Rayleigh and Brillouin scattering. The simulation part of the program has several model H₂O vapor, T, and aerosol profiles which can be combined to form different model atmospheres. The simulation program also permits the testing of different methods of numerical filtering to suppress noise, and testing the accuracy of different methods of numerical integration.

Initially the data reduction portion of the program will be checked by using it to retrieve H₂O vapor profiles from lidar signals generated in the simulation portion of the program. It will then be used to recover H₂O profiles from lidar data obtained in the lower troposphere (z=0 to 5km).

1. Visiting Research Associate, University of Maryland, College Park, MD, 20742, USA

The algorithm for H_2O retrieval is based on an iterative method developed by Zuev et al. (1983) for use in the lower troposphere. In the lower troposphere, H_2O vapor absorption linewidths are large enough compared to Doppler widths so that Rayleigh scattering can be treated as elastic scattering. The ratio of on-line to off-line signals to be analyzed is then given by

$$R_{nf}(z) = \int_0^{\infty} dv f_L(v-v_n) \tau^2(z, v-v_n)$$

where

$$\tau^2(z, v-v_n) = \exp(-2 \int_0^z dz' K(z', v-v_n) \rho_{H_2O}(z'))$$

z = altitude

ρ_{H_2O} = H_2O vapor density

K = H_2O vapor absorption coefficient

$f_L(v-v_n)$ = normalized frequency spectrum for
laser pulse as a function of frequency
 $v-v_n$ measured from center of
absorption line.

Some numerical and graphical examples of simulated and retrieved profiles will be given to demonstrate the operation of this program.

Reference

V. E. Zuev, Yu. S. Makushkin, V. N. Marichev, A. A. Mitsel, and V. V. Zuev, "Lidar differential absorption and scattering technique theory," Appl. Opt., 22 p. 3733, (1 Dec. 1983).

N87

103000

UNCLAS

CONVECTIVE STRUCTURE OF THE PLANETARY
BOUNDARY LAYER OVER THE OCEAN DURING GALE

S.H. Melfi and R. Boers
Laboratory for Oceans
NASA Goddard Space Flight Center
Greenbelt, Maryland, U.S.A.

The structure of the Planetary Boundary Layer (PBL) has been measured, using an airborne lidar, over the Atlantic Ocean during several intensive observation periods of the Genesis of Atlantic Lows Experiment (GALE).

Primary emphasis of this paper will be on the understanding of the convective structure within the PBL during cold air outbreaks. Cold outbreaks generally occur in between the development of coastal storms. They occur behind a cold front which sweeps down from Canada out across the Atlantic. As the cold dry air moves over the relatively warm ocean waters, it is heated and moistened. The transfer of latent and sensible heat during these events accounts for most of the heat transfer between the ocean and atmosphere during the winter. The moistening of the PBL during these events is believed to be an important factor in determining the strength of development of the storm system which likely follows. In general, the more PBL moisture which is available as latent heat the higher the probability that the storm will intensify.

The major mechanism for vertical mixing of heat and moisture within the PBL is cellular convection. Knowledge of the organization and structure of the convection is important for understanding the process.

Data from the downward-looking airborne lidar will be presented which clearly shows the structure of the convective cells both along and across the direction of the low level winds. The importance of the entrainment zone at the PBL top will be discussed as it relates to heat transfer at the ocean surface.

N87

10301

UNCLAS

METHODS FOR ESTIMATING THE OPTICAL CONSTANTS OF ATMOSPHERIC HAZES BASED ON COMPLEX OPTICAL MEASUREMENTS

V.E. Zuev, B.S. Kostin and I.E. Naats
The Institute of Atmospheric Optics SB USSR
Acad.Sci., Tomsk, 634055, U S S R

The methods of multifrequency laser sounding (MLS) are the most effective remote methods for investigating the atmospheric aerosols, since they have made it possible to obtain complete information on aerosol microstructure and the effective methods for estimating the aerosol optical constants can be developed.

The MLS data interpretation consists in the solution of the set of equations containing those of laser sounding and equations for polydispersed optical characteristics. As a rule, the laser sounding equation is written in the approximation of single scattering and the equations for optical characteristics are written assuming that the atmospheric aerosol is formed by spherical and homogeneous particles.

The above assumptions correspond to the characteristics of atmospheric aerosol only in a certain approximation. However, an analysis of equations in this case is very useful, indicating the peculiarities of interpreting the MLS data in most general cases. Moreover, such analysis allows the development of general methods for interpretation of optical measurements on the basis of simple examples.

The above set of equations of the MLS method has two peculiarities. The first one is associated with the solution of incorrect inverse problems and is studied completely at present. The second one is typical for interpreting the optical measurements and is due to indeterminacy of equations relative to optical constants.

To remove the indeterminacy of equations the authors have suggested the method of optical sounding of atmospheric aerosol, consisting in a joint use of a multifrequency lidar and a spectral photometer in common geometrical scheme of the optical experiment. The method is used for investigating aerosols in the cases when absorption by particles is small and indicates the minimum necessary for interpretation of a series of measurements. The scheme is given in Fig.1. The spectral photometer 3, the light source 4 and the reflecting screen 5 are intended for measuring the scattering radiation coefficients within the atmospheric layer from the lidar 1 up to the scattering volume 2.

The basis of the method is the numerical solution of equation $f(m, \lambda) = \beta_{sc}(\lambda)$, where $\beta_{sc}(\lambda)$ is the value of the scattering coefficient measured with the photometer, and $f(m, \lambda)$ is a certain additional function calculated in the process of the MLS data interpretation. The function $f(m, \lambda)$ in the scheme of the MLS data inversion gives the predicted values of $\beta_{sc}(\lambda)$ with variable m . This function can be called conditio-

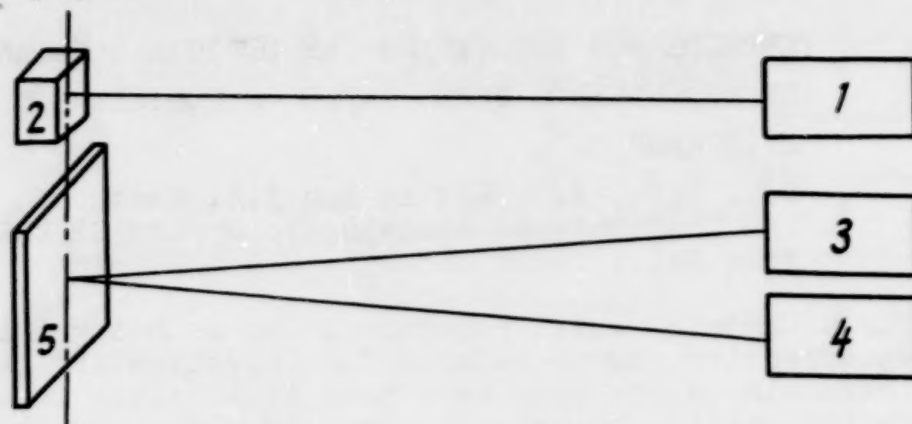


Fig.1. Scheme of the complex optical experiment on investigation of atmospheric aerosol parameters.

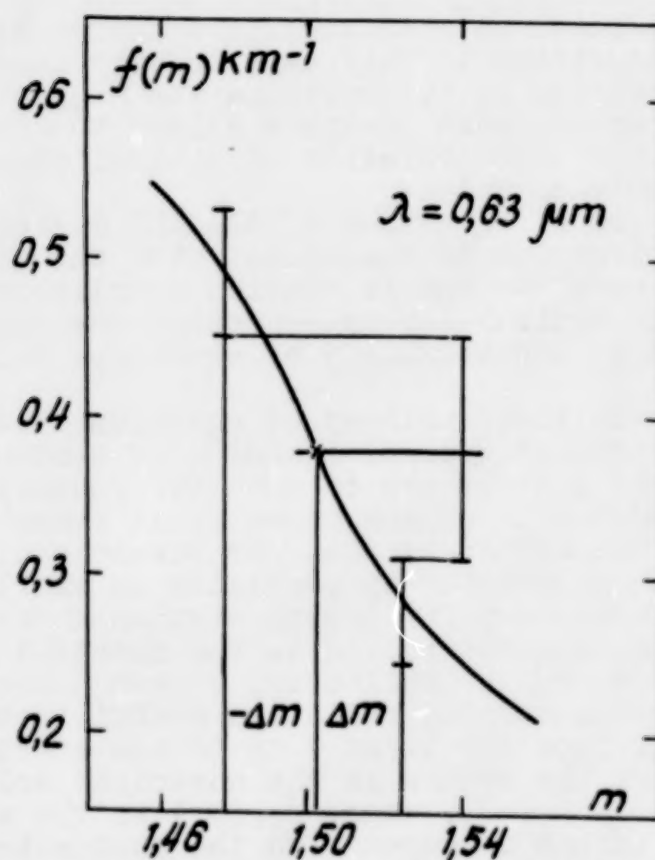


Fig.2. Example of determining m using the solution of equation $f(m, \lambda) = \tilde{\beta}_{3c}(\lambda)$ when interpreting the MLS data.

nally as a correction function, since it allows not only determination of optical constants but also calculation of the distribution function, representing more completely the aerosol microstructure.

An example of determination of optical constants using the above method is given in Fig.2. The correction function for the $0.63 \mu\text{m}$ wavelength was calculated while interpreting the data on three-frequency laser sounding ($\lambda = 0.53, 0.69$ and $1.06 \mu\text{m}$). The value of the extinction coefficient measured with the photometer (straight line) allows the determination of $m \approx 1.50$. If the lidar measurements are made with an error $\pm 10\%$ and the photometer measurements error is $\pm 20\%$, then, as follows from the figure, the error Δm in the determination of optical constants is equal to ± 0.025 . The decrease of the photometric measurements error up to $\pm 10\%$ results in $\Delta m = \pm 0.012$.

The method developed by the authors was used when sounding the surface aerosol. The obtained values of optical components and the data on aerosol microstructure for a number of measurements are in agreement with the results of direct measurements.

N87

103002

UNCLAS

MULTIFREQUENCY DIAL SENSING OF THE ATMOSPHERIC GASEOUS CONSTITUENTS USING THE FIRST AND SECOND HARMONICS OF A TUNABLE CO₂ LASER RADIATION

V.E. Zuev, Yu.M. Andreev, V.G. Voevodin,
A.I. Gribenyukov, V.A. Kapitanov, A.V. Sosnin,
G.A. Stuchebrov, G.S. Khmel'nitskii
The Institute of Atmospheric Optics SB USSR
Acad.Sci., Tomsk, 634055, USSR

High-energy and operation characteristics of a CO₂ laser have stipulated their wide use in absorption gas analyzers and lidars capable of measuring the concentrations of 30 gaseous components of the atmosphere with concentration sensitivity up to 10⁻⁹ atm. At the same time, the absorption lines of a number of important molecular species such as CO, N₂O, SO₂, etc. are off the range the CO₂ laser emits in. To measure the concentration of these components one can use the semiconductor lasers and parametric light generators, operating in the range of absorption bands of these gases.

However, in our opinion, more promising for these purposes is the development of simple reliable and effective parametric frequency converters of the CO₂ laser radiation.

This paper presents the results of field measurements of concentration of some gaseous components of the atmosphere along the paths, in Sofia, Bulgaria, using a gas analyzer based on the use of CO₂ laser radiation frequency-doubled with ZnGeP₂ monocrystal. The gas analyzer is a traditional long path absorption meter. Radiation from the tunable CO₂ laser of low pressure and from an additional He-Ne laser is directed to a collimating hundredfold Gregori telescope with a 300 mm diameter of principal mirror. The dimensions of mirrors of a retroreflector 500x500 mm and a receiving telescope (ø 500 mm) allow one to total intercept the beam passed through the atmospheric layer under study and back.

A detectable block of a frequency doubler is inserted into the beam at the gap between the laser and beam expander. The frequency doubler itself is a single crystal of triple semiconductor ZnGeP₂ of 10 x 20 mm cross section and 3-10 mm thickness with polished ends. In front of the crystal a focusing lens of BaF₂ is placed and after it a LiF collimating lens is located. The latter is used simultaneously as a filter, cutting off the CO₂ laser radiation.

The frequency doubler is described in detail in [1,2]. Although monocrystals of ZnGeP₂ have lower conversion efficiency compared with that of CdGeAs₂ monocrystals, they have better performance characteristics. In particular, they do not require the cryogenic temperatures for operation and have greater radiation resistance to CO₂ laser radiation (60 MW/cm² for laser pulses of 200 ns duration and more than 200 kW/cm² for c w lasers).

For tuning the CO_2 laser radiation onto the absorption lines of calibrated gaseous mixtures and for measuring the absorption coefficients of local air samples an optoacoustic detector (OAD) is mounted instead of the frequency doubler. The OAD sensitivity, determined using the mixture of ethylene and water vapor with pure nitrogen, was 30 V/W.cm^{-1} , and threshold sensitivity in terms of the absorption coefficient was 10^{-7} cm^{-1} for the output power of the CO_2 laser about 100 mW. The frequency tuning of the CO_2 laser radiation made with a stepping motor driven grating, as well as the alignment of a frequency doubler along the phase synchronism direction, and fine tuning of the radiation frequency with a piezoelectric corrector are automated and monitored by a micro-computer. Also automated is the process of data acquisition and processing.

The micro-computer allows also the solution of the ill-posed inverse problem on determining the gaseous concentration from the multifrequency sounding data to be found using the Tikhonov's regularization method. The results in the form of concentrations of sounded gases and residual (after subtracting the selective absorption) attenuation coefficients are stored on the flexible magnetic disks.

Figure 1 presents the fragment of one cycle of simultaneous low path absorption measurements of concentrations of four atmospheric components at 16 CO_2 laser radiation wavelengths and the atmospheric attenuation coefficient at

$\lambda = 0.63 \text{ }\mu\text{m}$. At two points the comparative measurements of local concentrations using OAD have been made, which show good agreement with the path measurements.

Figure 2 gives the spectral behavior of the atmospheric absorption coefficient for this spectral range to illustrate the possibilities of measurements at the wavelengths of the second harmonic of CO_2 laser radiation. The frequency doubler of the R(18) and R(20) lines of a nine microns CO_2 laser radiation band coincides with the absorption lines of the fundamental band. The corresponding absorption coefficients are equal to $25.7 \text{ cm}^{-1} \text{ atm}^{-1}$ and $10.28 \text{ cm}^{-1} \text{ atm}^{-1}$. The third peak is evidently due to the absorption at N_2O line, which is strongly disturbed by the spectrally close H_2O vapor absorption lines. This fact requires additional laboratory tests. Figure 3 presents the fragment of temporal variation of CO concentration obtained using a long-path absorption gas analyzer.

REFERENCES

1. Yu.M.Andreev, V.G.Voevodin, A.I.Gribenyukov et al. An Efficient Generation of the Tunable CO_2 Laser Radiation Second Harmonic in Zn Ge P_2 . *Kvant. Elektron.*, v.11, No.8, 1984, p.1511-1512.
2. Yu.M.Andreev, T.V.Vedernikova, A.A.Betin et al. Conversion of the Radiation from CO_2 and CO Lasers in Zn Ge P_2 into the Spectral Region of $2.3\text{--}3.1 \text{ }\mu\text{m}$. *Kvant. Elektron.*, v.12, No.7, 1985, p.1535-1537.

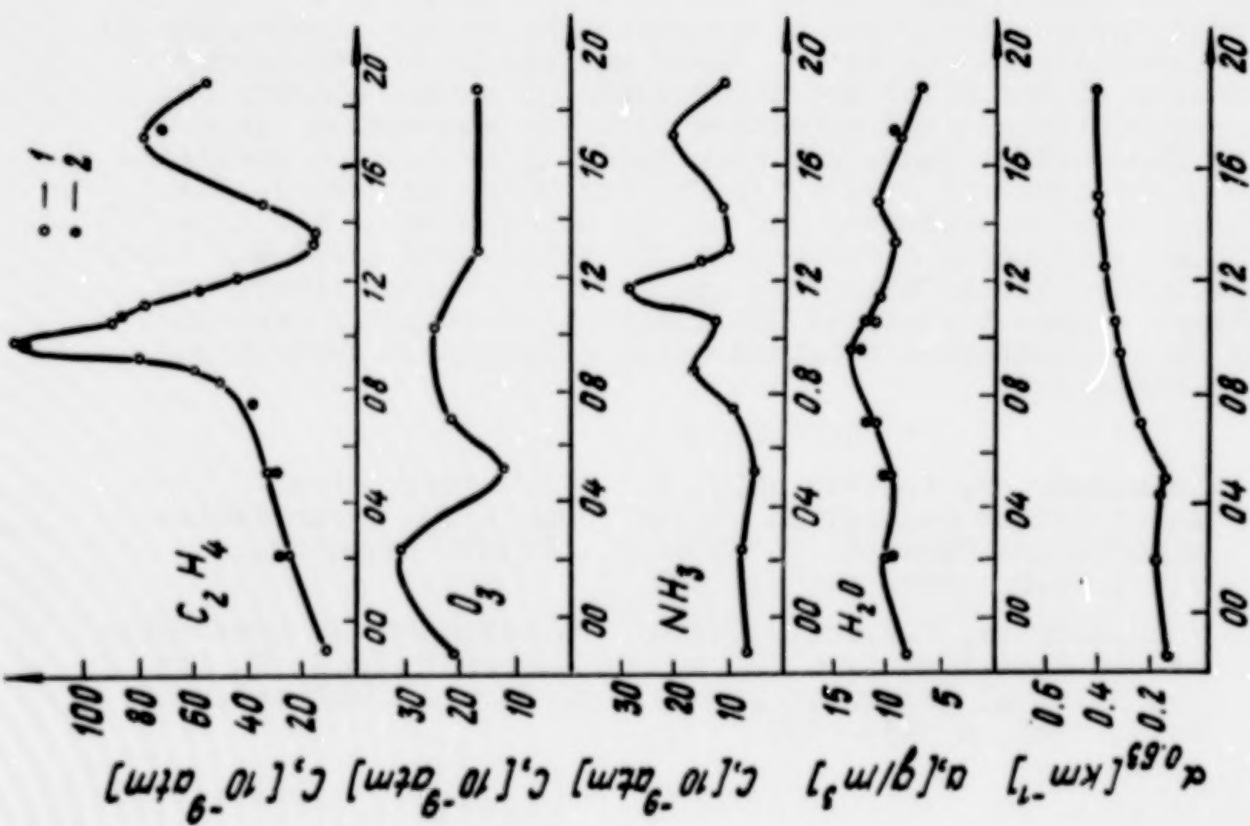


Fig. 1

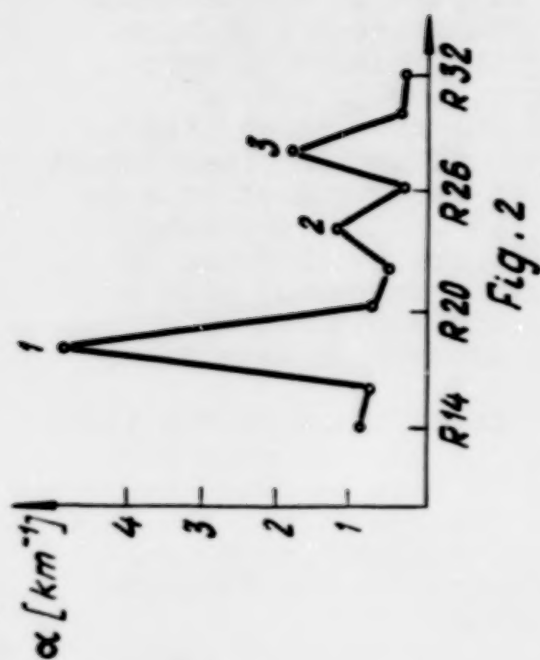


Fig. 2

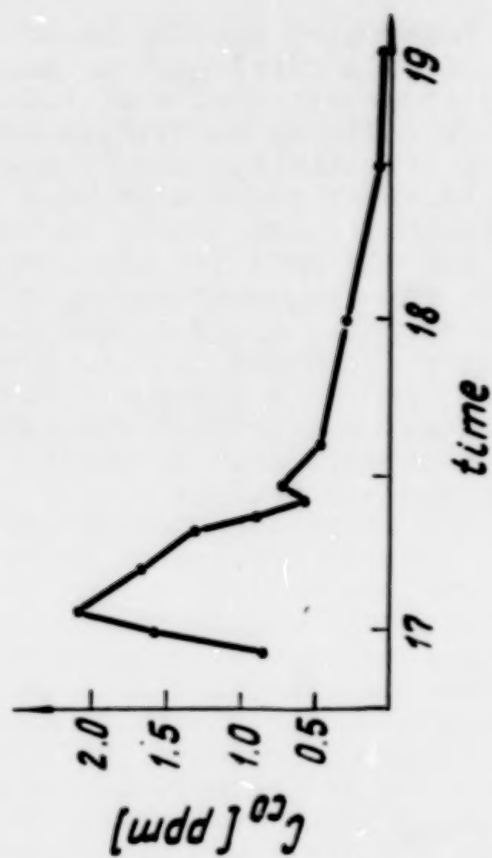


Fig. 3

N87

103003

UNCLAS

REMOTE EXPRESS ANALYSIS OF GROUND-LAYER AEROSOL
BASED ON LASER-INDUCED SPARK SPECTRA

V.E. Zuev, Yu.D. Kopytin, V.A. Korol'kov
M.E. Levitskii, M.F. Nebol'sin, B.G. Sidorov,
N.P. Soldatkin
The Institute of Atmospheric Optics, Siberian
Branch, USSR Academy of Sciences, Tomsk, 634055
U S S R

The state of the art of laser technique allows one to observe, in a ground-layer atmosphere, a large group of nonlinear optical effects which bear information on physico-chemical parameters of the atmosphere. In particular, the creation of high-power pulsed CO₂ and Nd-glass lasers enabled one to realize the method for remote spectro-chemical analysis of atmospheric aerosol based on excitation of the emission spectrum of aerosol particles atoms¹. The essence of the method is that at focusing of a high-power laser pulse in the atmosphere there occurs high-temperature heating and vaporization of solid-aerosol particle matter. In vapors of the matter there can also occur an optical breakdown accompanied by the development of plasma formations around the particles. The presence of free electrons in plasma leads to excitation of atoms and molecules due to inelastic collisions in vapors thus giving rise to their strong nonthermal glow. At remote spectro-chemical analysis the laser source should provide simultaneously developed vaporization of an impact target (aerosol suspension of oil particles, products of metallurgy, organic substances etc.) and excitation of a sufficiently strong linear spectrum in a gas-discharge plasma.

An emission spectral analysis of the matter vapors has high sensitivity. It allows one to identify and obtain quantitative information on element composition of atmospheric-aerosol particles, content of inert gases and vapors of substances.

The paper presents a description of construction and characteristics of a spectrochemical lidar based on both Nd-glass and CO₂ lasers.

In the case of a Nd-glass laser the scheme of a driving oscillator forming a laser 40 ns pulse and a block of an optical quantum amplifier has been used. The radiation at 1.06 μ m wavelength was focused at a given point of the atmosphere with the use of an optical Cassegrainian system which simultaneously received the optical breakdown emission. The Nd-glass laser lidar range of detection was 150 m. The spectral selection of plasma emission was carried out by a set of narrow-band interference filters placed into the photo-receiving blocks. The spectral range of the receiving system was 0.3 to 1.1 μ m. The spatial selection of radiation was carried out with a block of fibrous optical light conductors. The signals recorded with photo-electronic receivers were amplified,

converted into a numerical code with the use of quick-acting six-digit analog-to-digital converters with 0.1 μ s resolution and recorded in high-efficiency storage. Maximum duration of the recorded signal can reach 100 μ s. The subsequent processing of signals, according to a given algorithm, was carried out using the computational facilities based on a mini-computer.

When a mono-pulsed electro-ionized $\text{CO}_2:\text{N}_2$ laser with electron-beam pre-ionization of an active medium, 3 KJ power, 10.6 μ m wavelength, and variation of pulse duration 1 to 5 μ s was used as a source of high-power radiation for a spectrochemical lidar, its range of detection increased by an order of magnitude in comparison with the Nd-glass laser. The lidar provides for a quantitative express analysis simultaneously of 15 chemical elements with 30-50% error and mean concentration sensitivity 0.1 - 1.0 $\mu\text{g m}^{-3}$.

1. V.E.Zuev, A.A.Zemlyanov, A.V.Kuzikovskii. High-power laser radiation in the atmospheric aerosols. D.Reidel Publishing Company, Holland, Dordrecht, 1984.

N87

10304

UNCLAS

LASER SOUNDING OF INSTANTANEOUS AND MEAN SPEED
OF WIND USING CORRELATION METHOD

V.E. Zuev, I.V. Samokhvalov, G.G. Matvienko
The Institute of Atmospheric Optics SB USSR
Acad.Sci., Tomsk, 634055, USSR

I.N. Kolev, O.P. P'rrvanov
The Institute of Electronics, Bulgarian Academy
of Sciences, Sofia, Bulgaria

The correlation methods for laser sounding of wind speed are based on mutual processing of lidar signals scattered from several spatially separated volumes at each altitude investigated. The time of atmospheric aerosol transport between the scattering volumes estimated by the position of maximum of the mutual correlation function is the measure of corresponding wind speed. In this case the distance between the scattering volumes (the measuring base), defining the time of aerosol movement through the measuring base also determines the lidar possibilities for measuring the instantaneous (during the time interval of several seconds) or the mean wind speed (some minutes). In this paper, based on the experimental investigations carried out using two lidars, these possibilities have been analyzed.

In the temporal correlation method the information on wind speed is extracted from temporal realizations of lidar signals whose total duration is the time interval of averaging the measured wind speed. Taking into account the requirements on completeness of statistics, the duration of realizations T can be connected with the geometric lidar parameters and the least measured wind speed V_m by the relation [1]

$$T = 10 \xi_0 / V_m$$

where ξ_0 is the measuring base. If 1 m/s is taken as a threshold value of the measured speed, one can determine the value of the measuring base for the laser meter of instantaneous and mean wind speed. The measuring base should be about 0.5 m and 30 m, respectively.

Two lidars have been constructed which have sufficiently different measuring bases. The geometric scheme of lidar for measuring the instantaneous wind speed is given in Fig.1. The laser 1 generated the light pulses at the 0.53 μ m wavelength, 4 mrad divergence and 50 Hz pulse repetition rate. The radiation reflected by the atmosphere was collected with the objective 2 of 100 mm diameter and 1 m focal length. In the focal plane of the objective there was a mirror prism 3, which divided the image of scattering volumes into two parts (the shapes of the divided flows are shown in the top of the figure) and directed the light flows to the photomultipliers 4. The prism position corresponded to the measurement of the horizontal transverse speed of wind. The distance between the scattering

volumes, as a measuring base [1] depended on the range L and was $\xi_0 = 0.002 \cdot L$.

An example of measuring the transverse wind speed at sounding at an elevation angle of 20° is given in Figure 2, where the mutual-correlation functions at different ranges are shown. The values of transverse speed V_1 were determined from the expression $V_1 = 0.002 L / \tau'$, where τ' is the position of maximum of mutual-correlation function. The duration of temporal realizations was 5 s. The time of measurement can be further decreased if one increases the pulse repetition rate and decreases the divergence of laser pulses.

The lidar for measuring the mean speed had three sounding paths forming, at each altitude, the scattering volumes located at the vertices of a right-angled isosceles triangle, one of the cathetus of which coincides with direction to the north. The pulse repetition rate was 3.3 Hz. Figure 3 illustrates the mutual-correlation functions of signals at the 1 km altitude at wind speed 16.5 m/s and direction 153° (the point 2 is at the right-angle vertex). The distance between the scattering volumes at this altitude was 150 and 105 m, respectively. The correlation functions have maxima displaced from the origin of coordinates, which allow one to estimate the modulus and direction of wind using the method of complete correlation analysis [1]. The time of measuring the mean wind speed was 5...10 min.

Figure 4 gives the comparison of profiles of the mean wind speed modulus measured using lidar 1 and theodolite 2. As seen from Fig.4, the difference does not exceed 1 m/s.

The paper also presents the comparison with the aerological data on wind speed.

References

1. Correlation methods of laser-sounding measurements of wind speed / Matvienko G.G., Zadde G.O., Ferdinandov E.S. et al. Novosibirsk, Nauka, 1985.

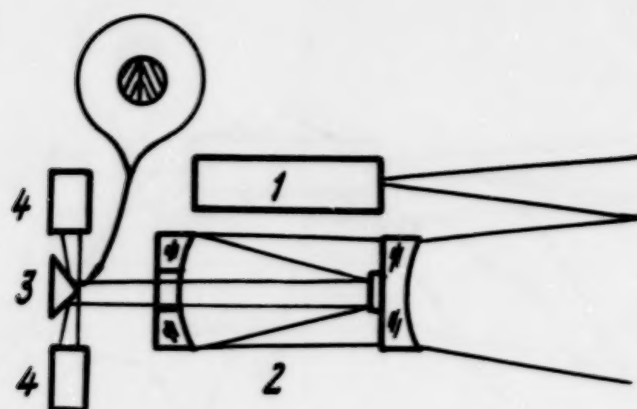


Fig. 1

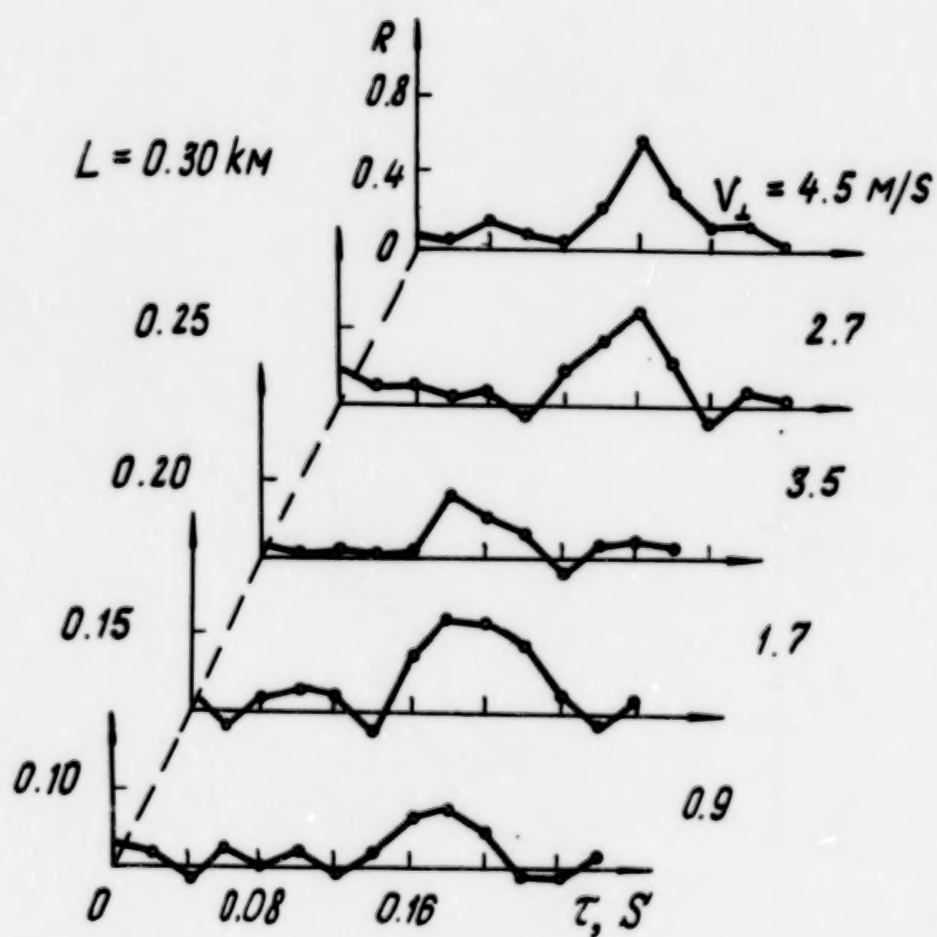


Fig. 2

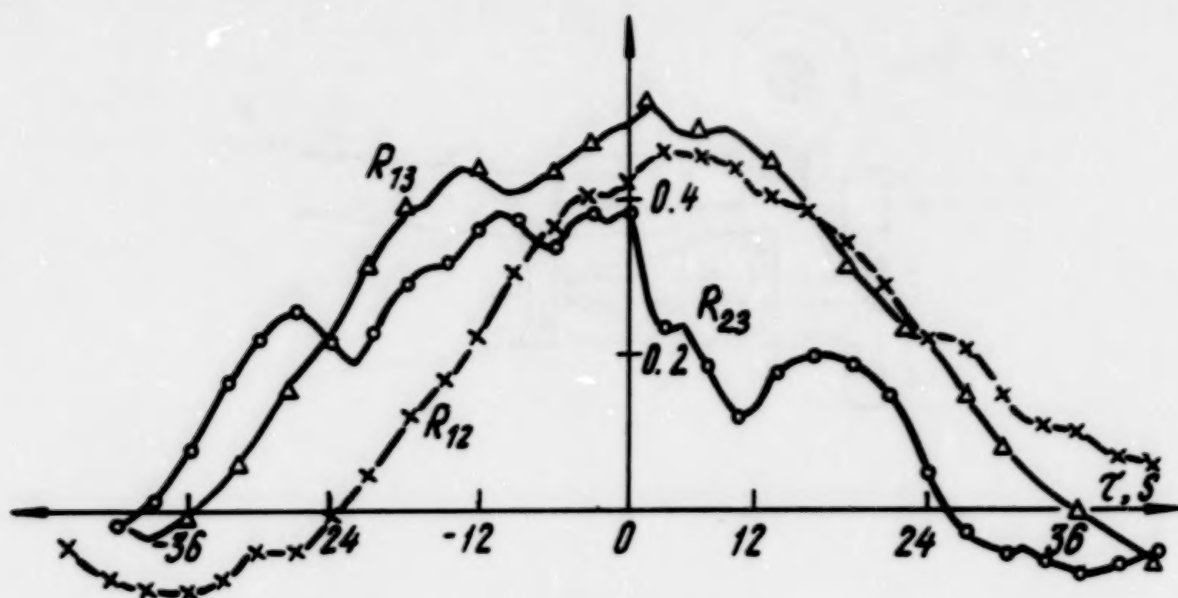


Fig. 3

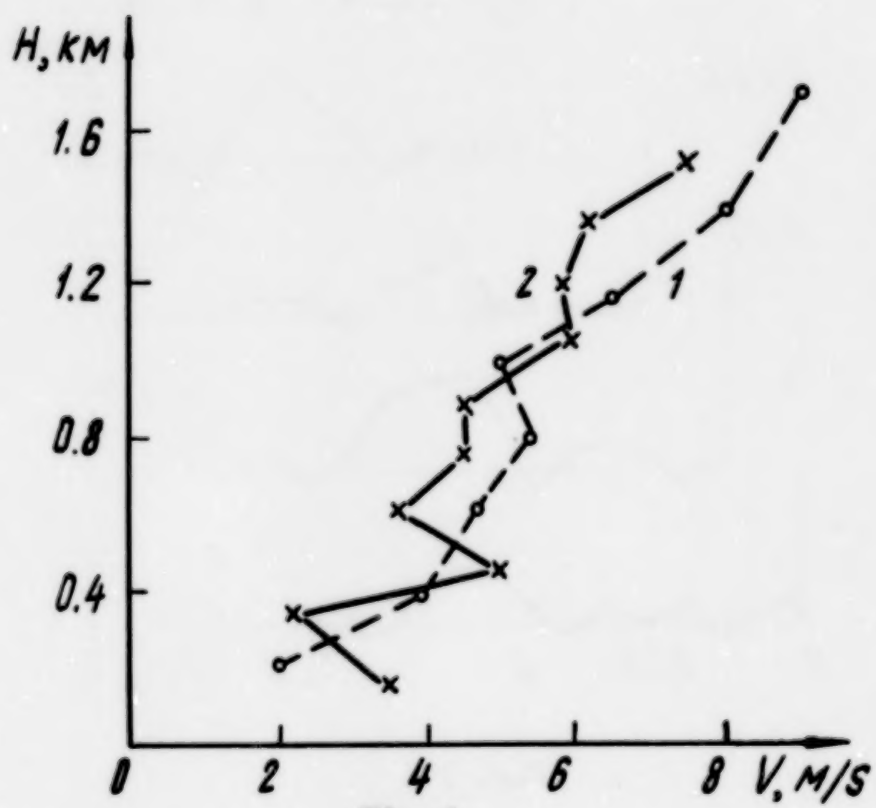


Fig. 4

N87

10305

UNCLAS

OPTIMAL FILTRATION OF THE ATMOSPHERIC PARAMETERS PROFILES

V.E. Zuev, G.N. Glazov, G.M. Igonin
The Institute of Atmospheric Optics SB
USSR Acad. Sci., Tomsk, 634055, USSR

The earlier suggested approach [1] for extracting the fluctuating profiles of temperature $T(z)$, density $\rho(z)$, pressure $p(z)$ and other atmospheric parameters related to a single-frequency lidar sounding did not take into account the contribution of aerosol scattering. Due to this fact it was only applicable to sounding based on either Raman scattering of nitrogen with a small cross section or Rayleigh scattering of air in the atmospheric regions with low aerosol content.

The present paper develops the same idea of optimal Marcovian filtration of fluctuating profiles from lidar signals but as applied to a double-frequency sounding which allows one to make use of large cross sections of elastic scattering and to correctly separate out the contributions due to aerosol and Rayleigh scatterings from the total lidar return.

In accordance with the lidar equation, a signal power component received from the altitude z is proportional to the smoothed backscattering coefficient

$$\beta_i(z) = 2(CE_i)^{-1} \int_0^z \beta_i^n(z') P_i[2(z-z')/c] dz' \quad (1)$$

where c is the speed of light, E_i is the energy of a radiated pulse with the power function $P_i(t)$, where $\beta_i^n(z) = \beta_{ar}^n(z) + \beta_{mi}^n(z)$ is the sum of natural nonsmoothed coefficients of aerosol and Rayleigh scatterings.

Let us assume the profiles of aerosol backscattering and transmittance to be determined during a single sounding, although unknown functions of altitude, and the relation g_a of backward and total coefficients of aerosol scattering to be constant in the interval of sounding altitudes. When the spectral dependence of aerosol scattering volume coefficients is used, it is sufficient to evaluate one of aerosol profiles, e.g., $Y_{ar}(z)$ being aerosol transmittance at one of the sounding wavelengths λ_i .

Under the assumptions made the smoothing (1) at the constant intervals of smoothing $L_i = c\tau_i/2$, where τ_i is the pulse duration, $i = 1, 2$, significantly changes only the profiles $\beta_{mi}^n(z)$ and connected with them $T(z)$, $\rho(z)$, $p(z)$. Under the conditions of laser sounding, if $L \gg z_{kr}^n$, where z_{kr}^n is the spatial correlation radius of nonsmoothed temperature fluctuations along the sounding path, these profiles are fully determined by the Marcovian vector-process $\vec{\eta}(t)$ satisfying the stochastic differential equation [1]

$$\dot{\vec{\eta}}(t) = A(t)\vec{\eta}(t) + \vec{w}(t)$$

where $\bar{\eta}(t) = \{\bar{\eta}_1, \bar{\eta}_2\}$, $\bar{\omega}^T(t) = \{\omega_1(t), 0\}$, $\omega_1(t)$ is the white Gaussian noise: $\langle \omega_1(t) \rangle = 0$, $\langle \omega_1(t) \omega_1(t') \rangle = 2\alpha \delta(t-t')$, $\alpha = \tau^{-1}$, $\tau = \min\{\tau_i\}$, $A = \|A_{ij}\|$, $A_{11} = -\alpha$, $A_{12} = A_{22} = 0$, $A_{21} = \bar{T}^2(z_0) / \bar{T}^2(z)$; the bar above the symbols denotes the averaging over the ensemble of the temperature fluctuations.

For the data of realization $\bar{\eta}(t)$ and $Y_{a1}(z)$ the photodetector current of the i -th channel $y_i(t)$ is the sum of the signal component $s_i(t; \bar{\eta}, Y_{a1})$ averaged over the ensemble of shot fluctuations and white Gaussian noises $n_i(t)$, if $\Pi_i \tau_i \gg 1$, where Π_i is the band of the postdetection filter of the i -th channel. The equations of quasioptimal filtration $\bar{\eta}(t)$ and simultaneous estimate of $Y_{a1}(z)$ using "the method of maximum probability" have the following forms:

$$\dot{\bar{\eta}}^* = A\bar{\eta}^* + KF_1(Y_{a1}^*)$$

$$\dot{K} = AK + KA^T + b + KF_2(Y_{a1}^*)K$$

$$\dot{Y}_{a1}^* = -\bar{\beta}_{m1}(z) \cdot C/g_a \{ [y_i(t) - s_{m1}(t; \bar{\eta}^*, Y_{a1}^*)] / \bar{s}_{m1}(t) \}$$

where F_1, F_2 are the first and second derivatives with respect to $\bar{\eta}$ of the function F , which is the derivative of probability-functional logarithm with respect to time; $b = \|b_{ij}\|$ is the matrix of diffusion coefficients $\bar{\eta}$, whose elements $b_{11} = -2\alpha$, $b_{ij} = 0$ at $(i, j) \neq (1, 1)$; $s_{m1}(t; \bar{\eta}^*; Y_{a1}^*)$ is the estimate of the photocurrent component s_i taking no account of the aerosol scattering, whose mean value is $\bar{s}_{m1}(t)$; $\bar{\beta}_{m1}(z)$ is the mean profile of Rayleigh scattering.

The paper shows the filtration efficiency under different conditions of sounding using a computer modeling. The accuracy of restituted profiles $\bar{T}(z)$, $\bar{\rho}(z)$, $\bar{p}(z)$ is determined by the elements of a posteriori matrix $\bar{K} = \langle (\bar{\eta} - \bar{\eta}^*)(\bar{\eta} - \bar{\eta}^*)^T \rangle$ of the vector $\bar{\eta}^*$. Therefore the profiles of K , of the atmospheric parameters filtration variances and the effect of aerosol on their altitude dependence. The results obtained allow one to determine the lidar power required for providing the necessary accuracy of restitution of the atmospheric parameters profiles at chosen wavelengths of sounding in the ultraviolet and visible ranges.

References

1. G.N.Glazov, G.M.Igonin. Optimal lidar filtration of the atmospheric parameters profiles: theory and numerical experiment. 12-th I.L.R.C., August, 1984.

N87

103006

UNCLAS

OPTICAL MODELS OF THE MOLECULAR ATMOSPHERE

V.E.Zuev, Yu.S.Makushkin, A.A.Mitsel,
Yu.N.Ponomarev, V.P.Rudenko, K.M.Pirsov
The Institute of Atmospheric Optics, Siberian
Branch, USSR Academy of Sciences, Tomsk, 634055
U S S R

The use of optical and laser methods for carrying out the atmospheric investigations has stimulated the development of the optical models of the atmosphere. The optical (laser) radiation absorption by molecular gases of the atmosphere is one of steady factors affecting the laser beams propagation along the atmospheric paths. A great bulk of stored information on absorption spectra of atmospheric gases and parameters of individual spectral lines, peculiarities of spectral characteristics dependence on variations of meteorological parameters, gas composition, and laser radiation characteristics [1-5] are the basis for developing the molecular atmosphere optical models.

The optical model of an absorbing molecular atmosphere is assumed to be the complex of information (in the form of plots, tables, analytical formulas, and computer programs) on molecular absorption characteristics along the path of light beam propagation taking into account the dependence on the path coordinate of meteorological parameters (temperature and pressure) and concentrations of the absorbing air components for given initial information on the light beam characteristics.

The paper considers the principles of constructing the optical models of molecular atmosphere for radiation with different spectral composition (wide-band, narrow-band, and monochromatic) in the case of linear and nonlinear absorptions.

The optical model of molecular atmosphere, in the case of linear interaction of monochromatic radiation with individual gas components, includes a quantitative information on vertical profiles of the volume coefficient of air absorption, optical depth and transmittance of the atmospheric vertical column, as well as the root-mean-square deviations of these values caused by variations of temperature, humidity and small gas-component concentrations. The analysis of the basic factors determining the value of the r.m.s. deviations of the optical-model parameters has been made for different spectral ranges.

The optical models for a narrow-band radiation have been developed for the case where the laser-radiation spectrum width is comparable with the resonance-absorption line width, and the form of spectral distribution is rectangular or Gaussian. The approximated analytical expressions [6] were suggested to simplify the procedure for calculating the energy absorbed from a laser beam with the Gaussian spectrum when

it propagates along the inhomogeneous vertical path.

The possibilities of increasing the accuracy of optical models of an absorbing atmosphere due to the use of additional information on altitude correlations of absorption characteristics [7] have been considered. The problems of calculating the atmospheric transmittance for the case of wide band ($\Delta\nu \gg \delta$) optical radiation are discussed. The comparative analysis of approximated calculational methods possibilities, in which the transmittance functions are calculated using the parametric formulas, has been made. The paper considers in detail the approach where the models parameters are calculated based on the data on a vibration-rotation structure of the spectrum obtained with the use of modern spectrometers with high spectral resolution. It was shown that in the framework of such an approach the model of an isolated spectral line is sufficiently simple and reliable for some individual spectral intervals of the IR range.

When constructing an optical model of the nonlinearly absorbing atmosphere for the wavelength range of CO_2 laser generation the nonlinear spectroscopic effects have been taken into account including the effects of absorption saturation in atmospheric CO_2 spectral lines and the new effect (theoretically and experimentally observed and studied at present at the Institute of Atmospheric Optics) of "blanching" of a line wing [8,9]. Both effects are characterized by a less intensive threshold than that of an air optical breakdown, and their actions result in significant increase of the atmosphere transmittance at easily attainable intensity levels of pulsed CO_2 lasers. Due to insufficient study of the considered nonlinear spectroscopic effects the suggested model can be considered as an evaluating one. The prospects for further development of a nonlinearly absorbing atmosphere model are discussed in the paper.

The solution of the problems on numerical simulation of the total sum of phenomena of optical radiation transformation in the atmosphere, even in the visible and IR, requires consideration of the order of 10^6 units of spectral information just as input data. Moreover, the variety of meteorological considerations and types of paths assumes a great number of calculations. Due to this fact an actual problem in developing numerical methods of atmospheric optics and spectroscopy is the problem of automated computation of absorption characteristics.

The paper presents the example of the development of such a system which provides for the modeling of the processes of optical-wave energy transfer in the atmosphere [10]. Its physical foundations, structure, programming software and functioning have been considered.

References

1. V.E.Zuev. Laser radiation propagation in the atmosphere.- Moscow, Radio i Svyaz, 1981, 288 p.

2. L.S.Rothman, R.R.Gamache, A.Barbe, A.Goldman, J.R.Gillis, L.R.Brown, R.A.Toth, J.M.Flaud and C.Camy-Peyret. AFGL Atmospheric absorption line parameters compilation. Appl.Opt., 1983, 22, N15, p.2247.
3. R.A.McClatchey, W.S.Benedict, S.A.Clough, D.E.Burch, R.P.Calfee, K.Fox, L.S.Rothman and Garing. AFGL Atmospheric absorption line parameters compilation. - ERP, N434, AFGL-TR-73-0096, 1973.
4. V.S.Komarov, N.Ya.Lomakina, S.A.Mikhailov. Evaluating model of altitude distribution of atmospheric gas traces. - Meteorologiya i gidrologiya, 1985, N1, p.56-61.
5. I.I.Ippolitov, V.S.Komarov, A.A.Mitsel. The atmospheric optico-meteorological model for modeling lidar measurement and calculating radiation propagation. - In: Spectroscopic methods for sounding the atmosphere. - Novosibirsk, Nauka, 1985, p.4-44.
6. A.A.Mitsel, Yu.N.Ponomarev, K.M.Firsov. Atmospheric-gas resonance absorption of narrow-band laser radiation. - Izv. Akad.Nauk SSSR, PAO, 1984, v.20, N3, p.327-329.
7. Yu.S.Makushkin, A.A.Mitsel, K.M.Firsov. Statistical method for calculating molecular absorption. - Izv. Akad.Nauk SSSR, PAO, 1983, v.19, N8, p.824-830.
8. B.G.Ageev, Yu.N.Ponomarev, L.K.Chistyakova. Investigation of the CO₂ pulsed laser radiation absorption by air and CO₂. - Izv. VUZov, Fizika, 1982, N10, p.49-51.
9. B.G.Ageev, E.P.Gordov, Yu.N.Ponomarev, S.D.Tvorogov, L.K.Chistyakova. The effect of laser radiation on absorption in far wings of spectral lines. - Dokl. Akad.Nauk SSSR, 1983, v.268, N5, p.1105-1107.
10. V.E.Zuev, Yu.S.Makushkin, A.A.Mitsel, L.I.Nesmelova, O.B.Rodimova, V.P.Rudenko, S.D.Tvorogov, K.M.Firsov, N.E.Yakovlev. Dialogue system for numerical modeling of energy losses of optical waves in the atmosphere. Dokl. Akad. Nauk SSSR, 1985, v.283, N2, p.345-348.

N87

10307

UNCLAS

THE INFLUENCE OF AN OPTICAL RECEIVING SYSTEM
ON STATISTICAL CHARACTERISTICS OF A LIDAR SIGNAL

V.E. Zuev, V.A. Banakh, V.L. Mironov
The Institute of Atmospheric Optics, Siberian
Branch, USSR Academy of Sciences, Tomsk, 634055
U S S R

The effects connected with correlation of direct and backward waves propagating through the same randomly inhomogeneous media can be observed along the paths with reflection in a turbulent atmosphere [1-3]. In particular, the mean intensity of the reflected wave can increase in comparison with the wave propagating in the forward direction at a doubled distance; the intensity fluctuations can become stronger and so on. These effects depend on the strength of optical turbulence β_0^2 ($\beta_0^2 = 1.23 C_n^2 k^3 L^3$, C_n^2 is the structure characteristics of the index of air refraction, k is the wave number, L is the path length), as well as on the diffraction sizes $\Omega = ka^2/L$, $\Omega_r = ka_r^2/L$ of the exit apertures of the source $2a$ and of the reflector $2a_r$, respectively.

However, as shown in Refs. [4-6] the focusing of radiation reflected with a receiving telescope leads, in some cases, to the fact that the dependence of amplification effects on the parameters Ω and Ω_r becomes essentially different. This should be taken into account when analyzing the lidar signals.

1. The Effect of Backscattering Amplification

The following relation [2,3] is fulfilled

$$\langle I^2(x_0, \vec{r}) \rangle = \frac{|U_0|^2}{(kL)^4} (1 + B_{I,S}(x, \vec{r})) \quad (1)$$

for a mean spherical-wave intensity scattered by a "point" reflector. Here $\langle I^2(x_0, \vec{r}) \rangle$ is the distribution of the reflected wave mean intensity in the plane of the source exit aperture $x' = x_0$, U_0 is the initial wave's amplitude, $B_{I,S}(x, \vec{r})$ is the normalized correlation function of the spherical-wave intensity in the reflector's plane $x' = x$.

It follows from Eq. (1) that in the strictly backward direction ($\vec{r} = 0$) there is amplification of the mean intensity by the value determined by variance of the direct spherical wave intensity $\sigma_{I,S}^2 = B_{I,S}(x, 0)$. In the region of weak fluctuations, when the parameter $\beta_0^2 < 1$, $\sigma_{I,S}^2 = 0.4\beta_0^2$ and $\langle I^2(x, 0) \rangle$ increases by the value $(|U_0|^2/(kL)^4) \cdot 0.4\beta_0^2$ [1] in comparison with propagation in a homogeneous medium.

If, however, the spherical wave after reflection is received with a telescope, then, at sufficiently large sizes of the objective ($\Omega_r = ka_r^2/L \geq 0.1$), the mean intensity amplification effect $\langle I^2(l, \vec{r}) \rangle$ is weakened, as the observation plane l approaches the plane l^* of the sharp receiving-lens image [6]. In the plane l^* it fully disappears.

In the region of strong fluctuations ($\beta_0^2 \gg 1$) $\sigma_{f,s}^2 = 1 + 2.7\beta_0^{-4/5}$ and, hence, at a telescope entrance, the reflected spherical wave intensity ($\Omega \ll \beta_0^{-12/5}$) increases by a factor of more than two in the direction $\vec{r} = 0$. If the reflector is irradiated by a source with the aperture $\Omega \gg \beta_0^{-12/5}$, then the amplification of mean intensity at a telescope entrance is small. It is determined by the value of asymptotically small terms of the order of $\beta_0^{-4/5}$.

It follows from the asymptotical expression for the function of the second-order mutual coherence of the reflected-wave field $\Gamma_2^R(x_0, \vec{r}, \vec{r}') \langle \langle I^R(x_0, \vec{r}) \rangle \rangle = \Gamma_2^R(x_0, \vec{r}, 0)$ at $\beta_0^2 \gg 1$ [1,6] that, when $\Omega \gg \beta_0^{-12/5}$, not only the term $O(\beta_0^{-4/5})$ but also the term of higher order of smallness $O(\beta_0^{-12/5})$ is responsible for the correlation of direct and reflected waves. It describes the so-called "far correlations" of the reflected field [1] and has a significant (of the order of $\sqrt{2\lambda} \beta_0^{4/5}$) scale of decrease in the plane transverse to the direction of propagation. This circumstance allows the effective focusing of the reflected radiation to be made if the sizes $2d_L$ of the receiving lens satisfy the condition $\Omega_L \gg \beta_0^{-12/5}$. Really, in the focus of such a lens the mean intensity increases by a factor of more than two in comparison with the intensity of the wave propagating along the path of a doubled length [1,4].

Thus, if in the plane of the entrance telescope lens there is no mean intensity amplification at $\beta_0^2 \gg 1, \Omega \gg \beta_0^{-12/5}$ then in the lens focus such an amplification arises. However, focusing of a spherical wave reflected with a lens with sizes $\Omega_L \gg \beta_0^{-12/5}$ at $\beta_0^2 \gg 1$ results in the fact that the larger than doubled mean intensity increase occurring at a telescope entrance disappears in the plane of sharp image of the receiving lens [6] just in the same way as at weak fluctuations.

2. Amplification of Intensity Fluctuations

As shown in [2,3], the significant amplification of strong ($\beta_0^2 \gg 1$) intensity fluctuations occurs only when scattering is on a point scatterer ($\Omega_L \ll \beta_0^{-12/5}$). In this case the saturation level of relative variance of the reflected radiation intensity is five, if the reference wave is spherical, and three if it is plane ($\Omega \gg \beta_0^{-12/5}$). When the reflectors have the sizes $\Omega_L \gg \beta_0^{-12/5}$, the increase of the relative intensity variance is observed in the asymptotically small terms $O(\beta_0^{-4/5})$ only, and the saturation level $\sigma_{f,R}^2$ equals unit as in the case of direct propagation [2,3].

The focusing of reflected radiation with the telescope results in variation of the value of intensity fluctuations. In particular, the saturation level of the plane-wave intensity fluctuations scattered with a point reflector increases from the value $\sigma_{f,R}^2 = 3$ at a telescope entrance to the value $\sigma_{f,f}^2 = 5$ in a focal plane [4,5].

It should be noted that if a spherical-wave field is

focused after reflection, then the saturation level of the relative intensity variance in the lens focus turns out to be lower than that in the plane of the lens itself [4,5].

These variations, however, are of local character. When the observation plane is displaced from a focus along the optical-system axis ($l \neq f$), the relative variance of the reflected radiation intensity takes again the same values as in the entrance-lens plane [5].

References

1. Yu.A.Kravtsov, A.I.Saichev. - Usp.Fiz.Nauk, 1982, v.237, ed. 3, p.501-527.
2. Signals and Noises in Laser Sounding /Orlov V.M. et al. Moscow, Radio i Svyaz, 1985.
3. V.P.Aksenov, V.A.Banakh, V.L.Mironov. - J.Opt.Soc. Am. A, 1984, vol.1, N3, p.263-274.
4. V.P.Aksernov, V.A.Banakh, V.M.Buldaikov et al. - Optics Letters, 1984, vol.10, N4, p.107-109.
5. V.P.Aksernov, V.A.Banakh, V.M.Buldaikov et al. - Kvant. Elektron., 1985, v.12, N10, p.2136-2140.
6. V.A.Banakh, V.L.Mironov, I.N.Smalikho. - In: VII All-Union Symposium on Laser and Acoustic Sounding of the Atmosphere. Abstracts of Papers, Part I, Tomsk, 1984, p.41-44.

N87

103008

UNCLAS

COHERENT LIDARS BASED ON INTRACAVITY
HETERODYNING OF ECHO SIGNALS

V.E. Zuev, S.D. Burakov, A.P. Godlevskii,
Yu.D. Kopytin, S.V. Lazarev, S.A. Ostanin
and P.P. Sharin

The Institute of Atmospheric Optics SB
USSR Acad. Sci., Tomsk, 634055, USSR

This paper presents the development and technical realization of the method of laser sounding of the atmosphere based on the effects of mixing of reference and external fields of scattering inside a laser cavity.

An approximate theory of the method has been developed on the basis of the investigations using the model of a three-mirror laser. The nonlinear effect of a wide-band laser on frequency-dependent external influences of the atmosphere is investigated. It is shown that at synchronous detection of external radiation the spectral sensitivity of a laser receiver is comparable with the sensitivity of the method of intracavity laser spectroscopy and in the case of incoherent reception it decreases by the value $\sim r_{\text{eff}} \sqrt{\bar{\delta}} / \ell$ and in the case of coherent reception the spectral sensitivity decreases by the value $\sqrt{r_{\text{eff}} \bar{\delta}} \sqrt{\ell} / \ell$. Here ℓ and $\bar{\delta}$ are the length of atmospheric path and the cavity length, respectively; r_{eff} is the coefficient of effective scattering, characterizing the energy introduced into the laser cavity, $\bar{\delta}$ is the coefficient of space-time field coherence in the plane of receiving-transmitting laser aperture. In the narrow-band (gaseous) lasers both the spectral sensitivity and the sensitivity to external influence can be increased due to competition of simultaneously generating transitions connected by the common laser level. The experimentally obtained values of sensitivities to selective and external influences of a CO_2 -laser at two-wave generation are 5-8 and 2-3 times greater, respectively, than sensitivities at single-wave generation.

The experiments on comparison of sensitivity of coherent reception at intracavity photomixing of reference and scattered radiation in the case of single-wave CO_2 laser generation and at photomixing directly on a photoreceiver have shown that the sensitivity of intracavity laser reception is more than one order of magnitude higher than that of the commercial cooled receivers and was 10^{-12} W/Hz.

The field measurements of gaseous composition of the atmosphere have been carried out on the basis of a given method of coherent reception using a tunable CO_2 laser.

N87

10309

UNCLAS

THE INFLUENCE OF SCATTERING PARTICLES MORPHOLOGY
ON THE CHARACTERISTICS OF LIDAR SIGNALS

V.E. Zuev, I.E. Naats and A.A. Popov

The Institute of Atmospheric Optics SB USSR Acad.
Sci., Tomsk, 634055, U S S R

The characteristics of light scattering by a separate spherical particle are used as a priori information when interpreting the data on laser sounding of atmospheric aerosol. Analogously, it is necessary to have a priori information on the characteristics of light scattering by single crystals in order to reconstitute the microstructure of crystal formation in the atmosphere. In contrast to the aerosol particles the crystals are of different shapes. On the one hand, this complicates the solution of electrodynamic problems on light scattering by such crystals. On the other hand, if obtaining such a solution is possible, one can determine the morphology of scattering particles according to the sounding data and this enables one to obtain additional indirect information on such meteorological parameters as temperature, pressure, humidity.

Linear dimensions of crystals in the atmosphere are tens and hundreds times greater than the wavelength sounded. Therefore the determination of a scattered field in the near area is possible only by means of geometric optics. In this case, it is reasonable to use the geometric optics in the limits of beam approach, i.e., to construct the beam path taking into account the beam distribution on crystal surfaces. When determining the scattered field in the far area it is reasonable to use the wave concept which enables us to consider analytically the beam transformation to a spherical wave. Using this geometric-wave approach the problem of scattering of plane electromagnetic wave on convex polyhedron of arbitrary form was solved. As a result, the expressions have been obtained for electric field components of perpendicular and parallel polarizations scattered in any given direction.

A hexagonal crystal was chosen as a numerical model of crystal particle. Figure 1 gives the scheme of beam distribution as a result of four interactions of the plane wave front with the prism surface. The beams 1 - 6 form the field of backscattering. In the backscattering all the features of the form of hexagonal prism are shown, i.e., the prism investigated is right, the opposite lateral faces are parallel, the lateral faces are located at angles of 60° . The beams 3 - 6 are typical only for hexagonal prisms and are stipulated by all these characteristics, and their paths represent the broken helical lines. The beams of 1,2 types are formed in any right regular prism with parallel opposite surfaces due to reflections from these surfaces and prism bottom. Thus, the field of backscattering is an interference field. The presence and absence of separate components in the field depend on the shape of crystal. Each interference field is strongly dependent on

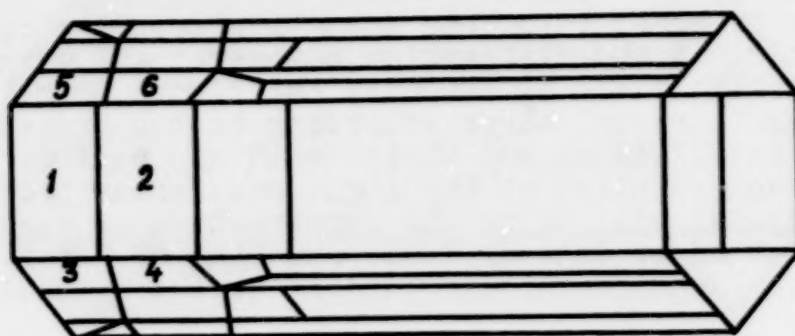


Figure 1. Scheme of the plane wave front distribution taking into account its four interactions with the surface of hexagonal crystal. The plane of wave incidence is perpendicular to a lateral surface, the angle of incidence is 30° . The ratio of the lengths of lateral edge to the side of the bottom $L/a = 5$. The complex refractive index $n = 1.31 + i \cdot 10^{-3}$.

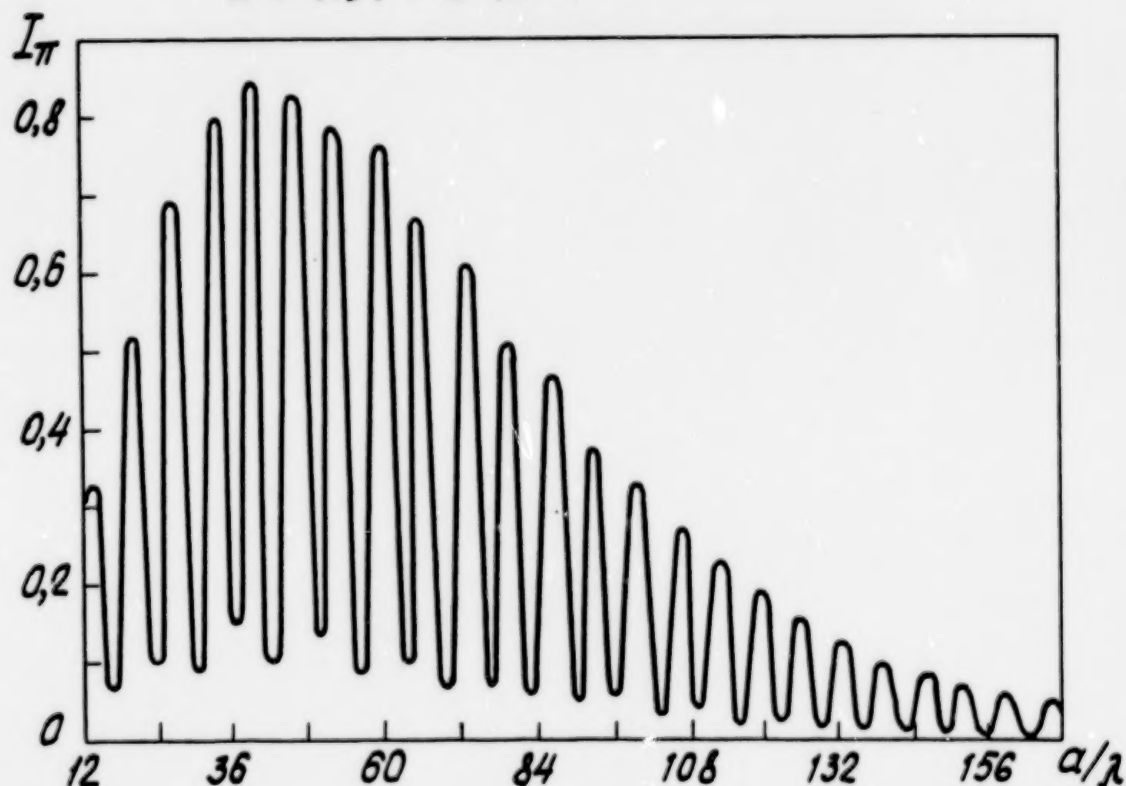


Figure 2. The dependence of field intensity of back-scattering I_π on the diffraction parameter a/λ for the system of similar hexagonal crystal ($L/a = 5$). The complex refractive index $n = 1.31 + i \cdot 10^{-3}$.

variation of phase relations among its separate components. As a result, if the diffraction parameter q/λ varies, the backscattering field I_r strongly oscillates (Fig.2). One can judge the crystal shape according to the presence or absence of oscillations and their depth and periodicity. Thus, the obtained solution of the light scattering problem by a separate crystal will allow the construction of algorithms of interpretation of data of laser sounding of crystal clouds with their identification according to the crystal shape.

N87

10310

UNCLAS

IMPROVED SOLUTION OF THE LIDAR EQUATION UTILIZING PARTICLE COUNTER MEASUREMENTS

H. Jäger and M. Littfass, Fraunhofer-Institute for Atmospheric Environmental Research, D-8100 Garmisch-Partenkirchen, FRG

D.J. Hofmann and J.M. Rosen, Department of Physics and Astronomy, University of Wyoming, Laramie, Wyoming 82071, USA

The extraction of particle backscattering from incoherent lidar measurements poses some problems. In the case of measurements of the stratospheric aerosol layer the solution of the lidar equation is based on two assumptions which are necessary to normalize the measured signal and to correct it with the two-way transmission of the laser pulse. Normalization and transmission are tackled by adding the information contained in aerosol particle counter measurements of the University of Wyoming to the ruby lidar measurements at Garmisch-Partenkirchen.

The widely accepted lidar normalization is the matching method which assumes a range existing in the stratosphere with negligible particle backscattering. The signals from such a range, usually from above 25 km, are adjusted to match the expected molecular return which is calculated from radiosonde density (or standard atmosphere) data.

The two-way transmission becomes an important correction when rather dense volcanic eruption clouds are observed. The correction is calculated from the extinction the laser pulse experiences on its way to and from the scattering volume under observation. The extinction in turn is calculated from particle backscattering measured by lidar thus causing an iterative calculation loop. The conversion factor involved, the backscatter-to-extinction ratio, is the crucial point in this procedure. For background or aged volcanic aerosol a value of about 0.015 1/sr is accepted (e.g. Russell and Hake, 1977), whereas much higher values are expected from fresh volcanic aerosols. Some values have been reported for the El Chichon period which are as high as 0.029 1/sr (Swissler et al., 1984).

Both quantities, normalization and transmission correction, can be calculated if the particle size distribution and the index of refraction are known. The balloon-borne particle counter soundings of the stratosphere by the University of Wyoming provide such data which allow the calculation of

- i time resolved particle backscattering from the height level of matching (which then adds to the molecular backscattering at this level)
- ii time and height resolved backscatter-to-extinction ratios

The cumulative particle concentrations of the six counter channels are differentiated with a height resolution of 1 km to fit a bimodal lognormal distribution. This model allows the description of the aerosol by 6 parameters (two modal radii, two modal widths and the total number concentrations in each distribution), thus providing for the proper treatment of the increased number of large particles after volcanic eruptions (Hofmann et al., 1983).

Calculated backscattering from height levels above 25 km for the El Chichon period will be compared with lidar measurements and necessary corrections will be discussed. The calculated backscatter-to-extinction ratios will be compared to those, which have been derived from a comparison of published extinction values (Rosen and Hofmann, 1986) to measured lidar backscattering at Garmisch (Jäger et al., 1984). These ratios have been used to calculate the Garmisch lidar returns. For the period 4 to 12 months after the El Chichon eruption a backscatter-to-extinction ratio of 0.026 1/sr has been applied with smaller values before and after that time.

References

- Russell, P.B. and R.D. Hake, J. Atmos. Sci, 34, 163, 1977.
- Swissler, T.J., D.J. Hofmann and J.M. Rosen, 12th Int. Laser Radar Conference, Aix en Provence, 1984.
- Hofmann, D.J., J.M. Rosen, R. Reiter and H. Jäger, J. Geophys. Res., 88, 3777, 1983.
- Rosen, J.M. and D.J. Hofmann, to be published in Appl. Opt., 1986.
- Jäger, H., R. Reiter, W. Carnuth and W. Funk, Geof. Int. 23-2, 243, 1984.

N87

10311

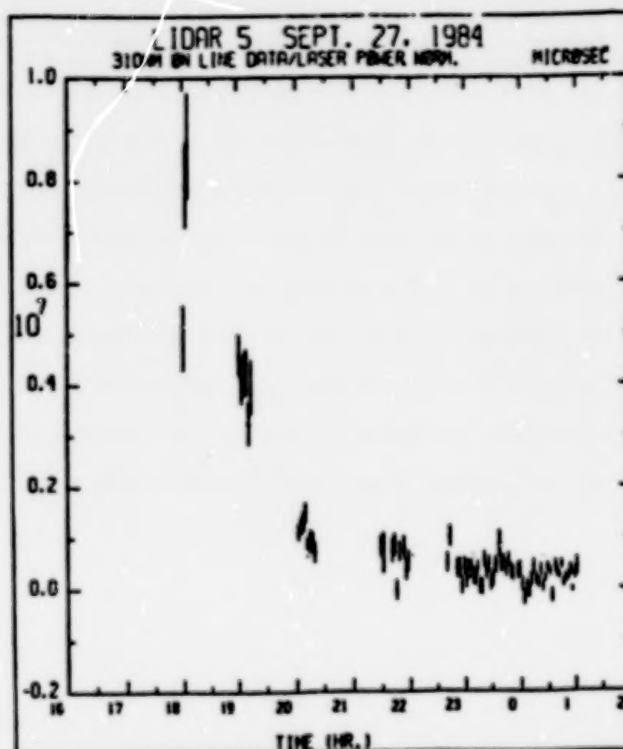
UNCLAS

51801-884

IMPROVEMENTS IN THE GODDARD BALLOON-BORNE LIDAR

William S. Heaps, Laboratory for Atmospheres, NASA Goddard Space Flight Center Greenbelt, Maryland, U.S.A.

The Goddard balloon-borne lidar system for the measurement of stratospheric ozone and the hydroxyl radical has made three additional flights since the last laser radar conference. On September 27, 1984 a flight was made from Palestine, Texas obtaining a measurement of hydroxyl diurnal variation at 36 km. These data are presented on the plot which shows hydroxyl concentration as a function of GMT for the range cell closest to the instrument. Local noon corresponds to 18 hours on the plot. The rapid drop in concentration after noon is not predicted by models of stratospheric chemistry. It may represent the effects of contamination of the sample volume by hydrocarbons outgassed from the balloon.



The more recent flights on June 30, 1985 and December 6, 1985 focussed on measurements of concentration in the lower stratosphere (<30 km). The June flight succeeded in obtaining an average concentration measurement $(1.8 \pm 1.8 \times 10^6 \text{ molecules/cm}^3)$ over the altitude range 21-26 km. The December flight obtained measurements down to 24 km with a better SNR than that obtained in June. Prospects for further improvement in sensitivity and absolute calibration will be discussed.

N87
10312

UNCLAS

Features of Stratospheric Aerosol Lidar Observations
at Mauna Loa, 1974 - 1985

J. J. DeLuisi, T. DeFoor, and D. U. Longenecker
NOAA/ERL, Boulder, CO 80303

Abstract

Lidar observations of the stratospheric aerosol over Mauna Loa were begun in the fall of 1974 and have continued to the present. An analysis of these observations has yielded interesting features of the stratospheric aerosol profile that change according to perturbed (from volcanic activity) and quiescent conditions. In the Mauna Loa lidar record there are two major perturbations that are contrasted, Fuego and El Chichon. The variations in relative aerosol cloud thickness, altitude of the maximum concentration and non-symmetry are compared for the quiescent and perturbed time periods. Also, a climatology of annual average aerosol profiles is described. A brief description will be given of procedures used to validate the lidar optical thickness information.

N87

10313

UNCLAS

EL CHICHON AEROSOLS IN THE STRATOSPHERE:
ANALYSES OF LIDAR DATA AND CALCULATIONS
OF RADIATION BUDGET

M. Fujiwara, H. Akiyoshi and N. Otsuka
Department of Physics, Kyushu University
Fukuoka 812, Japan

Lidar observation at Fukuoka (33°N , 130°E) has provided over four years the data of El Chichon aerosols in the stratosphere. Analyses of the data show that an enormous amount of volcanic aerosols has continuously decreased since the beginning of 1983 with significant fluctuations. These fluctuations reveal themselves as a seasonal variation of aerosol content with a maximum in winter-spring and a minimum in summer. The vertical structure of the aerosol layer also shows the seasonal variation. Although the height of a peak around 18 km in the vertical profile of scattering ratio shows little variation, the higher second peak appears frequently from late fall and the lower third peak from late winter to late spring just as two and more tropopause appear in these periods. The mechanism which causes the seasonal variation will be discussed in terms of the transport by the atmospheric circulation and the removal through the tropopause gap.

Radiation budget in the atmosphere has been calculated taking into account the large amount of aerosols observed in the early stages of the El Chichon event. The heating rate of the atmosphere is more than 1K in the bottom region of the stratosphere even in the nighttime. The possible effect of the volcanic aerosols on the other geophysical phenomena will be discussed using the calculated values of the heating rate.

On 29 November 1985 the Ruiz eruption cloud was detected at Fukuoka. Results of succeeding observations of this new volcanic cloud will be presented.

LIDAR OBSERVATIONS OF STRATOSPHERIC AEROSOL
AFTER MT. EL CHICHON ERUPTION

Sun Jinhui, Qiu Jinhuan, Xia Qilin, and
Zhang Jindin
Institute of Atmospheric Physics
Academia Sinica, Beijing, China

The observations of the stratospheric aerosol layer were made from February 1983 to November 1985, using a ground-based ruby laser radar at Beijing.

The vertical profiles of backscattering ratio were obtained. The height resolution of the data is 0.3km. The peak value of backscattering ratio was 2.5 on February 25, 1983. It decreased to 1.3 in November 1985.

The integrated backscattering coefficient was approximately $8 \times 10^{-4} \text{ sr}^{-1}$ (between 15-25km) in February 1983. It was approximately $2 \times 10^{-4} \text{ sr}^{-1}$ in November 1985.

The results of lidar observations will be discussed.

N87

10314

UNCLAS

LIDAR MEASUREMENT OF STRATOSPHERIC AEROSOL AT SYOWA STATION,
ANTARCTICA

Y. Iwasaka

Water Research Institute, Nagoya University, Nagoya 464

T. Hirasawa, H. Fukunishi, and T. Ono

National Institute of Polar Research, Itabashi-ku, Tokyo
173

A. Nomura

Faculty of Engineering, Shinshu University, Nagano 380

Lidar measurements on Antarctic aerosol were made during the AMA (Antarctic Middle Atmosphere) period, 1983-1985 at Syowa Station (69°00'S, 39°35'E). Topics measured are winter enhancement aerosol layer and volcanic effect of El Chichon on the Antarctic stratospheric aerosols.

Introduction

An extremely enhanced stratospheric aerosol layer, which was named Polar Stratospheric Clouds by McCormick et al. (1982) on the basis of satellite measurements SAM II, was observed by lidar. The noticeable increase in aerosol content possibly affects various fields: global budget of stratospheric water vapor, global budget of stratospheric sulfur compounds, sediments of sulfur on ice sheet of Antarctic land, and active formation of cirrus clouds in the winter Antarctic troposphere.

The volcanic effect on El Chichon was suggested from a long-term trend in the variation of the aerosol content from the vertically integrated backscatter coefficient. Chemical analysis on the ice core sampled in the Antarctic and Arctic regions revealed the presence of " Anomalously Enriched Elements " due to a possible global dispersion of volcanic materials into the stratosphere by severe volcanic eruptions (Mitchell, 1975; Boutron, 1980). There is a possibility that the winter enhanced aerosol layer plays an important role in the transport of such volcanic materials from the stratosphere to the ice surface.

In this report lidar measurements made at Syowa Station

(69°00'S, 39°35'E) are presented.

Lidar measurements

Specifications of lidar used here are described in Table 1 (detailed description was given by Iwasaka et al. (1985a)).

Integration given by the following equation is a useful parameter to discuss the change of stratospheric aerosol content

$$I = \int_{z_1}^{z_2} B(z) dz$$

where z_1 and z_2 are top and bottom height of aerosol layer respectively. The value increased to be about $2 \times 10^{-2} \text{ sr}^{-1}$ in the winter of 1983. A comparable value was measured also in the winter of 1985.

Depolarization ratio is defined here by

$$D(z) = P_{\perp}(z)/P_{\parallel}(z)$$

where $P_{\parallel}(z)$ and $P_{\perp}(z)$ are parallel and perpendicular components of the polarization plane of received pulse to emitted pulse plane. A large depolarization ratio of the stratospheric aerosol layer was measured during the winter enhancement (Iwasaka et al., 1985a; Iwasaka et al., 1985b; Iwasaka, 1986).

Comparing the aerosol densities measured in fall and in spring of 1983, 1984, and 1985, there is systematic decrease due to the possible effect of the El Chichon eruption. Concerning the winter measurements in 1983 and 1985, there is not a noticeable difference between them.

Discussion and summary

The large depolarization ratio (maximum value was about 0.8) seems to support sublimation growth of ice crystals (Swisler et al., 1983). The lidar measurements showed a meaningful time lag between aerosol content increase and depolarization ratio increase. Considering the balloon observations made

in early winter, we can speculate an increase in large particle number concentration also contributed to the winter enhancement.

The El Chichon cloud spread to the Antarctic region by the beginning of 1983. The temporal change of integrated backscatter coefficient shows a clear decay pattern, although strong winter enhancement superposes. The decay time scale is estimated by

$$I(T) = I(0)\exp(-T/\tau)$$

where T and τ are observational time and characteristic time of decay. The time scales estimated are summarized in Table 2. Time scales seem to be a little longer compared with estimations made on the mid/low latitude stratosphere. This may be due to active transportation of volcanic particles and related gases by stratospheric air motion.

References

- Boutron, C., 1980, J.Geophys. Res., 85, 7426-7432.
Iwasaka, Y., H.Fukunishi, R.Fujii, H.Miyaoka, and T.Hirasawa, 1985a, Mem. Nat. Inst. Polar Res., 39, 1-9.
Iwasaka, Y., H.Fukunishi, and T. Hirasawa, 1985b, J. Geomag. Geoelectr., 37, 1087-1095.
Iwasaka, Y., 1986, J.Meteor. Soc. Japan, 64, (accepted).
McCormick, M.P., H.M.Steele, P.Hamill, W.P.Chu and T.J. Swisler, 1982, J.Atmos. Sci., 39, 1387-1397.
Mitchell, M.J., 1975, The Changing global Environment (ed. by S.F.Singer), 149-173.

Table 1
Specifications of lidar

Transmitter	
Laser output	694nm <1J/pulse 347nm < 0.4J/pulse
Repetition rate	60ppm (Max)
Transmitter beam divergence	0.5 mrad
Receiver	
Receiver optics	Cassegrain telescope
Receiver diameter	500 mm
Detection system	
3-channel detection (typical configuration)	
A-channel	photoncounting (347nm)
B-channel	photoncounting (694nm)
C-channel	Analog detection (694nm)
Data processing	
CAMAC data logging system with minicomputer	

Table 2
Characteristic decay time

observation period	time scale
1983/3 - 1983/10	1.37 year
1983/3 - 1985/3	1.42 year

N87

10315

UNCLAS

MULTIPLE SCATTERING MEASUREMENTS IN LABORATORY AND FOGGY ATMOSPHERE

P. Bruscaaglioni, E. Battistelli, P. Pili, G. Zaccanti

Department of Physics - Via S. Marta, 3 Firenze Italy

Multiple scattering affects propagation of light beams in turbid media. Backscattering or forward scattering based measurements of atmospheric parameters are influenced by this effect. Although largely studied theoretically, the effect needs measurements in controlled situations due to the large variety of situations of practical importance.

The aim of this paper is to present the results of laboratory measurements pertaining to the transmission of a collimated light beam (HeNe source, 10 mW) through suspensions of latex spheres in water and to make a comparison with the predictions of calculations. Some results pertaining to light beam propagation in a foggy atmosphere will also be presented.

In the laboratory the transmitted power was measured by an optical receiving system whose Field of View was varied in 6 steps between $\alpha = 0.5$ and $\alpha = 3$ (semiaperture). The optical depth of the suspensions was also varied during the measurements.

The dependence of the received power, P_R , on the F.O.V. semiaperture α and on the optical depth τ was analyzed. By analyzing P_R as a function of α , with τ fixed, we were able to separate the contribution P_0 pertaining to the attenuated beam (1), since the transmitted power of the collimated beam did not vary with α .

The presence of inhomogeneities of the medium interposed between a source and a receiver can cause the amount of received scattered power to vary with respect to the case of a homogeneous medium with the same optical depth. Results of numerical computations indicated that, given the optical depth, when the extinction coefficient is larger in the proximity of the receiver the relative contribution of forward scattering to the received power increases. (2)

To make a simple verification of this effects, during laboratory measurements, for each value of the optical depth of the

suspension, measurements were repeated with different values of the distance D between the vessel containing the suspension and the receiver.

Fig.1 gives an example of a comparison between measured and calculated ratio P_s/P_0 (scattered power divided by attenuated beam power) plotted versus τ . The figure refers to polystyrene spheres with average radius $7.85 \mu m$. The crosses connected by the continuous lines in Fig. 1a, b indicate the measured ratios. The squares indicate the ratios calculated by taking into account ten orders of scattering (3).

A comparison between the data of Fig. 1a, b shows the increase of received scattered power occurring when the suspension is nearer the receiver.

The effect was confirmed for other cases relative to different types of spheres and other values of α .

To have a detailed comparison with the results of calculations an analysis was made aiming at examining the contributions of first and second orders of scattering separately. This was possible since, under assumption of validity of the small angle approximation, the ratio P_s/P_0 can be represented (for a given geometry) by a polynomial in τ (see for instance ref. (4) eq. 10, or also ref. (1)). Thus one can write for α and D fixed:

$$P/P_0 = K_1(\alpha)\tau + K_2(\alpha)\tau^2 + \dots$$

where the term $K_m(\alpha)$ corresponds to the contribution of m th order of scattering.

From the dependence on α of K_1 , one can deduce the scattering function $L(\theta)$ of the suspension.

Fig.2 shows an example of $K_1(\alpha)$ in the interval $0-3^\circ$ obtained for polystyrene spheres with average radius $7.85 \mu m$. The obtained scattering function was fitted to a Gaussian function: $A \exp(-\alpha \alpha^2)$.

The deduced parameters A and α are indicated in the figure and compared with those obtained from Mie theory.

Transmission measurements in a foggy atmosphere were also carried out, and the results analyzed to obtain the scattering function of the medium. Fig.3, referring to a measurement interval

of 330 minutes shows 3 curves, each giving the scattering function averaged in one of the intervals $0 - 1^\circ$, $1^\circ - 1.5^\circ$, $2^\circ - 2.5^\circ$.

The figure also shows the time evolution of the extinction coefficient σ of the medium. One can see that when σ increases (decreases) the peak value of $L(\theta)$ also increases (decreases), and the width of the forward peak decreases (increases). This effect was apparent during our series of measurements and is related to the evolution of the fog droplets size.

- (1) E. Battistelli, P. Brusaglioni, G. Zaccanti. "Separation and analysis of forward scattered power in laboratory measurements of the transmittance of light beam". In press (Applied Optics).
- (2) E. Battistelli, P. Brusaglioni, A. Ismaelli, G. Zaccanti. *Optica Acta*, 32, 717 (1985).
- (3) E. Battistelli, P. Brusaglioni, A. Ismaelli, G. Zaccanti. *J. Opt. Soc. Am. A*, 2, 903 (1985).
- (4) W.G. Tam, A. Zardecki. *Appl. Opt.* 21, 2405 (1982).

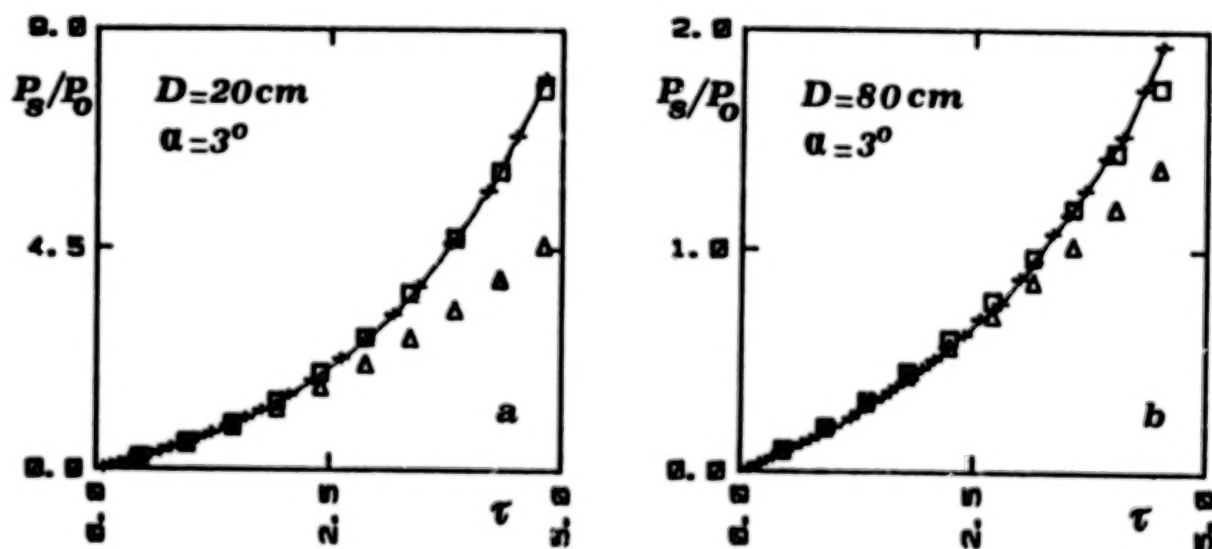


Fig. 1 - Comparison between calculated (squares) and measured (crosses connected by a continuous line) ratios P_s/P_0 between the received scattered power and the direct beam attenuated power. The ratios are plotted versus the optical depth τ . The triangular marks indicate the calculated summed contributions of the first two orders of scattering.

Spheres with average radius $7.85 \mu\text{m}$. Receiver's area radius 1 cm.

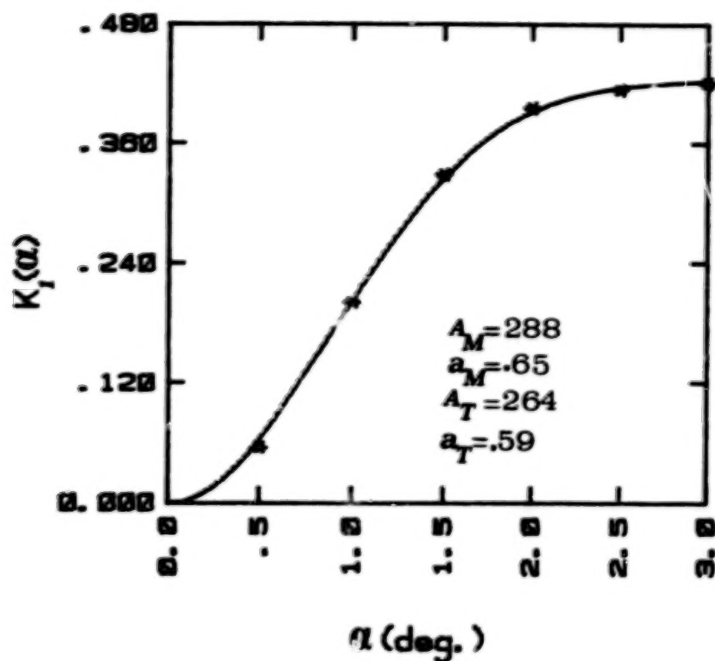


Fig. 2 - Stars: measured values of the coefficient $K_1(\alpha)$ of eq. 1. Continuous line: K_1 calculated by means of a Gaussian scattering function, $L(\vartheta) = A \exp(-a \vartheta^2)$. A_M , a_M : results of the Gaussian parameters best fitting the curve. A_T , a_T : parameters deduced by fitting to results of Mie theory.

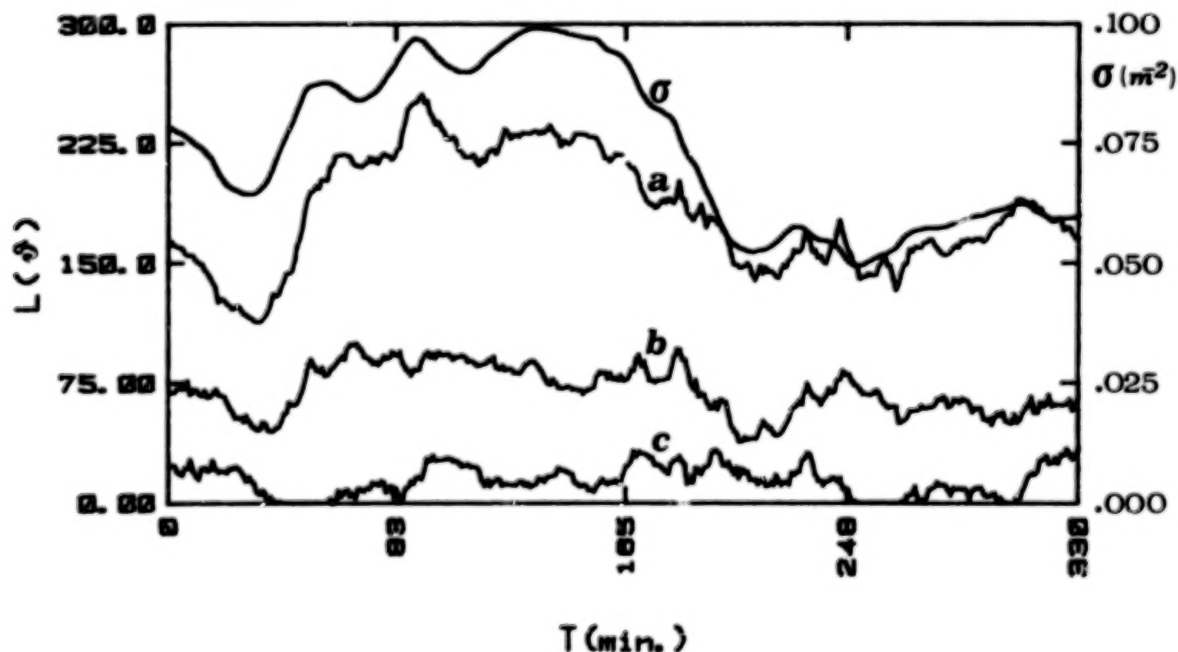


Fig. 3 - Fog measurements during a time interval of 330 minutes. The curves a, b, c show the average scattering function in the intervals: $0-1^\circ$, $1^\circ-1.5^\circ$, $2^\circ-2.5^\circ$ respectively, deduced by analyzing the received scattered power. Curve σ shows the measured extinction coefficient.

N87

10316

UNCLAS

MULTIPLE SCATTERING OF LASER BEAMS
IN DENSE HYDROSOLS

A. Zardecki, S.A.W. Gerstl, Theoretical Division
Wesley P. Unruh, International Technology Division
Grant H. Stokes, David M. Stupin and Norman E.
Elliott, Materials Science Technology Division
Los Alamos National Laboratory, Los Alamos, NM
87545, USA and J.A. Weinman, Dept. of Meteorology,
University of Wisconsin, Madison, WI 53706, USA.

The multiple scattering of laser beams is usually described within the framework of small-angle scattering theory. The purpose of this investigation is to study the validity of this approximation as well as improvements due to the incorporation of diffusion theory in the calculations.

We measured the intensity (power per unit area within the detector's field of view) of scattered laser light from an optically dense hydrosol and compared the measured intensities to those calculated from a multiple scattering theory. The nonabsorbing hydrosol was composed of $2.26 \pm 0.07 \mu\text{m}$ diameter polystyrene spheres suspended in essentially scatter-free water. We injected a HeNe laser beam perpendicular to and at the center of one face of a $10 \times 10 \times 10 \text{ cm}$ tank containing this suspension. The intensity of the scattered light at the exit face of the tank was measured to a relative accuracy of 1% with a photomultiplier tube (Fig. 1). The axis of the photomultiplier was parallel to the incident beam and the half-angle field of view (FOV) was either 0.357° or approximately 90° . In both cases the diameter of the detector aperture was $500 \mu\text{m}$. We measured the intensity at the exit face of the tank in $100 \mu\text{m}$ steps from the center of the emerging laser beam to a radial distance of 4 cm. We also recorded the shapes of the intensity distributions from both the exit face and side of the tank with a densitometric television camera (Fig. 2) and displayed them on a false-color image analyzer. An intensity distribution from the side of the tank is shown in Fig. 3, in which the laser beam enters from the left. Each color band, shown here in black and white, represents an equal range in the logarithm of the intensity.

An example of the comparison of the calculated and measured irradiances from the exit face of the tank is shown in Fig. 4 for the 90° half angle FOV detector and an optical depth of 5.02, as a function of radial distance from the beam center. In the figure both the measured irradiance and the calculated total scattering are normalized to unity at the beam center. The contributions to the total scattering from the attenuated laser beam, small-angle approximation and diffusion theory are separately displayed. They are labelled, respectively, unscattered, scattered and diffuse. The experimental data are shown by the open symbols which are considerably larger than the 1% errors in the measurement.

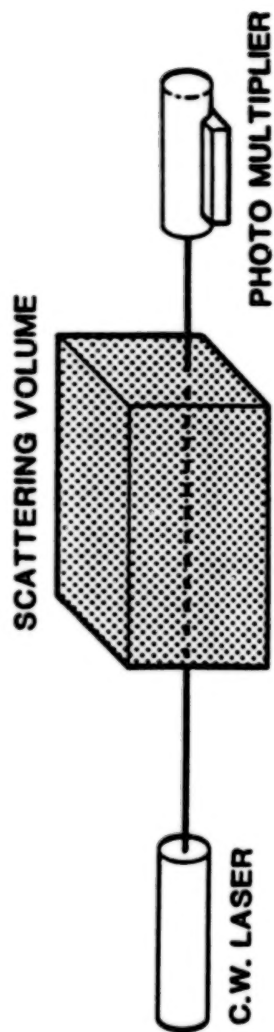


Fig. 1. Scattering geometry with the scanning photomultiplier tube detector.

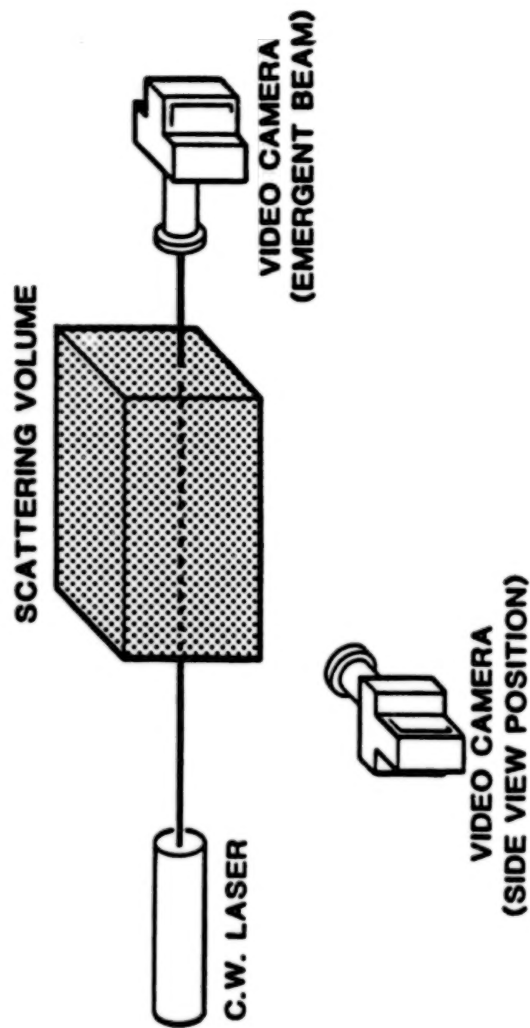


Fig. 2. Scattering geometry with the densitometric television system.

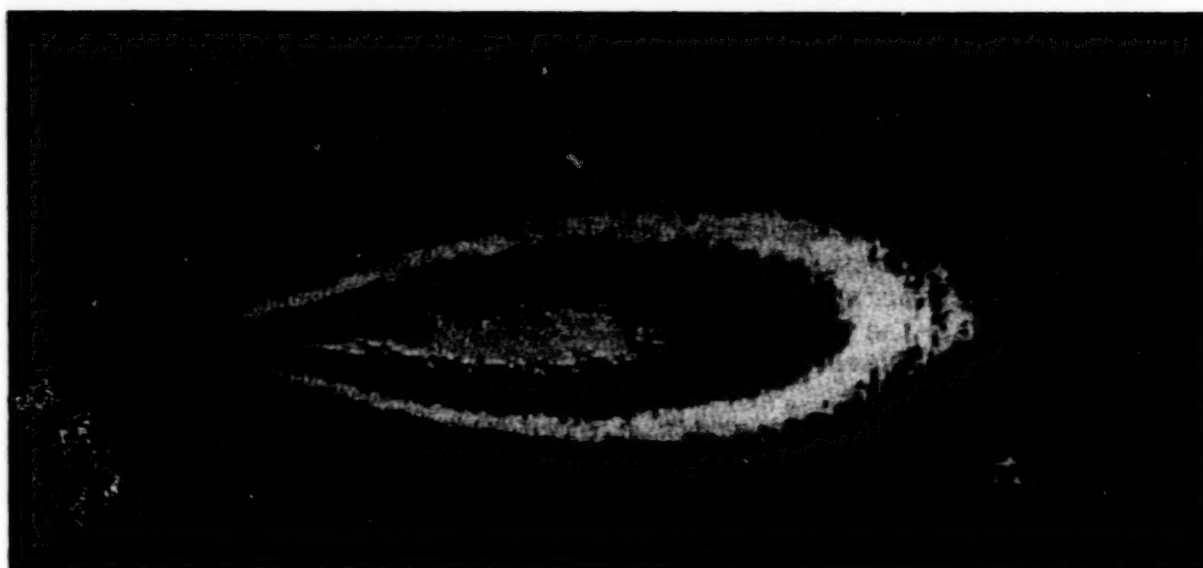


Fig. 3. Intensity contours measured from the side of the scattering tank. Equal ranges in the logarithm of the scattering intensity are plotted. The laser beam enters from the left in the figure.

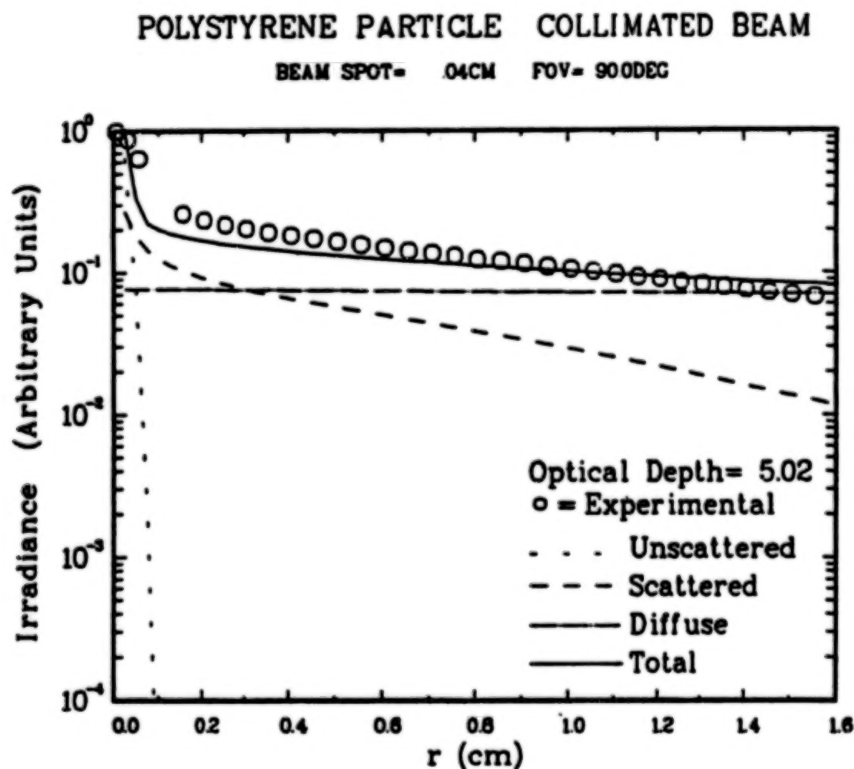


Fig. 4. A comparison between measured and calculated irradiances for the open FOV detector. The separate contributions to the calculated results are discussed in the text.

N87

10317

UNCLAS

TIME-RESOLVED LIDAR FLUOROSENSOR FOR SEA
POLLUTION DETECTION *A.Ferrario, P.L.Pizzolati, E.Zanzottera
CISE S.p.A., P.O.B.12081, 20134 Milano, Italy

As it has been demonstrated in another paper of this conference and earlier (1) by the researchers of JRC-Ispra, a contemporary time and spectral analysis of oil fluorescence is useful for the detection and the characterization of oil spills on the sea surface.

Nevertheless the fluorosensor lidars, which have been realized up to now, have only partial capability to perform this double analysis.

The main difficulties are the high resolution required (of the order of 1 nanosecond) and the complexity of the detection system for the recording of a two-dimensional matrix of data for each laser pulse.

CISE laboratories have been asked by JRC to design and construct an airborne system whose major specifications are:

- time range : 30 - 75 ns
- time resolution : 1 ns
- spectral range : 350 - 700 nm
- spectral resolution : 10 nm

In order to fulfill these requirements a short pulse UV laser source and a streak camera based detector have been designed (2).

Streak cameras are currently used for the analysis of fast optical phenomena, with resolution up to 1 ps; however, their two-dimensional pattern has been fully utilized in a few spectroscopic applications. In these cases the streak cathode is coupled to the output of a polychromator, so that one streak axis becomes the spectral axis, orthogonal to the time axis.

The laser source consists of a Nd-YAG laser, able to produce about 300 mJ at 1060 nm, in 3 ns, with 10 Hz repetition rate, in a single oscillator configuration. The emission at the third harmonic at 355 nm is expected to be about 50 mJ, in 2 ns.

The return signal consists of the water surface and bulk water direct backscattering, of the water Raman signal (at 400 nm) and of the fluorescence signal of oils and of suspended organic materials.

The signal is collected by a 30 cm telescope and sent, through a fiber optic, into a polychromator. The output light of the polychromator is a light strip whose width is equal to the telescope spot size and whose length depends on the polychromator dispersion and on the chosen spectral range.

* Work supported by JRC-Ispra Contract no.2613-84 12 AMISP I

The strip must have the same dimensions as the streak camera cathode. The streak camera time and spectral resolutions are mainly dependent on the ratio between the cathode size and the telescope spot size, which must be as small as possible. The telescope spot size can be reduced by reducing the laser spot size on the sea, which, in turn, can be reduced by using a small laser beam divergence (of the order of 0.1 mrad). The streak camera signal is then intensified and digitized by using a CCD read-out system. The digitized signal is sent into a computer as a matrix of about 40 spectral channels by 90 time channels and stored on Winchester disks for subsequent analysis.

The system should be ready for the first flight in summer 1987.

REFERENCES

- (1) P. Camagni et al. "Remote Fingerprinting of Oil Pollution by Means of Time Resolved Fluorosensing", 1984 World Conference on Remote Sensing, Bayreuth 8-11 October, 1984.
- (2) A. Ferrario, P. Pizzolati, E. Zanzottera "Feasibility Study for an airborne lidar fluorosensor", Final Report CISE 2563, March 1985.

N87

10318

UNCLAS

VARIATION OF THE URBAN NO₂ CONCENTRATION
DURING A GROUND INVERSION SITUATION

A. Sunesson, W. Wendt, and B. Galle*

Department of Physics, Lund Institute of Technology
P. O. Box 118, S-221 00 Lund, Sweden* Swedish Water and Air Pollution Research Institute
P. O. Box 5207, S-402 24 Göteborg, Sweden

In February 1985 the NO₂ concentration over Göteborg, a major Swedish city, was monitored during two inversion situations. The differential absorption technique was employed and the results show the build-up of the concentration.

A ground inversion is a situation that occurs mostly in cold weather. During a cloudfree night the temperature radiation from the surface to the air above may be sufficient to cool the ground. The surface will then be colder than the air above it, fig 1. If there, in addition, is no wind, the situation will be a stable one and no stirring of the air will occur. When the surface gets heated during daytime, the temperature gradient characteristic of the inversion will gradually vanish. An inversion layer is formed, under which the air is trapped. Finally, the layer is destroyed and convection stirs the system. During these stable conditions pollutants that are emitted will not be blown away or be removed by convection. They will remain around the sources or under the inversion layer. Very high concentrations resulting in extremely poor air quality will follow. The studies of NO₂ during these episodes can give information about the dangerous areas and sources that exist. Meteorological models can be tested. Dial measurements have previously been performed on NO₂, Ref 1.

In this experiment the laser beam was scanned horizontally over Göteborg. The results were presented as maps over the NO₂ concentration distribution, see for example fig 2. For security reasons the beam was not parallel to the ground, which gives a height gradient in some measurements. During the measurement period the NO₂ concentration build-up from the morning to the afternoon was monitored. Great concentration variations were seen. Later the mixing below the inversion layer, resulting in a more uniform, high concentration was seen. The breakdown of the inversion when stronger winds start was also seen.

Comparisons with a traditional point-measuring chemiluminescence instrument and an optical method, DOAS (Differential Optical Absorption Spectroscopy), were made (Ref 2). The results are discussed. Strong spatial concentration variations are shown by the lidar measurements. They are averaged out in the DOAS measurements. For a point-measuring system, the instrument must be very carefully placed since its location will strongly influence the values it gives.

References:

1. K. Fredriksson and H. M. Hertz, "Evaluation of the DIAL technique for studies on NO_2 using a mobile lidar system.", *Applied Optics* **23**, 1403 (1984).
2. B. Galle, A. Sunesson, L. Un  us, S. Wallin, and W. Wendt, "A comparison between different techniques for urban monitoring of NO_2 ", to be submitted to *Atmospheric Environment*.

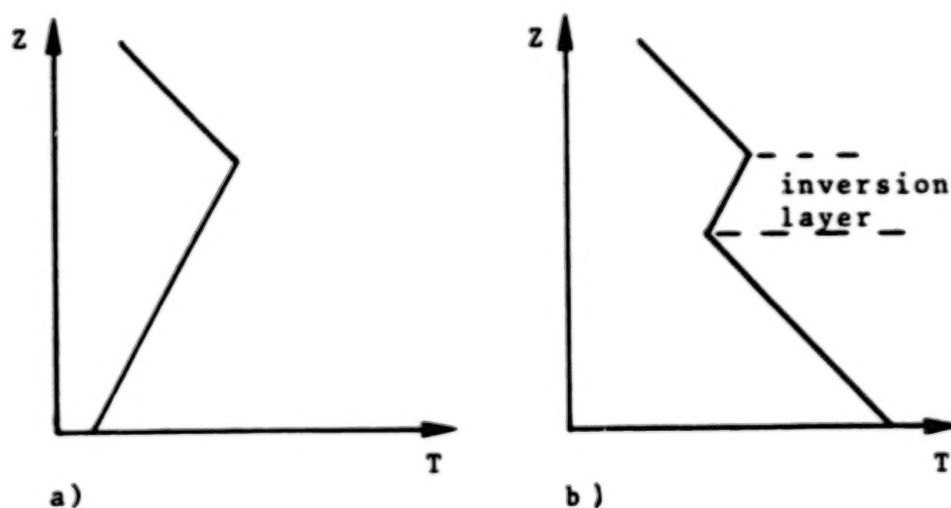


Figure 1. Schematic temperature profiles in an inversion
a) at the start
b) after the ground has been heated and an inversion layer has formed.

ORIGINAL PAGE IS
OF POOR QUALITY

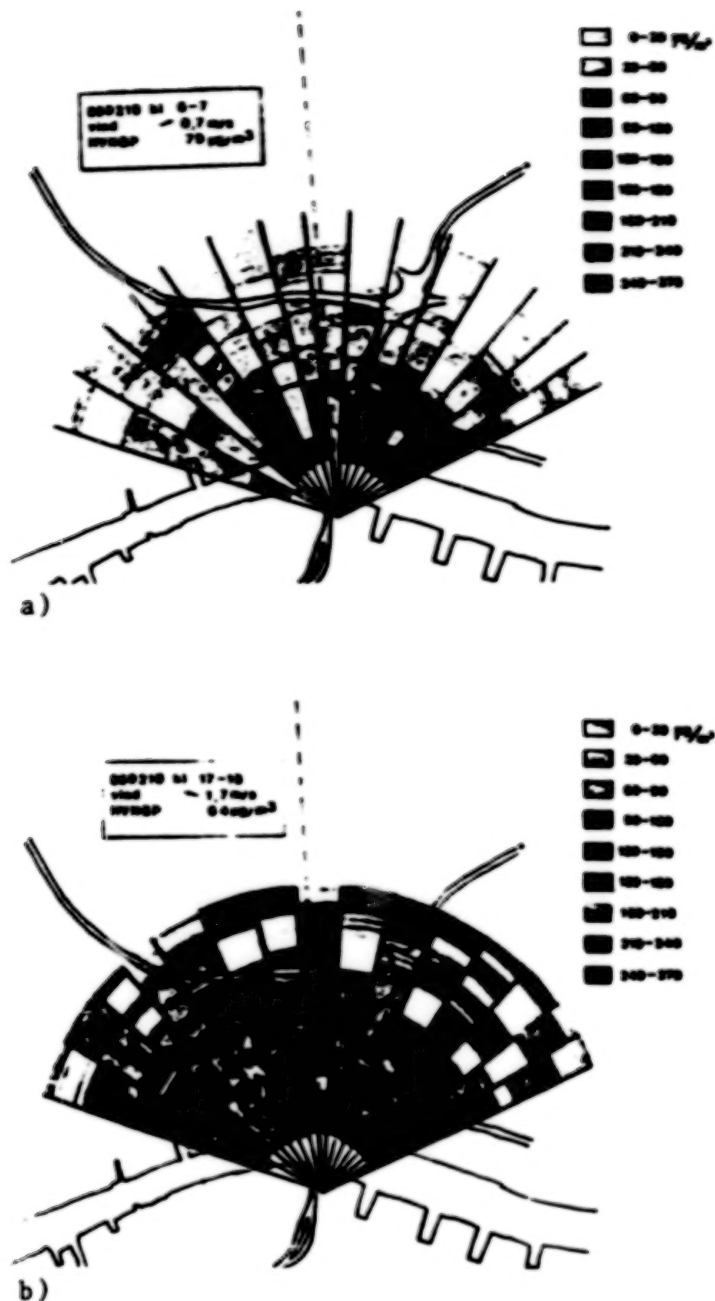


Figure 2. Horizontal mapping of the NO_2 concentration
a) early in the inversion
b) after some stirring of the system
The concentration map overlaps a map where
greater roads and a river are indicated.

N87

10319

UNCLAS

AN INTENSITY-MODULATED DUAL-WAVELENGTH He-Ne LASER

FOR REMOTE SENSING OF METHANE

Kiyoji UEHARA

Department of Physics, Faculty of Science and Technology
Keio University, Hiyoshi, Kohoku-ku, Yokohama 223, Japan

Fujitaka TAGUCHI

Research and Development Institute, Tokyo Gas Co., Ltd.
Shibaura, Minato-ku, Tokyo 105, Japan

1. Introduction

It is known that the $3.392\text{-}\mu\text{m}$ emission from a He-Ne laser is strongly absorbed by methane while the emission at a nearby wavelength, $3.391\text{ }\mu\text{m}$, is only weakly absorbed. The differential absorption at these wavelengths is expected to provide sensitive methods of detecting the presence of methane in the atmosphere(1). A straightforward way of the remote sensing is to direct a pair of lasers, one emitting at $3.391\text{ }\mu\text{m}$ and the other at $3.392\text{ }\mu\text{m}$, to the area being probed and to detect the backscattered radiation from topographical targets at the two wavelengths with two detectors. This method needs, however, not only a large volume of the whole system to include the two lasers, two detectors, two lock-in amplifiers and so on, but also precise alignment of the laser beams in order that they hit on the same target. Moreover, the laser output power has to be highly stabilized. One simplified method is to send two laser beams alternately using a chopper wheel and to monitor the returning radiation with a single detector coupled to a lock-in amplifier synchronized to the chopper. However, the laser-power stabilization and precise optical alignment are still essential.

In the present paper we describe a new type of dual-wavelength He-Ne laser in which the output power at each of the two wavelengths is modulated with equal amplitude and opposite phase to each other. This laser source can greatly simplify the setup and improve the sensitivity of the differential absorption measurements for the methane detection, as verified by a preliminary experiment. A simple scheme to measure the concentration of methane is also proposed.

2. Intensity-Modulated Dual-Wavelength He-Ne Laser

The structure of the intensity-modulated dual-wavelength He-Ne laser is shown in Fig.1. The principle of its operation has been reported elsewhere(2). Therefore, we mention it here only briefly. The alternate intensity modulation is accomplished by placing inside the laser cavity a cell filled with low pressure methane acting as a frequency-dependent loss to the $3.392\text{-}\mu\text{m}$ line and by vibrating one of the cavity mirrors. In Fig.2, if the cavity is tuned back and forth between A and B, the $3.391\text{-}\mu\text{m}$ emission increases when the $3.392\text{-}\mu\text{m}$ emission decreases and vice versa. The equal amplitudes and the opposite phases in the modulation of the two emissions are achieved by tuning the cavity automatically to a point which gives null intensity

modulation in the total output power at the modulation frequency. It has been shown both theoretically and experimentally that the modulation amplitude of the individual emissions thus available is appreciably affected by the crude manual change of the cavity length and that the maximum modulation is obtained repeatedly at every 5.7-mm change of the cavity length(2).

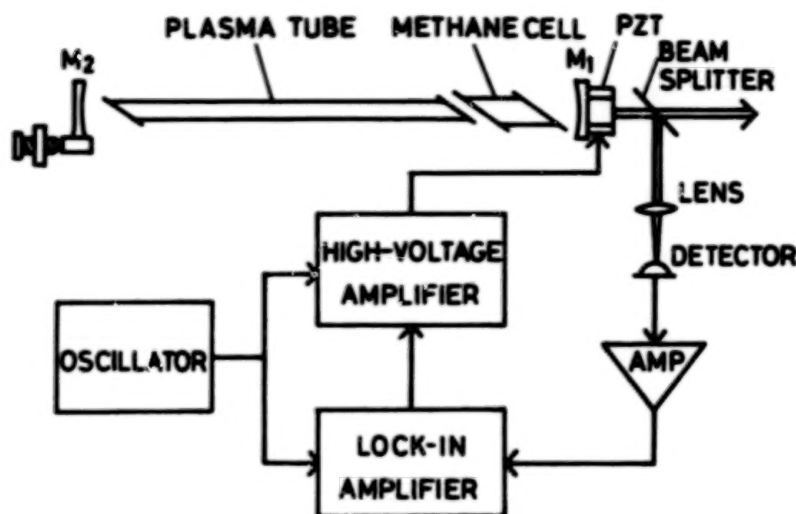


Fig.1 Schematic diagram of the intensity-modulated dual-wavelength He-Ne laser. Mirror M₂ is manually translatable by ± 3 mm. Cavity length: 68 cm; plasma length: 50 cm; methane cell length: 4.2 cm.

So far the modulation amplitude of up to 0.7 mW peak-to-peak at 1 kHz for individual emissions has been obtained from a plasma tube of 50-cm effective length while retaining the residual total-power modulation as low as 0.25 μ W peak-to-peak for 1 s of averaging. Therefore, in the ideal situation where the residual modulation in the total power is the dominant noise source, the minimum detectable methane density is estimated to be 0.02 ppm for a 10-m optical pathlength.

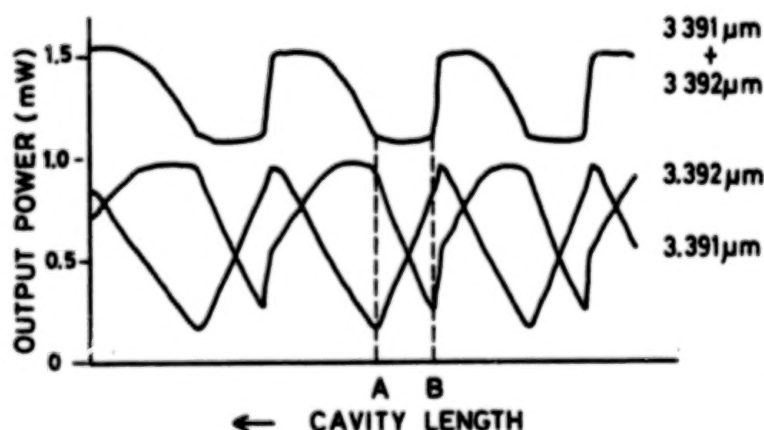


Fig.2 Variation of the output power of the individual emissions and the sum of both vs. cavity length. One cycle of the variation corresponds to a $\lambda/2$ change in the cavity length. Note that the total power is nearly equal at A and B while the individual emissions change appreciably.

3. Remote Differential Absorption Measurements

Fig.3 shows the schematic diagram of the DIAL system for methane sensing using the intensity-modulated dual-wavelength He-Ne laser. A laboratory simulation has been done using short-range targets and an absorption cell inserted between the mirrors M and M' instead of between M' and a target. The returning beam is collected by a spherical mirror of 10-cm diameter and focused by a lens onto an InSb detector cooled to 77 K. The detected signal is sent to a lock-in amplifier synchronized with the laser modulation frequency. Fig.4 shows an example of the signals recorded when a rough wood block as a target is placed at a distance of 5 m and a $\text{CH}_4\text{-N}_2$ mixture of 1% CH_4 concentration is introduced into the absorption cell 5 cm long and then evacuated. The signal averaging time is 3 s. Noting that the laser beam passes through the cell only once in this setup, the observed signal-to-noise ratio (~ 30) gives the minimum detectable concentration-pathlength product to be 8 ppm·m.

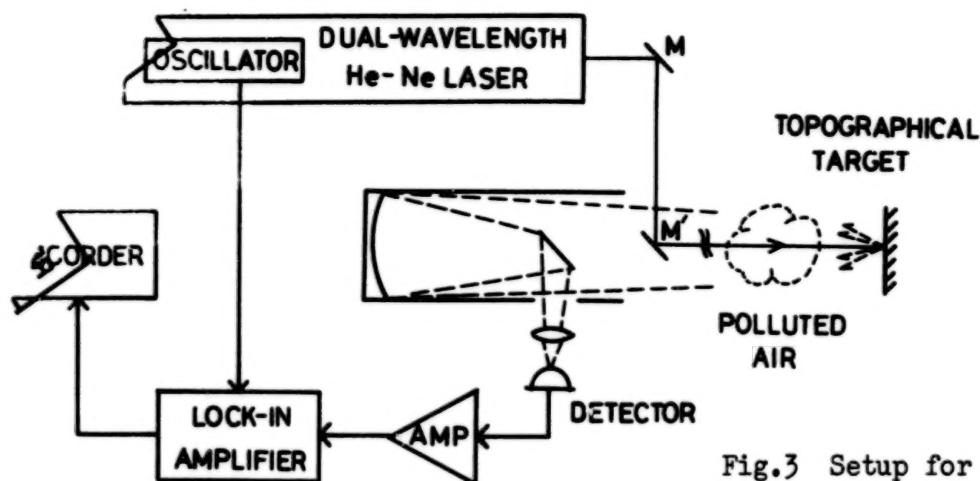


Fig.3 Setup for the remote differential absorption measurements.

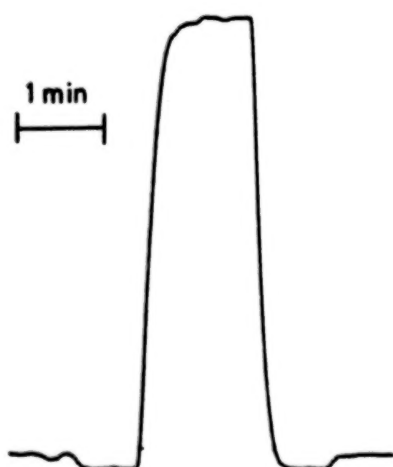


Fig.4 A recorded differential absorption signal. The effective concentration-pathlength of methane is 250 ppm·m.

4. Discussions

In this preliminary experiment the signal-to-noise ratio was limited by the amplifier noise. Therefore, a collecting mirror of 30-cm diameter will improve the sensitivity by a factor of ~ 10 .

The average concentration of methane can be determined by a calibration if the probe beam hits only some definite targets. When the targets cannot be specified as in a scannable system the quantitative measurement is possible by splitting the collected beam onto two detectors coupled to lock-in amplifiers. A methane cell is placed in front of one detector to monitor only the $3.391\text{-}\mu\text{m}$ radiation. The average methane concentration in the probed area is determined from the ratio of the signal strengths of the two lock-in amplifiers.

When a detector remote from the beam transmitter is usable to measure the transmittance through the probed area a very high sensitivity limited only by the laser noise is expected.

References

1. C. B. Moore: Appl. Opt. 4, 252(1965).
2. K. Uehara: Appl. Phys. B 38, 37(1985).

N87

10320

UNCLAS

Lidar Mapping of a Mixture of Aerosol Concentrations in a
Varying Atmosphere

Moshe Kleiman, Smadar Egert and Ariel Cohen^{*}
Israel Institute for Biological Research
Ness - Ziona, Israel

^{*}Department of Atmospheric Sciences, The Hebrew
University of Jerusalem, Israel

Abstract

In several recent applications dealing with lidar measurement of atmospheric pollution (see, for example, Cahen, 1984), two basic assumptions are made:

- 1) The investigated aerosol layer is the only particulate material within the scattering volume
- 2) The contribution of the gaseous atmosphere to the lidar backscattering signals can be estimated and deducted from the total backscattering measurements

It is useful to note that the second assumption is of less relevance when the turbidity ratio is relatively high, i.e. when the contribution to the scattered light by the Rayleigh molecules is negligible compared to the backscattering by the aerosol particles.

In tropospheric measurements the molecular scattering against aerosol can be neglected in many practical applications. A method which permits an unknown but considerable contribution of the molecular scattering in the stratosphere (or in the troposphere when applicable), was described by Cohen and Kleiman (1978).

However, in several realistic cases, both assumptions may introduce inaccuracies to the analysis. This is due to the fact that lidar measurements of plume concentrations and number densities are performed in the

vicinity of other sources of particulate pollutions. Such sources can originate from nearby natural dusty environment or urbanic artificial pollution forming a varying background which is constantly present in the investigated atmosphere. The situation is even more complicated when more than one source of different background aerosols are present (more than one source includes the case of low turbidity values, when the molecular contribution has to be taken into account separately).

In the method discussed a generalized method which allows the elimination of the above mentioned assumptions was developed using multi-parameter lidar measurements. The different parameters can be several wavelengths, polarization properties of the scattered light, scattering angles, or any combination of these parameters.

The basic requirements of the method are as follows:

- a. The background aerosol, although varying in concentration, has a known (experimentally or theoretically) dependence on the changing parameter, i.e. if the background is the molecular atmosphere the only required coefficient for the method would be λ^{-4} behavior when changing the wavelength. The knowledge of the air density is not required.
- b. When measuring echoes from an atmospheric volume in two consecutive time steps and/or two adjacent distances, the background aerosol, as well as the investigated plume, is allowed to change in number densities. However, it is assumed that it retains the same optical coefficient per unit mass (in particular - the backscattering coefficient).

Taking into consideration the fact that the separation of two adjacent lidar echoes is only limited by the spatial resolution of the lidar pulse: ΔR (being typically of the order of a few meters), this requirement is met in most practical applications.

19801-784

The detailed derivations will be presented and discussed.

References

- Cahen C. (1984): Lidar Measurements of Atmospheric Pollution. Proceedings of the 12th International Lidar Conference (ILRC), Aix en Provence, France, p. 225.
- Cohen, A., Kleiman M., (1978): On the Measurement of Atmospheric Aerosol Concentration by Lidar. J. Appl. Meteor. 17, 234-235.

N87

10321

UNCLAS

THREE ATMOSPHERIC DISPERSION EXPERIMENTS
INVOLVING OIL FOG PLUMES MEASURED BY LIDAR

W.L. Eberhard, G.T. McNice, and S.W. Troxel
National Oceanic and Atmospheric Administration
Wave Propagation Laboratory
Boulder, Colorado, U.S.A.

Introduction

The Wave Propagation Laboratory (WPL) participated with the U.S. Environmental Protection Agency (EPA) in a series of experiments with the goal of developing and validating dispersion models that perform substantially better than models currently available. We briefly describe the lidar system deployed and the data processing procedures used in these experiments. Highlights are presented of conclusions drawn thus far from the lidar data.

Equipment and Processing

The lidar was a substantially upgraded version of the one operated at the Cinder Cone Butte experiment (Eberhard and McNice, 1982; Eberhard, 1983). The laser for the experiments described here was a frequency-doubled Nd:YAG laser with a pulse rate of 10 s^{-1} . The data acquisition system was modernized to handle the higher pulse rate and to monitor system operation more fully. Automatic scan control by computer was implemented; operators can modify the scan instructions without interrupting data acquisition.

Computer processing programs to refine the plume data were also substantially improved over those used for the Cinder Cone Butte experiment. It was necessary to compensate the data for the attenuation by the plume and surrounding ambient air, to subtract out the backscatter from the ambient air, and to edit spurious signals such as those from the ground or vegetation. Earlier we performed these tasks through interactive graphics on a pulse-by-pulse basis; for these three experiments the interaction was with an entire scan, which was much more efficient. Other software interpolated the tracer distributions from lidar coordinates to rectangular grids that are more conducive to dispersion analysis. Concentration profiles and other plume parameters were calculated for both individual and averaged scans. The processing computer archived the results on digital magnetic tape, printed tables, and hardcopy graphs to make analysis as convenient as possible.

The tracer plume consisted of a polydispersion of oil drops with a mode diameter of several micrometers. The lidar performed a repeating sequence of vertical scans to obtain cross sections of the plume at typically five distances

12801-784

The detailed derivations will be presented and discussed.

References

- Cahen C. (1984): Lidar Measurements of Atmospheric Pollution. Proceedings of the 12th International Lidar Conference (ILRC), Aix en Provence, France, p. 225.
- Cohen, A., Kleiman M., (1978): On the Measurement of Atmospheric Aerosol Concentration by Lidar. J. Appl. Meteor. 17, 234-235.

downwind of release. Tracer concentrations were inferred from the elastic backscatter. We found that the backscatter coefficient of the oil fog was not fully conserved with distance downwind. We attribute the decline mainly to partial evaporation of the drops.

Hogback Ridge Experiment

The 1982 plume diffusion experiment at The Hogback, a ridge near Farmington, New Mexico, was the second field study in the Complex Terrain Model Development (CTMD) project of the EPA. The main objective was to study impaction of elevated plumes on a ridge during stable conditions. This experiment was similar to the one at Cinder Cone Butte (Eberhard and McNice, 1982), where the topographical "target" was a hill. Oil fog at The Hogback was released from a 150-m meteorological tower or a crane upwind of the ridge. The lidar scanned in vertical planes almost parallel with the crest of the ridge.

Important information from the lidar includes the small but significant amount of plume rise that was caused by the heat from the oil fogger. The lidar data reveal whether the released plume passed over the ridge, impacted its side, or was embedded in the blocked region. The vertical deflection of the plume relative to the surface is an important factor in modeling surface concentrations. Strimaitis *et al.* (1985) were able to substantiate the importance of the plume's position with respect to the height of the dividing streamline. Flow above the dividing streamline has sufficient kinetic energy to overcome the density gradient and pass above the crest of the hill or ridge. Flow below the dividing streamline must pass around the side of a hill or suffer blocking in front of long ridge. Strimaitis *et al.* found that the degree of stratification above the dividing streamline had a secondary but significant effect on the plume's standoff distance above the crest of the ridge, but accounting for the amount of wind shear in the same zone did not improve the prediction.

Processed data from this experiment are archived with EPA, and a technical report on the lidar data is under preparation. This data set includes 3079 individual and 304 averaged cross sections that span 84 hour-long analysis periods.

Tracy Power Plant Experiment

A 1984 experiment at Tracy Power Plant was the culminating field study in the CTMD project. The plant, which is located beside the Truckee River east of Reno, Nevada, is surrounded by hills and mountains. Drainage winds were expected frequently to carry a plume from the stack toward higher terrain near a bend in the river. The stack exhaust

was seeded with oil fog because the plume from the gas-fired plant is essentially free of particulates. Lidar scans were designed to monitor plume rise, to measure the plume's behavior and growth as it approached terrain, and to observe the initial encounter of the plume with the terrain.

The algorithm for vertical plume growth that was developed from the Cinder Cone Butte data substantially over-predicted the observed growth of the plant's plume. Since the plume at Cinder Cone Butte was within or near the top of the surface-based mixed layer, whereas the plant's plume was usually embedded in flow that was completely decoupled from the surface, the algorithm may not be valid in the latter setting. Work will continue on this and other problems that the lidar data are expected to help solve.

The lidar data from this experiment that is archived at EPA contains 4507 individual and 433 averaged cross sections that span 84 experimental hours. A technical report on the lidar data is in preparation.

CONDORS

The CONDORS (Convective Dispersion Observed with Remote Sensors) experiment took place during 1982 and 1983 at the Boulder Atmospheric Observatory (BAO). Eberhard et al. (1985) described the experiment and presented some preliminary results. The goal was to determine the validity of the tank model predictions of Willis and Deardorff (e.g., 1981). Under highly convective conditions, when buoyancy dominates shear as a source of turbulence, they found that the vertical profile of a tracer deviated markedly from the form predicted by a Gaussian model. For instance, their locus of maximum concentrations from a nonbuoyant, elevated release descended to the surface instead of remaining level at source height.

The 300-m meteorological tower at the BAO was the platform for elevated releases of oil fog, but several surface releases were also performed. The lidar monitored the height of the haze to infer the depth of the mixed layer, which is a critical scaling parameter in convective conditions. The shape of the vertical profiles of oil fog resembled the tank results in a general way, but some of the differences observed may prove to be significant. On the basis of an empirical calibration of the lidar-oil tracer system, the measured oil fog concentrations near the surface were in good agreement with surface samples of a gaseous tracer that was released from the same point as the oil fog. "Chaff" (aluminized filaments), which was tracked by a 3-cm-wavelength Doppler radar, was another important tracer used during CONDORS.

The tracer and meteorological data from CONDORS are comprehensive and of high quality. A data report is near completion, and analysis of results are in progress. They

will include 911 individual lidar scans that have been combined into 81 averaged cross sections; these data span a total of 10 experimental hours.

Summary

The WPL lidar was a key component of the Hogback, Tracy, and CONDORS plume dispersion experiments. The results are important for air pollution modeling because they address situations in which high concentrations of a pollutant can occur at the surface. We were pleased with the dependability of the lidar, which performed satisfactorily for about 95% of the scheduled operating time. The lidar acquired a voluminous amount of data, from which about 2/3 was selected for reduction. Processed lidar data have been archived and will be made available on request. Some of the scientific results are already available; additional interpretation of the lidar data is in progress.

Acknowledgement

The U.S. Environmental Protection Agency provided a major part of the funds for these projects. This abstract has not been subjected to EPA review and does not necessarily reflect the views or policies of EPA.

References

Eberhard, W. L., 1983: Eye-safe tracking of oil fog plumes by UV lidar. Appl. Opt., 22, 2282-2285.

Eberhard, W. L., and G. T. McNice, 1982: Plume dispersion tracked by UV lidar. Eleventh International Laser Radar Conference, NASA Conference Publication 2228, 145-148.

Eberhard, W. L., W. R. Moninger, T. Uttal, S. W. Troxel, J. E. Gaynor, and G. A. Briggs, 1985: Field measurements in three dimensions of plume dispersion in the highly convective boundary layer. Preprint Vol., Seventh Symposium on Turbulence and Diffusion, Amer. Meteorol. Soc., Boston, 115-118.

Strimaitis, D. G., D. C. DiCristofaro, R. J. Yamartino, and W. L. Eberhard, 1985: Modeling stratified flow over the crest of a two-dimensional hill: Field evaluation of the "cut-off" hill approach. Preprint Vol., Seventh Symposium on Turbulence and Diffusion, Amer. Meteorol. Soc., Boston, 300-303.

Willis, G. E., and J. W. Deardorff, 1981: A laboratory study of dispersion from a source in the middle of the convectively mixed layer. Atmos. Environ., 15, 109-117.

N87

10322

UNCLAS

FEASIBILITY EXPERIMENTS ON TIME-RESOLVED FLUOROSENSING APPLIED TO OIL
SLICKS

P. Camagni*, G. Colombo*, C. Koechler*, A. Pedrini*,
N. Omenetto°, G. Rossi°

Electronics(*) and Chemistry(°) Division
JRC - Ispra, Italy

The introduction of time-resolved observations can provide a very penetrating tool in the practice of laser fluorosensing (1). A general advantage is the possibility of isolating the signal from definite volumes within an extended fluorescing target, which may help to resolve between time-distributed and range-distributed contributions (surface vs. volume effects) (2). A specific advantage consists in giving access to the measurement of decay times, thus adding a further bonus to the spectral fingerprinting of complex fluorophores.

An experimental exploitation of these concepts was undertaken by us some time ago (3) in order to test possible applications to the case of oil polluted waters. Fluorescence studies and simulation experiments were devoted, in this phase, to assess the specific information content which can be gained from combined measurements of spectral and temporal response, as well as the technological limits to be encountered in the field practice.

Concerning the first point, our investigations have demonstrated a relevance of multi-spectral, time resolved analysis for oil fingerprinting. By comparative studies on a variety of crude oils and their most significant fractions, it was found that the process of time decay in a composite oil is characterized by a few steps, which are associated with specific components in the medium-light range (e.g., kerosene and gasoil). The average decay times of these "pure" fractions are markedly differentiated as to absolute values and spectral spread; as a consequence, the corresponding parameters in the resultant crude are quite sensitive to the particular mixture of these components. Measurements of the time response give then a finer discrimination between oil classes, depending on the relative content of certain fractions (see Fig. 1).

Experiments have been pursued with an improved fluorosensor facility, in order to test the application of time-resolved fluorosensing to remote samples on water. The apparatus is now based on excitation by the 3rd harmonic line of a Nd:YAG Laser, with pulse width of about 4 nanoseconds. Fast spectral analysis of the fluorescent return is carried out as before (see Ref. 2) by an OMA- multichannel analyzer with a gatable acquisition window of less than 5 nanoseconds. By accumulation of repetitive shots at

increasing delay, observation of spectral emission decay is obtained.

Figs. 2 and 3 show the results acquired from two representative crude oils. In each case, the semilog plots reproduce the time response of emission, as measured in fixed contiguous regions covering the entire emission spectrum from u.v. to the red. The visible differentiation between the two oils is well backed by the numerical inserts, showing systematic differences of $\tau(\lambda)$ and $\Delta\tau/\Delta\lambda$ for the two cases, which are in fair agreement with previous data obtained from laboratory measurements (compare with the results in Fig. 1 for the same samples). This is achieved at comfortable levels of detection ranging from $\sim 10^4$ to $\sim 10^3$ photon counts/shot/nanosecond, which should ensure good statistics over at least 3 lifetimes of any particular decay compatible with our resolution, even in view of finer wavelength subdivision.

Systematic collection of time-resolved signatures has been started on a variety of commercial oils. Results from a group of four typical crudes have been subjected to preliminary elaboration, in order to assess the elements for new time/spectral fingerprinting criteria. The use of regression and correlation techniques seems particularly appropriate to a multispectral analysis of time-decay, for in this case one expects that only a few parameters will enter the picture, namely weight and decay-time (at given λ) of one or two dominating components. The situation is quite different from that encountered in correlating full emission spectra, where the large number of emission and absorption unknowns, as well as the influence of the matrix, tend to obscure the role of deterministic correlations.

The successful performance of time-resolved fluorosensing, as obtained here, convinced us that this technique can be up-graded and fully exploited with technologically available means. These are: i) use of laser excitation in the range of 50 ~ 100 m J, with pulse-width of a few nanoseconds; ii) adoption of integrated multispectral detectors, providing a sensitive and truly simultaneous scanning of whole spectra over the time axis, at nanoseconds speeds. Recent development of streak-camera systems has led us to study the specifications for a compact field fluorosensor based on the above solutions. Construction of this apparatus is presently under way by terms of an external contract.

- 1) see for instance: R.M. MEASURES, W.R. HOUSTON, D.G. and STEPHENSON: Optical Eng., Vol. 13, 6, 494 (1974)
R.M. MEASURES, J. GARLICK, W.R. HOUSTON and D.G. STEPHENSON: Canad. Journ. Rem. Sens., Vol. 1, 2, 95 (1975)

- 2) P. CAMAGNI, G. COLOMBO, C. KOECHLER, N. OMENETTO, A. PEDRINI, G. ROSSI: Procs. of "Telerilevamento dei Mari Italiani", I.R.O.E., Florence, Oct. 1985 (to be published).
- 3) P. CAMAGNI, C. KOECHLER, N. OMENETTO, A. PEDRINI, G. ROSSI and G. TASSONE: Procs. 1984 World Conference on Remote Sensing, Bayreuth-October 1984 (K.M. Morgan, Ed.; University of Bayreuth and Texas Christian University).

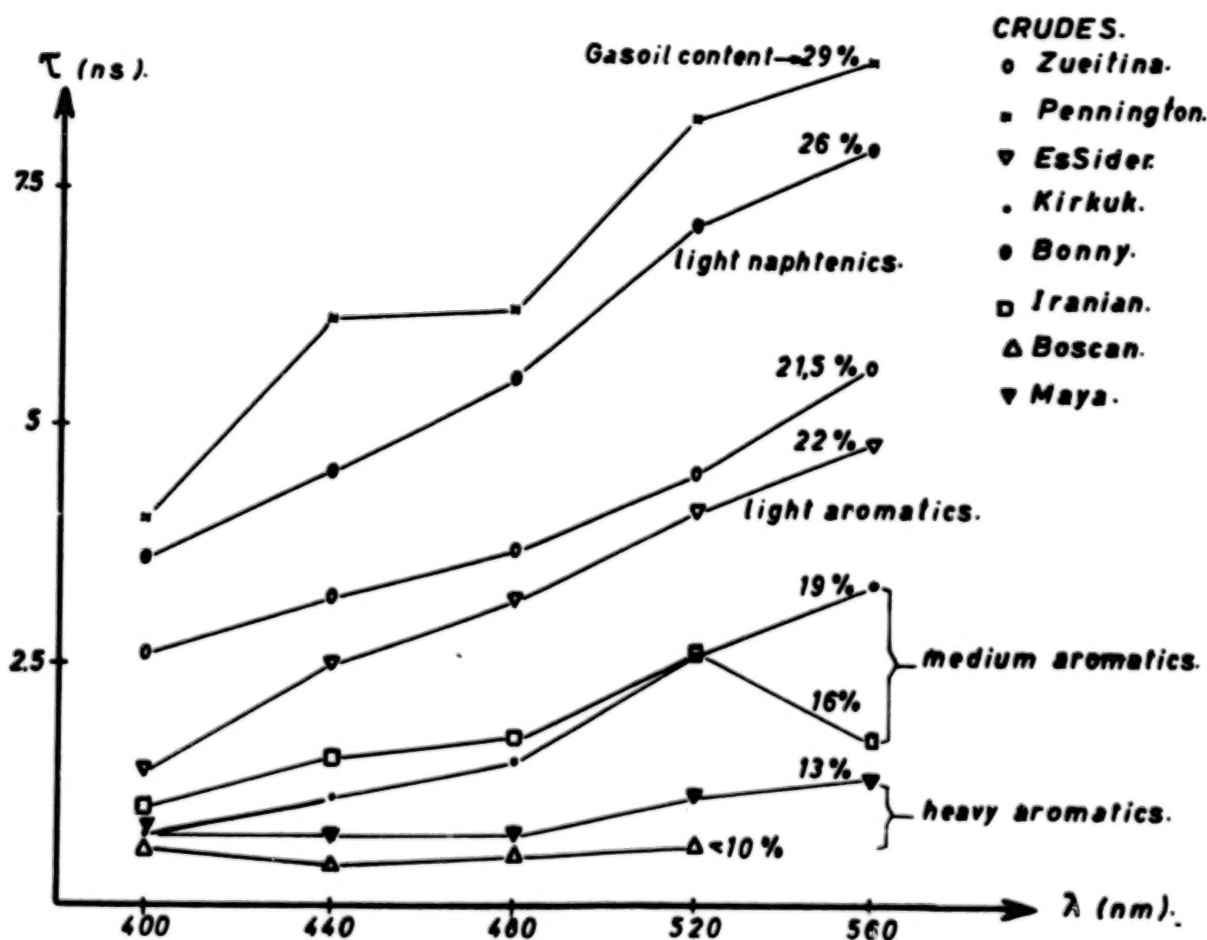


Figure 1): Distribution of fluorescent decay times vs. emission wavelength for various crude oils ($\lambda_{exc} = 337$ nm). Numerical inserts indicate weight percent of gasoil.

- 2) P. CAMAGNI, G. COLOMBO, C. KOECHLER, N. OMENETTO, A. PEDRINI, G. ROSSI: Procs. of "Telerilevamento dei Mari Italiani", I.R.O.E., Florence, Oct. 1985 (to be published).
- 3) P. CAMAGNI, C. KOECHLER, N. OMENETTO, A. PEDRINI, G. ROSSI and G. TASSONE: Procs. 1984 World Conference on Remote Sensing, Bayreuth-October 1984 (K.M. Morgan, Ed.; University of Bayreuth and Texas Christian University).

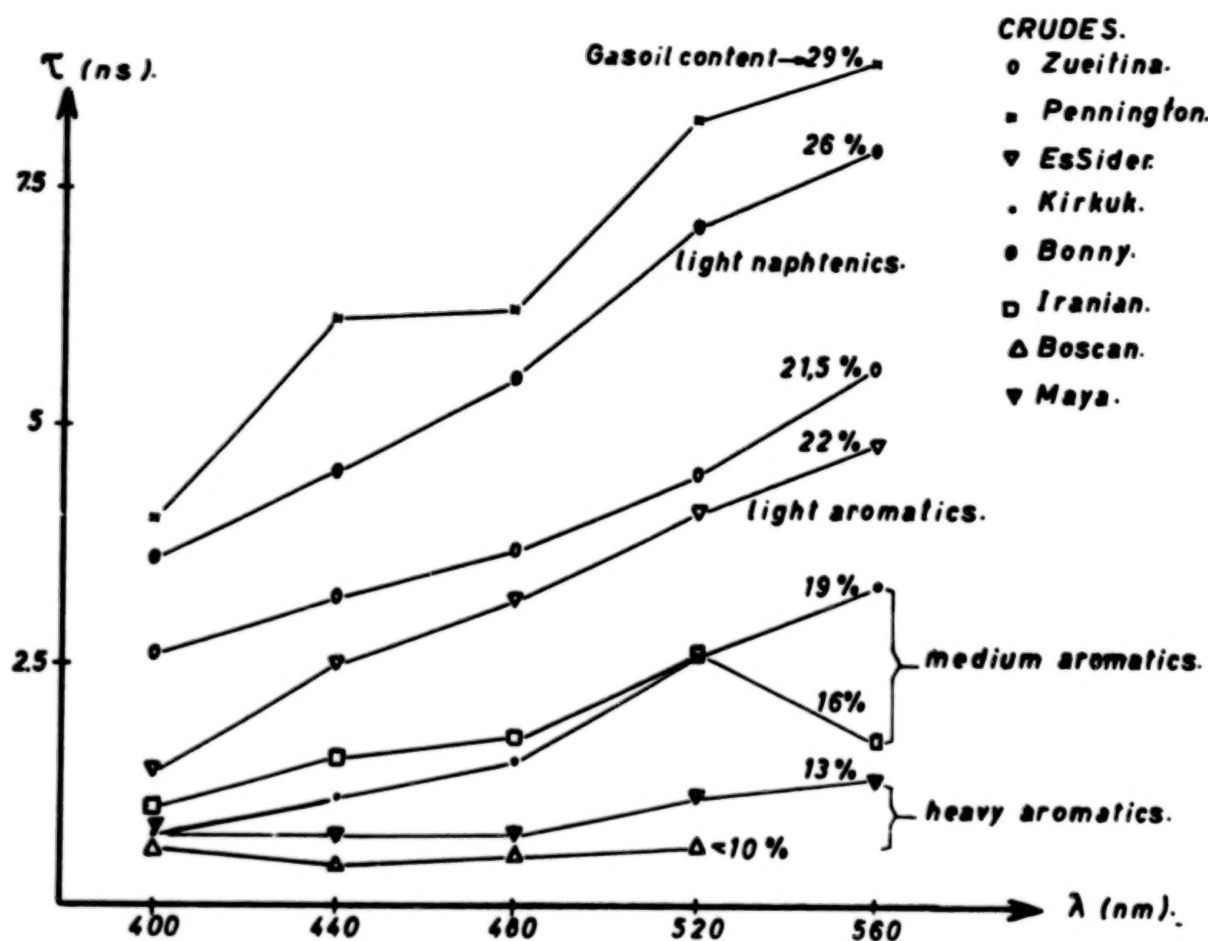


Figure 1): Distribution of fluorescent decay times vs. emission wavelength for various crude oils ($\lambda_{exc} = 337$ nm). Numerical inserts indicate weight percent of gasoil.

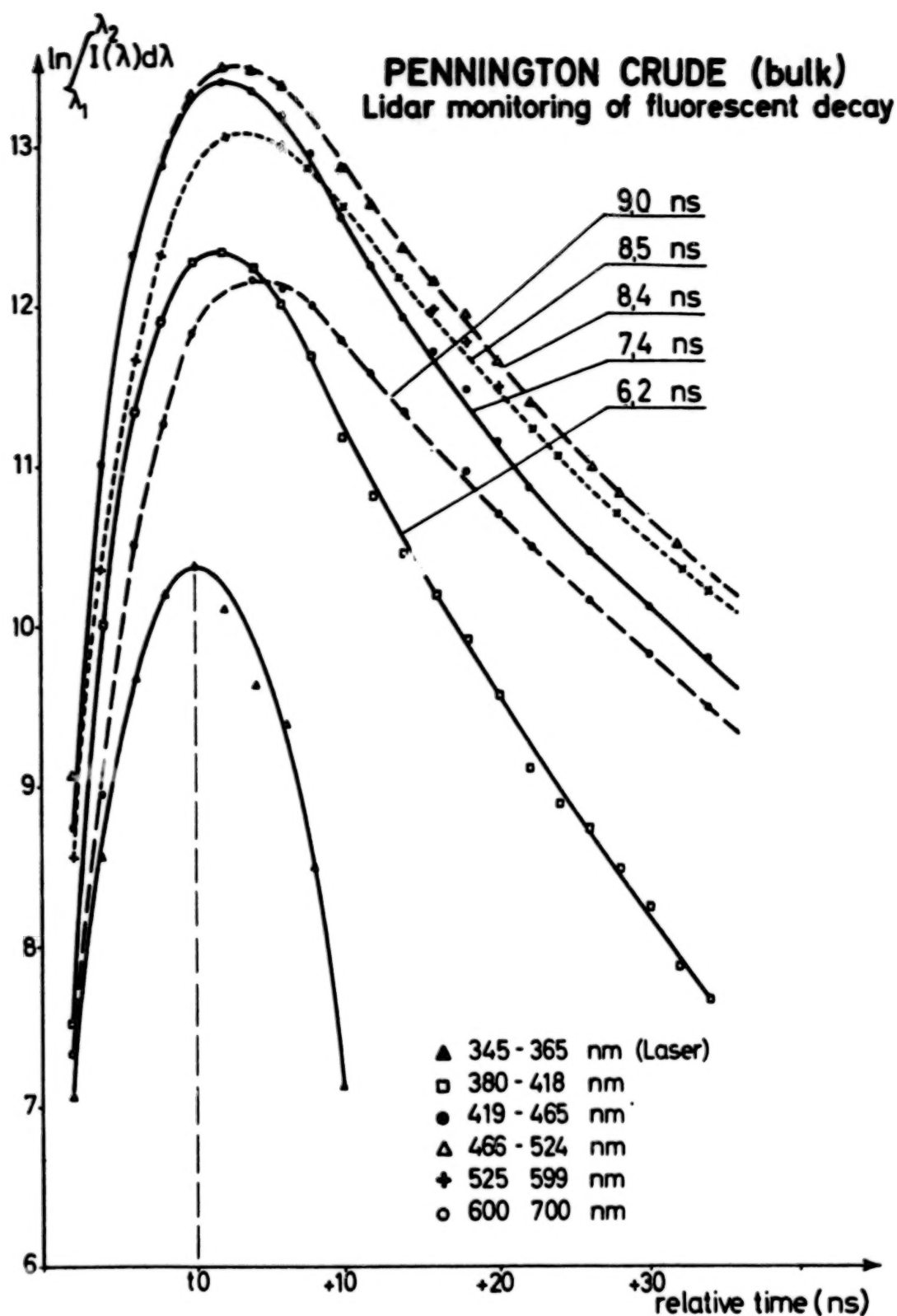


Figure 2): Decay of fluorescent emission (photon counts) in different spectral bands of a PENNINGTON light crude (200μ oil film on water; monitoring distance ~ 100 m; $\lambda_{exc.} = 355$ nm; 10 laser shots per point).

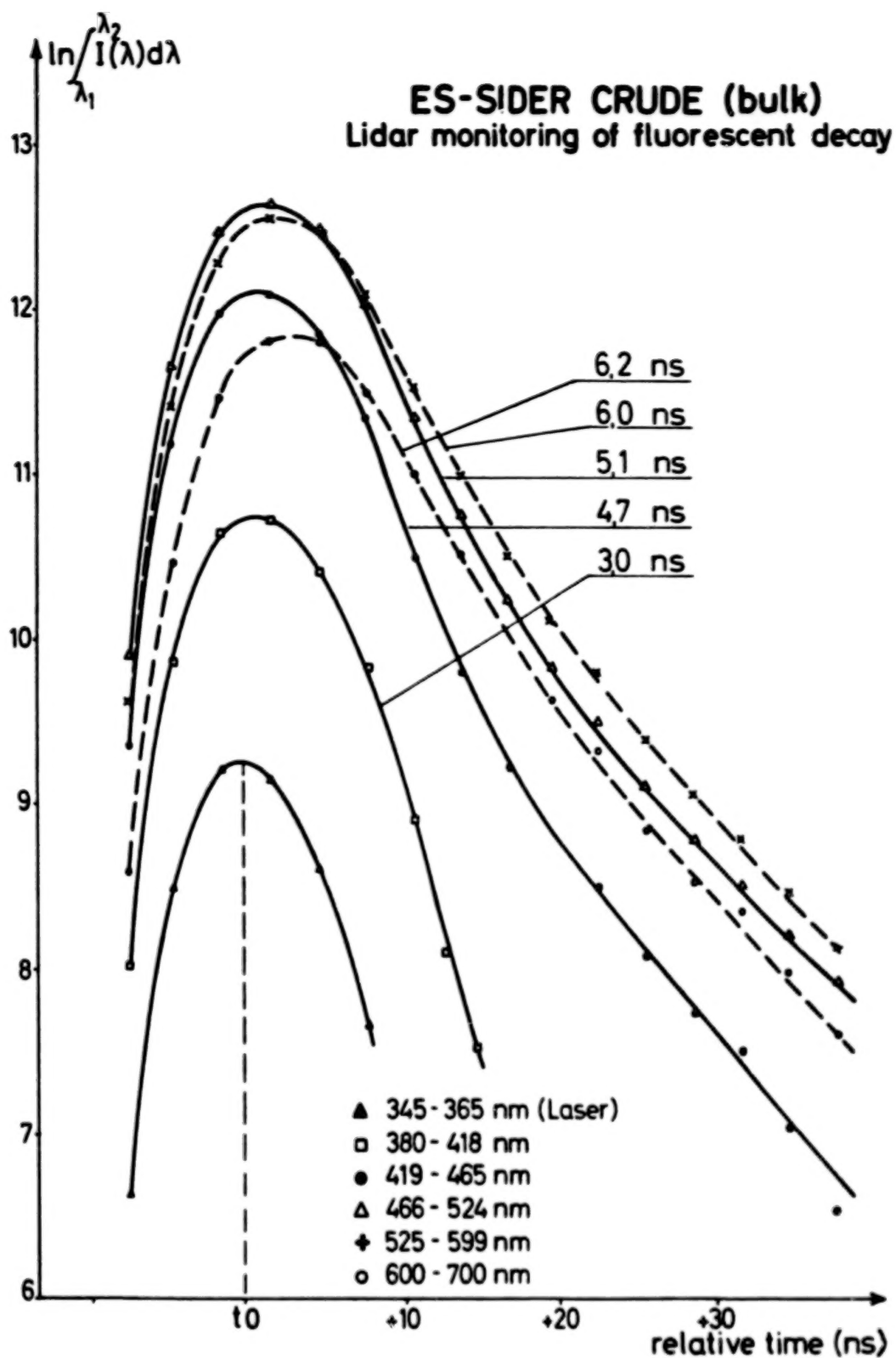


Figure 3): Same as 2 for an ES-SIDER medium-heavy crude.

N87

10323

UNCLAS

ROTATIONALLY RESOLVED COLLISIONAL TRANSFER RATES IN OH

Thomas J. McGee, James Butler¹, John Burris and William Heaps
NASA Goddard Space Flight Center Laboratory for Atmospheres
Greenbelt, Maryland U.S.A.

¹Sciences Applications Research, 4400 Forbes Boulevard
Lanham, Maryland U.S.A.

Fluorescence lidar measurements of the hydroxyl radical require detailed information concerning collision-induced processes in order to deduce the radical number density from a lidar return. The GSFC OH lidar currently utilizes a broadband detector which precludes the necessity of fully understanding collisional redistribution of rotational energy within the excited state. Numerous advantages result however from the inclusion of a detector with a bandpass only slightly larger than the Doppler width of a rotational line. This however places more stringent requirements on the spectroscopy. We have accordingly made measurements of rotationally resolved quenching rates for collisions with O₂, N₂, and H₂O. We have also measured rotational transfer rates for the same colliders.

Quenching rates have been measured using a Nd-YAG pumped Rh6G dye laser doubled into the UV. The measured linewidth at 2820 Å was 0.009 Å. Emission from the excited state was filtered through a 0.6 m monochromator with a 1 Å bandpass. This insured that only the laser-excited rotational level was observed. The output of the PMT was fed into a transient digitizer with a 10 nsec bin size. The OH radicals were produced in a flow system by the reaction:



The OH lifetimes were measured as a function of pressure of quenching gas at total pressures of between 50 and 250 microns. Quenching rate constants were measured from the slope of Stern-Volmer plots of the lifetimes data.

Rotational transfer rates have been measured by recording the emission spectrum on an intensified diode array and integrating over 10,000 laser shots. Spectra are recorded as a function of quencher pressure and rates are extracted from an analysis of the growth rate of emission from collisionally populated rotational levels.

N87

10324

UNCLAS

TIME-DOMAIN SENSITIVITY ENHANCEMENT IN PULSED Pb-TDL GAS MONITORS

R.Koga, M.Kosaka, and H.Sano *

Department of Electronics, Okayama University,
Okayama 700, JAPAN

*Faculty of Engineering, Fukuyama University,
Fukuyama 729-02, JAPAN

INTRODUCTION

A Pb-salt tunable diode laser (TDL) has found many applications in the field of atmospheric gas analysis. Its continuous tunability and fine spectral purity in the mid infrared region are outstanding from other lasers. The only shortcoming is that it requires cryogenic operating temperature, though it is improved year by year towards the room-temperature operation. Nevertheless, a repeated pulse operation of Pb salt diode lasers is possible with a thermoelectric cooling device, which allows an instrument a portable geometry disusing a heavy, bulky and power-consuming mechanical refrigerator.

A derivative spectrometry system has been exploiting the quick tunability of Pb-salt diode lasers, though they are cw operated with refrigerator or liquid nitrogen so far. A new system for derivative spectrometry with a pulsed diode laser will extend its field of applications because of reduced weights and size of measuring instruments.

Taylor and Thomas demonstrated the H_2O line profile measurement¹⁾. The authors showed a preliminary result that demonstrates the feasibility of an attempt to implement the derivative spectrometry with repeatedly pulse-driven diode lasers: atmospheric methane was measured with 8ppm·m sensitivity²⁾. This paper gives further results of the parametric optimization for the best SNR under any given device characteristics as well as for available real devices. A guiding principle has been obtained for selecting a HgCdTe infrared detector.

PRINCIPLES

Principle of the derivative spectrometry with a pulsed diode laser is explained by Fig.1. A rectangular pulse of width T_w and height i_p is imposed on a heat-up current i_h to control the laser frequency (a). The laser pulse is emitted only during this period with decreasing power due to the rising junction temperature θ_j , and the lasing frequency slightly chirps upwards (b). The driving pulse is again applied after the junction has been cooled down.

The pre-amplifier output responds to the ir-power transmitted through the specimen gas, which is a composite of signal $x(t)$ and white noise $n(t)$. The SNR of the lock-in amplifier output is poor if the crude signal $x(t) + n(t)$, (c), is fed. As shown in Fig. 2, a temporal gate which opens when the signal $x(t)$ arrives and closes when it disappears between the pulsed laser-emissions suppresses the noise on the lock-in amplifier output.

The driving pulse is applied repeatedly with period T , while the heat-up current i_h is controlled so as that laser frequency should change according to the sequence, $---$, ν_0 , ν^+ , ν_0 , ν^- , ν_0 , ν^+ , $---$, which implements the second-derivative spectrometry.

PARAMETER OPTIMIZATION

The optimal value of the gating width T_g was calculated for T_w , laser pulse width, as well as T_p and T_i , time constants of the pre-amplifier and the IRD, respectively.

A result of calculated SNR-enhancement performance is shown in Fig.3. The optimal gating width T_g is equivalent to a larger value of T_i and T_w , in either the case $T_w \ll T_i$ or $T_w \gg T_i$. This result is acceptable considering that the optimal gate-width should be equal to the signal width of the pre-amplifier output. Experimental results are given in Fig. 4 for three gating widths, where $T_g = 2\mu s$ had been calculated to be the optimal. The laser pulse-width is specific to a laser element and is fixed at $T_w = 300$ ns. The preamplifier bandwidth is not critical if it is wide enough to track the IRD output, being taken as $T_p = 50$ ns.

The achievable smallest error in the absolute absorption obtained with a measurement apparatus reported earlier²⁾ was calculated for various R_e , responsivity, and T_i of IRD and is shown in Fig.5. An assumption is made that the pre-amplifier noise is dominant over the IRD noise. The marks * denote possible combinations anticipated from a theoretical consideration made by Hamashima and Itoh³⁾. Detectors represented by marks Δ and \circ were actually tested by the authors. It is concluded that a sensitive IRD, though it does slowly respond, is desirable for a better system sensitivity.

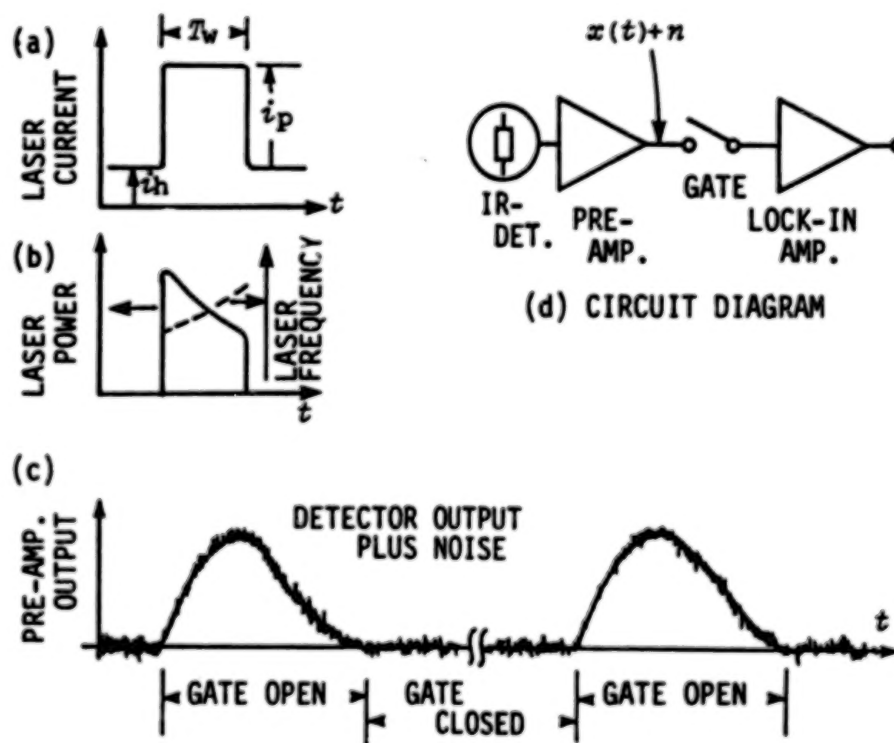


Fig.1 Principle of noise-suppression in pulsed TDL spectrometry.

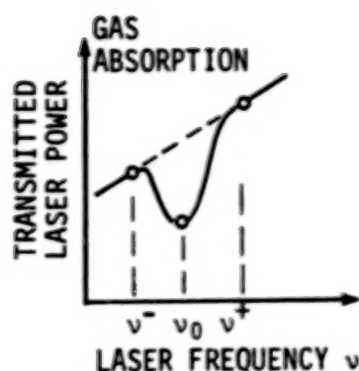


Fig.2 Implementation of the derivative spectrometry with successive laser pulses.

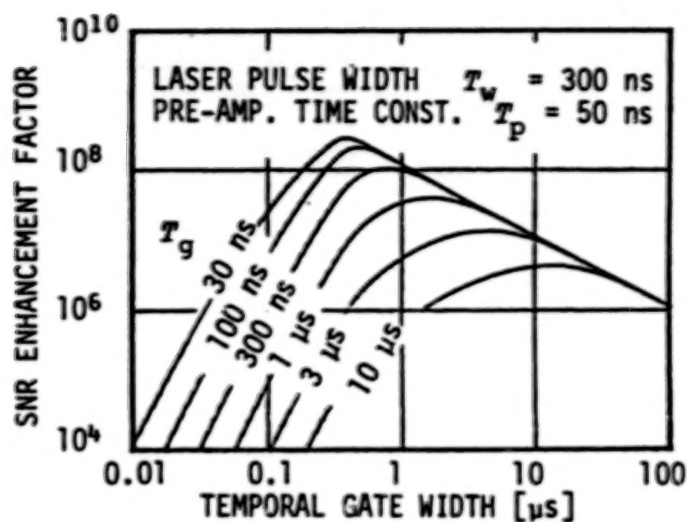


Fig.3 Effect of temporal gate width on the SNR enhancement in the 2nd derivative spectrometry.

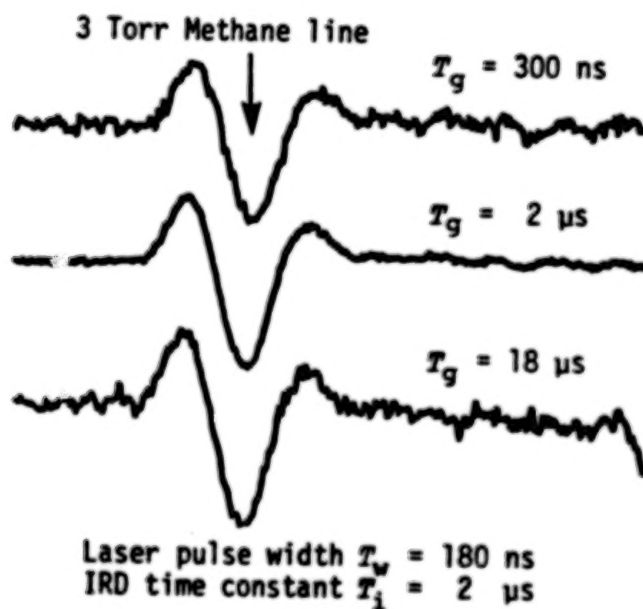
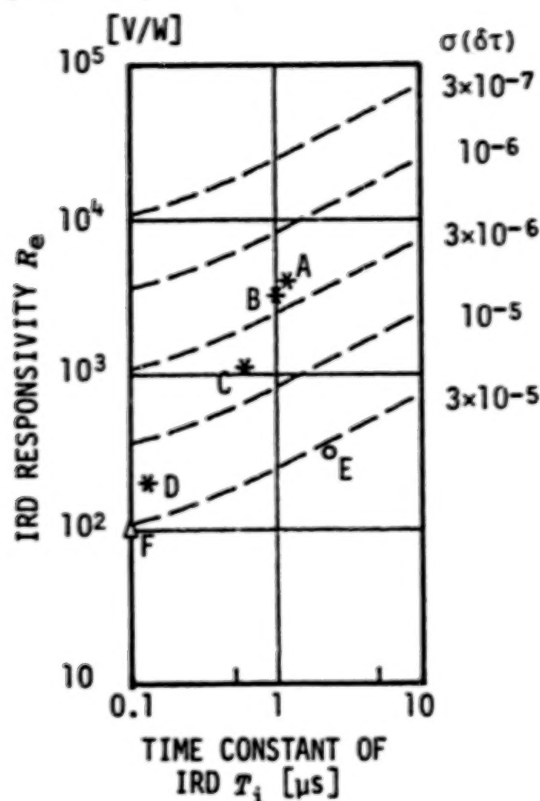


Fig.4 Spectra of methane lines with different temporal gate width. Magnitudes are normalized so that methane lines have the same strength.



PARAMETERS:

LASER PULSE WIDTH

$$T_w = 300 \text{ ns}$$

PRE-AMP. TIME CONST.

$$T_p = 50 \text{ ns}$$

EQUIVALENT NOISE
VOLTAGE AT PRE-AMP.
INPUT

$$e_n = 10 \text{ nV}/\sqrt{\text{Hz}}$$

LASER OUTPUT

$$P_o = 1 \text{ mW}$$

Fig.5 Attainable maximum sensitivity of the TDL absorption spectrometry system for various response time-constants and responsivities of infrared detectors.

CONCLUDING REMARKS

Random noise of a pulsed mode TDL absorption spectrometry can be suppressed down enough to 10^{-6} level in terms of absolute absorption, which is already dominated by the etalon fringe noise. This conclusion certifies a feasibility of a handheld TDL equipment for atmospheric surveillance.

REFERENCES

- 1) S.E.Taylor and E.L.Thomas, "Derivative monitoring of atmospheric species with pulsed lead-salt diode lasers", Conf. Lasers and Electrooptics (CLEO) (May 1983, Baltimore, USA)THP1.
- 2) R.Koga, M.Kosaka and H.Sano, "Higher Harmonic Detection of Trace-Gas Density with Pulse-Train Driven Pb-Salt Diode Laser", 12th Int. Laser Radar Conf. (Aug. 1984, Aix en PROVENCE, FRANCE) pp.419-422.
- 3) S.Hamashima and M.Itoh, "Characteristics of HgCdTe Photoconductive Detectors" IECE Japan. Tech. Rep. ED 84-159(1984).

N87

10325

UNCLAS

PERFORMANCE TESTING OF LIDAR RECEIVERS

M.Y. SHAMS, DEPARTMENT OF PHYSICS, UNIVERSITY OF
WEST INDIES MONA, KINGSTON, JAMAICA

In addition to the considerations about the different types of noise sources, dynamic range, and linearity of a lidar receiver, one requires information about the pulse shape retaining capabilities of the receiver. For this purpose, relatively precise information about the height resolution as well as the recovery time of the receiver, due both to large transients and to fast changes in the received signal, is required. As more and more analog receivers using fast analog-to-digital converters and transient recorders will be used in the future lidar systems, methods to test these devices are essential.

The method proposed for this purpose is shown in fig. A. Electronic circuits and the laser diode transmitter generate an optical pulse of the shape of a lidar return signal, with a single transient or a set of transients superimposed on it. The width, height, and the period of these transients can be varied. Also the total range of the lidar type pulse can be varied. To generate the lidar signal, the electronic circuits obey the common lidar equation for the power received by the detector for the range R due to elastic scattering:

$$P(\lambda_L, R) = P_L \frac{A_0}{R^2} \epsilon(\lambda_L) \beta(\lambda_L, R) \epsilon(R) \frac{c \tau_L}{2} e^{-2 \int_0^R \kappa(\lambda_L, R) dR}$$

In the case of a transient or a single pulse, the pulse function $f(R)$, for a pulse of height P_P and of duration ΔR is

$$f(R) = \frac{1}{2\pi} \int_{-\infty}^{\infty} g(\omega) \cdot e^{j\omega R} \cdot d\omega$$

where

$$g(\omega) = \int_{-\infty}^{\infty} f(R) \cdot e^{-j\omega R} \cdot dR = \frac{P_P}{j\omega} \left[e^{j\omega \frac{\Delta R}{2}} - e^{-j\omega \frac{\Delta R}{2}} \right]$$

If the transients possess a period T , then the function $f'(R)$ representing the transients is:

$$f'(R) = \frac{P_P \Delta R}{T} \left[1 + 2 \sum_{n=1}^{\infty} \frac{\sin(n\omega \Delta R/2)}{n\omega \Delta R/2} \cdot \cos n\omega R \right]$$

The signal emitted from the transmitter is received by the fast diode (calibrated) and the test receiver. The output signals are displayed optically as well as plotted. By changing the parameters of the transients (such as width, period, and height), the limitations of a given receiver can be determined.

Tests were carried out using LCW-10, LT-20, and FTVR-2 as optical parts of the optical pulse generator circuits. A commercial optical receiver, LNOR, and a transient recorder, VK 220-4, were parts of the receiver system.

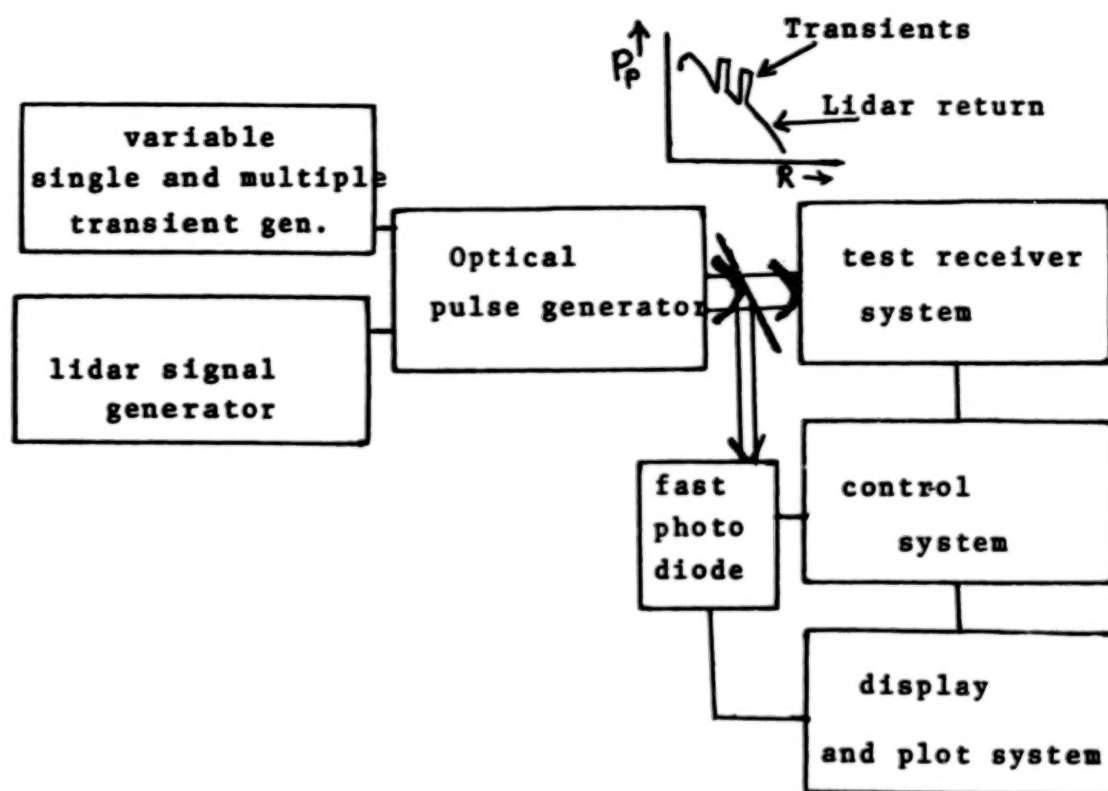


FIG. A

N87

10326

UNCLAS

PROGRESS IN COHERENT LASER RADAR

J M Vaughan

Royal Signals and Radar Establishment
Great Malvern, Worcestershire, UK

Considerable progress with coherent laser radar has been made over the last few years - most notably perhaps in the available range of high-performance devices and components and the confidence with which systems may now be taken into the field for prolonged periods of operation. Something of this increasing maturity was evident at the 3rd Topical Meeting on Coherent Laser Radar: Technology and Applications (3CLRM), which was held at Great Malvern last summer. As a matter of policy this series of meetings has sought to bring together the device physicists, the system builders and the end users. The conference attendance was well above expectation with 135 registrants, nearly one quarter from North America. Equipment, both systems and components, was shown by 7 industrial firms and 61 papers were given.

Presentation of their work was made by representatives from leading institutions in Canada, France, Great Britain, The Netherlands, Sweden, United States and West Germany. Topics included: mesoscale wind fields, nocturnal valley drainage and clear-air down bursts; airborne Doppler lidar studies and comparison of ground and airborne wind measurement; wind measurement over the sea for comparison with satellite-borne microwave sensors; transport of wake vortices at airfields; coherent DIAL methods; a newly assembled Nd-YAG coherent lidar system; backscatter profiles in the atmosphere and wavelength dependence over the 9-11 μm region; beam propagation; rock and soil classification with an airborne 4-laser system (LIMES); technology of a global wind profiling system; target calibration; ranging and imaging with coherent pulsed and CW systems; signal fluctuations and speckle. Some of these activities will be briefly outlined and reviewed.

On the device physics side a wide range of continuous wave CO₂ lasers, both conventional cavity and waveguide, and RF and DC excited, are now available from several manufacturers, with power levels between 3 and 20 Watts and with good stability and lifetime. Particularly valuable progress has been made with CO₂ oxidation catalysts for extending pulse laser lifetime; tin oxide base material impregnated with platinum and palladium salts is available in different forms and shows high activity. Recent improvements in extra-cavity acousto-optic modulators include increased optical power handling, reduced acoustic back reflection level and easier optical alignment. Detector advances include thermoelectric cooling of a packaged p-type CMT photoconductor device to produce a heterodyne NEP better than 2×10^{-19} W Hz⁻¹ and bandwidth of 100 MHz.

During the past 12 months two international working groups have been set up to study aspects of laser sensing from space; both are due to report in the early autumn. ESA established the Space Laser Sounding and Ranging Working Group which has now met on three occasions with a broad brief to consider a wide range of possible tasks. The first meeting of the NASA Working Group on Laser Atmospheric Wind Sounding (LAWS) was held in April 1986 and is aiming more specifically at global wind measurement in the troposphere.

In recent work at RSRE the program of flight trials with the Laser True Airspeed System (LATAS) has continued through the winter and spring. This equipment after four years still shows reliable and efficient performance. It is planned to discuss recent backscatter measurements in the atmosphere at altitudes to 13 km, including flights made north of Tromso in the Arctic Circle, and a series of three flights made in conjunction with passage of the SAGE II limb sounding satellite over the UK in April 1986. The LATAS equipment is now being installed in a Canberra aircraft which will allow flights of greater duration and to greater altitude.

N87

10327

UNCLAS

DOPPLER LIDAR STUDIES OF ATMOSPHERIC WIND FIELD DYNAMICS

R. M. Hardesty, M. J. Post, T. R. Lawrence, and F. F. Hall, Jr.

NOAA/ERL/Wave Propagation Laboratory
325 Broadway
Boulder, Colorado 80302

INTRODUCTION

For the past 5 years the Wave Propagation Laboratory has operated a pulsed CO₂ Doppler lidar system to evaluate coherent laser radar technology and to investigate applications of the technique in atmospheric research. The capability of the system to provide measurements of atmospheric winds, backscatter, and water vapor has been extensively studied over this period. Because Doppler lidar can measure atmospheric wind structure in the clear air without degradation by terrain features, it offers a unique capability as a research tool for studies of many transient or local-scale atmospheric events. This capability was demonstrated in recent field experiments near Boulder, Colo. and Midland, Tex., in which the lidar clearly depicted the wind field structure associated with several types of phenomena, including thunderstorm microbursts, valley drainage flow, and passage of a dryline front.

Until recently, the lidar operated with an output energy of 100 mJ per pulse, providing maximum ranges of 12-20 km in the boundary layer or lower troposphere, and 8-12 km when pointed vertically. Although adequate for most lower tropospheric applications, this pulse energy was insufficient for consistent measurement of winds throughout the troposphere and into the lower stratosphere. To improve sensitivity during the periods of low aerosol backscatter, the system has recently been upgraded with new transmitter/receiver hardware. The upgraded system, which transmits 2 J per pulse of output energy at a rate of 50 Hz and incorporates computer control for automated operation, underwent calibration testing during the spring of 1986.

MICROBURST AND DOWNBURST STUDIES

Because of their potentially hazardous effects on aircraft safety, thunderstorm-generated microbursts have received considerable attention in recent years (see e.g., Fujita, 1980). Microbursts are characterized by severe downdrafts that occur beneath convective clouds over scales of about 3 km or less. When the downdraft nears the surface, it spreads into a diverging horizontal wind. An aircraft flying through a microburst on approach or takeoff encounters a rapid change in

airspeed, which in the worst case produces an unexpected loss of altitude that can result in a crash.

Doppler radar is useful for detecting and tracking downbursts in precipitating environments. Under clear-air conditions, however, radar measurements near the surface can be severely limited by ground clutter. Because Doppler lidar operates in clear air with no sidelobe effects, it is useful for research into microbursts in the low radar-reflectivity environment.

The NOAA lidar has been used to track and observe gust fronts and outflows spawned by microbursts on several occasions. In at least one instance, an apparent microburst was observed. During a routine data-gathering session near Boulder, Colo., a member of the crew noticed a region of blowing dust beneath a virga-producing convective cloud. Horizontal scans of the disturbance revealed a region of strong divergence in the horizontal wind field just above the surface 6 km from the lidar. Maximum wind shift measured by the lidar in the region of the microburst was 11 m s^{-1} over a distance of 1.5 km, and 27 m s^{-1} across 3 km.

The disturbance spawned a well-defined gust front whose leading edge was clearly seen by the lidar as a strong shear in the velocity field and a line of enhanced backscatter (due to the dust cloud) in the intensity field. The progress and spread of the gust front from the point of the original disturbance was mapped over 10 km.

VALLEY DRAINAGE FLOW MAPPING

The WPL lidar was employed in a recent experiment sponsored by the Department of Energy to study drainage flow in a mountain valley near Parachute, Colo. (Post and Neff, 1986). The instrument was positioned in the middle of the valley, with line-of-sight views exceeding 10 km towards both the head and foot of the valley. By scanning the lidar beam first toward the head, then toward the foot of the valley in a raster-like scan, we were able to map out cross sections of the along-valley flow field at 300 m intervals along a 20 km segment.

In this experiment, the Doppler lidar provided data that were unobtainable by other means. It was able to scan within meters of the terrain at the sides of the valley, showing the effects of friction on the drainage flow. On seven occasions during a 1 month period a complete 3-dimensional map of the valley flow was obtained at half-hour intervals between 2200 and 1000 local time. From these maps, the formation and subsequent behavior of a compact jet core in the drainage flow field was observed. The jet core was seen to wander from one side of the valley to the other as the night progressed. From

the 300-m-long cross sections of along-valley wind, the contribution to the drainage flow at various points along the length of the valley was estimated by computation of the mass flux. Increase in flow due to the effects of side canyons was clearly seen as an increase in the mass flux below the entrance of each side canyon. Lidar results also permitted observation of the breakup and reversal of the drainage flow during the morning hours due to solar heating of the valley walls.

DRYLINE AND FRONTAL PASSAGE DYNAMICS

The capability of Doppler lidar to resolve the transverse fine structure of the wind fields in clear air makes it a valuable tool for studying wind field dynamics along frontal boundaries. During spring 1985, the instrument was used in an experiment to observe frontal hydraulics at the leading edges of cold fronts near Midland, Tex.. It has been postulated that vertical motion can occur over very short length scales along frontal boundaries, with sufficient intensity to trigger convective outbreaks in otherwise stable air (Shapiro et al., 1985). The lidar was employed in the experiment to map the small-scale wind field features vertically and along the frontal boundary during the period of frontal passage, and to monitor the tropospheric wind field with velocity-azimuth-display (VAD) wind profiling before and after the frontal passage.

Midland was selected as the site for the experiment because during April it is climatologically located west of the line of demarcation, often referred to as the dryline, that separates the moist Gulf of Mexico air over the southeastern states from the drier continental air to the west. A site located within the dry air but near the dryline was desirable for lidar operation, so as to reduce the likelihood that the vertical motion associated with the front would produce clouds that could limit measurement capability.

While at Midland, we observed several weak frontal passages with the lidar. We also were able to examine wind field structure along the edge of the moist air boundary as the dryline moved past Midland to the west. The well-defined leading edge of the dryline was detected by a vertically pointing radiometer, which showed a rise in precipitable water vapor from 1.3 to 2.5 cm over a 10 min interval.

Wind structure behind the leading edge of the moist air was seen to be similar to that produced by density currents such as cold fronts. Range-height-indicator (RHI) displays of radial winds indicated a sharp interface in the wind field sloping away from the direction of motion. Winds behind the boundary appeared to move toward the interface at the surface, then curl up and away from the interface at a height of about

2-3 km. Some evidence of Kelvin-Helmholz waves was observed in the region of strong shear at the top of the moist air surge. In general, the appearance of the wind field structure was quite similar to results obtained by Droegemeier (1985) in numerical simulations of density currents.

LIDAR UPGRADE

To improve the capability of the lidar for long range measurements of atmospheric parameters, especially in the upper stratosphere and lower stratosphere, a new, more powerful transmitter was incorporated into the system following the 1985 Texas experiment. The new transmitter employs an injection-locked, unstable resonator configuration to obtain 2 J per pulse of frequency-coherent energy at 50 Hz. Computer control of many functions makes the new system much easier to use than the previous 100 mJ system in field experiments.

The lidar underwent testing and calibration during spring 1986. It is scheduled for use in field experiments this summer to study the effects of terrain-induced, mesoscale convergence near Denver on convective activity, and to further study microburst occurrence and characteristics. Preliminary results from the summer experiments should be available for presentation at the meeting.

REFERENCES

- Droegemeier, K. K., 1985: The numerical simulation of thunderstorm outflow dynamics. Ph.D. Dissertation, University of Illinois, Urbana, 694 pp.
- Fujita, T. T., 1980: Downbursts and microbursts--an aviation hazard. Preprint, Ninth Conf. Radar Meteorol., Miami, Florida, April 15-18, 1980, American Meteorological Society.
- Post, M. J., and W. D. Neff, 1986: Doppler lidar measurements of winds in a narrow mountain valley. To be published in Bull. Amer. Meteorol. Soc., April 1986.
- Shapiro, M. A., T. Hampel, D. Rotzoll and F. Mosher, 1985: The frontal hydraulic head: a micro-alpha scale (approximately 1 km) triggering mechanism for mesoconvective weather systems. Mon. Wea. Rev., 113, 1166-1183.

N87

10328

UNCL

THE EFFECT OF TURBULENCE ON LIDAR
BACKSCATTERED SIGNAL FLUCTUATIONS

S. Fastig and A. Choen*

Atmospheric Optics Department

SOREQ N.R.C.

Yavne, 70600, Israel

*Department of Atmospheric Sciences

The Hebrew University of Jerusalem

Jerusalem, 91904, Israel

Co₂ Lidar measurements being subjected to uncertainties caused by strong fluctuations were explained to appear primarily due to speckle effects whereas turbulence was to be negligible.

Spectral cross-correlation measurements performed in the near IR and in the visible ($\lambda_1=1.06\mu\text{m}$ & $\lambda_2=0.56\mu\text{m}$) show that the main contribution to the fluctuation for the above lidar wavelengths originates from the atmospheric turbulence.

The standard deviation of the fluctuative signal was measured for the two wavelengths simultaneously.

A typical curve representing mid summer day changes in the value of σ as a function of time is shown in Fig 1.

The results, indicating the strong dependence on the turbulence, will be analyzed and discussed.

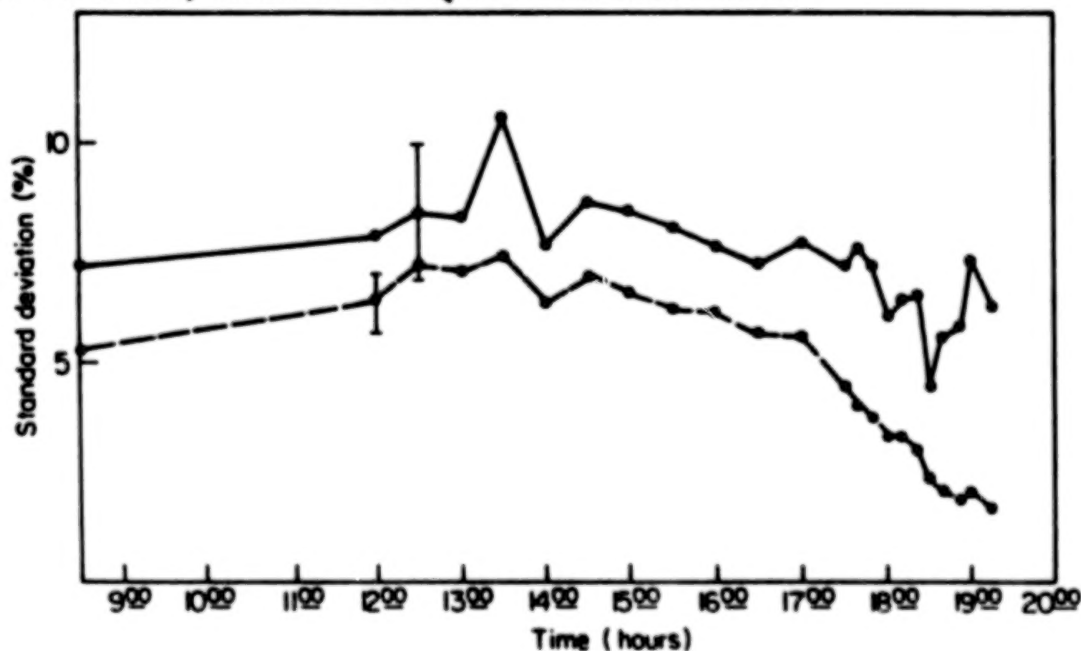


Fig 1: Standard deviation as function of time
(---- 1.06 μm ——— 0.56 μm)

N87

10329

UNCLAS

REMOTE SENSING OF ATMOSPHERIC WINDS USING
A COHERENT, CW LIDAR AND
SPECKLE-TURBULENCE INTERACTION

J. Fred Holmes, Farzin Amzajerddian,
V. S. Rao Gudimetla and John M. Hunt
Oregon Graduate Center

Department of Applied Physics and Electrical Engineering
19600 N.W. Von Neumann Drive
Beaverton, Oregon 97006-1999 U.S.A.

Abstract

Speckle-turbulence interaction has the potential for allowing single-ended remote sensing of the path averaged vector crosswind in a plane perpendicular to the line of sight to a target. If a laser transmitter is used to illuminate a target, the resultant speckle field generated by the target is randomly perturbed by the atmospheric turbulence as it propagates back to the location of the transmitter-receiver. When a crosswind is present, this scintillation pattern will move with time across the receiver.

A continuous wave (cw) laser transmitter of modest power level (a watt or two) in conjunction with optical heterodyne detection has been used to exploit the speckle-turbulence interaction and measure the crosswind. The use of a cw transmitter at 10.6 microns and optical heterodyne detection has many advantages over direct detection and a double pulsed source in the visible or near infrared. These advantages include the availability of compact, reliable and inexpensive transmitters; better penetration of smoke, dust and fog; stable output power; low beam pointing jitter; and considerably reduced complexity in the receiver electronics. In addition, with a cw transmitter, options exist for processing the received signals for the crosswind that do not require a knowledge of the strength of turbulence.

From previous work, the time lagged covariance (TCL) function using the joint Gaussian assumption is given for the focused case by

$$C_I(\bar{P}, \tau) = \langle (I(\bar{P}_2, t_2) - \langle I \rangle) (I(\bar{P}_1, t_1) - \langle I \rangle) \rangle \quad (1)$$

$$= \langle I \rangle^2 \exp \left[- \frac{P^2}{2\alpha_0^2} - \frac{32}{3\rho_0^{5/3}} \int_0^1 |(1-w)\bar{P} - \bar{V}\tau|^{5/3} dw \right] \quad (2)$$

where \bar{P}_1 and \bar{P}_2 designate the location of two detectors in the receiver plane; $\bar{P} = \bar{P}_2 - \bar{P}_1$; $\tau = t_2 - t_1$; α_0 = Transmitter Beam Radius; ρ_0 = Transverse Phase Coherence Length; \bar{V} = Vector

Wind Velocity; and W = Normalized Path Length from the Transmitter-Receiver to the Target. As can be seen from Eq.(1), if two detectors are separated by a vector distance \vec{P} , the time delayed covariance can be measured; and from Eq.(2) it can be seen that the measured quantity will be a function of the crosswind velocity.

Some of the options that exist for processing the data include: The Briggs method which measures the time delay at which the autocovariance and the time-lagged covariance curves cross; The delay-to-peak method, which measures the time delay where the time-lagged covariance reaches its peak value; The width of the autocovariance method which measures the time delay at which the autocovariance curve decreases to 67% of its peak value; and The slope method which measures the slope of the time-lagged covariance function at zero time delay. All of these methods have been used for the line of sight case and appear to have applicability to remote wind sensing using speckle turbulence interaction.

In addition some new methods have been developed that use both the autocovariance function and the time lagged covariance. Formulation for these quantities are functions of both the crosswind and ρ , the transverse phase coherence length. By combining them and also averaging the results for several different time delays, both the crosswind and ρ can be measured. One result for the crosswind which was used to process the data presented in Figure 1 is

$$V = \frac{1}{N} \sum_{i=1}^N \frac{P}{\tau_i} \left[\frac{\ln C_{IN}(0, \vec{V} \tau_i)}{\ln C_{IN}(\vec{P}, 0) + p^2/2\alpha_0^2} \right]^{3/5} \quad (3)$$

where $\tau_i = i^{\text{th}}$ time delay; C_{IN} = Normalized (to the mean squared) time lagged covariance; N = Number of time delays used; and where the direction of the crosswind is determined by the skewness of the TLC.

So far only a small amount of data has been taken. Figure 1 is representative of that data. The results are encouraging and have very positive implications with respect to remote sensing of winds and turbulence in the atmosphere, including global remote wind sensing from a satellite. The in situ data shown in Figure 1 were taken using a Campbell Scientific, CA-9, path averaging laser anemometer. The spring and summer of 1986 it is planned to obtain a significant amount of data at a variety of turbulence levels and ranges which will be processed using several of the above methods for comparison. The results of this work will be presented during the talk.

The transmitter/receiver system is shown in Figure 2. The source is a CO₂ waveguide laser. The beam is first directed through a 3X beam expander and then part of the laser radiation is split from the main beam for use as an optical local oscillator (LO). The remaining part of the beam is directed through an acoustooptic modulator (AOM) where its optical frequency is shifted by 37.5 MHz and then passed through a 10X beam expander that is focused on the target. The half-wave plate rotates the polarization of the beam from vertical to horizontal to match the AOM modulator and the quarter-wave plate provides a circularly polarized output beam.

One of the difficulties in designing a cw, optical heterodyne system is obtaining sufficient optical isolation between the transmitted beam and the LO beam. In order to accomplish this, a novel technique was used wherein a second AOM operated at 42.5 MHz was used in the LO path. This allows an intermediate (signal) frequency of either 5 MHz or 80 MHz to be used and provides an isolation that results in an equivalent fed through optical signal from the transmitter that is 170 dB below the LO power level.

The transmitted beam is scattered diffusely by a 4 foot x 4 foot sandblasted aluminum target. The returning radiation is directed by two one-inch mirrors onto lenses that focus it on the detectors. The effective area of the receivers is approximately one-half square inch and the transmitted power is around one watt, resulting in a useful range of around 3,000 meters.

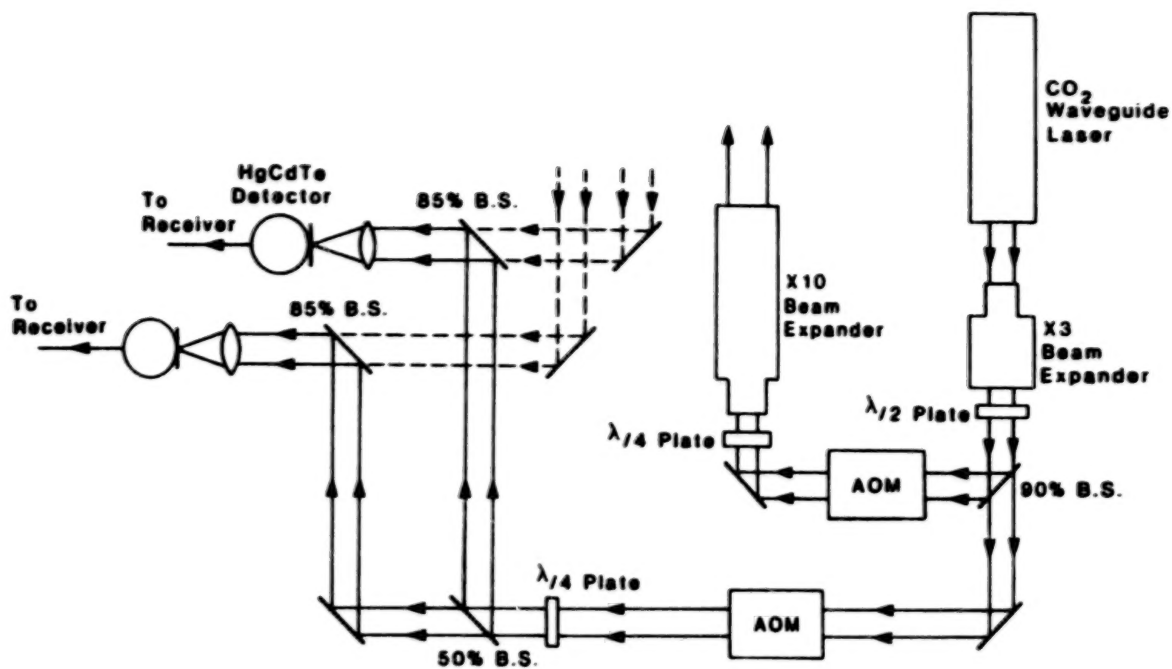


Figure 1 - Transmitter/Receiver System

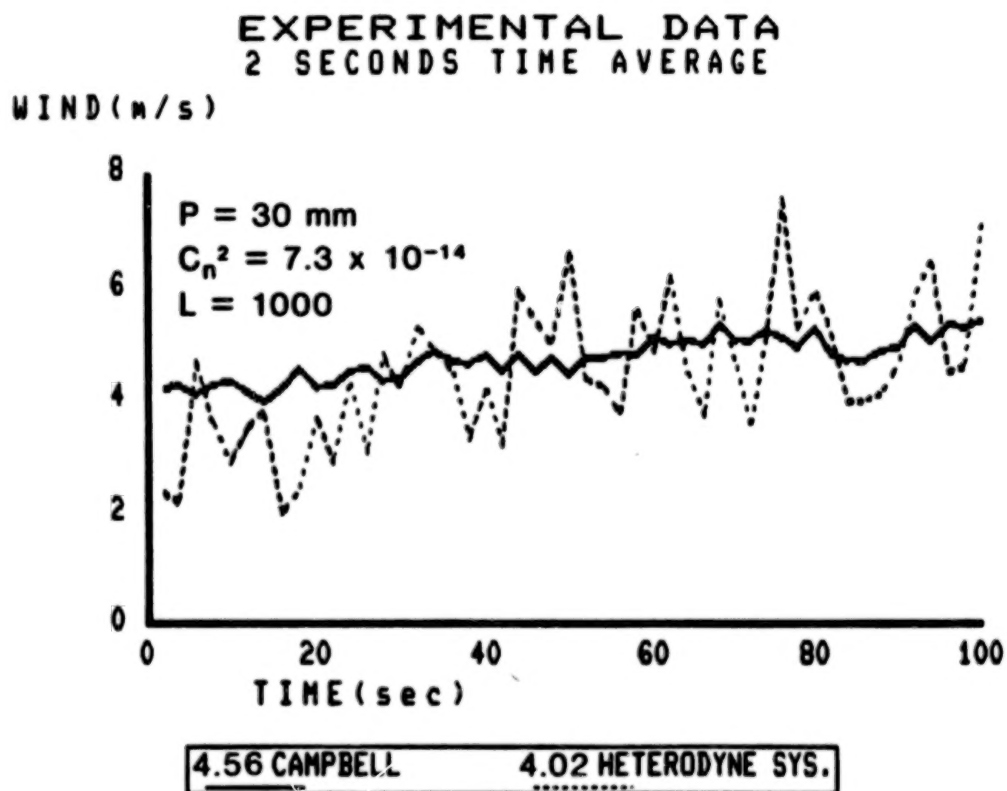


Figure 2 - 1000 Meters Experimental Data

N87

10330

UNCLAS

EXPERIMENTAL AND THEORETICAL DOPPLER-LIDAR
SIGNATURES OF AIRCRAFT WAKE VORTICES

F. Koepp and W.A. Krichbaumer

DFVLR-Institute for Optoelectronics
D-8031 Wessling, Fed. Rep. of Germany

The DFVLR laser Doppler anemometer (LDA) is a CO₂ cw homodyne system designed for boundary-layer wind measurements. During the last three years, it was mainly used in the wake-vortex program at Frankfurt airport for determination of vortex strength, transport, and lifetime. At 12th ILRC, 1984 we have reported in detail on the strategy for that special type of measurements and have presented single experimental results [1]. Therefore, our paper will start with a short summary of the data concerning questions of air-traffic control.

In addition to the experimental activities a computer model describing wake-vortex behavior has been installed. It allows us to compare the measured data with the hydrodynamically predicted quantities. On the other hand, it leads to an improved procedure for future wake-vortex measurements.

The computer simulation is based on an improved version of a program by D. C. Burnham*. It includes vortex motion by cross wind and by mutual induction in ground effect. The calculated tangential velocities of both vortices are projected on LOS (line of sight) and added up together with the wind component to get the LOS velocity proportional to the measured Doppler shift. We evaluate the velocities at discrete points along LOS. A weighting-factor proportional to the intensity of the backscattered radiation is attached to each of these points. Together with this weighting factor, the LOS velocities are sorted in velocity bins of given width to simulate the discrete velocity channels of the LDA. The spacing of the points is not constant in order to take care of the greater changes of tangential velocity near the core of each vortex. Varying the elevation angle related with LOS a complete LDA scan is simulated. Changing the parameters of our calculations in order to set up initial conditions as in our measurements we are able to compare measured and computer-simulated data.

One example concerning the comparison of experimental and model results is shown in Figure 1. The strong lines represent the tracks of the port and starboard vortices of a

*Private communication (1985): Feasibility of measuring aircraft wake vortices at 1500-foot altitude.

B-747 aircraft generated at an altitude of 280 m. The numbers indicate the time after generation in s. The distributions of tangential velocities through the vortices after 50 s lifetime are drawn for the model and the experiment. The main difference is caused by the homodyne operation of the LDA system which does not allow a sign determination. By direct comparison, some components of the experimental distribution can be attached to a negative sign (dashed line).

Reasons for additional deviations are specific system properties and the applied measuring procedure. The first point is the insufficient speed of the data system which reduces the number of individual measurements to 20 per second [2]. The corresponding integration time of 50 ms together with the high speed of the elevation scan smears the elevation range of one measurement over approximately 1° . Therefore, small structures like the areas of highest tangential velocity near the vortex core cannot be resolved. Another point is the detection and tracking of the vortices. The length of the sensing volume for distances of 200 - 300 m is sufficiently long to get some signal from a vortex. But it is quite difficult to track the moving vortex within the region of highest sensitivity.

The comparison of computed and measured signatures brought some recommendations for future wake-vortex measurements. Two of them are listed below:

- The data system has to be speeded up at least by a factor of 10 to preserve the high angular resolution inherent in Doppler lidar systems.
- The vortices should be automatically tracked by a signal controlled range scan. This can be achieved by installation of a jitter device which overlays the elevation scan by a fast range scan.

References:

1. Koepp, F. and Ch. Werner:
Measurement of aircraft wake vortices using the DFVLR laser Doppler anemometer.
12th ILRC, Aix en Provence, France (1984).
2. Werner, Ch.:
Fast sector scan and pattern recognition for a cw laser Doppler anemometer.
Appl. Opt. 24, 3557 (1984).

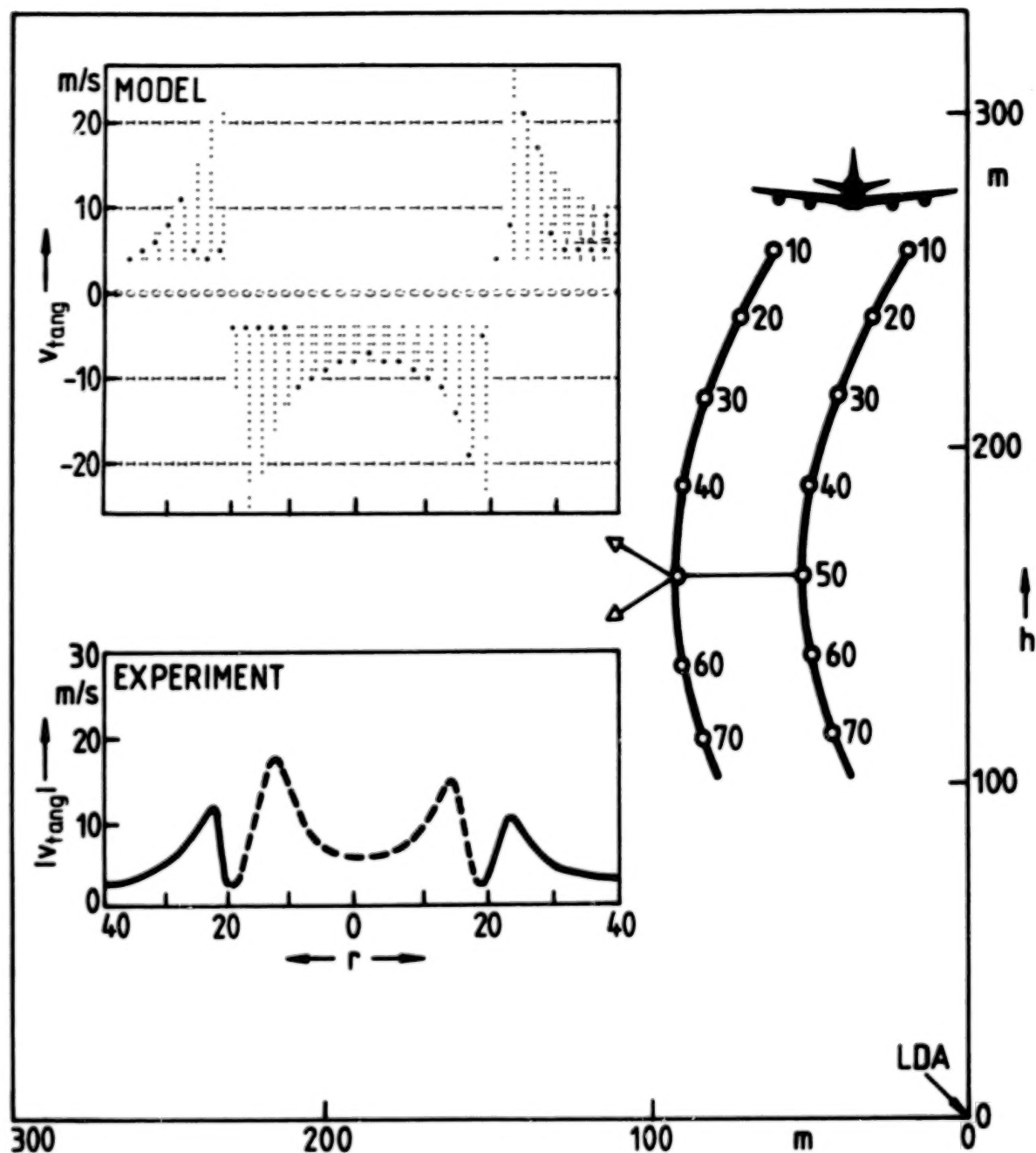


Figure 1. Tracks of both wake vortices generated by a B-747 aircraft passing at 280 m altitude. The theoretical and experimental distributions of tangential velocity 50 s after generation are drawn left. * points of highest signal power.

N87

10331

UNCLAS

LOWER ATMOSPHERIC TEMPERATURE PROFILE MEASUREMENTS USING A RAMAN LIDAR

S.H. Melfi and D. Whiteman
Laboratory for Oceans
NASA Goddard Space Flight Center
Greenbelt, Maryland, U.S.A.

A Raman lidar system has been used to measure the temperature profile of the upper troposphere and lower stratosphere.

The system consists of a tripled Nd-YAG laser ($0.354 \mu\text{m}$) and a 1.5 meter diameter telescope. Two photomultipliers are used at the output of the telescope to allow for measurements at both the laser wavelength and at the Raman shifted wavelength due to atmospheric nitrogen. The signal from the photomultipliers is recorded as photon counts in 1 μsec bins. The results of a number of laser shots are summed together to provide atmospheric returns which have acceptable signal-to-noise characteristics.

Measurements of the Raman nitrogen return have been acquired up to an altitude in excess of 20 km. Temperature profiles have been retrieved from the attenuation corrected Raman nitrogen return assuming the atmosphere to be in hydrostatic equilibrium and using the ideal gas law. Retrieved temperature profiles will be shown compared with independent temperature measurements. The agreement is very good in the upper troposphere and lower stratosphere. In the lower troposphere, attenuation due to aerosols results in poorer agreement.

N87

10332

UNCLAS

A COMBINED RAMAN LIDAR FOR LOW TROPOSPHERIC STUDIES

Yu.F.Arshinov, S.M.Bobrovnikov, V.E.Zuev,
A.I.Nadeev, K.D.Shelevoy
The Institute of Atmospheric Optics, Siberian
Branch, USSR Academy of Sciences, Tomsk, 634055
U S S R

One of the main goals of laser sensing of the atmosphere that was aimed at from the very beginning was the development of techniques and facilities for remote determination of the atmospheric meteorological and optical parameters[1].

Of the lidar techniques known at present the Raman-lidar technique occupies, in a certain sense, some specific place. Really, on the one hand Raman lidar returns due to scattering on different molecular species are very simple for interpretation and for extracting the information on the atmospheric parameters sought, but, on the other hand, the performance of these techniques in a lidar facility is overburdened with some serious technical difficulties due to extremely low cross sections of Raman effect. As a consequence, Raman lidars are not yet widely used in the atmospheric studies, although the advantages of such lidars have already been clearly demonstrated in many experimental works.

During the last decade some efforts have been undertaken at the Institute of Atmospheric Optics, Tomsk, USSR, to develop Raman lidar techniques for remote determination of the atmospheric temperature and optical parameters profiles based on the use of pure rotational Raman spectra of molecular oxygen and nitrogen as well as of the aerosol light scattering [2,3].

The present paper presents some results of further investigations into this problem, which enabled us to construct a combined Raman lidar capable of acquiring simultaneously the profiles of atmospheric temperature, humidity and some optical characteristics in the ground atmospheric layer up to 1 km height. Basic parameters of the lidar have been described earlier in [2] and [3].

Raman spectra of atmospheric species are excited in this lidar with the radiation of a copper-vapor laser emitting the beam of about 6 W mean power at a PRF of 7 kHz at $\lambda = 510.6$ nm. The use of an unstable resonator in this laser provides for obtaining a 1 minute angular wide beam with no additional beam expansion at the laser output.

The spectroscopic problem of isolating simultaneously two portions of pure rotational Raman spectra of N_2 and O_2 and vibrational Raman line of H_2O vapor is solved with the use of a specialized double grating monochromator, in which the vibrational Raman line of H_2O vapor ($\lambda = 627.4$ nm) is isolated at the exit of the first monochromator. The spurious signal due to Mie Rayleigh scattering in the "humidity" cha-

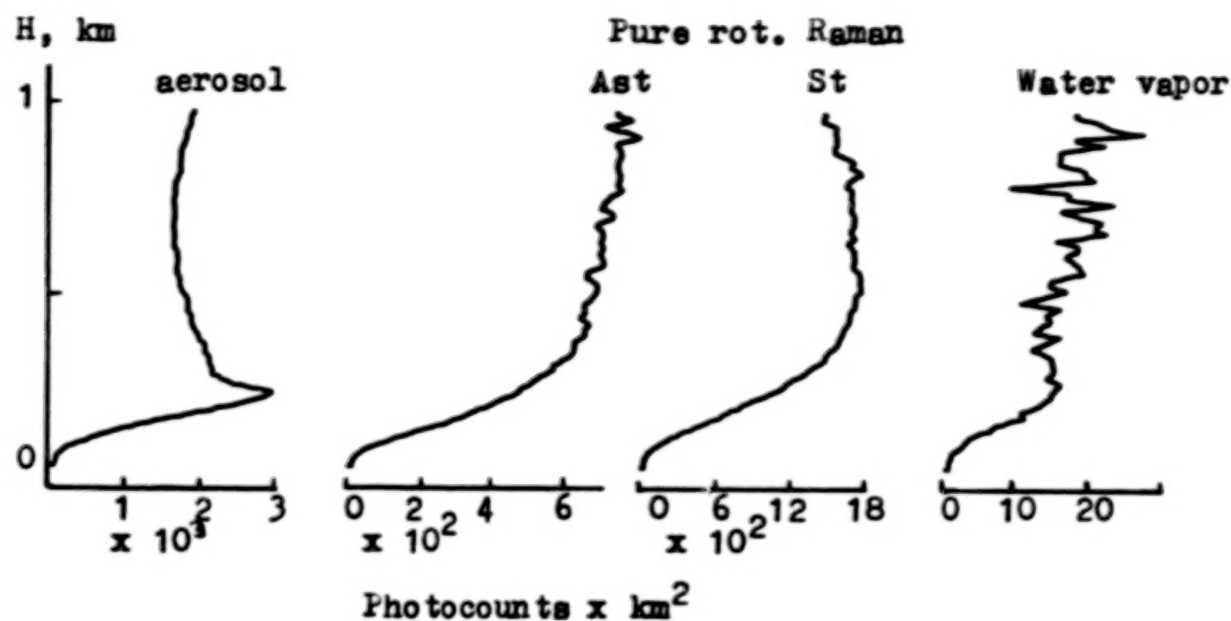


Fig. 1
Lidar returns corrected for r^2 dependence

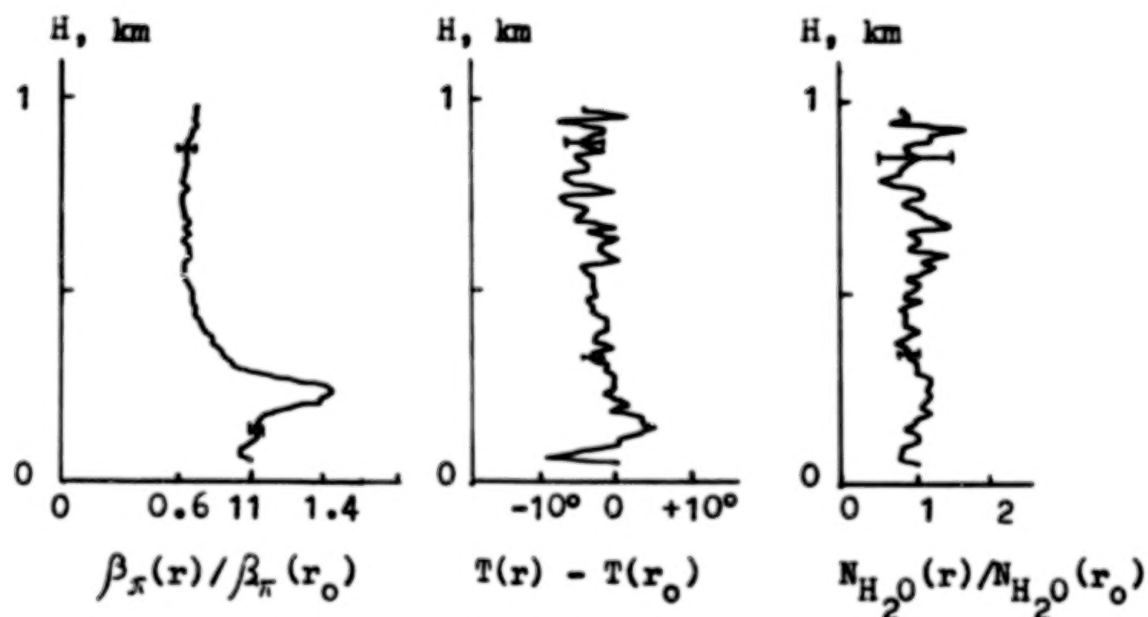


Fig. 2
Atmospheric parameters' profiles obtained from lidar
returns presented in Fig. 1

nnel is suppressed by a properly chosen red-glass band filter.

The lidar data digital acquisition system used in our lidar allows four lidar returns (three Raman signals + one due to aerosol scattering) to be recorded simultaneously using the photon counting technique, up to 2 km height with the spatial resolution of 15 m. The on-line micro-computer enables one to perform the data acquisition, storage and processing in real time. The profiles of the atmospheric parameters sought can be finally plotted in the form of altitude or range functions.

Figure 1 presents the lidar returns recorded with this lidar from the ground atmospheric layer, as functions of altitude. The signals are corrected for r^2 dependence (r is the range). Figure 2 represents the profiles of atmospheric temperature, humidity and aerosol backscattering coefficient retrieved from the signals of Fig. 1. It should be noted that in the cases of humidity and aerosol backscattering the functions $\beta_a(r)/\beta_a(r_0)$ and $N_{vap}(r)/N_{vap}(r_0)$ are presented in Fig. 2, showing the vertical distribution of water vapor number density and aerosol backscatter as normalized by their values at the lowest point of the path.

In conclusion we should like to underline that the results presented in this paper only demonstrate the capabilities of the combined Raman lidar to investigate some physical processes occurring in the ground atmospheric layer, while the results of such studies are yet to be obtained in the near future. Also some technical improvements are needed in order to make this version of Raman lidar operate in the daytime.

References

1. Laser Monitoring of the Atmosphere. Ed. by Hinkley, Springer Verlag, Berlin, Heidelberg, London, New-York 1976.
2. Yu.F.Arshinov, S.M.Bobrovnikov, V.E.Zuev, and V.M.Mitev. Appl.Opt., v.22, N19, pp.2984-2990, 1983.
3. S.M.Bobrovnikov, Remote determination of optical parameters of the atmosphere using pure rotational Raman lidar, The 7-th All-Union Symposium on Laser and Acoustic Sensing of the Atmosphere. Conference Abstracts, Tomsk, USSR, 1982, pp.16-18.

N87

10333

UNCLAS

**INTERCOMPARISONS OF HIGH-RESOLUTION SOLAR BLIND
RAMAN LIDAR ATMOSPHERIC PROFILES OF WATER
VAPOR WITH RADIOSONDES AND KYTOON**

**V. PETRI & A. SALIK
NAVAL AIR DEVELOPMENT CENTER
WARMINSTER, PA.**

**J. COONEY
DREXEL UNIVERSITY
PHILADELPHIA, PA.**

A report is given of measurements of atmospheric profiles of water vapor in the boundary layer by use of solar blind Raman lidar. These measurement episodes, occurring twice a day over a two-week period, were accompanied by a dense net of supporting measurements. The support included two radiosonde launches per measurement episode as well as a kytoon support measurement of water vapor using a wet bulb-dry bulb instrument. The kytoon strategy included ten minute stops at strategic altitudes. Additional kytoon measurements included ozone profiles and nephelometric extinction profiles in the visible. Typically, six or seven 1000 shot lidar profile averages were collected during a measurement episode.

Overall performance comparisons are provided and intercomparisons between auxiliary measurement devices are presented. Data on the accuracy of the lidar water vapor profiles are presented.

N87

10334

UNCLAS

LIDAR METHOD OF MEASUREMENT OF ATMOSPHERIC
EXTINCTION AND OZONE PROFILES

JOHN A. COONEY
DREXEL UNIV.
PHILADELPHIA, PA. 19104
DEPT. OF PHY. & ATMOS. SCI.

Reported here is a description of a method of measurement of atmospheric extinction and of ozone profiles by use of the backscatter signal from a monostatic lidar. The central feature of the procedure involves a measurement of the ratio of the Raman backscatter returns of both the oxygen and nitrogen atmospheric content. Because the ratio of the number density of both species as well as the ratio of the two Q-branch vibrational cross sections is known to high accuracy, the measurement itself becomes a measure of the ratio of two transmissions to altitude along with a ratio of the two system constants. The calibration measurement for determining the value of the ratio of the two system constants or electro-optical conversion constants is accomplished by a lidar measurement of identical atmospheric targets while at the same time interchanging the two optical filters in the two optical channels of the receiver. Further details of this procedure will be discussed.

Factoring this calibrated value into the measured O₂/N₂ profile ratio provides a measured value of the ratio of the two transmissions. Or equivalently, it provides a measurement of the difference of the two extinction coefficients at the O₂ & N₂ Raman wavelengths as a function of the height. A significant body of experience permits the use of a power law as a wavelength scaling law for say aerosol extinction. Thus an aerosol extinction $a(\lambda)$ at a wavelength λ_1 is related to the extinction of the identical atmospheric target at a wavelength λ_2 by the expression

$$a(\lambda_1) = a(\lambda_2)(\lambda_2/\lambda_1)^n \quad \text{Where } 1 \leq n \leq 1.1$$

Should it be argued that the exponent n is really an unknown which can exceed the limits shown, a second procedure is available to measure the value of n as a function of height. This is accomplished by a second measurement of the O₂/N₂ profile ratio in which the second exciting line is chosen such that the N₂ return of the second ratio falls on the same wavelength as the O₂ line of the first ratio. Further efforts are being expanded to determine what the measurement of n can reveal about the aerosol size distributions.

Generalizations to include a second type of extinction term such as ozone extinction in the uv are provided for. Complete details for a useful measurement scenario will be discussed.

N87

10335

UNCLAS

VERTICAL STRUCTURE OF ARCTIC HAZE OBSERVED BY LIDAR

R. M. Hoff, Atmospheric Environment Service
4905 Dufferin Street, Downsview, Ontario, Canada

In the study of the Arctic Haze phenomenon, understanding the vertical structure of the haze aerosol is crucial in defining mechanisms of haze transport. Questions have also arisen concerning the representativeness of surface observations of Arctic Haze. Due to the strongly stratified nature of the Arctic troposphere, the mechanisms which transport aerosol to the surface from the transport altitudes of the lower troposphere are not obvious. In order to examine these questions, a Mie scattering lidar was installed at Alert, NWT, Canada, from September, 1984 to March, 1985. Lidar observes atmospheric aerosols and hydrometeors as they appear in nature, unmodified by sampling effects. As such the results obtained are more realistic of the light scattering characteristics of the in situ aerosol than are those obtained by integrating nephelometers, for example, which heat the aerosol and dry it before measurement. With this lidar, a pulse (694.3 nm at 0.5 Joules output energy) was transmitted vertically through an evacuated tube in the roof of a building at Alert. The receiver consisted of a 20cm diameter Fresnel telescope, neutral density and polarizing filters, an RCA C31000A PMT, Analog Modules LA-90-P logarithmic amplifier and a LeCroy TR8827 32 MHz digitizer. Data were recorded on a Compaq Plus portable PC.

Lidar pulses were fired on two minute intervals for the operational periods of one week per month. The lidar equation was solved for the backscattering coefficient of the aerosol assuming no two-way transmission losses in the signal (an excellent assumption for much of the clear air situations encountered in the Arctic). After output power normalization and range scaling of the return signal, color displays of the time-height lidar profiles of the Rayleigh ratio were prepared. The Rayleigh ratio is the ratio of the backscattered power (backscatter coefficient of the aerosol) to the backscattered power expected from a clear air (Rayleigh) atmosphere at STP. Minimum vertical resolution of the lidar was 4.6 m with a range of 2400 m.

The lidar results have shown that intercomparison between lidar-obtained visibilities and observer visibilities (Figure 1) are in much better agreement than for other optical or aerosol monitors. Visibility was calculated from the lidar Rayleigh backscattering ratio using two distinct backscattering-to-extinction ratios. For Rayleigh ratios greater than 10, it was assumed that ice crystals were adding appreciably to the scattering and Volkovitskii's (1980) results for β_{π}/ω of $0.05 \pm 30\%$ were used. For Mie scattering aerosols the β_{π}/ω ratio was assumed to be 0.03. Using the same stratification given by

the Rayleigh ratio, a minus-one power law correction for wavelength (obtained from in situ particle size measurements) was applied for the Mie scatterers and no wavelength correction (Volkovitskii et al., 1980) was used for ice crystal scattering. Visibility at 500 nm was calculated using Koschmeider's relationship assuming the extinction coefficient is equal to the scattering coefficient. The results in Figure 1 show that ice crystal scattering effects are responsible for a portion of the low visibility events. Ice crystal scattering would not be seen by in situ sensors such as an integrating nephelometer.

Three new effects have been identified in the lidar profiles which contribute to the vertical transport of haze:

(1) Isentropic forcing and inversion breakup followed by intense surface mixing. It has been postulated for several years now that haze layers will follow isentropic (equal potential temperature) surfaces from their source regions to the Arctic. A problem with this theory is that air masses cool substantially moving into and within the Arctic. We have obtained evidence that isentropic forcing of the height of haze layers does occur and controls the altitude at which the layers travel. Breakdown in the radiative inversion structure also provides "events" at the surface which are properly viewed as vertical rather than horizontal transport signatures.

(2) Subsidence due to foehns near Greenland. A large scale haze feature (1000 km in horizontal extent and 200 m thick) was observed in February, 1985, in a foehn off Greenland. The layer subsided from 3.5 km altitude to about 0.8 km and then rose again. At the end of the event, snow occurred and the layer was lost in precipitation. This identifies foehns as a mechanism for downward transport of upper tropospheric air to the inversion top.

(3) Ice crystal nucleation and precipitation with subsequent sublimation at the top of the inversion. A third mechanism which appears to move nuclei to the inversion level is clear air ice crystal precipitation. At Arctic temperatures and humidities the atmosphere is often ice saturated. During the fall months, ice crystal precipitation is not as common as it is in spring, indicating that haze may be serving as a source of nuclei for forming ice crystals. An example of clear air ice crystal precipitation from 2.4 km altitude will be shown and after the event an intensification of the backscatter from the top of the inversion is seen. This indicates that this process may be responsible for the vertical structure of Arctic Haze.

Reference:

O. A. Volkovitskii, L. N. Pavlova, and A. G. Petrushin, *Meteorologiya i Gidrologiya*, 3, 114-121, 1980.

Lidar Visibility Estimates (from 280 meter level)

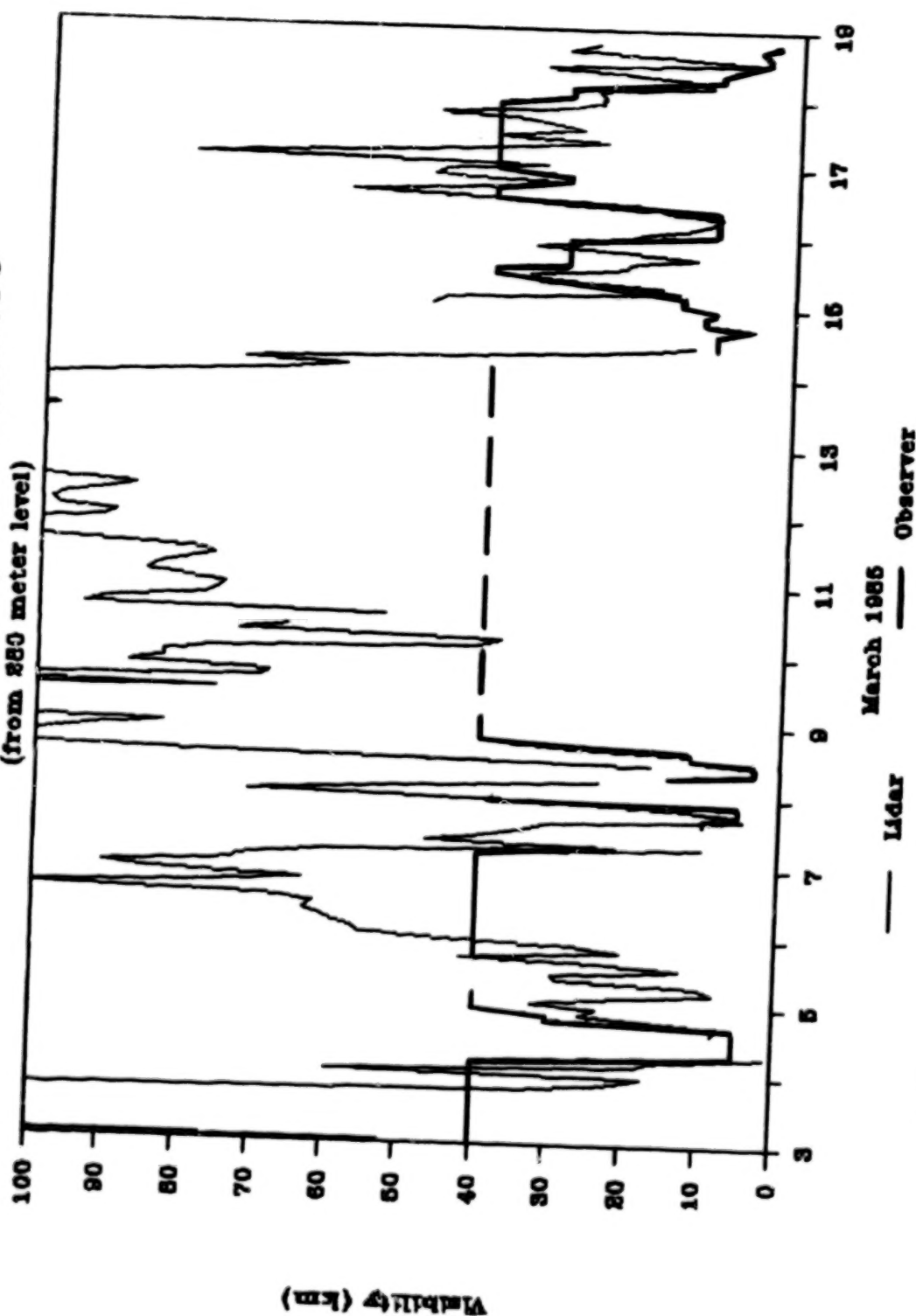


Figure 1. A comparison of lidar estimated visibility (fine line) in a layer from 280-420 m above the surface with the visibility estimated by observers (bold line).

N87

10336

UNCLAS

LIDAR OBSERVATIONS AND MODELING OF COLD AIR OUTBREAKS DURING MASEX AND GALE

R. Boers and S. H. Melfi
NASA Goddard Space Flight Center
Greenbelt, MD 20771

As part of MASEX (1983) and GALE (1986) a number of research flights were carried out over the Marine Boundary Layer (MBL) during periods when extremely cold and dry continental air was flowing out over the warm costal waters at the east coast of the United States. Such periods, which are named "cold air outbreaks," are characterized by massive warming and moistening of the MBL resulting in rapid entrainment conditions. As the MBL deepens as a function of fetch over the ocean, clouds develop. The line of cloud formation typically follows the coast line closely as has been observed many times from satellite imagery.

The backscatter data from the NASA Goddard airborne lidar (Nd:YAG, 10 Hz repetition rate, 200 mJ/pulse), which was used to measure the depth of the MBL in great detail, is ideally suited to verify parameterized models of boundary layer growth rate. The data indicates that the deepening MBL gradually develops clouds at its top. Those clouds form an integral part of the MBL and exercise an important influence on the energy cycle within the MBL. First, clouds are only present at the tops of the largest overshooting domes. Later, as the cloud cover increases they expand into the down draft region at the side of the convective domes.

Figure 1 shows a typical flight line of lidar MBL-depth data. The lidar (mounted in the NASA/Electra) was operated in the downward pointing mode at a nominal altitude of 3 km. The picture indicates a distinct increase in local variance of MBL-depth at those times when clouds fill the upper region of the MBL. This could be related to the idea that local production of buoyancy in

the presence of clouds introduces a turbulence length scale much smaller than the typical sizes of overshooting convective cells.

Figure 2 shows a map of one research flight over the Atlantic Ocean near Cape Hatteras, North Carolina. In the overcast region the MBL-depth was increasing at a much more rapid rate than in the clear and partly cloudy regions. We performed tests of models specifically developed to study boundary layer evolution during clear and cloudy conditions. One of the models was developed by Stage and Businger (1981, abbreviated as SB), the other by Randall (1980, abbreviated as RA). The two models are identical for clear conditions but differ significantly in parameterizations under cloudy conditions. Figure 3 shows the predictions of MBL-depth for the eastern part of the experimental area. The results from both models do not differ much from one another, even in the presence of clouds. However, both models clearly underpredict the MBL growth rate in overcast conditions. Since all external conditions should remain the same as the transition from clear to cloudy sky takes place this result gives some important insights into the entrainment mechanism.

We suggest that the rapid entrainment observed during overcast conditions represents an increase in efficiency of conversion of available turbulence kinetic energy into entrainment energy. For SB and RA models this efficiency factor is represented by one model coefficient which has been experimentally determined to be constant around 0.2. There are, however, good arguments to support the idea that under certain conditions this efficiency factor will increase. The formation of large-scale convective rolls, which satellite imagery shows to be present in the form of cloud streets, could effectively organize the upward transport of turbulent kinetic energy. Additional model tests to be presented during the talk suggest an increase of

the efficiency factor to .7 to .9 could account for the observed entrainment rate.

References

Randall, D. A., 1980: Entrainment into a stratocumulus layer with distribution relative cooling. J. Atmos. Sci., 37, 148.

Stage, S. A. and G. A. Businger, 1981: A model for entrainment into a cloud topped marine boundary layer during a cold air outbreak, Part I. J. Atmos. Sci., 38, 2213-2229.

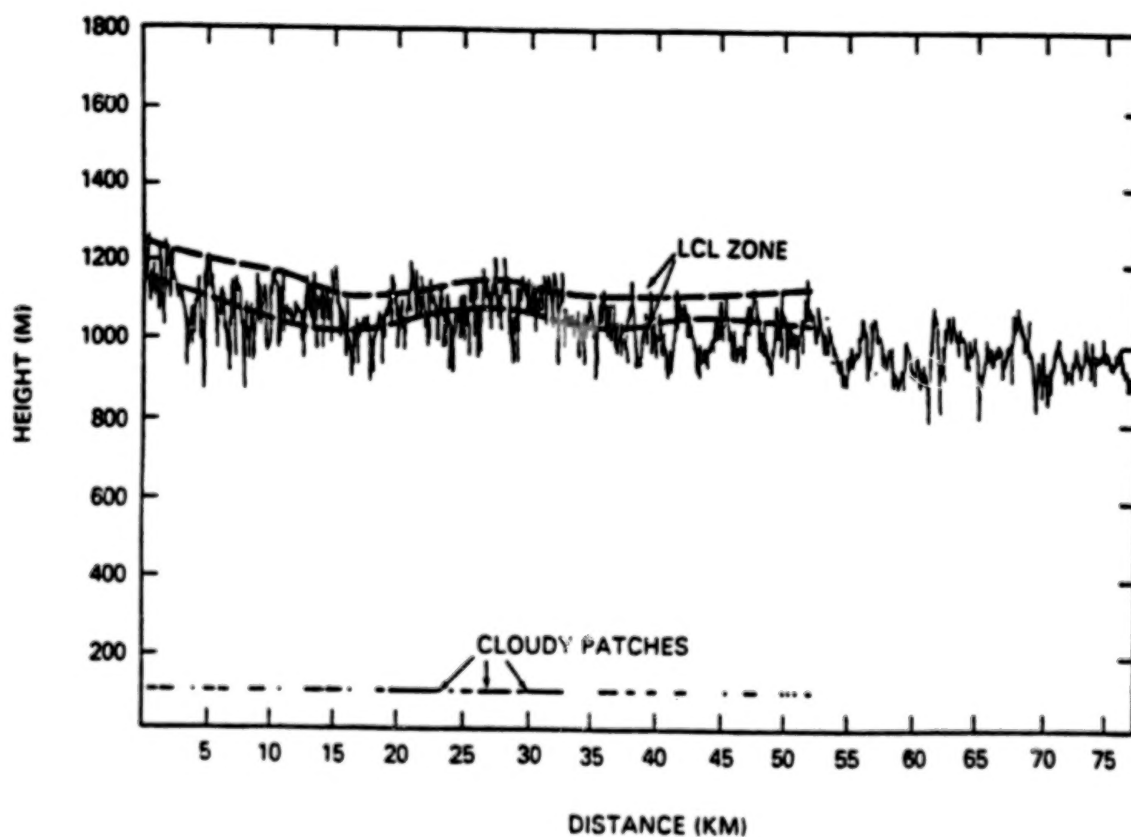


Figure 1. MBL-depth as function of distance in partly cloudy region. Broken horizontal line at bottom indicates clouds.

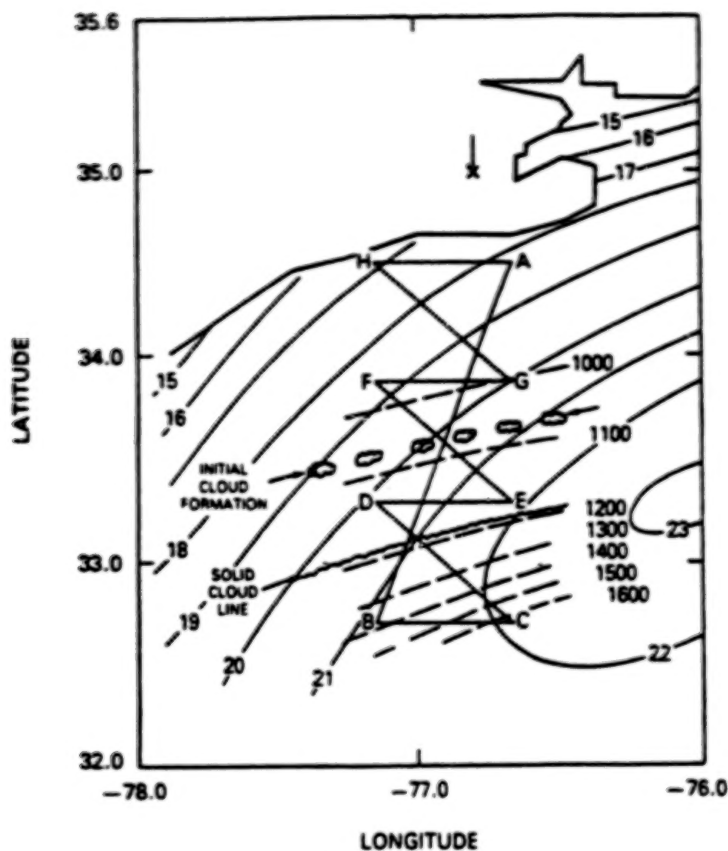


Figure 2. Map of flight near Cape Hatteras, North Carolina, on January 19, 1983. Way points are alphabetically ordered. Sea surface temperatures MBL-depth isopleths and cloud formation are indicated on the plot.

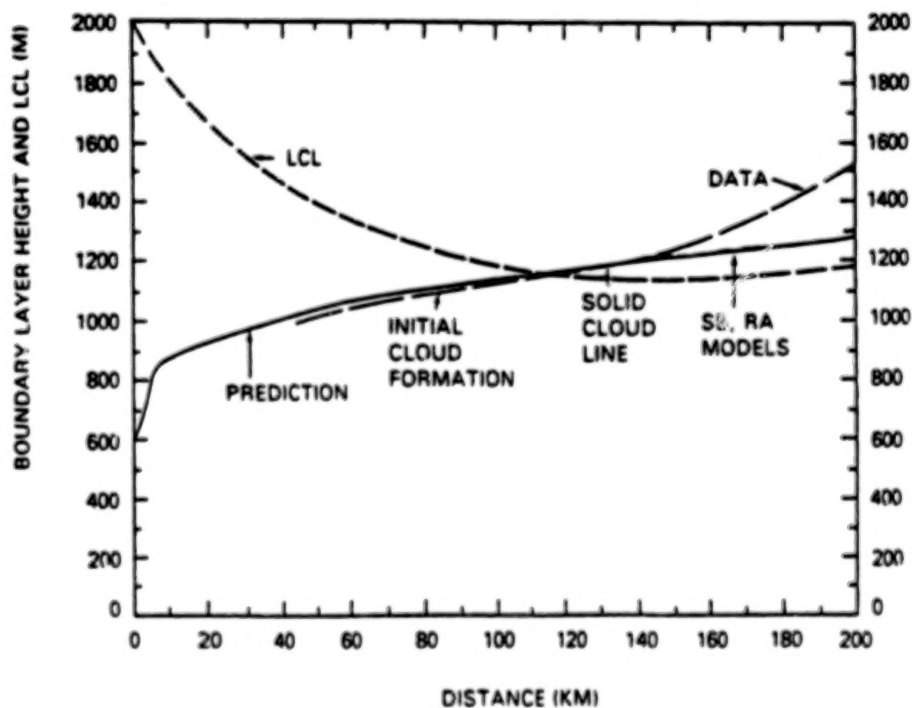


Figure 3. Model prediction and MBL-depth data as function of fetch.

N87

10337

UNCLAS

THE APPLICATION OF LIDAR TO STRATOSPHERIC AEROSOL STUDIES

M. P. McCormick

NASA Langley Research Center, Atmospheric Sciences Division
Hampton, VA 23665 U.S.A.

The trend in stratospheric aerosol column mass and, in general, lidar peak backscatter ratio is driven by volcanic perturbations. During the period 1979 through 1982, a number of volcanic eruptions powerful enough to place material into the stratosphere occurred. The largest of these impacts, many times the others, was due to the March-April 1982 eruptions of El Chichon in Mexico. Fortunately, during this period of increased volcanic activity, both groundbased and airborne lidars and satellite instruments for measuring stratospheric aerosols were in place and operational. Seasonal variations are also observed in the stratospheric aerosol. In the polar regions during winter, for example, polar stratospheric clouds (PSC's) form in regions of cold temperatures at altitudes of about 100 mb to 30 mb. These PSC's are thought to form by growth of existing aerosol particles, and after the winter season and evaporation of the PSC's, the aerosol population reaches a relative minimum due to sedimentation of these particles and the subsidence of air that occurs in these regions. Large variations in stratospheric aerosols are also observed over short geographical distances in the polar regions in the absence of PSC's. These variations are associated with the polar night jet stream which defines the stratospheric polar vortex. In the winter months, a very strong vortex forms in the Antarctic region which is much more long lived and larger geographically than in the Arctic region. Isolation causes large variations of stratospheric aerosol to exist between the inside and outside of the vortex. The vortex dissipates later in the winter during a warming period, and aerosols from lower latitudes mix with those previously inside the vortex. At mid-latitudes, variations in stratospheric aerosols are also observed near regions of the downward transport of stratospheric air associated with tropopause folds. Evidence is also becoming available that aerosol layers at mid- and high latitudes at 20-30 km are appearing in the winter hemisphere originating from equatorial latitudes.

Studies of stratospheric aerosols are important to various disciplines. The understanding of the effects of aerosols on radiation budget and climate, heterogeneous chemistry (especially ozone destruction), and transport are examples. In addition, it has been shown that aerosols can be used as tracers for stratospheric diffusion, advection, sedimentation, and subsidence. Also, aerosols were shown to affect various remote sensors during the period after the 1982 eruption of El Chichon, producing artifacts in their data sets, which again shows the importance of properly understanding stratospheric aerosols on a global scale.

This paper will present the global climatology and present understanding of stratospheric aerosols evolving primarily from lidar and satellite measurements. The importance of validation of these remotely sensed data with in situ measurements will also be discussed. The advantages of lidar for providing high vertical and horizontal resolution and its independence from a remote source for measurement will become evident with examples of long-term

lidar data sets at fixed sites and the use of lidar on airborne platforms. Volcanic impacts of the last 20 years will be described with emphasis on the last 8 years where satellite data are available. With satellite and high-resolution lidar measurements, an understanding of the global circulation of volcanic material will be attempted along with the temporal change of aerosol physical parameters and the stratospheric cleansing or decay times associated with these eruptions. Finally, through both satellite and airborne lidar measurements, the dynamics associated with the polar regions and characteristics of PSC's will be presented.

Volcanic Eruptions and the Increases in the
Stratospheric Aerosol Content
- Lidar Measurements from 1982 to 1986

S. Hayashida, Y. Iikura, H. Shimizu, Y. Sasano,
H. Nakane, N. Sugimoto, I. Matsui and N. Takeuchi
National Institute for Environmental Studies,
Onogawa 16-2, Yatabe-machi, Tsukuba, Ibaraki,
305, Japan

This paper describes the results of the observation for stratospheric aerosols which we have been carrying out since the autumn of 1982 by using the NIES large lidar.

Specifications of the lidar system are shown in Table 1. The lidar has two wavelengths of 1.06 μm and 0.53 μm . We use mainly 0.53 μm for the stratospheric aerosols, because the PMT for 0.53 μm has higher sensitivity than that for 1.06 μm and the total efficiency is higher in the former. A switching circuit is used to control the PMT gain for avoiding signal-induced noise in PMT (Shimizu et al., 1985).

For the last four years, we have observed the stratospheric aerosol layer significantly perturbed by the El Chichon volcanic eruption (March and April 1982, Mexico). The scattering ratio profiles observed from 1982 through 1983 are shown in Fig.1. The integrated backscattering coefficient in the height region from 12km to 27km (IBC) was about $6-7 \times 10^{-3} / \text{sr}^{-1}$ in the winter of 1982/83 when IBC became largest in mid-latitudes (e.g. Hayashida and Iwasaka, 1985). Through 1983, the aerosol layer became broader and the IBC decreased to about $2-3 \times 10^{-3} / \text{sr}^{-1}$ in the winter of 1983/84.

Through 1984 and 1985 the stratospheric aerosol layer was almost quiet and the peak value of the scattering ratio was about as large as 1.2-4 for the whole stratosphere.

On December 11 and 12, we found a new aerosol layer around 18km in altitude. The peak value of the scattering ratio was only about 1.4 and fluctuated. However, we believe this new aerosol layer should be attributed to a volcanic eruption, because there had been no evident peak around 18km through November 1985. Fig. 2 shows the profiles of the scattering ratio observed from November, 1985 through February, 1986. Since the signals were collected with a sampling time of 500nsec (=75m of spacial resolution), we could find the peak layer very clearly in spite of the fact it was very thin. The new layer seems to have appeared already on December 1, though the peak value of scattering ratio was only about 1.3. The new aerosol layer on December 11 and 12 was confined to only about 1km in thickness. On December 13 and 16, the layer became more obscure while another thin layer appeared around 22 km. Through December, 1985, the aerosol layer around 18km was observed continuously, but the peak value of the scattering ratio was only as small as 1.3. The upper aerosol layer around 22km in altitude began to increase in scattering ratio on January 6. On January 9 and 10, the scattering ratio

of the upper layer increased to about 2.8. However, the peak value of the scattering ratio obtained after January 14 shows a fluctuation. This fact indicates that the aerosols came over the lidar side at Tsukuba sporadically, suggesting a large-scale fluctuation in high-altitude air flow.

At Mauna Loa, Hawaii, a distinct new layer was observed on November 26 and 27 at 25-25.5 km (SEAN Bulletin, 1986). On December 5, a 10-fold increase in condensation nuclei was detected by balloon-borne counters between 15-17 km in altitude over Wyoming (41 N, 105.5 W). These new aerosols are considered to have their origin in the eruption of the volcano Nevado del Ruiz on November 13, 1985 in Colombia (SEAN Bulletin, 1986). The aerosol layers observed by the NIES lidar would be attributed to the Nevado del Ruiz eruption, although further verification is required.

References

- 1) Shimizu, H., Y. Sasano, H. Nakane, N. Sugimoto, I. Matsui, and N. Takeuchi (1985); Large scale laser radar for measuring aerosol distribution over wide area. Appl. Opt., 24, 617-626.
- 2) Hayashida, S. and Y. Iwasaka (1985); On the long term variation of stratospheric aerosol content after the eruption of volcano El Chichon: Lidar measurements at Nagoya, Japan. J. Meteor. Soc. Japan, 63, 465-473.
- 3) Scientific Event Alert Network (1986); Smithsonian Institution.

Table 1 Specifications of NIES LAMP lidar

Laser		
Material	Nd: YAG	KD*P (SHG)
Average output power	30 W	10 W
Output energy/pulse	1.2 J	0.4 J
Repetition rate	25 pps	
Pulse duration	15 nsec	
Beam divergence	0.3 mrad	
Receiving telescope		
Type	Cassegrain	
Effective aperture	1.67 m	
Focal length	8 m	
Spot size on focus	1 mm	
Scanner		
Scan type	azimuth-elevation	
Scan rate	600-0.25 deg/min	
Accuracy of aiming	1 min (0.3 mrad)	
Accuracy of scan	1 min (0.3 mrad)	
Light transmission	Semi-Coude	
Receiving optics		
Field of view	0.15-4.8 mrad	
Monochromatization	If filters and double monochromator	
Band width of filters	0.7 Å	1.5 Å
Transmittance of filters	12%	24%
Focal length of monochromator	30 cm	
Signal processor		
Type	Digital processing	
Min. sample rate	10 nsec	
Accuracy	8 bits	
Memory	2 ch: 2048 words/ch	
Data processor		
Type	Mini computer-large computer combined system	
Mini computer	TOSBAC 7/40D	
Large computer	HITAC M-180	

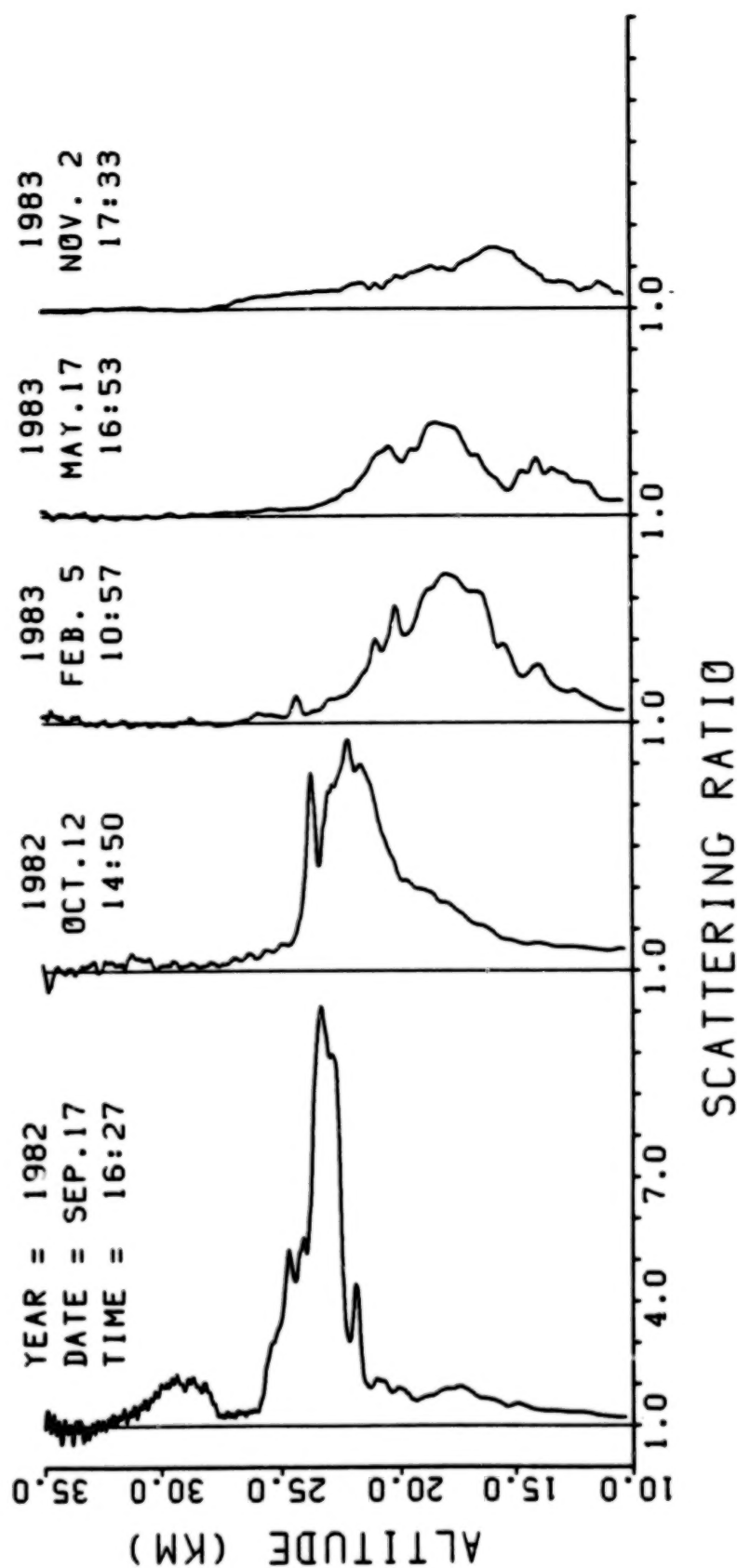


Fig. 1. The scattering ratio profiles from September 1982 to November 1983.

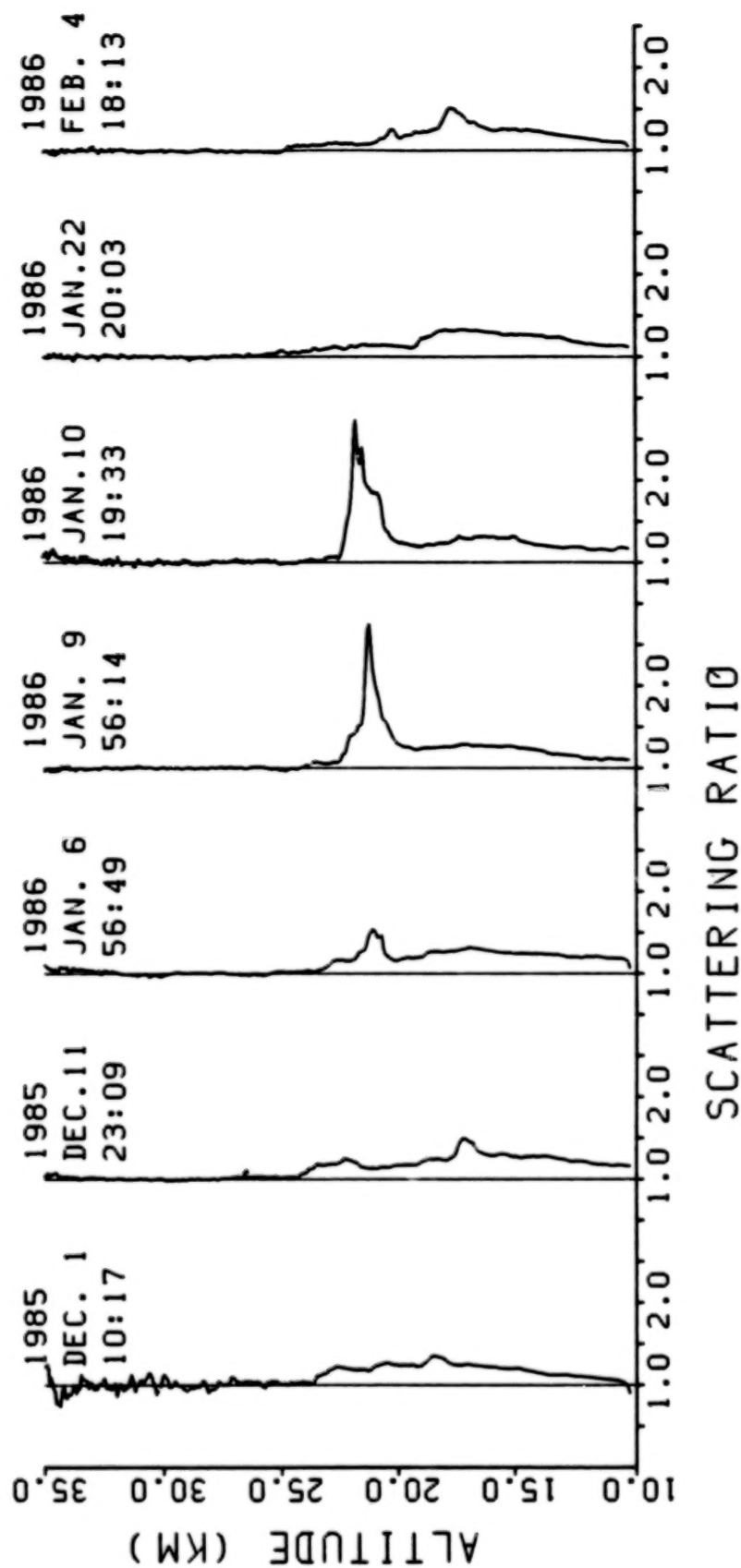


Fig. 2. The scattering ratio profiles from December 1985 to February 1986.

N87

10339

UNCLAS

OBSERVATIONS OF STRATOSPHERIC AEROSOLS ASSOCIATED
WITH THE EL CHICHON ERUPTION

L. Thomas, G. Vaughan, D. B. Jenkins, D. Wareing and M. Farrington
Department of Physics, University College of Wales, Aberystwyth, UK

Lidar observations of aerosols have been carried out at Aberystwyth ($52^{\circ} 25' \text{ N}$, $4^{\circ} 04' \text{ N}$) between November 1982 and December 1985 using a frequency doubled and frequency tripled Nd/Yag laser and a receiver incorporating a 1 m diameter in a Newtonian telescope configuration. Studies of the data obtained have been concerned both with different features of the aerosol distribution over the three-year period and the detailed changes which occurred in late winter and spring months in 1983.

In the analyses of the experimental data attention is paid to the magnitude of the coefficient relating extinction and backscatter, the choice being related to the possible presence of aerosols in the upper troposphere and the atmospheric densities employed in the normalisation procedure. The aerosol loading showed marked day to day changes in early months and an overall decay was apparent only after April 1983, this decay being consistent with an e^{-1} time of about 7 months. The general decay was accompanied by a lowering of the layer but layers of aerosols were shown intermittently at heights above the main layer in winter months. The height variations of photon counts corrected for range, or of aerosol backscatter ratio ($R-1$), showed clear signatures of the tropopause. A strong correlation was found between the heights of the tropopause identified from the lidar measurements and from radiosonde-borne temperature measurements. The month of February 1983 corresponded to a period of intense blocking activity in the vicinity of the UK. An examination of synoptic charts indicated that the measurements in this month refer to air that had been transported from a more northerly latitude. One notable feature of the observations is the appearance of very sharp height gradients of backscatter ratio which seem to be produced by differential advection. Statistical studies of the data recorded in February and April have shown an increase in the degree of variability with height, especially above 16 km, with the horizontal coherence length being greater above this height than below.

N87

10340

UNCLAS

LIDAR OBSERVATIONS OF THE DECLINE OF THE EL CHICHON STRATOSPHERIC LOAD

H. Jäger and W. Carnuth, Fraunhofer-Institute for
Atmospheric Environmental Research, D-8100 Garmisch
-Partenkirchen, FRG

The eruption of the Mexican volcano El Chichon in April 1982 enhanced the stratospheric aerosol load to a level which so far has not been observed by remote sensing techniques. The ruby lidar system at Garmisch-Partenkirchen (47.5 N, 11.0 E) recorded an increase of integral stratospheric particle backscattering of about two orders of magnitude above the background level of the years 1977/78. At northern midlatitudes backscattering was peaking in January/February 1983, as shown in Figure 1. This paper will discuss the decline of the El Chichon stratospheric perturbation.

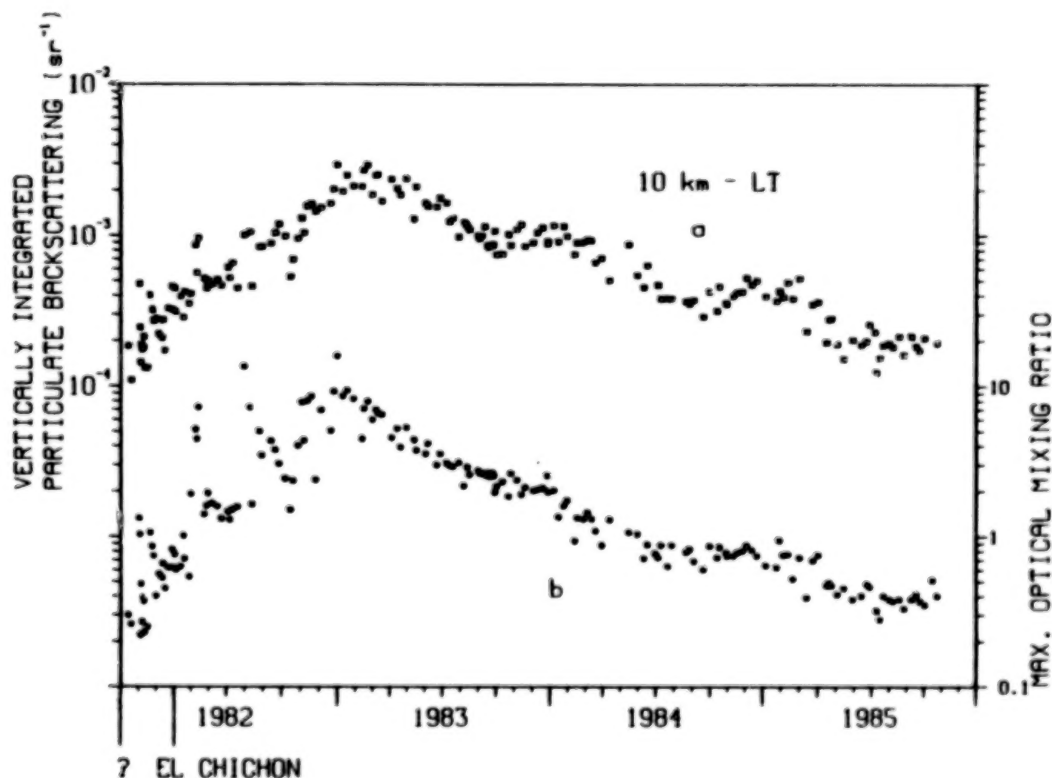


Figure 1. Time variation of the vertically integrated particulate backscattering coefficient (from 10 km to top of layer) and maximum optical mixing ratio (maximum scattering ratio - 1).

The decay of the El Chichon stratospheric cloud is characterized by an overall 1/e lifetime of about 12 months. Thus the background level of 1977/78 can again be reached in 1987. But recently (January 1986) observed fresh stratospheric aerosol layers at 18 to 21 km point at a new volcanic phase,

probably caused by the November 1985 eruption of the Ruiz Volcano in Colombia.

The El Chichon decay is further characterized by seasonal variations of the integral backscattering coefficient (integral between 10 km and layer top, Fig. 1a), which exhibit a winter maximum and a summer minimum. These variations are inversely correlated with the seasonal mean movement of the tropopause height, which was also noticed by Hofmann and Rosen (1984), indicating transport processes. At Garmisch-Partenkirchen the tropopause height usually varies between 9 and 13 km. Since the maximum optical mixing ratio, which is found well above the tropopause between 16 and 20 km, shows comparable - though less prominent - variations (Fig. 1b), a seasonal temperature effect due to particle growth at decreasing temperature (as discussed by Steele and Hamill, 1981) might add to the observed backscatter variations.

References

Hofmann, D.J. and J.M. Rosen, Intern. Radiation Symposium, Perugia, 1984.

Steele, H.M. and P. Hamill, J. Aerosol Sci. 12, 517, 1981.

N87

10341

UNCLAS

AIRBORNE LIDAR OBSERVATIONS OF ARCTIC POLAR STRATOSPHERIC CLOUDS

L. R. Poole

NASA Langley Research Center, Atmospheric Sciences Division
Hampton, VA 23665 U.S.A.

G. S. Kent

Science and Technology Corporation
Hampton, VA 23666 U.S.A.

Polar stratospheric clouds (PSC's) have been detected repeatedly during Arctic and Antarctic winters since 1978-1979 by the SAM II (Stratospheric Aerosol Measurement II) instrument aboard the NIMBUS-7 satellite. PSC's are believed to form when supercooled sulfuric acid droplets freeze, and subsequently grow by deposition of ambient water vapor as the local stratospheric temperature falls below the frost point (which is typically less than -80°C .)

In order to study the characteristics of PSC's at higher spatial and temporal resolution than that possible from the satellite observations, aircraft missions were conducted within the Arctic polar night vortex in January 1984 and January 1986 using the NASA Langley Research Center airborne dual-polarization ruby lidar system. The 1984 measurements spanned a 4-day period during which PSC's were observed in the 17-23-km-altitude range over an extensive area of the polar cap (from about 80°N to the Pole). In contrast, PSC's were observed only on a single flight during the 1986 mission over the 23-26-km-altitude range in a limited area between Iceland and Scotland. These measurements were made apparently near the southern edge of a PSC formation and in a time period just prior to a rather rapid warming at the cloud level, which led to dissipation.

This paper will present a synopsis of the 1984 and 1986 PSC observations, illustrating short-range spatial changes in cloud structure, the variation of backscatter ratio with temperature, and the depolarization characteristics of cloud layers. Implications will be noted with regard to PSC particle characteristics and the physical process by which the clouds are thought to form.

N87

10342

UNCLAS

XeF LIDAR MEASUREMENTS OF DENSITY AND TEMPERATURE
IN THE MIDDLE ATMOSPHERE

T. Shibata and M. Maeda
Department of Electronical Engineering
Kyushu University, Hakozaki, Higashi-ku
Fukuoka 812 Japan

In recent years, it has been widely recognized that vertically propagating internal gravity waves in the middle atmosphere play an important role in determining the large-scale wind field by their momentum transport and deposition.¹ However, very little is known about them in the upper stratosphere and lower mesosphere (between 30-60 km altitude range) because of the lack of adequate techniques to observe small-scale motions. The works by Chanin et al.² proved that a Rayleigh lidar, using a high-power frequency doubled Nd:YAG laser (532 nm), is a very useful tool to study gravity waves in this height range through the observations of the density and the temperature.

In this paper, we used an XeF excimer laser for the Rayleigh lidar observation.³ The characteristics of our XeF lidar system are shown in Table 1. The wavelength of the XeF laser (~351 nm) is in the region that is ozone absorption free, and the Rayleigh scattering cross section is 5 times larger than in 532 nm. We have discussed in detail the advantages of using the XeF laser, as against the YAG laser, for the measurements of density and temperature in Ref.3.

Fig.1 a and b show density and temperature profiles between the altitude range of 30 and 70 km measured with this lidar system. The accuracy of the density and the temperature measurements is less than $\pm 3\%$ and 10 K at 60 km for an observation time of 15 min. Due to the first repetition rate, the XeF laser is suitable for the observation of the short term fluctuation in the density. Fig.2 shows the time-height section of the density fluctuation on 25-26 November. To take this data, we continuously emitted about 1.3×10^6 laser shots without changing the laser gas. Isolines are for zero density change, and separate the zones of positive difference (hatched area) from the negative difference. In this case the phase of the waves is downward propagating, and an average vertical wavelength is about 10 km. The results on the gravity waves by the observation through about one year since April 1985 will be presented.

References

1. Fritts, D.C., Rev. Geophys. Space Phys. Vol.22 275(1984)
2. Chanin, M.L. and A. Hauchecorne, J. Geophys. Res. Vol.86 9715(1981)
3. Shibata, T. et al., Appl. Opt. 1 March (1986)

Table 1 Characteristics of the XeF lidar system

Transmitter

Laser	XeF
Wavelength	351,353 nm
Energy per pulse	200 mJ
Pulse duration	20 nsec
Pulse repetition rate	80 Hz
Beam divergence	1 mrad

Receiver

Telescope	50 cm diameter Coude-type
Field of view	2 mrad
Photomultiplier	EMI9558QB
Filter FWHM (transmission)	3 nm (30 %)
Photon counter	
vertical resolution	1 μ sec
channel number	1000
memory	floppy disk

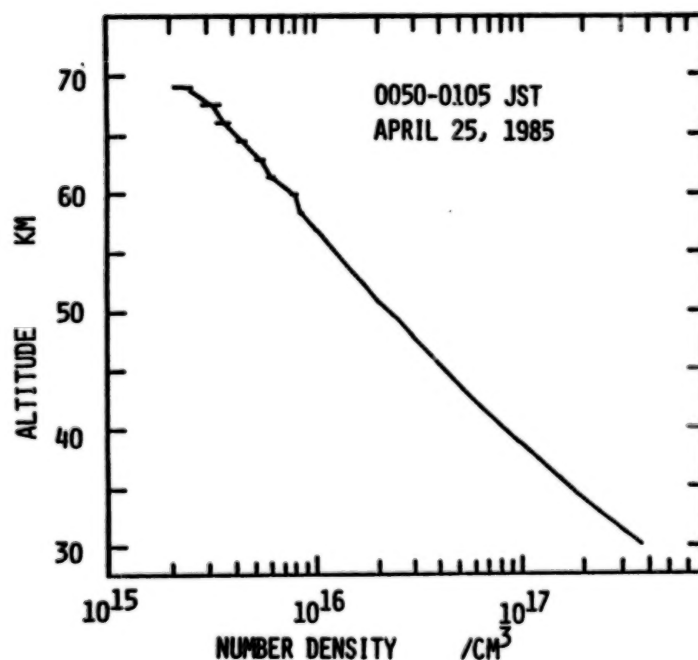


Fig. 1a Density profile measured between 0050 and 0105 JST on 25 April, 1985. The profile was normalized at 39 km with CIRA '72.

84801-58M

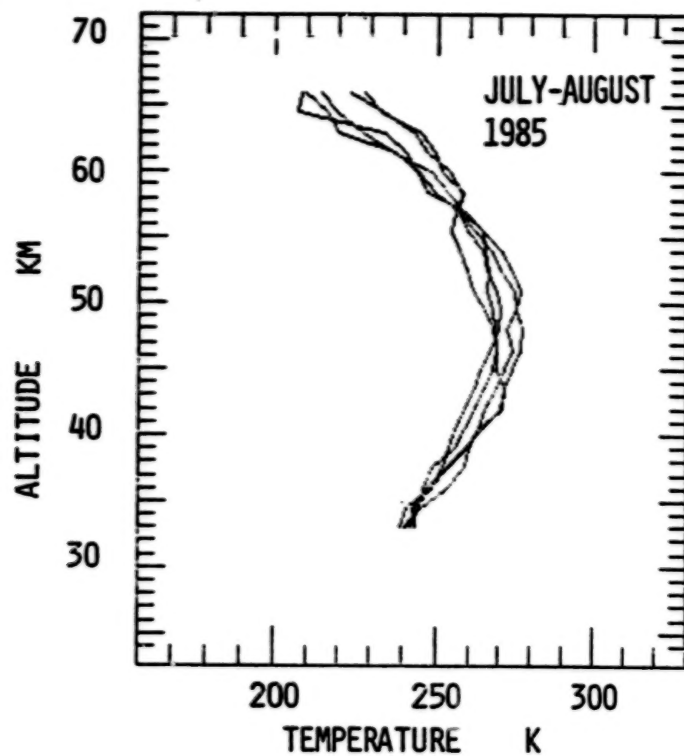


Fig.1 b Temperature profiles in July and August, 1985

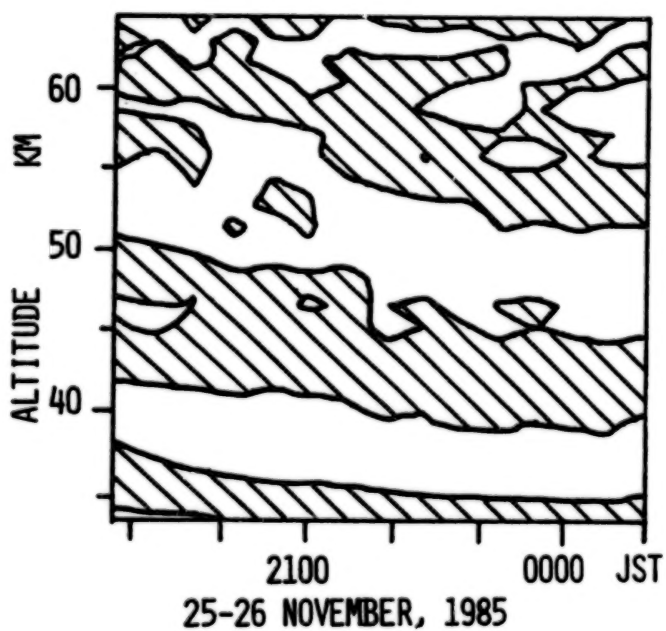


Fig. 2 Time-height section of the density fluctuation

N87

10343

UNCLAS

LIDAR MEASUREMENTS OF THERMAL STRUCTURE

D. B. JENKINS, D. P. WAREING, L. THOMAS AND G. VAUGHAN

Department of Physics, University College of Wales, Aberystwyth, UK

Rayleigh backscatter observations at 532 nm and 355 nm of relative atmospheric density above Aberystwyth ($52^{\circ} 25' \text{ N}$, $4^{\circ} 04' \text{ W}$) on a total of 93 nights between December 1982 and February 1985 have been used to derive the height variation of temperature in the upper stratosphere and mesosphere. Preliminary results for heights up to about 25 km have also been obtained from observations of Raman backscattering from nitrogen molecules. Comparisons have been carried out for stratospheric heights with satellite-borne measurements; good agreement has been found between equivalent black-body temperatures derived from the lidar observations and those obtained from nadir measurements in three channels of the stratosphere sounder units on NOAA satellites; the lidar-based atmospheric temperatures have shown general agreement with but a greater degree of structure than the limb-sounding measurements obtained using the SAMS experiment on the NOAA-7 satellite.

In summer, stratospheric and mesospheric temperatures showed a smooth height variation similar to that of the CIRA model atmosphere. In contrast, the winter data showed a great variability with height, and marked temperature changes both from night to night and within a given night. A notable feature of the winter data was the frequent occurrence of large amplitude wave-like structures in the height variation of temperature above about 60 km. Night-to-night changes in the appearance of these structures were apparent but vertical-phase progression of the structure was observed on only one winter night. Data for three winters showed the lidar technique is capable of resolving large enhancements of stratopause temperature and marked height gradients of temperature during stratospheric warmings.

N87

10344

UNCLAS

LIDAR STRATOSPHERIC OZONE MEASUREMENTS AT THE
OBSERVATOIRE DE HAUTE PROVENCE (FRANCE)

S. Godin, J. Pelon, G. Mégie
Service d'Aéronomie du CNRS BP 3
91370 Verrières le Buisson (France)

Stratospheric ozone monitoring is of particular importance to confirm present day theories predicting a maximal ozone depletion, due to chlorofluorocarbon emission, in the 35-45 km altitude range. Measurements presently rely on both ground-based (Dobson spectrophotometer using the Umkehr technique) and satellite-borne passive experiments (BUV, SBUV). Such systems, however, have been recently shown to have intrinsic limitations mainly due to atmospheric aerosol presence and calibration problems (De Luisi, 1979 ; Fleig et al., 1980).

Consequently during the last few years, active lidar profiling of the ozone vertical distribution by the Differential Absorption Laser technique (DIAL) in the UV wavelength range has been developed using two different type of laser sources:

a) Nd-Yag pumped dye lasers which enable a large tuning range of the UV emitted wavelengths from 280 nm to 320 nm (Pelon and Mégie, 1982a ; 1982b) ;

b) exciplex laser sources using Xenon Chloride (XeCl) as an active medium and emitting at 308 nm, the off wavelength being usually generated by Raman shifting techniques (Uchino et al, 1983 ; Werner et al., 1983).

The first systems have proven their ability to study the ozone number density variations in the troposphere and stratosphere associated with short-scale and mesoscale dynamic processes. However the rapid decrease in both atmospheric total density, which provides the support for light backscattering, and ozone number density, which relates to the local optical thickness to be measured, makes measurements above 35 km very difficult without greatly increasing the laser-emitted power.

The exciplex laser sources at least ten times more powerful are thus very attractive to monitor ozone in the high stratosphere. First measurements using such a source emitting 70 mJ at 20 Hz were performed and validated during the Map/Globus Campaign in September 1983.

Figure 1 shows the average profile of the ozone distribution between 25 km (above the ozone maximum) and 48 km integrated over five nights between September 17 and September 24, 1983. The total integration time of 4 hours corresponds to 10^5 laser shots sequentially emitted on each wavelength. The altitude resolution is determined by the smoothing filter applied to the rough data and ranges from 0.6 km at the lower altitudes to 7.2 km at the uppermost level. Up to 30 km the statistical error stays below 2 % ; it increases rapidly above and reaches 18 % at 45 km. The results obtained by Brewer-Mast sondes and Umkehr method averaged between September 17 and September 24 are compared with the lidar measurements on the same figure.

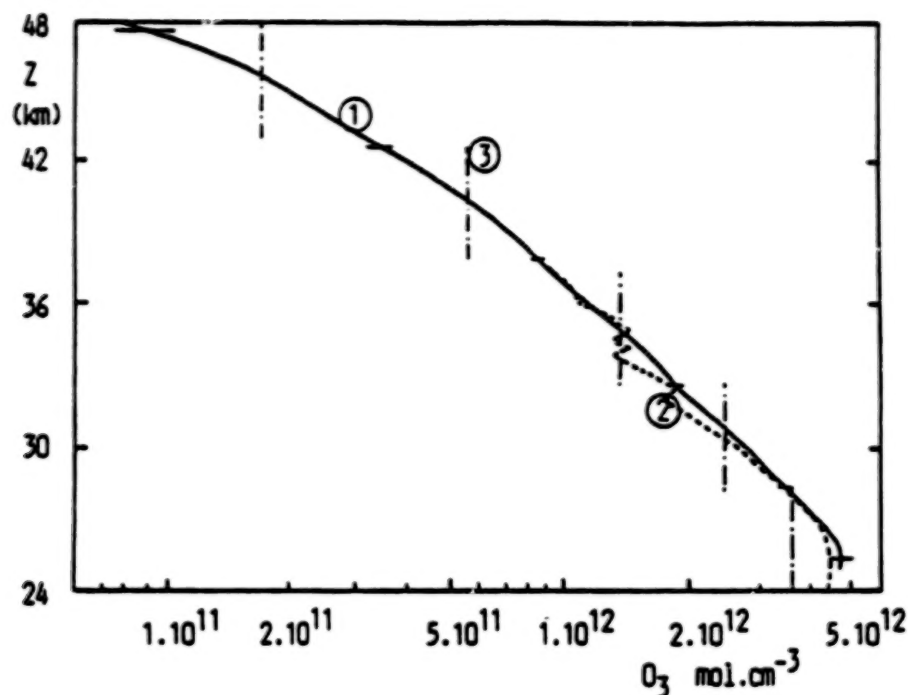


Fig. 1 Lidar averaged ozone profile (1-Full line) during five nights between September 17 and September 24, 1983, compared to the average balloons Brewer-Mast sondes profile (2-Dotted line) and to average the Umkehr profile (3-Vertical dotted line) obtained during the same period of time.

At the lower altitudes the sonde data can be considered as reliable whereas some scattering in the measurements above 30 km can already be detected due to pump efficiency problems. Considering the Umkehr data, the differences for layers 7 to 9 (32 to 48 km) are lower than 3 % e.g. within the error bars of the measurements including the uncertainties due to the calculation of the ozone concentration from Umkehr measurements and the accuracy on the ozone absorption cross sections. In layers 5 (23.5 to 28 km) and 6 (28 to 32 km), Umkehr values are lower by 20 % and 8 % respectively. This difference can most likely be attributed to the presence of aerosols at lower latitudes (De Luisi, 1979).

These measurements already give a fair evaluation of the lidar system accuracy for ozone measurements in the upper stratosphere. It can still be improved as the energy emitted by this first system is one order of magnitude lower than the one delivered by present sources. As part of the development of the OHP lidar facility an exciplex lidar system is under study to monitor stratospheric ozone concentration on a routine basis. First measurements with an oscillator delivering 100 mJ at 20 Hz were

performed in July and December 1985.

Average profiles obtained during these campaigns are compared on figure 2. They show an important difference (up to 30 %) between 28 and 40 km due to the influence of planetary waves. This dynamical perturbation must be taken into account for ozone trend determination since it represents an important part of the fluctuation spectrum and leads to uncertainties in characterizing the mean ozone trend. An evolution of the exciplex laser (emitted energy : 250 mJ at 20 Hz) will be implemented in March 1986 at the OHP for several campaigns. The whole lidar system should allow to measure ozone and temperature simultaneously.

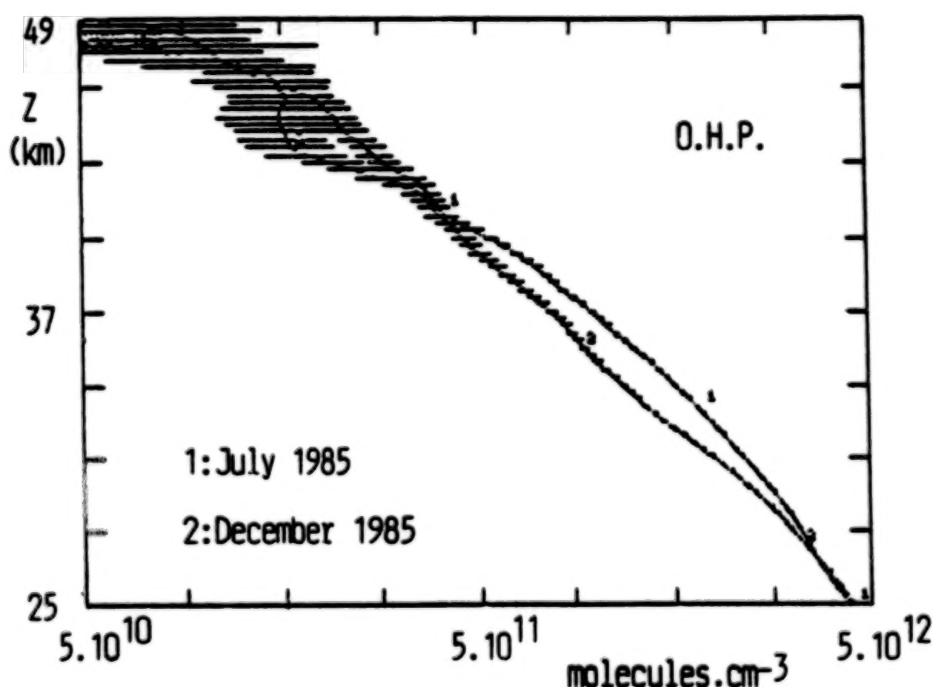


Fig. 2 Average ozone profiles measured in mid-July and mid-December 1985 at the O.H.P.

References

- DE LUISI J.J., Umkehr vertical ozone profile error caused by the presence of stratospheric aerosols, J. Geophys. Res., 84, 1766, 1979.
- FLEIG A.J., V.G. KAVEESHWAR, K.F. KLENK, M.R. HINMAN, P.I. BHARTIA, and P.M. SMITH, Characteristics of space and ground based total ozone observing systems investigated by intercomparison of Nimbus 4 backscattered ultra-

violet (BUV) data with Dobson and M-83 results, Proc. of the Quad. Int. Ozone Symp. J. London ed., 9, 1980.

PELON J. and G. MÉGIE, Ozone monitoring in the troposphere and lower stratosphere : evaluation and operation of a ground based lidar station, J. Geosph. Res., 87, 4947, 1982 (a).

PELON J. and G. MÉGIE, Ozone vertical distribution and total content as monitored using a ground based active remote sensing system, Nature, Lond., 299, 137, 1982 (b).

UCHINO O., M. TOKUNAGA, M. MAEDA, and Y. MIYAZOE, Differential Absorption Lidar measurement of tropospheric ozone with excimer-Raman hybrid Laser, Opt. Lett. 8, 347, 1983.

WERNER J., K.W. ROTHE, H. WALTHER, Monitoring of the ozone layer by laser radar, Appl. Phys. B, 32, 1983.

N87

10345

UNCLAS

LIDAR OBSERVATION OF THE MESOSPHERIC SODIUM LAYER IN
ANTARCTICA

A.Nomura

Faculty of Engineering, Shinshu University, Nagano 380

Y.Iwasaka

Water Research Institute, Nagoya University, Nagoya 464

H.Fukunishi, T.Hirasawa, and S.Kawaguchi

National Institute of Polar Research, Itabashi-ku, Tokyo 173

T.Kano

Faculty of Engineering, Shinshu University, Nagano 380

The mesospheric sodium layer has been observed at Syowa Station in Antarctica (geographic longitude 39.6°E , geographic latitude 69.0°S , geomagnetic longitude 79.4°E , geomagnetic latitude 70.0°S) during the wintering period (January 1985 to January 1986) of the 26th Japanese Antarctic Research Expedition (JARE-26). A lidar observation of the polar middle atmosphere at the station has been performed as a part of the Middle Atmosphere Program (MAP) since 1983. At first stratospheric aerosols have been observed by the system based on a ruby laser (694.3 nm and 347.2 nm). In 1985 a new transmitting system consisting of a tunable dye laser (589.0 nm) was added to that system to observe the sodium layer, too. The characteristics of the lidar system are given in table 1.

In this paper we report the results of the mesospheric sodium layer observed on 42 nights during the period from March to October in 1985.

There appears to be no significant winter maximum in variation of nightly average abundance for that period. This result is different from those obtained at mid-latitude in the northern hemisphere. Moreover the results of the nightly average height distribution showed that the sodium layer was stable for that period, that is, the height of the maximum density was $90\pm 3\text{ km}$ and the width of the layer was $13\pm 3\text{ km}$. These results are similar to those obtained in the southern

hemisphere by Simonich et al. (1979). But it may be found to oscillate with a period of several hours in the nocturnal variation of abundance. The variation of amplitude (maximum to minimum of abundance) is large compared with those obtained at mid- or low- latitude, which is similar to that at high latitude in the northern hemisphere by Juramy et al. (1981). This oscillation has been frequently observed, especially in winter. We may consider that the oscillatory variation has been caused by dynamic processes rather than by photochemical ones because the solar activity has been very weak in winter in the polar region.

Fortunately we had a chance to study a rare occurrence with the appearance of an aurora that largely influenced the profile and abundance of the sodium layer. These variations are compared with those of the geomagnetic field and of the cosmic noise absorption (CNA) observed by a Riometer. It is found that the abundance suddenly decreases when associated with a geomagnetic field and the CNA decreases when the breakup of the aurora occurs. Moreover the topside of the layer appears to be modified by that breakup. From a sequence of observations under the existing aurora it has been observed that the modification of the layer by the appearance of this aurora is related to the decrease of CNA rather than the geomagnetic variation.

References

- (1) D. M. Simonich, B. R. Clemesha and V. W. J. H. Kirchhoff;
J. Geophys. Res. 84, 1543 (1979)
- (2) P. Juramy, M. L. Chanin, C. Megie, G. F. Toulainov and Y. P. Doudoladov; J. Atmos. Phys. 43, 209 (1981)

Table 1 Characteristics of lidar system	
Transmitter	
wavelength	Ruby 694 nm 347 nm YAG 589 nm
Energy	0.8J/pulse 0.3J/pulse 0.2J/pulse
Linewidth	
Pulse width	38ns 0.003nm
Repetition rate	0.5 Hz 500ns 0.5Hz
Receiver	
Telescope Dia.	0.5 m 0.1 - 10 km { Photon counting mode }
Height resolution	7.5 - 750 m { Analog mode }

N87

10346

UNCLAS

LIDAR DETECTION OF METALLIC SPECIES
AT THE MESOPAUSE LEVEL

C. Granier, J.P. Jegou and G. Mégie
Service d'Aéronomie du CNRS - B.P.3 -
91370 Verrières le Buisson France

The measurement alkali species present in the atomic form at the mesopause level has been performed by lidar for more than ten years. Atomic and ionic calcium density profiles are obtained for 3 years by the same technique in the visible range, at 423 nm for atomic calcium, and 393 nm for ionic calcium Ca^+ . The experimental set-up and the preliminary results have been presented in Granier et al. (1985). The 423 nm wavelength is directly obtained by the emission of a dye laser pumped by the third harmonic of a Nd-Yag laser. For the generation of the 393 nm wavelength, we have used frequency mixing : the emission at 624 nm of a dye laser pumped by the 2nd harmonic of a Nd-Yag laser is mixed with the fundamental infrared emission (remaining after frequency doubling), in a non-linear KDP crystal, which gives the 393 nm emission.

Atomic calcium

Measurements of the atomic calcium densities have been performed over 31 nights between December 1982 and December 1985. The atomic calcium layer is situated between 80 and 105 km, and the calcium averaged total content is $1.8 \cdot 10^7 \text{ cm}^{-2}$. We have compared the behaviour of the two atomic species, calcium and sodium, which are in the same altitude range, and besides present a similar abundance in the meteoric source. Simultaneous lidar measurements of these two species are available for 17 nights distributed over 3 seasons, summer, autumn and winter. Table 1 presents the averaged calcium contents and the corresponding sodium ones.

The atomic calcium content is always much lower than the sodium one, the averaged sodium to calcium abundances ratio being about 140. As it has been usually observed at mid-latitudes, the sodium content presents an important seasonal variation between summer and winter ; however, no significant seasonal variation can be noticed on the atomic calcium data. Typical calcium profiles obtained in different seasons will be presented and compared.

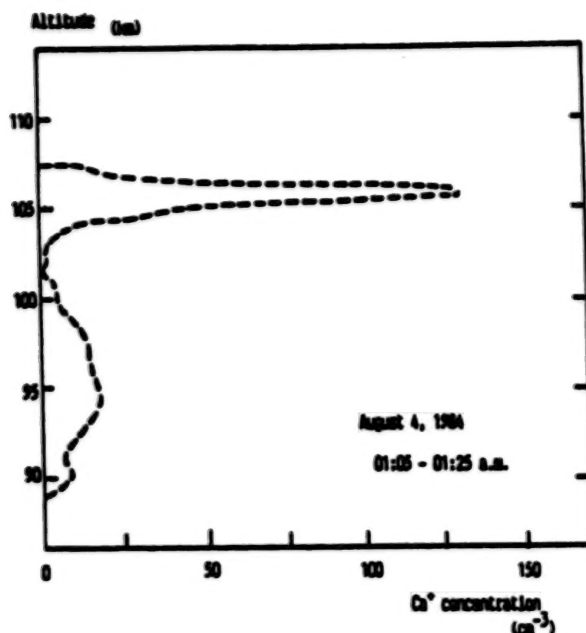
		Ca	Na
DECEMBER 1982	(1)	$9.1 \cdot 10^6$	$5.7 \cdot 10^9$
OCTOBER 1983	(1)	$2.4 \cdot 10^7$	$9.9 \cdot 10^8$
JULY 1984	(3)	$1.2 \cdot 10^7$	$1.2 \cdot 10^9$
AUGUST 1984	(4)	$2. \cdot 10^7$	$2.1 \cdot 10^9$
OCTOBER 1984	(2)	$2.3 \cdot 10^7$	$2.3 \cdot 10^9$
DECEMBER 1985	(6)	$1.9 \cdot 10^7$	$3.2 \cdot 10^9$
AVERAGED TOTAL CONTENT		$1.8 \cdot 10^7$	$2.5 \cdot 10^9$

Table 1 - Monthly averaged calcium and sodium total content (atoms.cm⁻²).

Ionic calcium

For 45 % of the observations, no ionic calcium has been detected : the ionic calcium abundance was thus below the detection threshold, estimated to be $6 \cdot 10^6$ cm⁻². Contrasting with the density profiles of the atomic species, sodium and calcium, the ionic calcium profiles present important variations on small time scales.

For 50 % of the effective observations (19 nights), the density profile shows a very thin layer centered at altitudes higher than 100km, in which the ionic density varies very rapidly from 100 to 1000 cm⁻³, which corresponds to total abundance values from $3 \cdot 10^7$ to 10^8 ions.cm⁻². The existence of such layers has been attributed to the presence of sporadic-E layers. For 20 % of the effective observations, the ionic layer is more diffused and centered around 91-95 km. The averaged ionic calcium content in these layers is about $2 \cdot 10^7$ cm⁻², which can be compared with the $1.8 \cdot 10^7$ cm⁻² value of the atomic calcium averaged content. The rest of the effective observations shows profiles combining the preceding features as shown for example in fig. 1, which represents a ionic calcium profile obtained on August 4, 1984.



Ca⁺ content : 89.2 < z < 101.2 km : 1.5 10⁷ cm⁻²
 101.8 < z < 107.8 km : 1.4 10⁷ cm⁻²

Fig. Ionic calcium profile obtained on August 4, 1984, between 1.05 and 1.25 a.m.

The main characteristics of the atomic and ionic calcium behaviours we can deduce from these measurements are :

- the atomic calcium content is more than 100 times lower than the sodium one, though they have similar abundances in the meteoric source
- no significant seasonal variation of the calcium atom has been observed
- atomic and ionic calcium total contents have similar values, when profiles in the same altitude range are compared

Other metallic elements

In order to improve our knowledge on the atomic metallic species behaviour, it would be important to obtain measurements of at least one of the major metallic meteoric elements : the iron atom has a resonance wavelength in the visible range at 372 nm, and it is thus possible to detect it from the ground, as demonstrated by the photometric observations of Tepley et al. (1981). For lidar experiments, this resonance wavelength can be obtained by different techniques :

- frequency mixing of the fundamental emission of a Nd-Yag laser (1.064 μ m) and of the 572 nm emission of a dye laser
- frequency doubling of the 744 nm emission of an Alexandrite solid laser possessing spectral narrowing and wavelength tunability

The feasibility of this experiment is in progress.

44801-58W

References

- Granier C., Jegou J.P., Mégie C. (1985)
Resonant lidar detection of Ca and Ca⁺ in the upper
atmosphere.
Geophys. Res. Lett., 12, 10, 655-658.
- Tepley C.A., Meriwether J.W., Walter J.C.G. (1981)
Observations of neutral iron emission in twilight spec-
tra.
J. Geophys. Res. 86, 4831-4835.

N87

10347

UNCLAS

DAYTIME LIDAR MEASUREMENTS OF TIDAL WINDS IN THE MESOSPHERIC
SODIUM LAYER AT URBANA, ILLINOIS

K. H. Kwon, D. C. Senft, C. S. Gardner, D. G. Voelz and C. F. Sechrist, Jr.

Department of Electrical and Computer Engineering
University of Illinois at Urbana-Champaign
Urbana, Illinois 61801

F. L. Roesler

Department of Physics
University of Wisconsin
Madison, Wisconsin 53706

SUMMARY

For more than 15 years lidar systems have been used to study the chemistry and dynamics of the mesospheric sodium layer. Because the layer is an excellent tracer of atmospheric wave motions, sodium lidar has proven to be particularly useful for studying the influence of gravity waves and tides on mesospheric dynamics. These waves, which originate in the troposphere and stratosphere, propagate through the mesosphere and dissipate their energy near the mesopause making important contributions to the momentum and turbulence budget in this region of the atmosphere. Recently, the UIUC sodium lidar was modified for daytime operation so that wave phenomena and chemical effects could be monitored throughout the complete diurnal cycle. This paper describes the results of continuous 24 hour lidar observations of the sodium layer structure and presents measurements of the semidiurnal tidal winds.

The first daytime sodium lidar measurements were reported by Gibson and Sandford [1972] at Winkfield, UK (51°N , 1°W). Their measurements were obtained on a total of 7 days in 1971 and 1972 and revealed no pronounced change in sodium abundance between day and night. Granier and Megie [1982] reported daytime observations at Haute Provence, France (44°N , 6°E) which also showed no consistent diurnal or semidiurnal variations in the layer. The most extensive set of daytime lidar measurements was reported by Clemesha et al. [1982] and Batista et al. [1985]. Their data were obtained at Sao Paulo, Brazil (23°S , 46°W) during 10 days in May 1981 and included one period of 100 hours of continuous measurements. Significant semidiurnal variations in the column abundance and centroid height were observed and attributed to the semidiurnal tide. The measured peak-to-peak abundance variation was approximately 30% and the peak-to-peak centroid displacement was approximately 2 km. Tidal perturbations of the nocturnal sodium layer are often observed at Urbana (40°N , 88°W) [Gardner et al., 1986] where vertical wind velocities due to the semidiurnal tide of up to 30 cm s^{-1} with vertical wavelengths of the order of 50 km have been measured.

During the late summer and early fall 1985, the UIUC lidar system was modified for daytime operation. The modifications were required to reduce the high background photocount level from the bright daytime sky. The 1.22 m diameter Fresnel lens telescope was replaced by a diffraction limited 0.35 m diameter astronomical telescope (Celestron 14). The planar field of view of the telescope was reduced to 0.7 mrad and a pressure-tuned etalon filter was added to reduce the bandwidth to 33 pm FWHM. The laser divergence was also reduced to about 0.7 mrad ($\text{FW @ } e^{-2}$) by expanding the beam by a factor of 22.

The first daytime measurements were obtained at Urbana on October 5, 1985. Continuous 24 hour measurements were first made on January 15 and 16, 1986. Figure 1 is a summary of the profiles collected during these two days. The layer column abundance, centroid height and rms width are plotted versus time in Figure 2. Notice the strong semidiurnal oscillations in these parameters. The abundance varied by almost a factor of 3 reaching a maximum value of $2.5 \times 10^{10} \text{ cm}^{-2}$ at 1545 LST and a minimum value of $1 \times 10^{10} \text{ cm}^{-2}$ at 1050 LST and 2230 LST. The vertical wind velocity associated with these tidal perturbations can be inferred from the data by measuring the movement of the layer bottomside. The vertical wind velocity at 85 km altitude and the column abundance are plotted in Figure 3. A strong semidiurnal oscillation in the wind velocity is clearly evident. The 30 cms⁻¹ wind amplitude is typical of the semidiurnal tide and is consistent with recent tidal models.

This work was supported in part by the National Science Foundation Grant ATM 85-11330.

REFERENCES

1. Batista, P. P., B. R. Clemesha, D. M. Simonich and V. W. J. H. Kirchhoff, "Tidal oscillations in the atmospheric sodium layer," *J. Geophys. Res.*, **90**, p. 3881-3888, 1985.
2. Clemesha, B. R., D. M. Simonich, P. P. Batista and V. W. J. H. Kirchhoff, "The diurnal variations of atmospheric sodium," *J. Geophys. Res.*, **87**, p. 181-186, 1982.
3. Gardner, C. S., D. G. Voelz, C. F. Sechrist, Jr. and A. C. Segal, "Lidar studies of the nighttime sodium layer over Urbana, Illinois. 1. Seasonal and nocturnal variations," *Electro-Optic Systems Laboratory, EOSL 86-001, University of Illinois (UILU-ENG-85-2547)*, January 1986.
4. Gibson, A. J. and M. C. W. Sandford, "Daytime laser radar measurements of the atmospheric sodium layer," *Nature*, **239**, 509-511, 1972.
5. Granier, C. and G. Megie, "Daytime lidar measurements of the mesospheric sodium layer," *Planet Space Sci.*, **30**, 169-177, 1982.

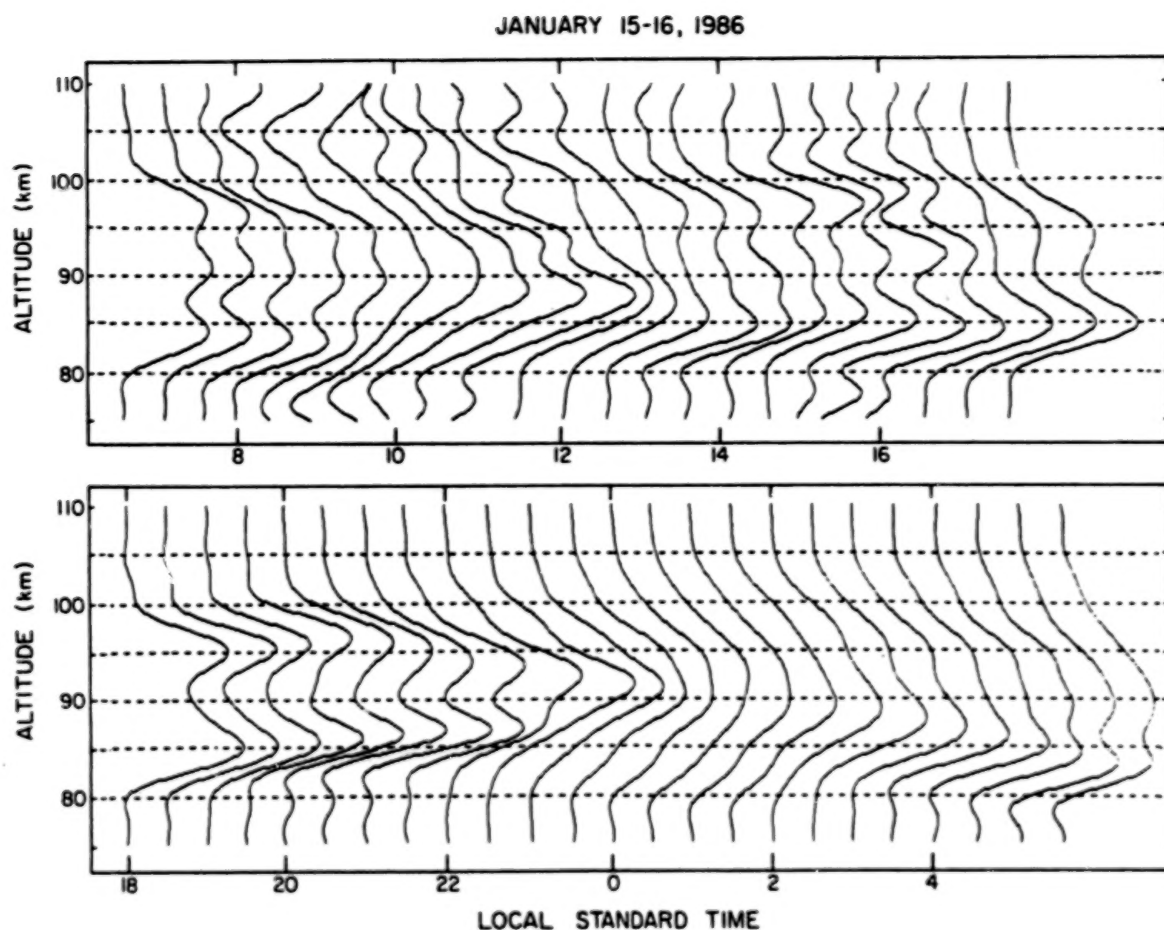


Figure 1. Na density profiles measured during the 24 hour period starting at 0600 LST on January 15, 1985 and ending at 0600 LST on January 16, 1985. The profiles are plotted at 30 min intervals and have been low-pass spatially filtered with a cutoff frequency of 0.16 km^{-1} .

JANUARY 15-16 1986

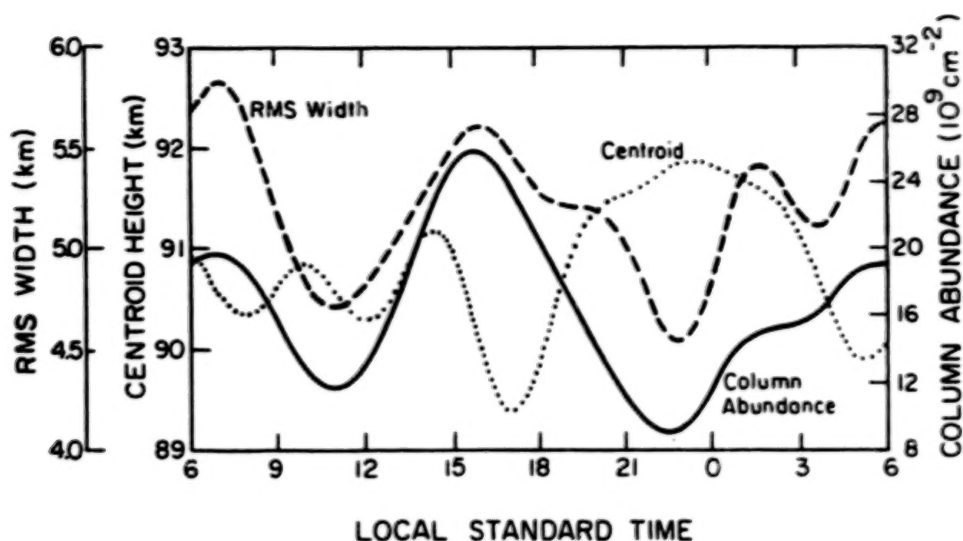


Figure 2. Temporal variations of the layer column abundance, centroid height and rms width measured during the 24 hr period starting at 0600 LST on January 15, 1986. The data were low-pass filtered with a spatial cutoff frequency of 0.05 km^{-1} and a temporal cutoff frequency of 0.25 hr^{-1} .

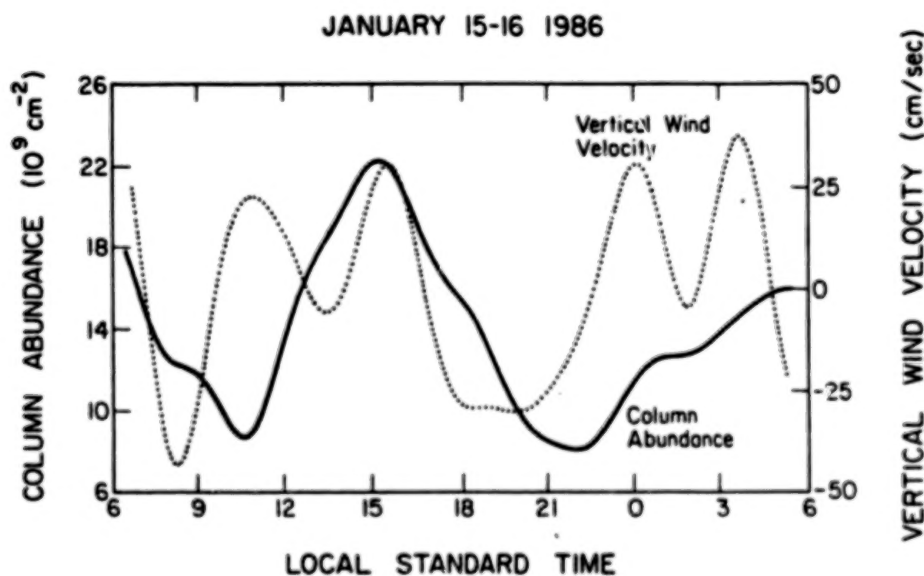


Figure 3. Comparison of the measured column abundance and vertical wind velocity (@ 85 km altitude). To eliminate shorter wavelength gravity wave perturbations the density profiles were initially low-pass spatially and temporally filtered with respective frequency cutoffs of 0.05 km^{-1} and 0.33 hr^{-1} . The wind velocity was then determined from the displacement of the bottomside of the filtered profiles.

N87

10348

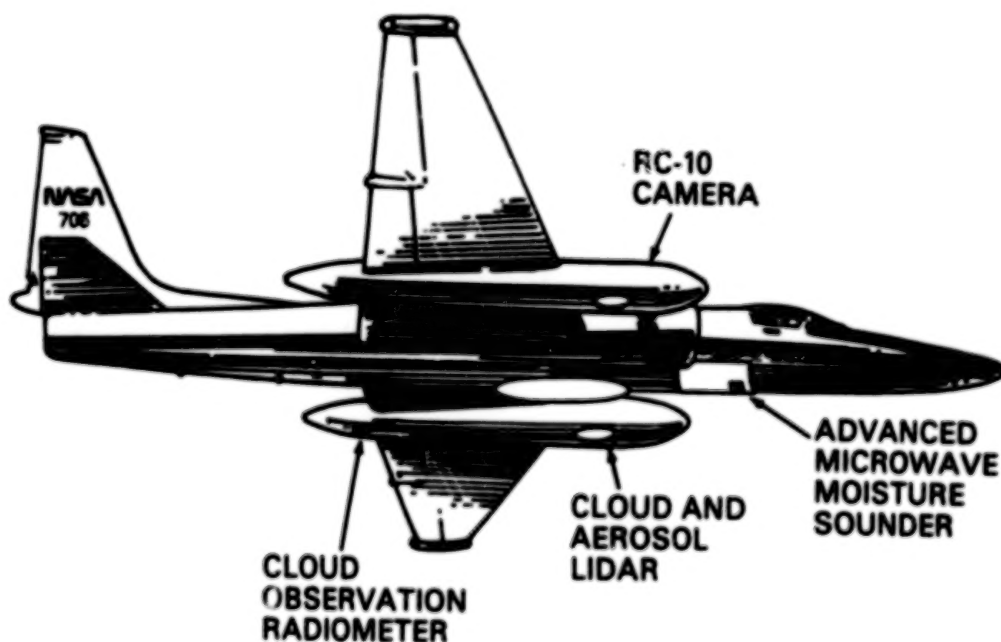
UNCLAS

LIDAR STUDY OF STORM TOPS

J. D. Spinhirne and W. D. Hart
Laboratory for Atmospheres, NASA Goddard Space Flight
Center, Greenbelt, MD 20771, U.S.A.

Satellite thermal and visible observations are routinely used for storm tracking and diagnostics. In recent years attempts have also been made to apply satellite measurements to the study of evolutionary factors for storms such as divergence and subsidence mechanisms. These studies involve analysis of the thermal height structure of the storm tops as obtained from the satellite observations. An outstanding problem is the importance of emissivity effects for the interpretation of the storm top thermal radiance measurements. In part to understand the correct interpretation of satellite observations, a storm top observation experiment involving advanced instrumentation on board a high-altitude NASA aircraft has been in progress. A downlooking lidar system has been an important part of the instrument complement. A combined analysis of the lidar return data and thermal radiance measurements has been developed to study cloud top emissivity effects and their relation to satellite observations.

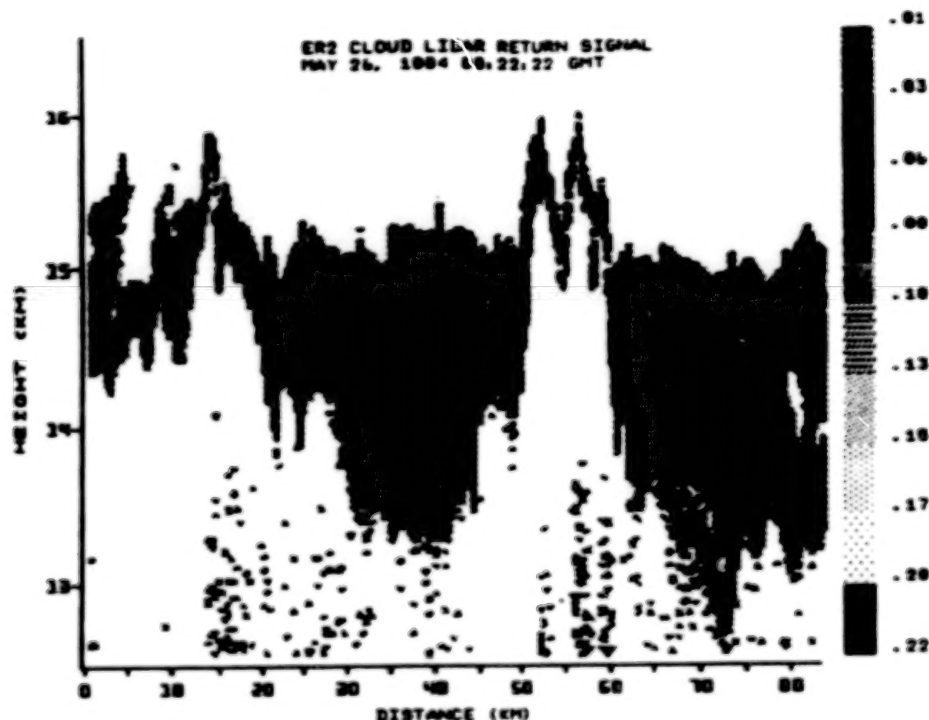
As shown in the first figure, the cloud and aerosol lidar experiment has been flown on board the ER-2 aircraft along with a



Cloud and storm observation experiment

ORIGINAL PAGE 55
OF POOR QUALITY

multi-spectral scanning radiometer and a microwave sounding instrument. A description of the lidar system and initial results for lidar observations of the structure of severe storm tops have been given in Spinhirne et al. (1983). The most recent experiment was a study of midwest severe storms in May 1984. An example of the lidar return data for an 80 km flight line over an intense storm is shown in the second figure. The flight data

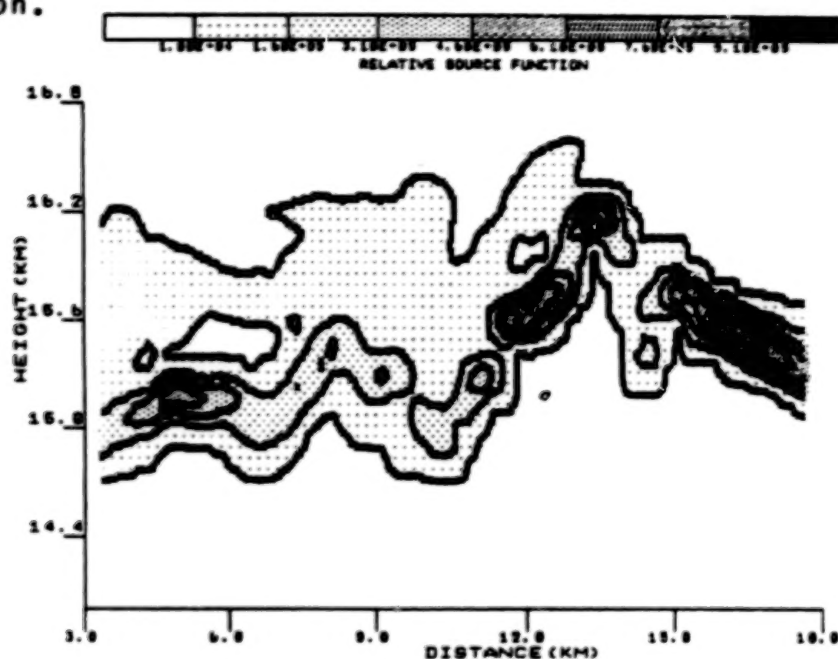


Lidar return from storm top

indicate several overshooting convective towers surrounded by areas of diffuse cloud structure. The nadir radiance measurement at 11 μ m corresponding to each lidar return is obtained from the cloud radiometer.

The thermal radiation emission from a cloud top is related to the vertical cloud temperature and the vertical particle density structure. An analysis of the thermal radiance based on the lidar return data is possible since the lidar return is also dependent on the vertical cloud density. The initial procedure of the combined analysis is a correction of the backscatter lidar return signal for the apparent attenuation. The assumption is made that the optical characteristics of the cloud particles are constant with altitude, and a constant factor which relates the lidar backscatter cross section to the thermal absorption cross section may then be derived. The actual solution involves an iterative procedure. The emitted radiance is calculated from the absorption cross section profile and an assumed vertical

temperature structure. An example of the result for a segment of the flight line shown in the second figure is given in the third figure. The contribution to the radiance from a given cloud top area would be proportional to the indicated relative source function.



Relative contribution function for the emitted thermal radiance of a cloud top segment

The following preliminary conclusions may be presented. The density for the top of convective cells overshooting the tropopause is such that the observed brightness temperature gives an accurate measurement of the cloud top temperature. The penetrating cells are surrounded by a diffuse anvil structure from which the upward radiation at the cloud top may arise from several kilometers into the cloud. Isolated cirrus layers, which are at times found in the stratosphere overlying the storm tops, are typically too thin and of too limited an areal extent to have an important effect on the observed thermal brightness. Such results may be applied to give a clearer dynamical interpretation from satellite observations of storm systems.

REFERENCE

Spinhirne, J. D., M. Z. Hansen, and J. Simpson, 1983: The structure and phase of cloud tops as observed by polarization lidar. J. Clim. Appl. Meteo., 22, 1319.

N87

10349

UNCLAS

INVESTIGATION OF CLOUDS SPATIAL DISTRIBUTION USING GROUND-BASED LIDAR

I.N. Kolev, O.P. Parvanov, B.K. Kaprielov, I.K. Ilev
Institute of Electronics-Bulgarian Academy of Sciences
Sofia, Bulgaria

Certain investigations of spatial distribution of clouds by employing ground-based lidar are presented.

The great changeability is one of the main properties of the clouds in the boundary layer. As a result, their optical properties change rapidly which complicates the modelling of cloud evolution/1/. Suitable equipped lidars are widely used for diagnostics of the clouds via a number of scattering and absorption processes. In particular, lidar can provide information on the distribution of meteorological parameters and of the other important cloud characteristics both in vertical and horizontal directions.

The well-known inhomogeneities in vertical direction might be accounted to a certain extent for heavy gradients of the meteorological parameters in the clouds. However in the case of S_t and S_c types these gradients are negligible in the horizontal direction /2/ and nevertheless certain inhomogeneities were found to exist.

In the represented work the time and spatial distribution of the aerosol backscattering coefficient of S_t and S_c clouds was investigated by means of a correlation analysis of the lidar-obtained data provided from several arbitrary directions and heights.

Similar measurements of the other cloud characteristics were conducted basically by means of air-planes /2,3/.

The three-beam lidar employed for the present investigation is a twenty-four-hour running computerized ground-based system /4/ using Q-switched second harmonic YAG:Nd³⁺ laser of about 35 mJ with variable repetition rate from 1 to 10 Hz as the transmitter and a 0.15 m telescope as the receiver. The 64 K byte RAM computer controls the data acquisition system and stores the data on a floppy disc. The scheme of sounding is shown on Fig. 1.

The lidar designed at our institute permits time and spatial distribution of the aerosol backscattering coefficient close to the cloud base to be obtained and in the case of low density to be penetrated for a few hundred meters.

The results of the analysis are presented in the form of autocorrelation function curves computed from return signals which are proportional to the aerosol backscattering coefficient value /5/. The time scales at half amplitude are determined. Different methods have been used hence to estimate the spatial dimensions: firstly, theodolite measurements of the wind velocity in the area of the cloud base, secondly, determination of the distance between remote located signal volumes in

which the autocorrelation functions are still selfsimilar and thirdly, proceeding from the horizontal clouds motion velocity derived by using correlation techniques applied to the lidar returns. All three methods have led to similar results and can be used versus the lidar properties and the synoptic situation. The determined spatial dimensions locate areas in which the mean value of the aerosol backscattering coefficient is constant.

Fig. 2 shows three autocorrelation functions computed from data which have been simultaneously obtained from three space volumes at the same height $H=360$ m in case of S_t clouds with thickness $\Delta H \sim 100-150$ m on Nov. 11-th 1983. Proceeding from the determined wind velocity of 4-5 m/s the spatial dimensions have been estimated within 20 to 150 meters.

Fig. 3 shows autocorrelation functions related to S_c clouds. The curve shapes are smoother than those from the S_t clouds which points to more revealed details in stratus cumulus. In this case the mean spatial dimensions have been estimated within 380 to 580 meters.

Fig. 4 shows autocorrelation functions which conform to the data simultaneously obtained from four heights ($H_1=200$ m, $H_2=225$ m, $H_3=250$ m and $H_4=400$ m) in case of S_t clouds. To simplify the drawing only curves bearing on one direction are shown (from other directions the picture is similar to that shown).

Autocorrelation functions derived from different heights in the clouds are in good agreement with the results of studies by air-planes which show that the low part of the clouds is considerably more inhomogeneous than their middle part. This fact might be visually seen when observing the cloud base (from below) which shows great changeability obviously caused by considerable turbulence. Apparently the lower degree of inhomogeneity of the middle part of clouds is conditioned by the so-called "retentive layer" located above the clouds /2/.

The shapes of the autocorrelation function curves (Fig. 2) might be related to the local microstructure of the S_t clouds too. During the air-plane investigations of the local characteristics of stratus it had been found that the particle size changeability coefficient value was about 7-8 percent and the particle concentration changeability coefficient value ranged from 3 to 5 percent in the middle part of the S_t clouds whereas in the low part those coefficients increased to a values of 25 and 60 percent respectively.

In conclusion it should be noted that the obtained lidar data contained information about the temporal and spatial changes of the cloud base and in certain cases (low density) of the cloud top as well. When wave motions have existed in the atmosphere their undulation characteristics like wavelength, amplitude, speed rate and height of display have been determined /4/.

References:

1. Carswell A.I., p. 318 in "Optical and Laser Remote Sensing",

- edited by D.K. Killinger and A. Mooradian, 1983, Springer.
2. Matveev L.G., "Physics of the Atmosphere, Leningrad, Gidrometeoizdat, 1976.
 3. Judin K.B., Some Results of Local Characteristic Measurements of Stratus Form Clouds, Meteorol. and Hydrol., 12, (1976), p44.
 4. Kolev I., O.Parvanov, B.Kaprielov, Remote Determination of Orographic Undulation Characteristics from Lidar Measurements, 12-th International Laser Radar Conference, Aix-En-Provence, France, 1984, p. 399.
 5. Zuev V.E., G.G.Matvienko, I.N.Kolev, O.P.Parvanov, Laser Sounding of Wind Velocity Using a Correlation Method, 12-th International Laser Radar Conference, Aix-En-Provence, France, 1984, p. 145.

BIBLIOGRAPHY

Kolev I.N., O.P.Parvanov, R.P.Svramova, B.K.Kaprielov, I.K.Ilev, Lidar Measurements of Cloud Formation Drift Velocity, Bulg. Geophys. J., XI, 4, (1985).

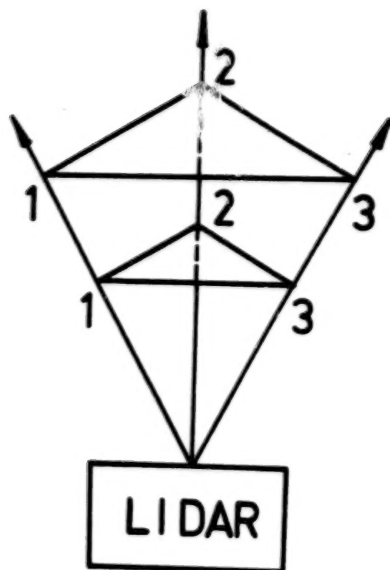


Fig.1

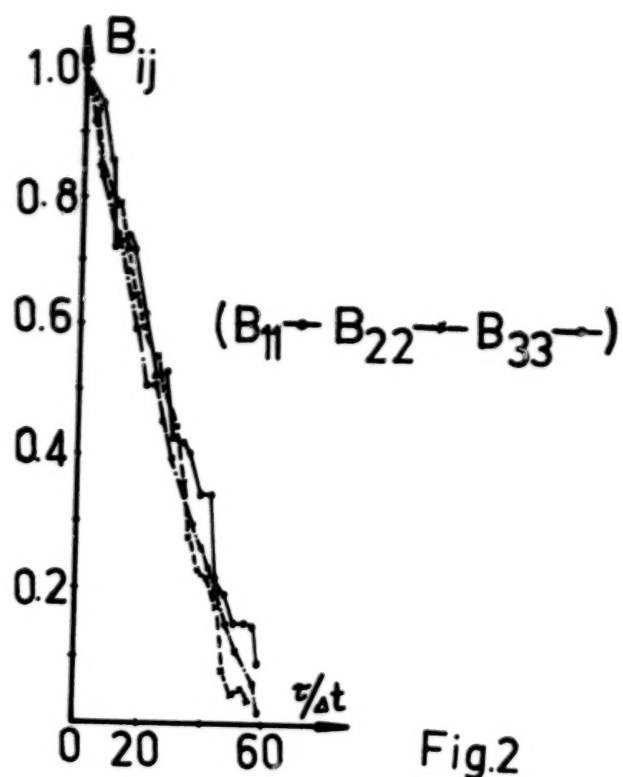


Fig.2

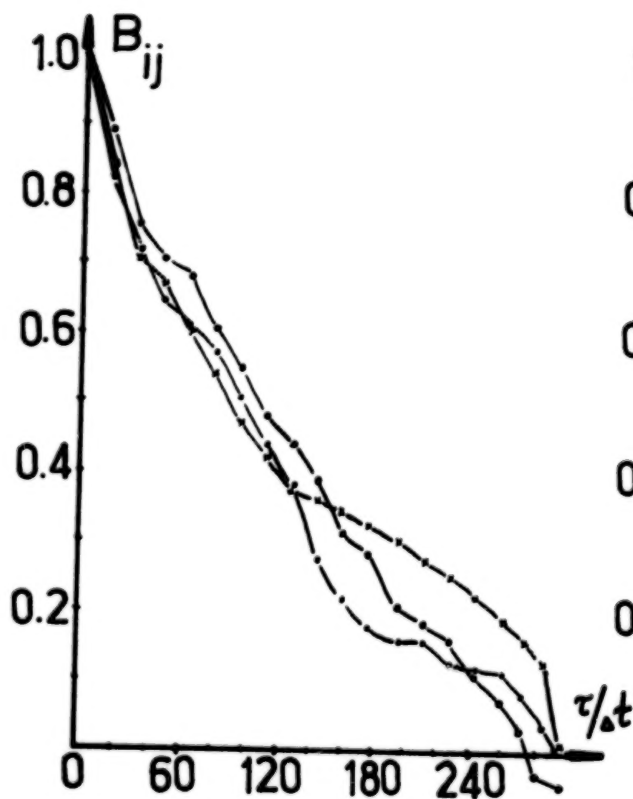


Fig.3 ($B_{11} \rightarrow B_{22} \rightarrow B_{33}$)

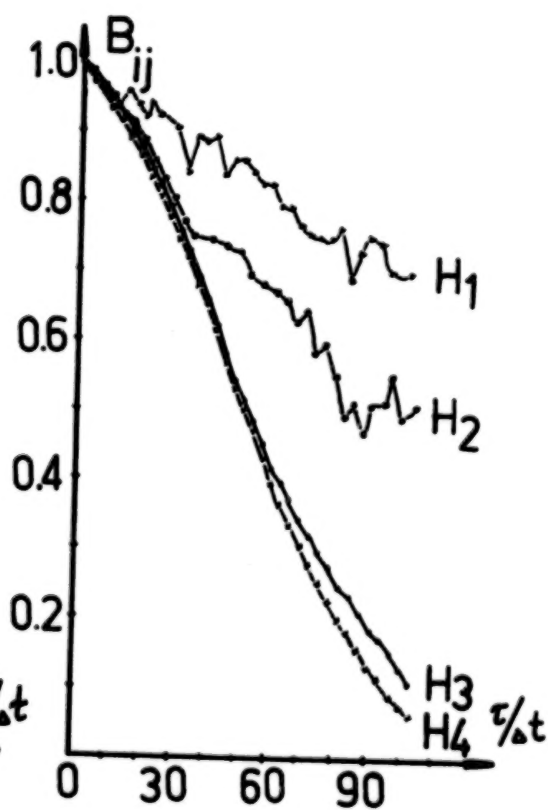


Fig.4

N87

103550

UNCLAS

MULTIPLE SCATTERING DEPOLARIZATION IN MARINE STRATUS
CLOUDS: LIDAR EXPERIMENTS

Kenneth Sassen and Richard L. Petrilla*

Department of Meteorology
University of Utah
Salt Lake City, Utah 84112

ABSTRACT

The depolarization of ruby lidar backscattering caused by multiple scattering in marine stratus clouds has been examined systematically from a field site on the southern California coast. Investigated were the effects on the linear depolarization ratio δ of lidar receiver field-of-view (FOV), elevation angle and laser beam pointing errors. An approximately linear increase in maximum δ values was observed with increasing receiver FOV, and the importance of accurate transmitter/receiver beam alignment was demonstrated during experiments in which the laser axis was deliberately misaligned. An elevation angle dependence to the δ values was observed as a consequence of the natural vertical inhomogeneity of water cloud content above the cloud base. Time histories of the depolarization characteristics of dissipating stratus clouds revealed significant spatial and temporal variability in δ values attributed to cloud composition variations. Employing a 1 mrad transmitter FOV, maximum δ values of 0.21 and 0.33 were observed with 1 and 3 mrad receiver FOVs, respectively, from the low stratus clouds. The fundamental causes and effects on the lidar equation of multiple scattering will also be discussed.

*Current Affiliation: Electronic System Division, Hanscom Air Force Base, MA 01731.

N87

10351

UNCLAS

NEAR-IR EXTINCTION AND BACKSCATTER COEFFICIENT
MEASUREMENTS IN LOW- AND MID-ALTITUDE CLOUDS

Z. G. Sztankay
U.S. Army Laboratory Command
Harry Diamond Laboratories
Adelphi, MD 20783, USA

Knowledge of the attenuation and backscattering properties of clouds is required to high resolution for several types of optical sensing systems. We obtained such data in about 15 hours of flights through clouds in the vicinity of Washington, D.C. The flights were mainly through stratocumulus, altocumulus, stratus, and stratus fractus clouds and covered an altitude and temperature range of 300 to 3200 m and -13 to 17 C.

Two instruments were flown, each of which measured the backscatter from close range in two range bins to independently determine both the extinction and backscatter coefficients. One instrument was a short-range, ≈ 6 -ns pulse length lidar system using a 0.9- μ m injection laser source. The two receiver channels of this system measured the backscatter from 1.5- and 4.0-m range at 30 Hz, providing an along-flight measurement resolution of about 1.3 m at a 75-kt airspeed. The other instrument was an arc-lamp source nephelometer with a 0.8- to 1.0- μ m spectral response and two independent transmitter/receiver channels with optically limited sensitivity regions at ranges of 4 and 8 m. Figure 1 shows the sensitivity versus range curve of this instrument as measured with a diffusely reflecting target board. The along-flight resolution of the nephelometer was about 3 m. As illustrated in figure 2, both instruments looked in a direction perpendicular to the flight path and provided data as a function of position along this trajectory. The flight paths were generally horizontal along a straight trajectory; the processed data, therefore, provide maps of the variation of the measured parameters along a horizontal line through the clouds.

The extinction and backscatter coefficients can be obtained from the signals in the two channels of each instrument, provided that the aerosol is uniform over the measurement region. When this assumption holds, the extinction coefficient is derived basically from the ratio of the signal in the two channels; the backscatter coefficient can then be obtained from the signal in either channel. The calculation procedure takes into account the precise sensitivity versus range curve (and pulse shape in case of the lidar) of the instrument. The systems are calibrated using standard targets on the ground, and fiber-optic coupled reference pulses account for system sensitivity changes. Multiple scattering effects are minimized but not entirely eliminated by the narrowness of the fields of view.

Both channels of the nephelometer measure backscatter from an angular range of 178.2 to 179.8 deg. This slight difference from pure backscatter is insignificant for many aerosols but makes a sizeable difference for clouds. Figure 3 shows the results of Mie scattering calculations of the 0.9- μ m backscatter-to-extinction ratio, or $1/4\pi$ times the normalized phase function, for Deirmendjian's¹ Cl cloud distribution, and for Cl-type distributions with mode radii of 3, 6, and 8 μ m instead of Deirmendjian's 4 μ m. It is apparent that the backscatter-to-extinction ratio in the range of the nephelometer's angular region is significantly less than it is at 180 deg. The lidar

angular range was farther from 180 deg, and in addition was not equal in the two channels; this inequality also affects its extinction measurements. The results of the lidar measurements were therefore used mainly to confirm variation of the coefficients with position as determined from nephelometer data and to obtain approximate but very high spatial resolution maps.

Figures 4 and 5 show examples of the results calculated from the nephelometer data. Figure 4 is an extinction coefficient plot for a straight flight path at an altitude of 950 m through a stratocumulus cloud. Scattered points far removed from the main curve and widely fluctuating regions such as near the 4-km point are probably the result of lack of uniformity of the cloud in the measurement region. This cloud segment exhibits structure that is about median among our data, with many clouds being more uniform and others showing gradients as great as our instruments could resolve.

The backscatter-to-extinction ratio F of the same cloud segment is shown in figure 5. Note that F is relatively constant over the first half of this cloud, where the extinction coefficient varies roughly from 50 to 200 km^{-1} . In the second half of the cloud, F at first has a constant but lower value, then decreases slowly; F also shows a decrease at the sharp break in the middle of the plot where the extinction coefficient almost goes to zero. The general trend in these data, including the decrease in the middle, is also seen in the lidar results for this segment. Similar results were obtained in many other cloud segments, although still other segments showed a constant F while the extinction coefficient varied greatly.

We interpret the variations in F as evidence of different size distributions. This does not contradict Derr² and Pinnick et al.,³ who obtained a relatively constant $F(\pi)$ by Mie calculations for various size distributions appropriate for clouds. While our calculations also show that $F(\pi)$ varies little for Ci clouds with mode radii varying from 2 to 8 μm , they show that $F(178 \text{ to } 180 \text{ deg})$ varies considerably for those same clouds. This variation, seen in figure 3, results because the backscatter lobe width is strongly size-dependent.

The median value of the extinction coefficient for all our nephelometer-obtained data was 70 km^{-1} . This compares well with values calculated by Carrier et al.⁴ for his continental stratus and stratocumulus models. The maximum levels attained in all our flights, where we endeavored to sample the densest clouds we could reach, was around 300 km^{-1} .

The median value of the backscatter-to-extinction ratio F for all our data was 0.034 sr^{-1} . This compares to a median of 0.038 sr^{-1} from Mie calculations in the same 178 to 180 deg angular range for Deirmendjian Ci clouds with mode radii of 3, 4, 6, and 8 μm . (The same calculations show a median $F(\pi) = 0.052 \text{ sr}^{-1}$.) The median values for individual flights ranged from 0.024 to 0.051 sr^{-1} . The variation of F within a given flight was usually 20 to 25 percent to the 3-dB points of the distribution, including both the apparently real variations due to different size distributions and variations due to cloud nonuniformity within the measurement volume and instrumentation noise.

References

1. Deirmendjian, D., "Electromagnetic Scattering on Spherical Polydispersions," American Elsevier, 1969.
2. Derr, V. E., "Estimation of the Extinction Coefficient of Clouds from Multiwavelength Lidar Backscatter Measurements," Appl. Opt. 19, 2310 (1980).
3. Pinnick, R. G., Jennings, S. G., Chylek, P., and Ham, C., "Backscatter and Extinction in Water Clouds," Conf. Abstracts, Tenth International Laser Radar Conference, 6-9 Oct 80, pp 40-41.
4. Carrier, L. W., Cato, G. A., and Von Essen, K. J., "The Backscattering and Extinction of Visible and Infrared Radiation by Selected Major Cloud Models," Appl. Opt. 6, 1209 (1967).

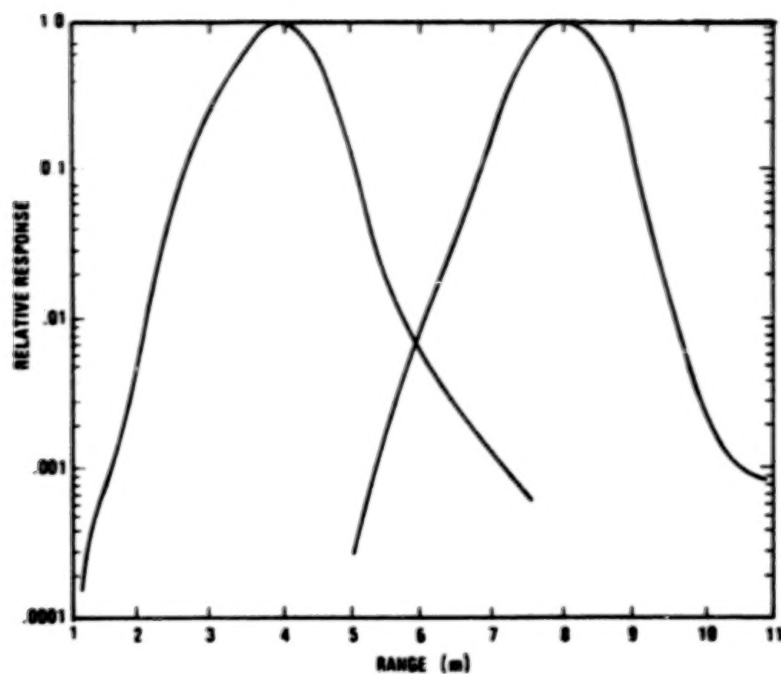


Figure 1. Sensitivity versus range curve for the two nephelometer channels.

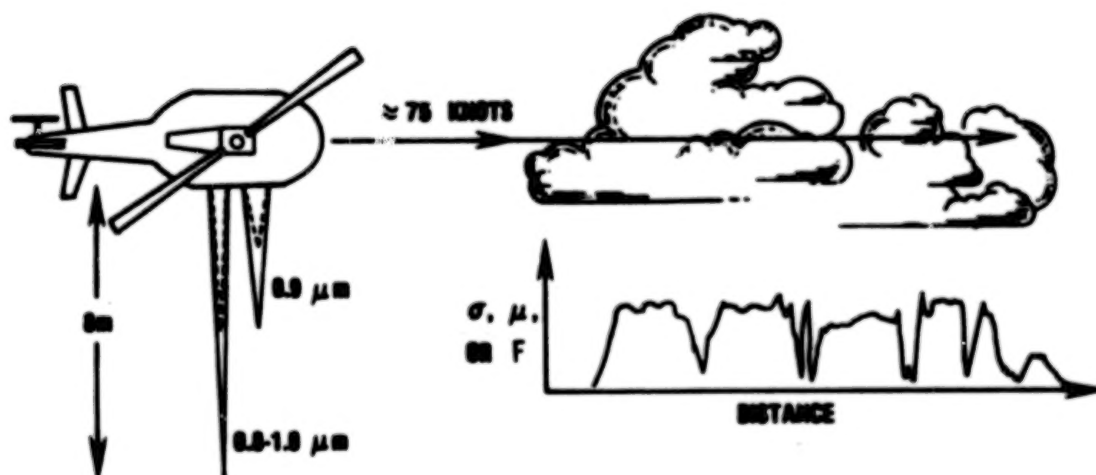


Figure 2. Schematic of cloud parameter measurements.

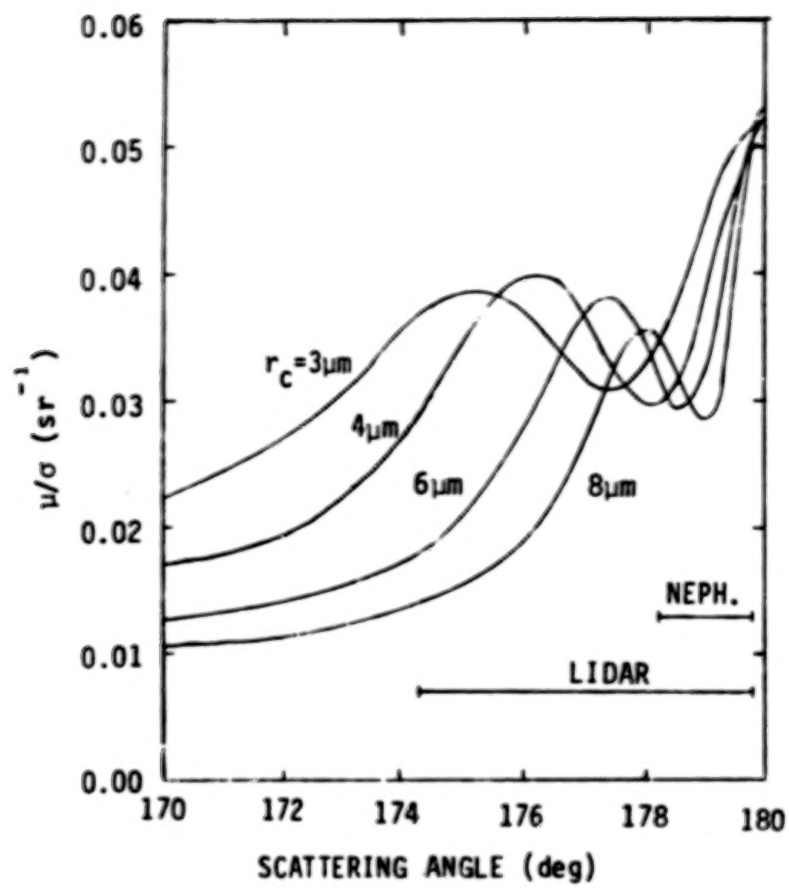


Figure 3. Calculated backscatter coefficient to extinction coefficient ratio for Cl cloud distributions with various mode radii r_c .

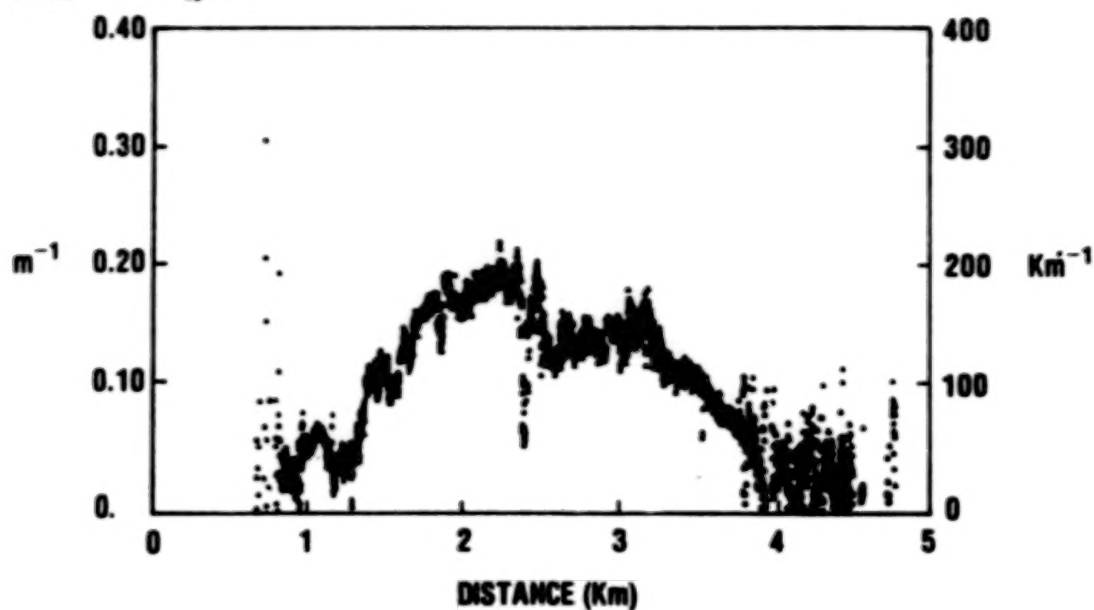


Figure 4. Extinction coefficient versus distance in stratocumulus cloud.

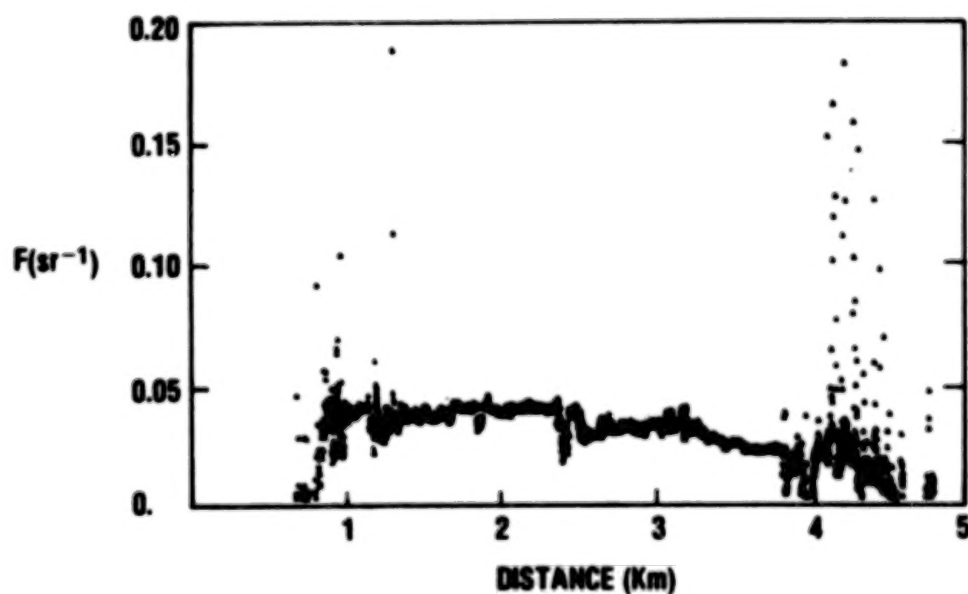


Figure 5. Backscatter coefficient to extinction coefficient ratio versus distance in same cloud segment as figure 4.

N87

10352

UNCLAS

BACKSCATTER AND EXTINCTION MEASUREMENTS IN CLOUD AND DRIZZLE AT CO₂ LASER WAVELENGTHS*

S. G. Jennings†
Department of Experimental Physics
University College
Galway, Ireland

The backscatter and extinction of laboratory generated cloud and drizzle sized water drops have been measured at CO₂ laser wavelengths (predominately at $\lambda = 10.591 \mu\text{m}$). Two distinctly different drop size regimes were studied: one which covers the range normally encompassed by natural cloud droplets ($1 < \text{radius } (r) < 20 \mu\text{m}$) and the other representative of mist or drizzle sized drops ($20 < r < 150 \mu\text{m}$).

BACKSCATTER AND EXTINCTION FOR LARGE WATER DROPS

We consider cloud and drizzle sized drops with size parameter $x \gg 12$, ($r \gg 20 \mu\text{m}$ at $\lambda = 10.591 \mu\text{m}$). The efficiency factor for extinction, Q_e , approaches 2 asymptotically for an absorbing droplet as x gets larger.¹ Also, the backscatter gain G approaches the geometrical limit which equals the reflectivity R of the material at normal incidence² where $R = \{(n-1)^2 + k^2\} / \{(n+1)^2 + k^2\}$, n and k are the real and imaginary indices of refraction; R equals 0.0078255 for water ($m = 1.179 - 0.0718 i$) at $\lambda = 10.591 \mu\text{m}$. [The calculated Mie value for $G(m, x)$ at $\lambda = 10.591 \mu\text{m}$ for $x = 150$, is equal to 0.0078258.]

The asymptotic values of Q_e and G in the expressions for extinction and backscatter coefficient lead to an appealingly simple form, independent of size distribution

$$\sigma_e / \sigma_b = 4\pi Q_e / G = 3.21 \times 10^3 \text{ sr} \quad (1)$$

Numerical calculations of extinction to backscatter ratio at $\lambda = 10.591 \mu\text{m}$ for water droplets up to radius 50 micrometres plotted in Fig. 1 show the extinction to backscatter ratio oscillating about a relatively constant value of $3.40 \times 10^3 \text{ sr}$, some six percent larger than the asymptotic limit of Eq. (1).

EXPERIMENTAL APPARATUS AND TECHNIQUES

The apparatus used to measure backscatter and extinction in water cloud is shown schematically in Fig. 2. A 1 m³

* A more complete version of this paper has been submitted to Applied Optics.

† Currently on sabbatical leave as a NRC Research Associate at the Environmental Research Laboratories, GMCC, NOAA, 325 Broadway, Boulder, Colorado 80303, USA.

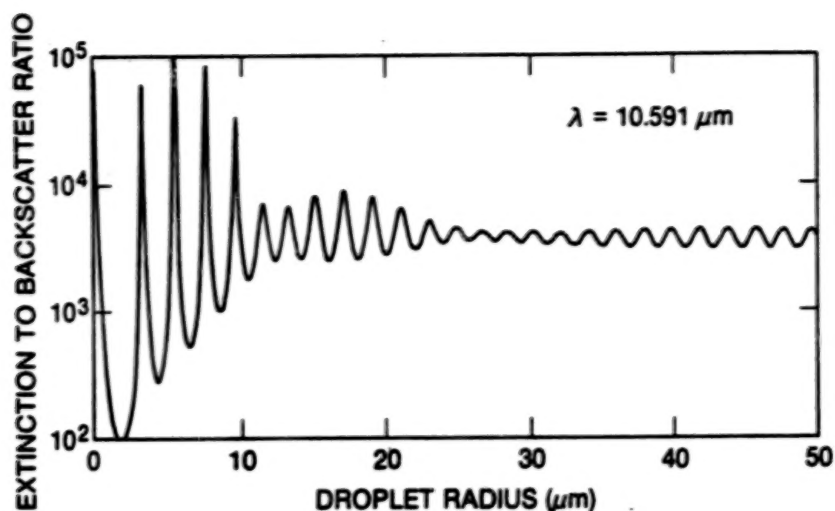


Figure 1. Extinction to backscatter ratio for water droplets versus droplet radius at wavelength $\lambda = 10.591 \mu\text{m}$ (index of refraction $m = 1.179 - 0.0718i$).

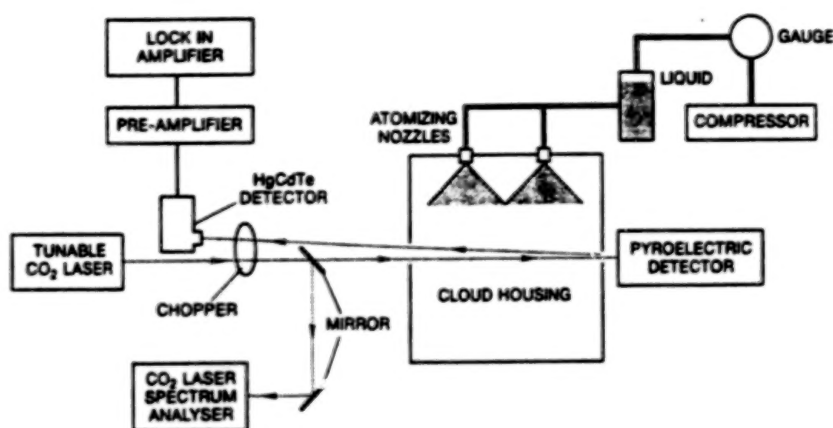


Figure 2. Schematic diagram of the experimental apparatus.

chamber of path length $L = 1 \text{ m}$ was used for all measurements. The optical arrangement used a tunable vertically polarized CO_2 laser source (Sylvania Model 941S). The main beam and reference detectors consist of a pyroelectric laser probe together with a synchronous radiometer readout.

A HgCdTe liquid nitrogen cooled $8\text{--}13 \mu\text{m}$ radiation photoconductive detector with sensing area 1 mm^2 was used for measuring the backscattered radiation. The detector was placed close to the CO_2 laser axis in the backward direction, subtending an angle not less than 177.4° with the forward direction, at the chamber centre. The signal from the detector was fed via a pre-amplifier into the input of a lock-in amplifier. The backscatter output signal from the lock-in amplifier was calibrated by directing a range of known low CO_2 laser radiation signals onto the HgCdTe detector.

Water droplet clouds were normally produced by a pair of Hanksraft spinning disk humidifiers diagonally positioned

within the cloud chamber. The cloud droplet size distribution was determined by a Particle Measuring Systems (PMS) classical scattering aerosol spectrometer probe (CSASP). A modified two-stage impactor³ mounted in a wind tunnel allowed droplet sizes greater than 14 μm radius (upper limit of the particle scattering counter) to be measured.

Drizzle sized drops with radius ranging from 20 to about 150 μm were produced by a pair of fine spray atomizing nozzles. Hydraulic pressures from 20 to 60 psi from a compressed nitrogen line applied to a stainless steel vessel containing doubly distilled water produced a cone spray drizzle pattern.

BACKSCATTER AND EXTINCTION MEASUREMENTS

Measurements of backscatter coefficient and extinction coefficient in laboratory cloud at wavelength $\lambda = 10.591 \mu\text{m}$ are presented in Fig. 3(a). Measured values taken in steady state cloud conditions using a pair of spinning disk humidifiers are indicated by the solid dots "•". The experimental points "o" represent measurements of backscatter and extinction coefficients made at five second intervals during cloud decay. Steady state measurements using a combination of two spinning disk devices together with an ultrasonic nebulizer are indicated by the points "Δ" in Fig. 3, while decay values are shown by the symbol "Δ". A measurement made at $\lambda = 10.247 \mu\text{m}$ is indicated by the symbol "■", while decay values are given by symbol "□". The horizontal and vertical "error" bars shown for a representative measurement result from an estimated ± 2 percent variation in pathlength coverage by the water droplets.

The results of the measurements for larger sized drops at wavelength 10.591 μm are shown in Fig. 3(b). Steady state measurements are represented by solid symbols (example •) while

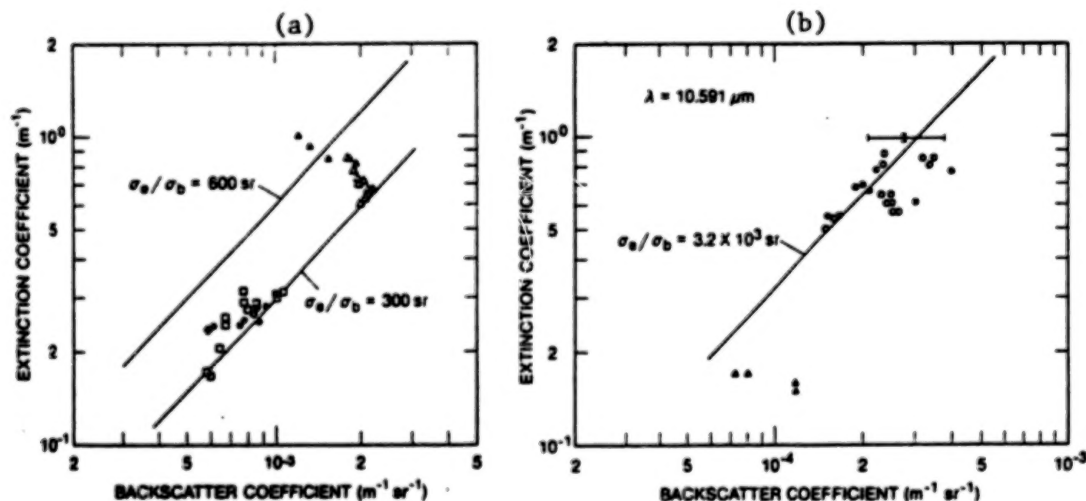


Figure 3. Measured values of backscatter and extinction coefficient for (a) laboratory cloud and (b) for larger sized (drizzle) drops at wavelength $\lambda = 10.591 \mu\text{m}$.

measurements made under cloud growth or decay conditions are shown by open symbol (example o). Most measurements were made for drizzle sized drops produced by the atomizing spray nozzles while some (represented by triangular symbols) were produced by a Micromax spinning disk spraying device.

DISCUSSION AND CONCLUSIONS

Measured extinction to backscatter ratios were generally found to range from 300 sr to about 600 sr for laboratory clouds produced by a pair of spinning disk humidifiers at $\lambda = 10.591 \mu\text{m}$ which broadly agrees with lower bound numerical values mainly representative of small scale cumulus and stratocumulus cloud calculated by Pinnick et al.⁴

The measured backscatter to extinction ratio values for drop size $> 20 \mu\text{m}$ shown in Fig. 3(b) are in reasonably good agreement (generally better than a factor 2) with the asymptotic value of 3.2×10^3 sr. The measurements also compare favorably with calculation which predicts extinction to backscatter ratios of between about 3 to 4×10^3 sr for $20 < r < 50 \mu\text{m}$ as shown in Fig. 1.

The derivation and verification of the relation, Eq. (1) between extinction and backscatter at CO_2 laser wavelengths should allow the determination of large cloud drop and drizzle extinction coefficient solely from a lidar return signal without requiring knowledge of the drop size distribution. This result will also apply to precipitation sized drops so long as they are spherical.

ACKNOWLEDGMENTS

This work has been supported by the European Research Office, U.S. Army Research, Development and Standardization Group, London, England, Contract Number DAJA37-81-C-0003.

REFERENCES

1. H. C. van de Hulst. "Light scattering by small particles." Wiley, New York (1957).
2. J. E. McDonald. "Large sphere limit of the radar back-scattering coefficient." Q. J. Roy. Meteorol. Soc., 88, 183 (1962).
3. J. A. Garland. "Some fog droplet size distributions obtained by an impaction method." Q. J. Roy. Meteorol. Soc., 97, 483 (1971).
4. R. G. Pinnick, S. G. Jennings, P. Chylek, C. Ham, and W. T. Grandy, Jr. "Backscatter and extinction in water clouds." J. Geophys. Res., 88, 6787 (1983).

N87

10353

UNCLAS

CLOUD DETECTION BY LIDAR EXTINCTION CALCULATIONS

W. J. Lentz

Naval Postgraduate School, Physics Dept Code 61
Monterey, California, U.S.A.

A new lidar method of measuring cloud ceiling height using the Klett solution to the lidar equation has been developed. This simple technique will find cloud ceiling heights for clouds that rangefinder-like lidars cannot theoretically detect. In addition, the noise signals that do not correspond to clouds are removed by using the convergence of the Klett solution to discriminate between transient signal changes and broader signal changes due to clouds. Clouds above rain or light fog can be detected without error, and it is possible to discriminate against haze layers by the magnitude of their maximum extinction.

Not all lidar returns from clouds produce an abrupt increase in the scattered signal like that associated with the return from a hard target. In many cases, there is not clear air between the cloud and the ground, and the extinction increases slowly with altitude rather than abruptly. In many cases a light haze or fog may be associated at low altitudes with the cloud layer. An example of the type of lidar return that may occur from such a cloud is shown in figure 1.

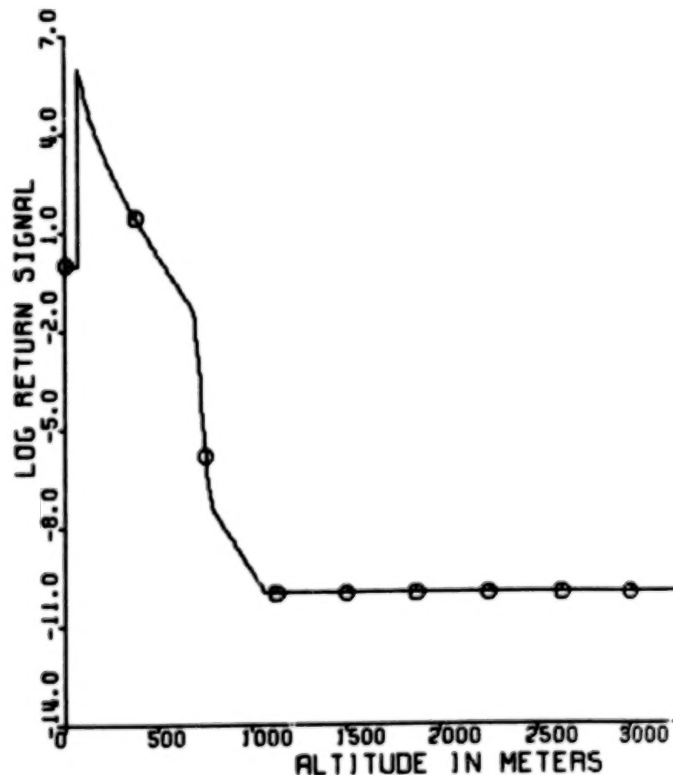


Figure 1. Theoretical Lidar Return from Opaque Cloud Layer

The lidar return was calculated by assuming a vertically pointing lidar that is firing into a totally opaque cloud of extinction similar to that obtained by independent measurements. It should be emphasized that the lidar return does not exhibit an abrupt increase such as that associated with a target anywhere along the path. Instead, the lidar return shows a rather marked decrease in backscattered signal when it strikes the cloud, and the scattered signal drops till it reaches an assumed minimum noise floor. The extinction from which this lidar return was calculated is shown in figure 2. The peak value of extinction is 30 kilometer, and the cloud is totally opaque to the eye.

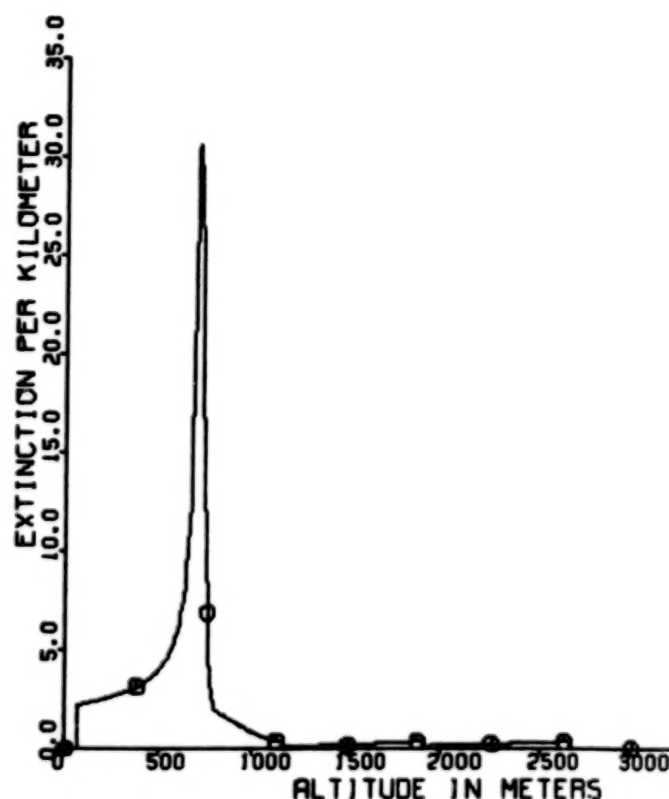


Figure 2. Theoretical Extinction Producing No Increased Lidar Return

Figure 3 shows experimental data obtained by a hand held lidar in Cardington, England in 1982. The solid line was calculated from aerosol size distributions measured by a balloon borne particle counter that slowly ascended while the lidar made several vertical shots. Each triangle corresponds to the extinction extracted from the lidar return at the altitude that the balloon was measuring aerosols. The extinction from each aerosol size distribution at a given altitude was calculated from Mie scattering theory.

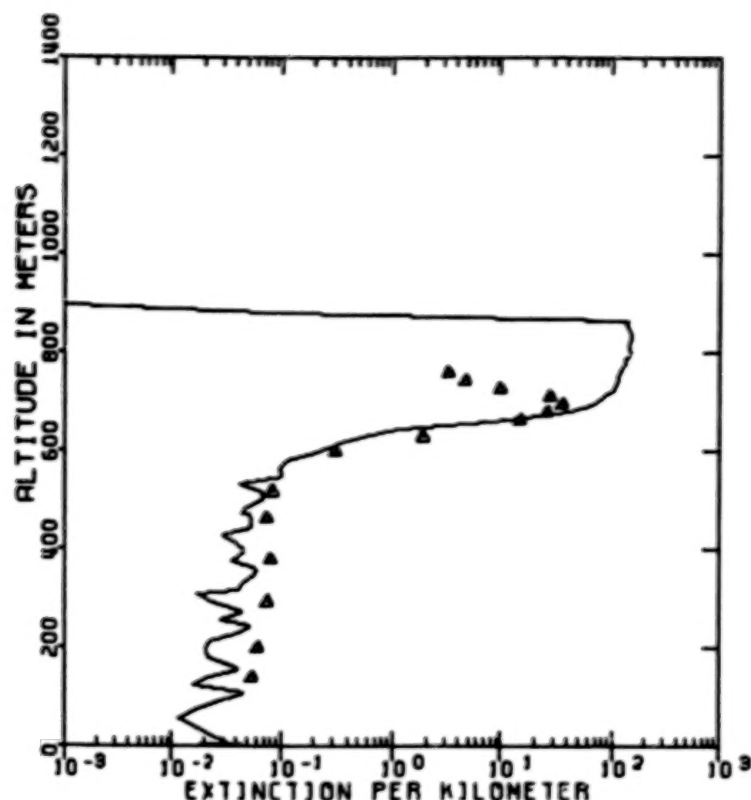


Figure 3. Comparison of Lidar and Particulate Measured Cloud Height

The agreement between the balloon extinctions and the lidar extinctions is very good, and the difference in altitude at which the cloud begins is very small. The fall of the lidar extinction in the cloud is due to the convergence of the extinction in the Klett method when a smaller boundary value than the actual value is put in the solution. This same convergence is used to eliminate false convergence to 'spikes' in the return that might be caused by rain or noise as the signal decreases.

J.D. Klett, "Stable Analytical Inversion Solution for Processing Lidar Returns," Appl. Opt. 20,211 (1981).

J.D. Lindberg et al, "Lidar Determinations of Extinction in Stratus Clouds," Appl. Opt. 23(13) 2172-2177, 1 July 1984.

N87

10354

UNCLAS

WIDE-AREA REMOTE-SENSING SYSTEM OF POLLUTION AND GAS DISPERSAL BY
NEAR-INFRARED ABSORPTION BASED ON LOW-LOSS OPTICAL FIBER NETWORK

Humio Inaba

Research Institute of Electrical Communication
Tohoku University, Sendai 980, Japan

Abstract — An all-optical remote-sensing system utilizing long-distance, ultralow-loss optical fiber networks is studied and discussed for near-infrared absorption measurements of combustible and/or explosive gases such as CH_4 and C_2H_2 in our environment, including experimental results achieved in a diameter more than 20 km.

I. Introduction

Optical fiber sensor technology is being developed currently for a wide variety of applications, and the technical advantages are well recognized so that its impact is now evident. Based on the idea of the first author [1] for a new capability of this technology, an optical network system employing low-loss optical fibers has been analyzed and examined for remote sensing of environmental pollution and spilled dispersals of inflammable, explosive and toxic gases/vapors in various industrial and mining facilities as well as in urban and residential areas by the spectroscopic absorption method [2, 3].

This regime of fiber-optic remote monitoring and detection has various advantages since the optical energy can be concentrated and transmitted in low-loss optical fibers even for long distances over several tens km, instead of the open atmosphere. Hence fully optical, reliable, sensitive, economical with low-power lasers or even incoherent sources, feasible, real-time, nonhazardous, e.g., eye-safe and explosion-free technique can be realized, along with capabilities of little optical interference and of continuous surveillance with easy calibration and selectivity as well as no electrical induction, for various stressing environments and severe conditions. The experimental feasibility of a fiber-optic gas sensor system has been demonstrated for remote absorption measurement of NO_2 in the visible spectrum using an Ar ion laser [3, 4], and CH_4 in the near-infrared region employing InGaAsP light emitting diodes (LED's) [3, 5-7] by our group.

This paper reports and summarizes experimental results of a low-loss optical fiber-based remote-sensing system of CH_4 and C_2H_2 gases which have been investigated in our laboratory, with specific emphasis on the use of a near-infrared wavelength range for this purpose.

II. Near-Infrared Absorption Spectra and Basic Arrangement

Currently, ultralow-loss silica optical fibers exhibiting transmission loss as low as 1 dB/km or less over the range of about 1.05 - 1.7 μm as well as high-quality optical sources and detectors have been developed primarily for long-distance, high-bit-rate optical communications, as shown in Fig. 1. Typical absorption wavelengths of various molecular species present in the atmosphere and environment are also depicted. Consequently, it becomes fairly apparent that the fiber-optic remote gas sensor system should be substantially operated in this near-infrared region to achieve a wide area coverage such as, for instance, a few tens km in diameter [1-3].

From this point of view, we have performed spectroscopic measurements

and analyses of combination and overtone bands of a number of molecules such as CH_4 , C_2H_6 , C_2H_4 , C_2H_2 , C_2H_6 , C_4H_{10} , NH_3 , H_2O , those contained in LNG, LPG and city gases, and others in this near-infrared range [3, 5-9].

On the basis of this spectral information, we are pursuing the remote absorption measurements using InGaAsP and InGaP LED's in conjunction with a few to several tens km-long, ultralow-loss silica optical fiber links. Figure 2 shows the basic arrangement of a fully optical remote gas sensor system employing a compact absorption cell as a sensor head. Near-infrared LED's used for the experiment are laser diodes (LD's) operated under threshold current level with output powers less than 0.1 mW. The optical beam from the LED was transmitted through a transmitting multimode optical fiber to a remotely located gas sensor head and then returned to the transmitter/receiver location via the receiving multimode optical fiber. The transmission loss of the silica optical fibers was lower than 1 dB/km in the 1.3 - 1.7 μm region. Absorption measurement was performed by using a grating spectrometer to change the detecting spectral width or a dielectric interference filter for a practical simplification in the system operation [6, 7].

III. Remote Monitoring of Methane Gas at 1.33 and 1.66 μm

The experimental demonstration of remote detection of low-level CH_4 gas was carried out for the first time employing a 2-km-long low-loss silica optical fiber link and a 50-cm-long compact absorption cell incorporating InGaAsP LED's operated around 1.34 and 1.61 μm . We observed that the detec-

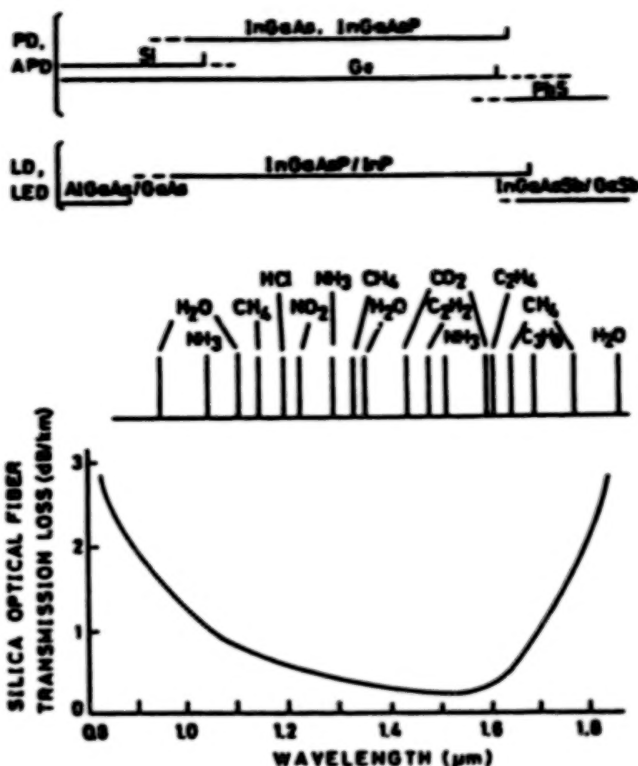


Fig. 1 Currently available high-quality semiconductor light sources (LD and LED) and detectors (PD and APD) in conjunction with ultralow-loss silica optical fibers in the near-infrared region, and typical absorption wavelengths of various molecular species present in the atmosphere and environment.

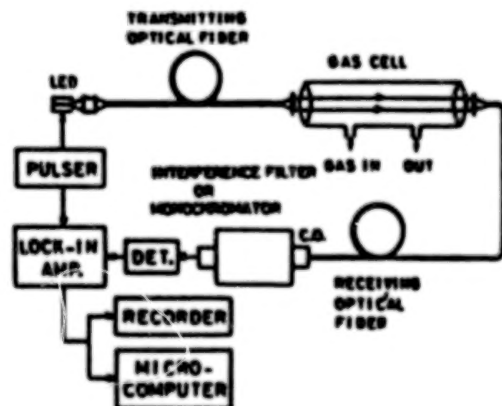


Fig. 2 Block diagram of an all-optical fiber-based remote-sensing system for absorption measurement of low-level combustible, explosive and toxic gases/vapors in the near-infrared region.

tion sensitivity of CH_4 gas in air is approximately 4 % of the lower explosion limit (LEL) at the 1.331- μm Q-branch of the $\nu_2 + 2\nu_3$ band using a grating monochromator with the spectral resolution of 0.3 nm [5], and about 1.3 % of the LEL at the 1.666- μm Q-branch of the $2\nu_3$ band employing a dielectric interference filter with the spectral width of nearly 3 nm [6], respectively.

A compact and reliable remote-sensing system was also realized by utilizing the power-balanced, two-wavelength differential absorption method [10], which enables one direct detection of differential absorption signals for the specific substance to be monitored [7]. Thus we confirmed that this technique is capable of achieving the sensitivity of about 0.8 % of the LEL of CH_4 density in air with easy calibration, using two dielectric interference filters centered at 1.666 μm as the on-absorption filter and at 1.528 μm as the off-absorption filter, respectively [7].

Based on these experiments demonstrating the feasibility of low-level CH_4 gas remote sensing employing very low-loss optical fiber links, we planned to extend the length of optical fibers to achieve a capability of a wider area coverage of this fully optical system. Figure 3 summarizes the measured result for the silica optical fiber links of the length of 5, 10, 16 and 20 km. The minimum detectable pressure of CH_4 gas in air was measured for each optical fiber link at 1.33 and 1.66- μm bands using a dielectric interference filter with the transmission center at 1.331 μm and about 2.5 nm spectral width, and a similar filter around 1.666 μm as mentioned above, respectively. It was verified that the detection sensitivity of 25 % of the LEL of CH_4 gas density in air, which is normally required for any practical CH_4 gas sensor, can be realized up to a 20-km-long optical fiber link with the detection time longer than 3 sec for 1.666- μm band, and also up to nearly 12 km with the detection time of 30 sec for 1.331- μm band. We should note that since the absorption of CH_4 molecules in 1.66- μm region is usually stronger than that in 1.33- μm region, higher sensitivity or longer detectable range for the fiber-optic CH_4 gas remote sensing is achievable in 1.66- μm region as is seen in this figure.

IV. Remote Monitoring of Propane Gas at 1.68 μm

As a further extension of our all-optical fiber-based remote gas sensing scheme, we have performed the remote measurement of low-level C_3H_8 gas in 1.68- μm region for the first time [11]. This gas is known to be the predominant component of LPG, and an inflammable and explosive species.

From the spectroscopic measurement using InGaAsP and InGaP LED's, C_3H_8

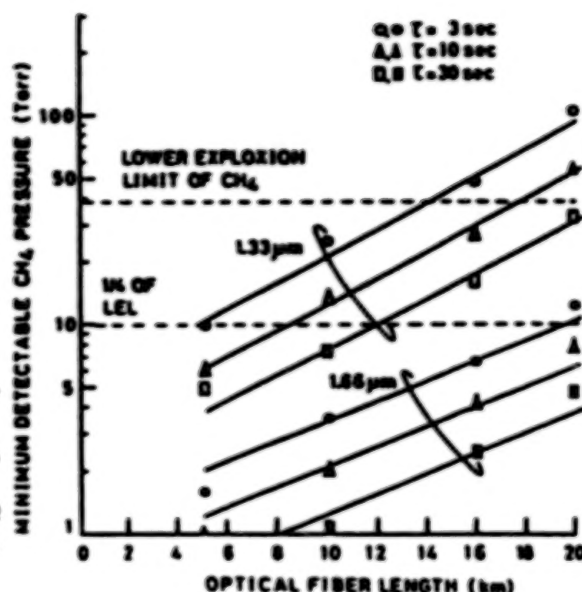


Fig. 3 Minimum detectable pressure of CH_4 gas in air at 1.331 and 1.666 μm as a function of the optical fiber length and the detection time in the all-optical remote measurement employing 5 - 20 km-long ultralow-loss silica optical fiber links in conjunction with InGaAsP LED's and a 50-cm-long absorption cell as the gas sensor head.

molecules were found to have absorption spectra in 1.3 - 1.7 μm region and the strongest absorption at 1.6837 μm [9, 11]. Then remote detection of C_3H_8 gas was pursued employing the experimental setup shown in Fig. 2 incorporating an InGaP LED and a 50-cm-long compact absorption cell.

Figure 4 shows the measured dependence of absorbance at the wavelength of 1.6837 μm on C_3H_8 partial pressure in the cell using a 2-km-long low-loss silica optical fiber link. Here, I and I_0 represent the intensity of optical signal which passed through the evacuated and C_3H_8 -air mixture contained absorption cell, respectively. The spectral resolution was 1.0 nm and the detection time was 3 sec. In this measurement, the minimum detectable pressure of C_3H_8 gas in air was confirmed to be lower than 2 Torr, which corresponds to nearly 12 % of the LEL.

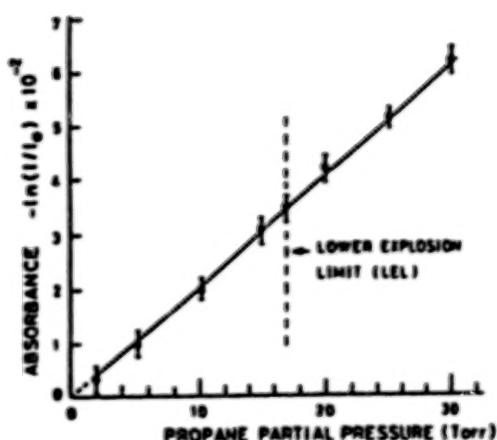


Fig. 4 Measured dependence of the absorbance at 1.6837 μm on C_3H_8 partial pressure in 1 atm. C_3H_8 -air mixture contained in a 50-cm-long gas sensor head using a 2-km-long very low-loss silica optical fiber link.

Moreover, we have realized that the same system utilizing a 5-km-long silica optical fiber link is capable of achieving reproducibly the detection sensitivity of about 2.4 Torr for C_3H_8 gas in air with the resolution of 1.2 - 1.5 nm, i.e., 14 % of the LEL [11]. The similar remote-sensing system is being applied to other gases by suitably selecting the measuring wavelength in the near-infrared region as illustrated in Fig. 1[12].

V. Conclusion

On the basis of the present state of the art of optical electronics technology, this kind of optical fiber network incorporating LED's or LD's and detectors in the near-infrared range should prove a very powerful scheme and provide extensively an all-optical safe way for remote sensing of various dangerous and toxic gases/vapors at strategic points over a wide area within the environment, e.g., industrial complexes, factories, mines, fuel storage yards, tunnels, undergrounds, ships, offices, hospitals, hotels, apartments, and so on.

References

- [1] H. Inaba, in Conference Abstracts, 9th International Laser Radar Conference, Munich, July 1979, Invited paper 2 - 2, pp. 61 - 67.
- [2] H. Inaba, T. Kobayashi, M. Hirama, and M. Hamza, *Electron. Lett.* **15**, 749 (1979).
- [3] H. Inaba, in *Optical and Laser Remote Sensing*, D. K. Killinger and A. Mooradian, Eds. (Springer, Berlin, 1983) p. 288.
- [4] T. Kobayashi, M. Hirama, and H. Inaba, *Appl. Opt.* **20**, 3279 (1981).
- [5] K. Chan, H. Ito, and H. Inaba, *Appl. Phys. Lett.* **43**, 634 (1983).
- [6] K. Chan, H. Ito, and H. Inaba, *IEEE/OSA J. Lightwave Technol.* **LT-2**, 234 (1984).
- [7] K. Chan, H. Ito, and H. Inaba, *Appl. Opt.* **23**, 1 Oct. 1984 issue, to be published.
- [8] K. Chan, H. Ito, and H. Inaba, *Appl. Opt.* **22**, 3802 (1983).
- [9] H. Inaba, K. Chan, and H. Ito, in *Dig. Tech. Papers, Conference on Lasers and Electro-Optics (CLEO'84)*, Anaheim, California, June 1984, Invited paper WN3, pp. 118 - 120.
- [10] M. Hamza, T. Kobayashi, and H. Inaba, *Opt. and Quantum Electron.* **13**, 187 (1981) and **14**, 339 (1982).
- [11] K. Chan, H. Ito, and H. Inaba, *Appl. Phys. Lett.* **45**, 220 (1984).
- [12] H. Inaba, in *Laser/Optoelectronics in Engineering - Laser 85 Optoelektronik*, W. Waldelich, Ed. (Springer, Berlin, 1986) p. 619.

N87

10355

UNCLAS

A MOBILE SYSTEM FOR ACTIVE OPTICAL
POLLUTION MONITORING

A. Sunesson, H. Edner, S. Svanberg, L. Unéus,
W. Wendt, and K. Fredriksson*
Department of Physics, Lund Institute of Techno-
logy, P. O. Box 118, S-221 00 Lund, Sweden
*National Swedish Environment Protection Board

The remote monitoring of atmospheric pollutants can now be performed in several ways. Laser radar techniques have proven their ability to reveal the spatial distribution of different species or particles. Classical optical techniques can also be used, but yield the average concentration over a given path and hence no range resolution. One such technique is Differential Optical Absorption Spectroscopy, DOAS. Such schemes can be used to monitor paths that a preliminary lidar investigation has shown to be of interest.

In our group, we have previously had access to one mobile lidar system constructed in Göteborg 1979-1980 (Ref. 1). Now a new system has been completed. The construction builds on experience from using the other system and it is meant to be more of a mobile optical laboratory than "just" a lidar system.

The system is built up on an ordinary truck chassis, and the laboratory measures 2.5 m x 6 m, fig 1. Electric power can be supplied from a 20 kW motor generator, housed in a trailer towed by the bus. The laboratory is equipped with a laser bench that besides the laser can hold an experimental setup and a detection bench that will allow different detection arrangements, for example a monochromator or a multichannel arrangement. The design is primarily intended for an Nd:YAG+dye laser system but it allows the use of different lasers. Frequency mixing units and a Raman shifter can be included to extend the wavelength region. Currently we employ a Quanta-Ray DCR-1 with a PDL-1 dye laser. Wavelength tuning is done by tilting the grating with a rotating excenter wheel or a piezo crystal. A future development incorporates a device for simultaneous dual-wavelength operation. The detection system is prepared for this option. The dyelaser wavelength can be calibrated in two ways, either against lines in the spectrum of neon or by measurements through a gas absorption cell.

The telescope, a Newtonian 400-mm diameter telescope, is mounted pointing vertically, coaxial with the exiting laser beam. The measurement direction is chosen with a large folding mirror, 400 mm x 700 mm, which is mounted in a retractable dome construction. When the system is not in use the dome is lowered. The folding mirror is protected by a 450 mm x 600 mm quartz window to make operation during rain or in wintertime possible.

The backscattered light is detected by an EMI 9816 QA photomultiplier, modulated according to Ref. 2 to prevent overload. This permits daytime measurements of e.g. NO₂ in the blue spectral region. Two PMT:s can be mounted for two-channel detection via dichroic mirrors or beamsplitters. The electrical signal is sampled by a LeCroy 8013 transient recorder assembly, with two 100-MHz

8-bits digitizer units. Signal averaging and system control is handled by an ITT XT computer with a hard disk and a floppy drive for data storage. The computer has graphic capabilities to present data. A printer and a plotter are incorporated for the final presentation of evaluated data. The computer can, on its own, perform a complete measurement sequence once the directions have been entered. System steering is performed with an additional microprocessor, which takes care of stepper motors, chopper, laser etc.

The system has the function of a laboratory when no field campaign is performed. It has a stationary docking place at our institute that makes it possible to walk directly from the fixed laboratories into the bus. So far, the system has participated in two field campaigns, one for SO_2 and one for NO_2 . A result from the SO_2 campaign is shown in figure 2.

Future use of the system will be in development of lidar techniques, where we try to widen the range of species that can be monitored. In specific, we will investigate range resolved measurements of NO and mercury. Other experiments are also planned - a monochromator on the detection side allows measurements with the DOAS (Differential Optical Absorption Spectroscopy) technique to be performed. This method, where the absorption of light from a high pressure Xenon lamp is measured in a way that eliminates atmospheric turbulence, gives the average concentration of the monitored species over the measured path. The sensitivity can be made extremely high. Remote laser induced fluorescence activities such as mineral monitoring or monitoring of pollution effects on plants might be considered. Other applications can be to provide a mobile lab or laser source for combustion studies in the industry.

References:

1. K. Fredriksson, B. Galle, K. Nyström, and S. Svanberg, "Mobile lidar system for environmental probing", *Applied Optics* **20**, 4181 (1981).
2. R. J. Allen and W. E. Evans, *Rev. Sci. Instruments* **43**, 1422 (1972).

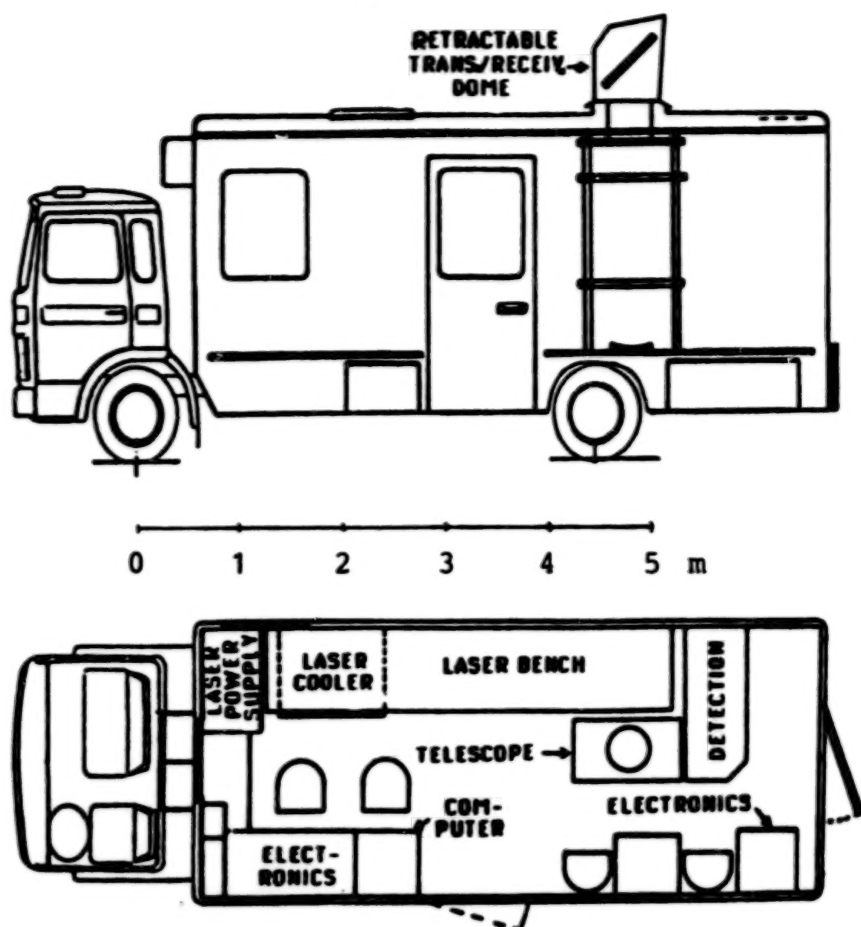


Figure 1. View of the lidar system

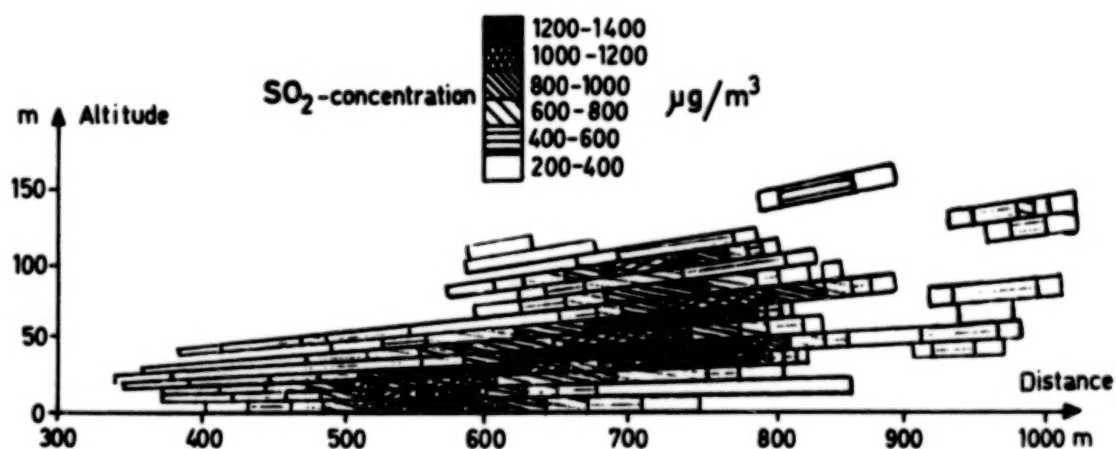


Figure 2. Vertical mapping of an SO₂ plume from a paper mill; 120 shots were averaged per wavelength and direction. The pulse energy was 2-3 mJ.

N87

10356

UNCLAS

GAS CORRELATION LIDAR FOR METHANE DETECTION

E.Galletti, E.Zanzottera, S.Draghi, M.Garbi, R.Petroni
CISE S.p.A., P.O.B.12081, 20134 Milano, Italy

A new type of dial system for the detection of methane in the atmosphere is being developed. The main feature of this lidar is the use of a gas correlation technique to obtain the reference signal by means of a single laser pulse, instead of two shots at different wavelengths (*). This fact is useful to make measurements on fast moving platforms.

To meet the ν_3 infrared absorption band of methane we use an optical parametric oscillator (O.P.O.) with a LiNbO_3 crystal as active element, and a tuning range between 1.5 ± 4 microns. As known (1), the major problems to overcome in parametric oscillators are the pump beam quality and the difficulty in reducing the linewidth. The first requirement is met by using, as a pump, a Nd-YAG laser based on a new type of resonator cavity, named SFUR (Self Filtering Unstable Resonator). The laser emits, with high efficiency, near diffraction limited pulsed beams (2,3,4) of about 250 mJ of energy, 20 ns of duration at 10 pps of frequency repetition rate. On the other hand, the gas correlation technique allows the operation with a bandwidth as large as 1 cm^{-1} , which is obtainable using only a diffraction grating as a dispersive element in the O.P.O. cavity. Output energy from O.P.O. is expected to be some mJ, which is sufficient for methane detection on paths of several hundred meters.

Laboratory tests of the system are scheduled for June, while field trials will be carried out in the fall of the year.

The system will be also operated to detect other hydrocarbons, carbon dioxide and carbon monoxide molecules.

*H.Edner, S.Svanberg, L.Uneus, W.Wendt, "Gas Correlation Lidar", Private Communication.

REFERENCES

- (1) S.J.Brosnan, R.L.Byer: IEEE J.Quant.Elect.QE-15,6, June 1979.
- (2) P.G.Gobbi, G.C.Reali: Opt.Comm.52(3),195,(1984).
- (3) P.G.Gobbi, S.Morosi, G.C.Reali, A.S.Zarkasi: Appl.Opt. 24(26),1985.
- (4) P.G.Gobbi, G.C.Reali, C.Malvicini: CLEO'85, Baltimore, May 21-24,1985.

Work supported by AEM/CISE Contract no. 00.8107/PP.

N87

10357

UNCLAS

DETECTION OF NO_x , C_2H_4 CONCENTRATIONS
BY USING CO AND CO_2 LASERS

Wang Gengchen and Kong Qinxin
Institute of Atmospheric Physics, Academia Sinica
Beijing, China

A laser, especially the infrared line-tunable laser, opens up a new way to monitor the atmospheric environment, and already has gotten effective practical application. One of the most serious problems in open-path remote measurement at atmospheric pressure is the broadening effect which leads to increased linewidths, spectral interferences, and, as a result, tends to reduce detection sensitivity, so measuring laser wavelengths should be selected carefully, and interaction between the measuring wavelength and gas to be measured must be known very well. Therefore, N_2O , NO , NO_2 , CH_4 , NH_3 and C_2H_4 absorption properties at some lines of CO and CO_2 line-tunable lasers were studied in our laboratory. The absorption coefficients of NO , NO_2 and C_2H_4 ; some results on detection of NO_x , C_2H_4 concentrations in both laboratory and field; and selection of measuring wavelengths and error analysis are discussed in this paper.

1. EXPERIMENT

Fig.1 is a schematic diagram of the experimental system used for absorption coefficient measurements and simulation detection of NO_x , C_2H_4 concentrations. The whole experimental equipment consists of a laser source, external optical system, sample absorption cell, detector, lock-in amplifier, and recording and data processing systems. CO and CO_2 line-tunable lasers are

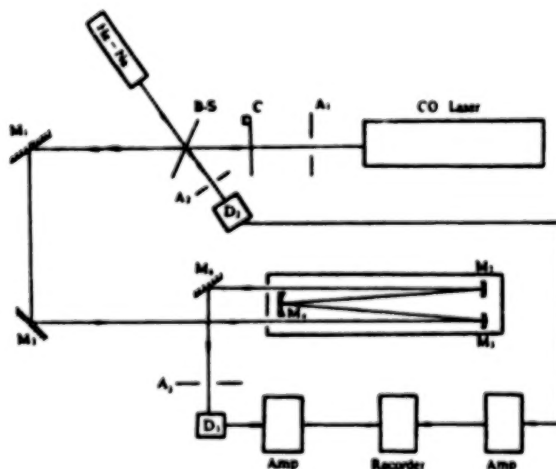


Fig.1 Schematic diagram of the experimental system

used as a radiation source; the typical output power of single laser line is about 1 watt. The sample cell is a multi-path absorption cell with a physical length of 3m. The infrared spectrophotometer is used as a line-monitoring device. Absorption coefficients at a given laser line are obtained from a transmittance, which is measured by using the ratio of the measuring and controlling beams in order to eliminate errors caused by instability of the laser source and possible variation of instrumental constant.

2. NO, NO₂, C₂H₄ ABSORPTION COEFFICIENTS

A vibration-rotational spectrum of NO 5.3 μ absorption band consists of two subbands, as a result, a double-line series of NO spectrum is produced. Line intensities of subband 2 $\pi_{1/2}$ are about two times more than that of subband 2 $\pi_{3/2}$. A wavenumber range of NO 5.3 μ absorption band is about 1985cm⁻¹ - 1777cm⁻¹. The two subbands can be easily separated by using a laser as a monochromatic radiation source according to absorption properties of NO 5.3 μ band. As wavelength range of used CO laser is limited, the P-branch of NO 5.3 μ absorption band was studied only. The selected laser frequencies and obtained NO absorption coefficients are listed in Tab.1.

Tab.1 Absorption coefficients of NO

$\nu_{CO}(cm^{-1})$	$k_{NO}(atm-cm)^{-1}$	$k_{H_2O}(cm^2/g)$	$u_{NO}(atm-cm/km)$
1784.153	0.41	40.26	34.37
1788.397	0.32	54.54	59.66
1801.120	0.34	71.63	72.88
1826.217	0.34	51.80	53.01
1829.592	1.21	362.40	104.70
1834.593	0.27	14.77	19.08
1838.708	0.24	12.49	18.52
1842.808	3.29	40.49	4.31
1847.131	0.33	27.20	28.67
1859.842	0.37	19.31	18.42
1863.655	1.07	8.71	2.86
1876.630	0.12	20.20	57.48
1880.901	0.63	2.29	1.28

NO₂ 6.2 μ absorption band is an A-type band; its spectral range is about 1660 - 1550 cm⁻¹; the high resolution spectrum of this band shows a very complicated spectral structure, that is, lines of this band seriously overlap and mix. Absorption coefficients of NO₂ at 29 CO laser frequencies are given in Tab.2. Absorption coefficients of water vapor at all listed laser frequencies are also given in Tab.1 and Tab.2 in order to provide reliable information for suitable wavelength selection and reasonable data processing in detection of NO

Tab.2 Absorption coefficients of NO₂

ν_{CO} (cm ⁻¹)	k_{NO_2} (atm-cm) ⁻¹	k_{H_2O} (cm ² /g)	u_{NO_2} (atm-cm/km)	ν_{CO} (cm ⁻¹)	k_{NO_2} (atm-cm) ⁻¹	k_{H_2O} (cm ² /g)	u_{NO_2} (atm-cm/km)
1575.200	8.3	76.57	3.22	1614.909	23.38	110.5	1.65
1580.778	10.1	62.63	2.17	1618.699	21.44	101.7	1.66
1582.880	15.5	33.09	0.75	1619.564	32.35	66.29	0.72
1584.359	8.6	25.57	1.04	1622.455	76.91	417.2	1.90
1587.907	45.6	18.69	0.14	1626.175	83.64	64.06	0.27
1590.457	32.4	35.77	0.39	1629.862	71.86	36.97	0.18
1595.609	53.6	106.8	0.70	1631.721	76.83	47.63	0.22
1597.929	28.7	34.06	0.41	1633.313	74.76	76.11	0.36
1599.488	41.2	18.83	0.16	1640.743	12.87	66.60	1.81
1601.614	19.2	19.00	0.35	1643.272	7.28	55.94	2.69
1603.386	55.4	33.89	0.21	1644.277	10.24	70.29	2.40
1605.265	41.4	22.03	0.19	1647.067	9.51	468.2	17.24
1607.252	54.9	22.23	0.14	1650.819	4.48	200.1	15.62
1611.084	50.4	62.31	0.43	1656.260	1.63	129.4	27.76
1612.487	50.7	33.86	0.23				

and NO₂ concentrations. The u_{NO} in column 4 of Tab.1 and u_{NO_2} in column 4, 8 of Tab.2 denote equivalent contents of NO and NO₂, respectively; these values correspond to such atmospheric transmittance to which corresponds the water vapor content of 0.35g/km in the atmosphere.

Absorption of ethylene at CO₂ laser lines is essentially due to the intense ν_2 C-type infrared band which presents a strong Q-branch near 950 cm⁻¹; its R and P branches cover the region from 1100 to 800 cm⁻¹. So it is not difficult to find some coincidences between C₂H₄ absorption lines and CO₂ laser lines. As an example, the absorption coefficients of ethylene at P-branch of CO₂ 00⁰1-10⁰0 band are listed in Tab.3.

Tab.3 C₂H₄ Absorption coefficients $k(\text{atm-cm})^{-1}$ at 285K

laser line	k	MSE	laser line	k	MSE
10p6	2.25	0.10	10p24	2.47	0.10
10p8	1.85	0.09	10p26	1.97	0.17
10p10	3.54	0.37	10p28	1.36	0.05
10p12	4.92	0.58	10p30	1.56	0.05
10p14	33.47	2.04	10p32	1.18	0.07
10p16	5.09	0.53	10p34	1.63	0.05
10p18	3.40	0.22	10p36	1.34	0.05
10p20	1.98	0.14	10p38	2.12	0.10
10p22	1.57	0.09			

3. DETECTION OF NO_x, C₂H₄ CONCENTRATIONS

Based on the above obtained absorption coefficients, a simulation detection of NO, NO₂ and C₂H₄ concentrations by means of the two-wavelength differential absorption method was made in our laboratory. Several sets of laser lines and given concentrations of samples were used for this purpose. The diagram of used equipment is similar to Fig.1. Results for all measurements are more satisfied, the variation range of relative error in concentration detection for NO is 2-15%, and for NO₂, C₂H₄ is less than 10%.

Moreover, a detection of NO concentration in the actual urban atmosphere was made by using CO laser lines of 1863.655 and 1842.808 cm⁻¹ as the measuring wavelengths, and of 1880.901 cm⁻¹ as a reference wavelength. The results show that NO concentration produced by traveling automobiles may go up to about 1 atm-cm/km, that is about 10-20 times higher than the NO background concentration.

4. ERROR ANALYSIS

Errors in long-path laser monitoring NO, NO₂, C₂H₄ concentrations are mainly caused by factors such as accuracy in absorption coefficient measurement, selection of used laser lines, interference of nonmonitored gases in the atmosphere and atmospheric aerosol, and atmospheric turbulence as well.

It should be noted firstly that accuracy of NO, NO₂ and C₂H₄ absorption coefficients at corresponding CO, CO₂ laser lines is not satisfied enough up to now, although many works have been done in this respect. For example, a typical discrepancy in C₂H₄ absorption coefficients at CO₂ laser lines measured by various authors varies from 10% to 40%, as a result, a corresponding error in ethylene concentration detection is produced by this reason. Another problem to be emphasized is an interference of nonmonitored atmospheric species. Here, the most important gases are carbon dioxide and water vapour, whose absorptions cover almost the whole infrared region and strongly vary with a selected wavelength. For example, the smallest value of water vapour absorption coefficient at all CO laser lines within the 6.2 μ NO₂ band is about 20 cm²/g, in other words, the equivalent content of NO₂ caused by absorption effect of water vapour in the middle-latitude winter atmosphere is about 0.2 atm-cm/km.

N87

10358

UNCLAS

MAPM: A COHERENT DUAL CO₂ LASER DIAL SYSTEM¹

William B. Grant, James R. Bogan
Jet Propulsion Laboratory, MS 183-401
California Institute of Technology,
4800 Oak Grove Drive, Pasadena, CA 91109

The Mobile Atmospheric Pollutant Mapping System (MAPM) is a dual CO₂ laser DIAL system with heterodyne detection that is being developed for large distance range-resolved measurement of organic solvent vapors and aerosol clouds. The components have been chosen to allow measurements to be made to distances of 6-7 km in a period of 20-30 s.

The major components of MAPM are:

- 1) a 35-ft transportable semitrailer
- 2) a pair of pulsed CO₂ lasers capable of 50-150 Hz operation at pulse energies of 50-200 mJ
- 3) a pair of cw CO₂ lasers for use as local oscillators
- 4) non-coaxial transmit/receive optics and scan mirror
- 5) a 10-bit, 20-MHz transient digitizer
- 6) a computer capable of acquiring lidar data at a rate of 100-150 Hz and subsequently processing the data

MAPM is being integrated into a system and will be tested with several organic solvent gases and vapors in a remotely positioned sample chamber and with a free release of ethylene. Attention will be given to system performance and sensitivity and factors which limit it, such as spectral and spatial variations in aerosol backscatter and laser beam speckle.

The talk will describe MAPM in more detail and discuss experimental results and system performance to date.

¹ Work sponsored by the Air Force Engineering and Services Center, Tyndall Air Force Base, Florida.

N87

10359

UNCLAS

LASER HETERODYNE SYSTEM FOR OBTAINING HEIGHT PROFILES OF
MINOR SPECIES IN THE ATMOSPHERE

S.L. JAIN AND A.K. SAHA
Radio Science Division
National Physical Laboratory
New Delhi-110012

ABSTRACT

An infrared Laser Heterodyne system for obtaining height profiles of minor constituents of the atmosphere has been developed and set up at National Physical Laboratory, New Delhi. A brief description of the system is given here. The system consists of a tunable CO_2 waveguide laser in the 9-11 μm band, that is used as a local oscillator and a heliostat that follows the sun and brings in solar radiation, that is mixed with the laser beam in a high speed (1 GHz) liquid Nitrogen cooled Mercury Cadmium Telluride detector. The detected signal is analysed in an RF spectrum analyser that allows tracing absorption line profiles. Absorption lines of a number of minor constituents in the troposphere and stratosphere, such as O_3 , NH_3 , H_2O , SO_2 , ClO , N_2O , are in the 9-11 μm band and overlap with that of CO_2 laser range. The experimental system has been made operational and trial observations taken. Current measurements are limited to ozone height profiles. Results will be presented.

A computer program of the inversion technique has been developed based on the inverse solution of the radiative transfer equation. In the present analysis, a Lorentz profile was used below 25 km, while above 25 km, a Voigt profile was used where Doppler broadening is dominant, for computation of line parameters such as line half width, line strength etc. for a strong Ozone absorption line, 1053.96 cm^{-1} . In all, sixteen channels, one at line center and fifteen in the wings of the line, were chosen to resolve the line and hence to get proper height resolution (1 to 3 km). The spectral intensity for each channel was computed using the U.S. Standard atmosphere (1976) Ozone model. To invert the computed spectral intensity of these channels an initial uniform vertical distribution of ozone, say 3 ppmv, was assumed. This distribution was modified in each iteration and in 20 iterations the profile was obtained. Proper interpolation was done to get a complete profile up to a 40 km altitude. The inverted profile compares well with the model ozone profile. The inversion method was tested with different assumed distributions and found to be independent of the initial assumptions.

A CORRELATION LIDAR WITH IMAGE RECEIVER

V.K. Beljaev, K.S. Gochelashvily, N.N. Denisov, A.A. Manenkov,
V.L. Mitev, TS.A. Mitsev, A.M. Prochorov, E.V. Stoikova,
E. Ferdinandov, V.K. Chevokin, M.JA. Schelev
General Physics Institute
Moscow, USSR

ABSTRACT

The principles and feasibilities of lidar systems employing image reception and correlation technique are discussed. Full consideration is given to the energy balance of the lidar and the effects of atmospheric turbulence on the accuracy of lidar measurements. The results of experiments in the atmosphere are presented.

N87

10360

UNCLAS

COHERENT LIDAR SIGNAL
FLUCTUATION REDUCTION BY MEANS OF
FREQUENCY DIVERSITY TECHNIQUE

R. M. Schotland, P. Vujkovic Cvijin* and Yan-Zeng Zhao
University of Arizona, Tucson, Arizona 85721

The atmospheric return measured by a coherent lidar is typically characterized by rapid and deep fluctuations in signal strength. These fluctuations result from the interference of the fields backscattered to the lidar from randomly located aerosol particles which move relative to the lidar pulse. In many applications, it is necessary to determine the average value of the lidar signal intensity at some range. The usual procedure employed is to average N uncorrelated measurements from this range and then, under the assumption that the system statistics are stationary, assume that signal uncertainty improves inversely with the square root of N (for large carrier to noise ratios). Because of the large number of independent samples required to obtain accurate intensity estimates, consideration was given to an alternate method to obtain additional independent samples. The method utilizes frequency diversity initially suggested by Goldstein [1] and subsequently studied in the microwave radar domain by Marshall and Hitschfeld [2] and by Nathanson and Reilly [3]. The idea has apparently not yet been applied to coherent lidar. It is expected that the application of the frequency diversity method in the coherent lidar domain will eventually provide greater efficiency and speed in the return signal averaging needed to obtain accurate intensity estimates.

The frequency diversity method recognizes that the transmitted lidar pulse is very long compared to a wavelength and consequently a given phase, θ_i , is repeated many times within the pulse. The backscattered signal corresponding to θ_i samples those aerosols located in range corresponding to θ_i . If the frequency is increased so that an additional wavelength is contained within the lidar pulse then θ_i will be redistributed over the pulse volume and consequently sample a new set of aerosol particles [2].

In order to test this concept, a fairly simple laboratory experiment has been designed which, to a degree acceptable for this purpose, simulates scattering of a lidar pulse from atmospheric aerosol. The purpose of the experiment is to compare the standard deviation of the signal fluctuation in two cases: the first, when the laser is allowed to operate on a single line and second, when the laser operates on two lines

* Permanent address: Institute of Physics, P.O. Box 57,
11001 Belgrade, Yugoslavia.

sufficiently separated to provide a test of frequency diversity.

In the experimental apparatus shown in Fig. 1 the beam from a continuous wave CO₂ waveguide laser is aimed at an aluminum disk whose edge has been uniformly roughened and whose rotation provides the Doppler-shifted frequency of the scattered radiation. A portion of the laser beam is diverted to a concave mirror and serves as a local oscillator beam. This beam is then heterodyned with the collected scattered radiation (signal beam) at the surface of a photoconductive HgCdTe detector. The scattering of light from an extended rough surface which introduces path differences greater than one wavelength is statistically similar to that from atmospheric aerosols distributed over a large volume.

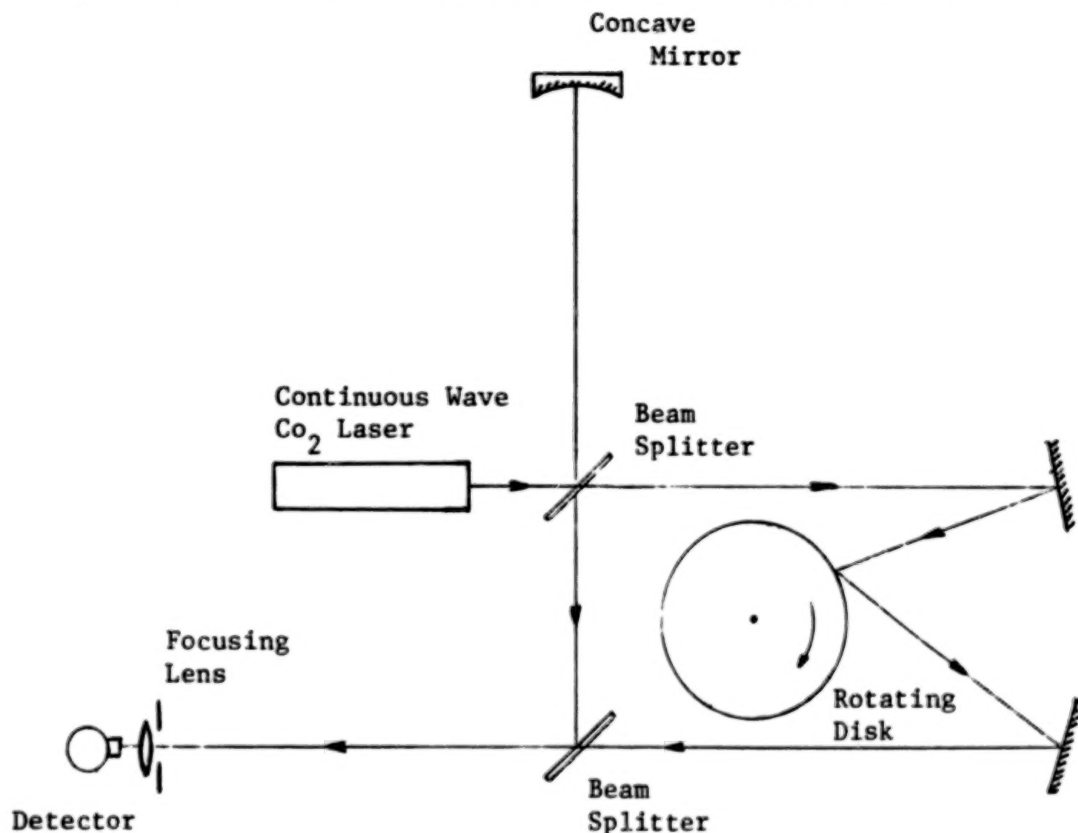


Fig. 1 Apparatus designed to test the frequency diversity concept in a laboratory experiment.

The CO₂ laser is deliberately tuned to operate simultaneously at two vibrational-rotational lines in the R branch of the 9 μ m band with the frequency separation between the two lines approximately being 4×10^{10} Hz. For this case, if the product of the effective depth of the target L and the frequency difference $\Delta\nu$ satisfies the relation $L\Delta\nu > c$, where c is the speed of light, then independence of the scattering at

these two frequencies is provided. It is important to note that the illuminated spot at the rotating disk in Fig. 1 has spatial extent, L , in the direction of receiver's axis. Owing to the large frequency separation between the two components of the transmitted radiation the minimum depth of the target required to obtain independent return signals is only $L = 7.5$ mm. This is easily provided in laboratory by the experimental setup of Fig. 1.

The signal processing is performed in the following manner. The preamplified output of the radiation detector on Fig. 1 is filtered, envelope detected and digitized by a 10 bit, 10 MHz waveform recorder. The waveforms acquired are then transferred to a computer for further analysis. Based on the frequency diversity concept, the contrast C (the ratio of the standard deviation of the heterodyne signal to its mean value) in the dual line case is expected to have the value $C = C_1/\sqrt{2}$ where C_1 is the contrast for the single line case. Decrease of the contrast when the laser is operating at two lines simultaneously in comparison to single line operation has been proven experimentally. The amount of decrease in the value of contrast has been somewhat corrupted by inherent fluctuations of the output of the waveguide CO_2 laser whose cavity has been critically adjusted to provide lasing at two vibrational-rotational lines simultaneously.

References

1. Goldstein, H.: "The Origin of Echo Fluctuation," in "Propagation of Short Radio Waves" edited by D. Kerr, New York: Dover, 1951.
2. Marshall, J. S. and Hitschfeld, W.: "Interpretation of the Fluctuating Echo From Randomly Distributed Scatterers," Can. J. Phys. 31, 962, (1953).
3. Nathanson, F. E. and Reilly, J. P.: "Radar Precipitation Echoes," IEEE Trans. Vol. AES-4, No. 4, 505 (1968).

N87

10361

UNCLAS

WAVELENGTH DEPENDENCE OF COHERENT AND INCOHERENT
SATELLITE-BASED LIDAR MEASUREMENTS OF
WIND VELOCITY AND AEROSOL BACKSCATTER

ORIGINAL PAGE IS
OF POOR QUALITY

Michael J. Kavaya
R. Milton Huffaker

Coherent Technologies, Inc.
P.O. Box 7488
Boulder, Colorado 80306-0403
USA

INTRODUCTION

Global profiling of Earth's wind from a satellite would provide numerous civilian, commercial, military, and scientific benefits. In addition, satellite-based measurements of aerosol and cloud backscatter are of great interest. Studies sponsored by the Defense Meteorological Satellite Program (DMSBP) have shown the feasibility of measuring the global wind field using a satellite-based pulsed coherent CO₂ laser radar [1]. RCA Corp. has recently completed a study for an Earth-orbiting lidar to measure aerosol backscatter and cloud top heights using a Nd:YAG and doubled Nd:YAG laser operating in an incoherent mode. The Nd:YAG wavelengths at 1.06 and 0.53 microns are in a wavelength region where strong consideration must be given to eye safety. Only coherent CO₂ laser radars, which operate in the 9-11 micron wavelength region, have demonstrated accurate long-range remote wind velocity measurements to date. However, solid-state laser technology has progressed to the point where it should also be considered. Stanford University researchers have built a solid-state Nd:YAG lidar and have recently demonstrated coherent return signals from clouds and aerosols. Solid-state laser systems, compared to CO₂ systems, will be smaller, lighter, may require less power, may not require cooled detectors, and have the potential of several years lifetime in space. A technology assessment has shown the feasibility of fabricating a ground-based Nd:YAG solid-state coherent lidar system at this time for wind velocity and aerosol backscatter measurements [2]. Research is progressing at Stanford University and elsewhere on eyesafe solid-state sources suitable for coherent lidar measurements. The "modular" nature of solid-state systems would allow for the eventual upgrade of Nd:YAG systems to an eyesafe wavelength as the technology permits.

This paper presents the results of a capability study of Earth-orbiting lidar systems, at various wavelengths from 1.06 to 10.6 microns, for the measurement of wind velocity and aerosol backscatter, and for the detection of clouds [3]. Both coherent and incoherent lidar systems were modeled and

compared for the aerosol backscatter and cloud detection applications.

COMPUTER SIMULATION

The Coherent Technologies, Inc. lidar computer simulation was used to estimate the performance of a satellite-based laser radar system [1]. A set of satellite base parameters was selected which was used in an earlier analysis by NOAA to determine global wind velocity monitoring feasibility at 9.11-micron wavelength. The wavelength dependence of several of the parameters was reviewed and incorporated in the simulation. The wavelength and height variation of the atmospheric extinction was modeled through the use of the 1982 AFGL atmospheric absorption line parameters compilation. A simplified wavelength^{-2.5} dependence of the aerosol backscatter coefficient was adopted after reviewing recent modeling results and measurements. A factor of 2 was used at 9.11 microns (vs 10.6 microns), instead of 1.5, due to the predicted and measured enhancement at that wavelength. Atmospheric refractive turbulence is modeled in the computer simulation but was found to have a negligible impact even at 1.06 microns. A pulse duration of 6.67 microseconds was used at 10.6 and 9.11 microns yielding a 1 km range resolution and a Gaussian pulse Fourier transform-limited radial wind velocity resolution of approximately 1 m/s. The pulse duration at other wavelengths was made proportional to wavelength in order to preserve a constant velocity resolution.

WIND VELOCITY PERFORMANCE

An example of the satellite-based coherent lidar performance in measuring the horizontal wind velocity component along the track of the satellite is shown in Figure 1 for a wavelength of 2.10 microns. The pulse duration and 10.6-micron backscatter profile multiplying factors are shown in the figure. The corresponding along-track RMS error at 9.11 microns (not shown) varied between 0.8 and 2 m/s for altitudes between ground level and 20 km. The CO₂ isotopic laser wavelength at 9.11 microns is a strong candidate due to the lower atmospheric CO₂ absorption and due to the enhanced aerosol backscatter coefficient. The eyesafe wavelength at 2.10 microns also has relatively low atmospheric absorption and is a promising solid-state laser wavelength [3].

Using the backscatter multiplier of 60 at 2.10 microns, we see in Figure 1 that the wind velocity error is much greater than at 9.11 microns. Adding a further backscatter enhancement of 10 for a total enhancement of 600 results in better performance at 2.10 microns than at 9.11 microns and much better than is needed. The aerosol model assumed in the

ORIGINAL PAGE IS
OF POOR QUALITY

computer simulation is the most uncertain parameter in the performance estimate. Aerosol backscatter measurements at several eyesafe wavelengths in addition to the CO₂ laser wavelengths are needed. The performance curves in Figure 1 do not include any range-gate averaging. The factor of 5 shorter pulse duration at 2.10 microns would allow the averaging of 5 range gates while preserving range and wind velocity resolutions equal to those at 9.11 microns. This would reduce the wind errors shown in Figure 1.

BACKSCATTER PERFORMANCE

An example of satellite-based coherent and incoherent lidar cloud detection performance at 1.06 microns is shown in Figure 2. The 10.6-micron aerosol backscatter profile was multiplied by a factor of 316 above 5 km altitude. To simulate a cloud, the backscatter coefficient below 5 km was set to a value of $1.0E-5$ 1/m 1/sr. The correct SNR expression for incoherent detection depends on the type of detector in use, how it is used, the measurement scenario, and whether detection is in the pulse-counting or current-measurement mode. No SNR expression covers all cases. Realistic device parameters were inserted into an equation for non-avalanche photodiodes and the results are shown in Figure 2 as curve A. A state-of-the-art SNR expression, which allows variation of wavelength and detection bandwidth, is shown as curve B. The effect of the cloud on the SNR is clear for all 3 curves. Detection should be possible with either coherent or incoherent systems.

REFERENCES

1. R.M. Huffaker, T.R. Lawrence, M.J. Post, J.T. Priestly, F.F. Hall, Jr., R.A. Richter, and R.J. Keeler, "Feasibility studies for a global wind measuring satellite system (Windsat): analysis of simulated performance," *Applied Optics* 23, 2523 (1984).
2. R.M. Huffaker, M.J. Kavaya, and D.M. Geiger, "Specify and Design a Solid-State Pulsed Coherent Laser Radar," Technical Report CTI-TR-B601, Coherent Technologies, Inc. (January 1986).
3. R.M. Huffaker, M.J. Kavaya, and D.M. Geiger, "Coherent-Incoherent Lidar System Capability Study," Technical Report CTI-TR-B602, Coherent Technologies, Inc. (January 1986).

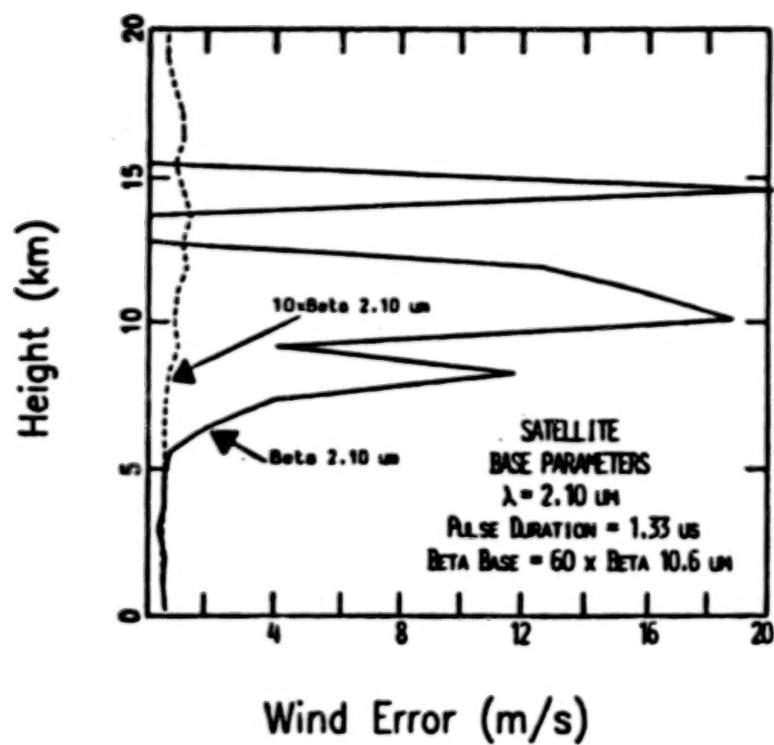


FIGURE 1

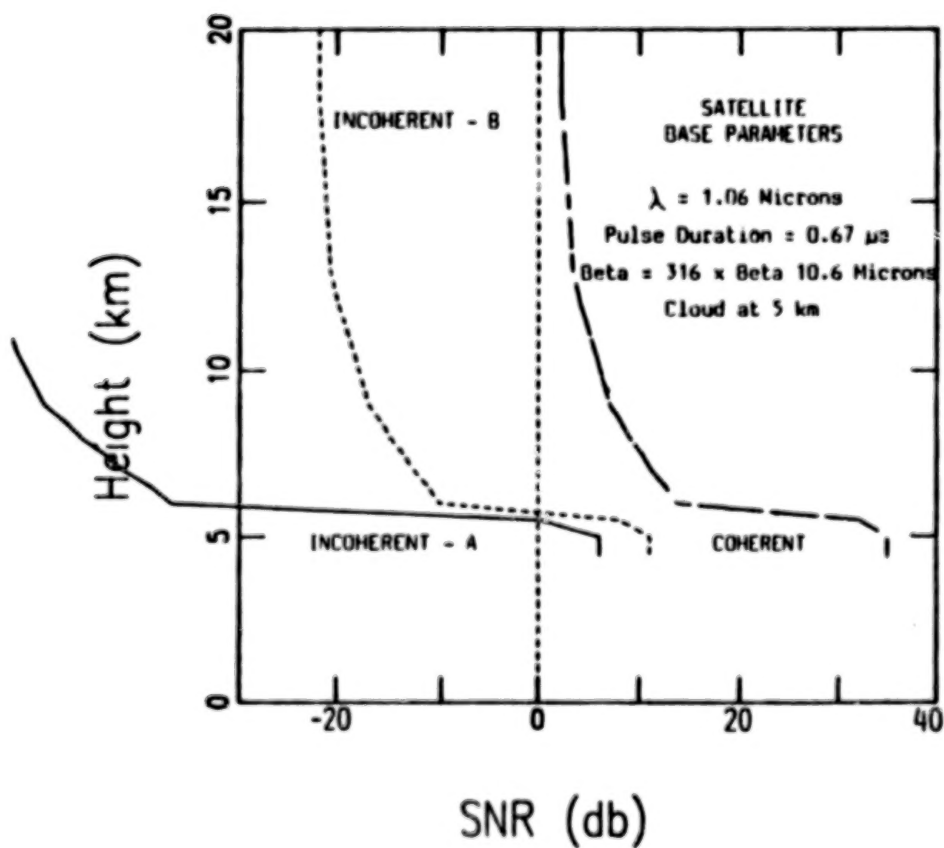


FIGURE 2

N87

10362

UNCLAS

THE NCAR AIRBORNE INFRARED LIDAR SYSTEM (NAILS)

R. L. Schwiesow and P. A. Lightsey¹
 Research Aviation Facility, National Center for
 Atmospheric Research, Boulder, Colorado, 80307,
 U.S.A.

Purpose. This paper presents a planned airborne lidar system, which is intended to provide the university atmospheric science research community with a remote sensing facility for a variety of applications. The eventual goal of the system development is a Doppler wind measurement capability for boundary layer dynamics and cloud physics applications, among others. However, the first stage of development (and this presentation) is focused initially on a direct-detection lidar to measure aerosol profiles and depolarization from cloud backscatter. Because of the Doppler goal, interest in larger particles to define the top of the mixed layer, and eye safety, the first stage of the system is based on a pulsed CO₂ laser.

Our philosophy emphasizes a compact, relatively simple and inexpensive system that achieves flexibility to meet the data requirements of a variety of investigators by being easily modified rather than having many different capabilities built in. Although the direct-detection sensitivity is less than that for heterodyne detection, the simpler system allows us to obtain useful scientific results and operating experience toward more complex lidars while staying within budget and time constraints. Initial tests of the system in a downlooking mode are planned for a King Air twin-turboprop aircraft.

Relation to previous work. NAILS represents an evolution from previous work, not a revolutionary step. Steinvall et al. (1983) used a direct-detection lidar, based on a pulsed CO₂ laser, for ground-based aerosol profile measurements to approximately 1-km altitude, and Uthe (1981) mentioned the use of a ground-based lidar using a CO₂ laser and direct detection. In contrast to the ground-based systems, Itabe et al. (1984) reported on a direct-detection CO₂ lidar for a small aircraft, and Bilbro et al. (1984) have been flying a heterodyne Doppler lidar in a large aircraft for a number of years. Participants in the conference are well aware of less directly related CO₂ lidars involving ground-based Doppler systems and airborne CW Doppler lidars.

We calculate a signal-to-noise ratio of approximately one at a range of 1 km for a backscatter coefficient of $5 \times 10^{-9} \text{ m}^{-1} \text{ sr}^{-1}$ for a single pulse from a lidar with the parameters mentioned below. This is consistent with the observations of Steinvall et al. (1983), and emphasizes the necessity for signal averaging with a direct-detection infrared lidar.

¹ On leave from the University of Northern Colorado, Greeley.

Design details. NAILS uses a Dall-Kirkham telescope as a transceiver. The Dall-Kirkham layout will permit repackaging the system in an external pod with minimum frontal area as an external store on the aircraft. Use of a common transmit and receive aperture minimizes the angular field, and therefore detector size and noise, gives geometrical compression of the dynamic range of the return (Harms et al., 1978), and allows later heterodyne operation. Transceiver operation will probably require considerable development to reduce parasitic scattering.

Some of the parameter values are listed below:

Laser: LSI 150G. 300 mJ at 50 Hz multimode,
130 ns pulsewidth, 210 mJ TEM₀₀, 150 Hz
max, separable head and power supply

Transceiver: 30 cm, f/3 Dall-Kirkham

Detector: HgCdTe, 0.25 mm ϕ

Digitizer: logamp to Tek 2430, 8 bits with on-board averaging

For aerosol profiling, the transceiver operates with a quarter wave plate and polarizing beam splitter as a beam switch. To reduce parasitic scattering, the phase retarder is the last element before the telescope secondary, and to reduce cost for the 50-mm beam, the element is a reflective phase retarder. For cloud depolarization measurements, the polarizing beam splitter separates parallel and cross polarization components, and we accept the loss of 6 dB involved in using a 50% beam splitter as a transmit-receive beam switch rather than sacrifice the transceiver arrangement.

Status. First ground tests are planned for summer, 1986. If the system debugging goes well, we could perform flight tests in September 1986, with first scientific applications in spring 1987. One early application could be to study the structure of the top of the boundary layer, analogous to the research of Melfi et al. (1985). Because the CO₂ lidar is sensitive to larger particles than a short-wavelength lidar is, it may give a different perspective on the thickness of the mixed layer.

The next step, after downlooking tests and field application, is to install NAILS for viewing in other directions. The next stage in system development is to increase the sensitivity by using heterodyne detection without trying to stabilize the laser frequency better than is required for a reasonable intermediate-frequency filter.

References.

- Bilbro, J., G. Fichtl, D. Fitzjarrald, M. Krause, and R. Lee, 1984: Airborne Doppler lidar wind field measurements. Bull. Amer. Meteor. Soc., 65, 348-359.
- Harms, J., W. Lahmann, and C. Weitkamp, 1978: Geometrical compression of lidar return signals. Appl. Opt., 17, 1131-1135.

- Itabe, T., K. Asai, R. Hayashi, and T. Igarashi, 1984: A range resolved airborne CO₂ laser radar system for a small aircraft. Abstracts, 12th International Laser Radar Conference, Aix en Provence, 189-190.
- Melfi, S.H., J.D. Spinhirne, S-H. Chou, and S.P. Palm, 1985: Lidar observations of vertically organized convection in the planetary boundary layer over the ocean. J. Climate Appl. Meteor., 24, 806-821.
- Steinvall, O., G. Bolander, and T. Claesson, 1983: Measuring atmospheric scattering and extinction at 10 μ m using a CO₂ lidar. Appl. Opt., 22, 1688-1695.
- Uthe, E.E., 1981: Lidar evaluation of smoke and dust clouds. Appl. Opt., 20, 1503-1510.

N87

10363

UNCLAS

ATMOSPHERIC CORRELATION TIME MEASUREMENTS USING
COHERENT CO₂ LIDAR

G. M. Ancellet, R. T. Menzies
Jet Propulsion Laboratory
California Institute of Technology
Pasadena, California, U.S.A.

A pulsed TEA-CO₂ lidar with coherent detection has been used to measure the correlation time of backscatter from an ensemble of atmospheric aerosol particles which are illuminated by the pulsed radiation. The correlation time of the backscatter return signal is important in studies of atmospheric turbulence and its effects on optical propagation and backscatter. If the temporal coherence of the pulse is large enough (several microseconds), then the temporal coherence of the return signal is dominated by the turbulence and shear for a variety of interesting atmospheric conditions. Various techniques for correlation time measurement are discussed and evaluated.

The theoretical formulation of the spatio-temporal correlation function for the return signal field of a pulsed lidar, recently developed by Churnside and Yura [1] is used to provide correlation time estimates. (This formalism applies to turbulence scale sizes larger than the inner limit of the inertial sub-range.) In this study we have incorporated a laser pulse shape which is a better approximation of a TEA-CO₂ laser pulse than the Gaussian pulse shape used as an example by Churnside and Yura. The analytical results obtained are used to gain a better understanding of experimentally observed return signals using an injection-controlled TEA-CO₂ coherent lidar system described in an earlier publication [2].

The temporal autocovariance function of the pulsed lidar return signal amplitude $U(t)$ is defined as $\langle U(t)U(t+\tau) \rangle$ and can be written as in Ref. [1]:

$$\Gamma(\tau) = \frac{\beta(z)}{2z^2} \exp[-2k^2 \sigma_z^2 \tau^2] + \int_0^\infty dt' [P(t-t')P(t+\tau-t')]^{1/2} \quad (1)$$

where $P(t)$ = transmitted power at time t , $\beta(z)$ = aerosol backscatter coefficient at range z , $k = 2\pi/\lambda$. The aerosol velocity distributions $p(v_z)$, $p(v_t)$ are assumed to be Gaussian within the volume of interest (100 m - 500 m) [3]:

$$p(v_z) = \frac{1}{\sqrt{2\pi} \sigma_z} \exp[-(v_z - \bar{v}_z)^2 / 2\sigma_z^2] \quad (2)$$

$$p(v_t) = \frac{1}{2\pi \sigma_t^2} \exp[-(v_t - \bar{v}_t)^2 / 2\sigma_t^2] \quad (3)$$

where v_z , v_t and σ_z^2 , σ_t^2 are the means and variances of the corresponding wind components. These two conditions and the expression for the equation (1) are only valid within the inertial subrange, considering that the outer scale of turbulence is approximately equal to the depth of the mixing layer, or to the spatial scale of organized convective motions.

Using Equation (1), we can calculate the temporal autocovariance function of the return signal field for modelled laser pulse shapes. A good approximation to the TEA-CO₂ laser pulse is a two-step function. Three different laser pulse shapes are considered in Figure 1, together with aerosol velocity fluctuation levels of $\sigma_z = 0$ and $\sigma_z = 1 \text{ ms}^{-1}$. The relationship between σ_z and ϵ , the viscous dissipation rate of turbulence, is obtained assuming the Kolmogoroff spectrum, where the spectral density of the average kinetic energy of the turbulence, $S(k) dk = A \epsilon^{2/3} k^{-5/3} dk$ [4], where $A = 0.5$ for longitudinal velocity fluctuations. By integrating the spectral density over the inertial subrange, assuming an outer scale length, $L_0 = 100 \text{ m}$ ($k_{\min} = 2\pi/L_0$), the value for ϵ which is determined for $\sigma_z = 1 \text{ ms}^{-1}$ is $\epsilon = 1.7 \times 10^{-2} \text{ m}^2 \text{ s}^{-3}$. This corresponds to "light to moderate" turbulence [5,6]. Characterization of clear air turbulence appears to be possible using the correlation measurements, however further developments of this study require, for the purpose of comparison, supporting information about atmospheric turbulence based on standard meteorological data.

Hardesty [7] recently reported observing typical velocity standard deviations of 2 ms^{-1} , based on pulsed CO₂ Doppler lidar spectral widths, corresponding to a correlation time of $0.7 \mu\text{s}$. Such a short correlation time, if representative of typical atmospheric conditions, places a significant limitation on the temporal coherence of a monochromatic laser pulse which is backscattered from a distant volume, and would have major implications on the performance characteristics of coherent Doppler lidars in the visible and infrared wavelengths. Further studies of this sort are important in assessing the effects of the atmosphere in various shear and stability regimes on the correlation time of aerosol backscatter.

Our experimental observations of correlation time are deduced from the statistical distribution properties of the return signal intensity from shot to shot, using the Inverse Relative Root Variance (IRRV) concept. The statistics of monochromatic, fully developed speckle patterns correspond to those of Rayleigh phasers with a Rayleigh distributed amplitude and uniformly distributed phase, and probability density functions (PDFs) of the intensity obey to an exponential distribution. This is applicable to atmospheric aerosol backscatter signals detected using a coherent receiver. The PDF of the atmospheric return intensity changes from an exponential distribution to a Gamma distribution as the turbulence level increases and as a temporal averaging of the signal is performed (long laser pulse or low-pass filtering at the output of the receiver) [8]. The first and the second moments of the statistical distribution of

the received power P_r , $\langle P_r \rangle$ and $\text{var}(P_r)$ are from their ratio $\langle P_r \rangle / [\text{var}(P_r)]^{1/2}$ a measure of the relative amplitude accuracy. This ratio is referred to as the inverse relative root variance (IRRV) and is related to the carrier-to-noise ratio (CNR) and to the IRRV₀ of the atmospheric signal.

$$\text{IRRV} = \left[\frac{\text{CNR}/2}{1 + \text{CNR}/2\text{IRRV}_0^2 + (2\text{CNR})^{-1}} \right]^{1/2} \quad (7)$$

In the limit of large signal ($\text{CNR} > 5$), the IRRV is reduced to IRRV₀. When this is the case, and when the received signal is subsequently smoothed by a RC filter, the IRRV is given as [9].

$$\text{IRRV} = [1 + 4\pi T/\tau_c]^{1/2} \quad (8)$$

where $T = RC$ and τ_c = correlation time of the atmospheric backscatter signal. Consequently a measure of IRRV leads to a measure of the correlation time.

Measurements were conducted at a given range, along a horizontal path and a slant path in order to investigate the effect of the turbulent eddies encountered within or near the top of the boundary layer. In order to reduce the spectral broadening induced by the laser pulse length, the CO₂ TEA laser was operated using a long pulse similar to the case (c) in Fig. 1. Measurements of the temporal coherence of the aerosol backscatter signal have resulted in a range between 2-2.5 μs for the correlation time under small to moderate turbulence conditions, which were the conditions observed most often. Much lower values ($< 1 \mu\text{s}$) were found for higher turbulence as encountered at the interface between the boundary layer and the free troposphere. Thus the use of coherent integration times much longer than 2.5 μs in feasibility studies of Doppler lidar performance may lead to overly optimistic conclusions.

REFERENCES

1. J. H. Churnside and H. T. Yura, "Speckle statistics of atmospherically backscattered laser light", *Appl. Opt.* **22**, 2559 (1983).
2. R. T. Menzies, M. Kavaya, P. H. Flamant, D. A. Haner, "Atmospheric aerosol backscatter measurements using a tunable coherent CO₂ lidar", *Appl. Opt.* **15**, 2510 (1984).
3. F. Pasquill, *Atmospheric Diffusion*, Ellis Horwood Ltd., John Wiley, New York, p. 71 (1974).
4. V. I. Tatarski, *The Effects of Turbulent Atmosphere on Wave Propagation*, (Translated from Russian, Israel Program for Scientific Translations), National Scientific Foundation edition, TT-68-50464 (1971).
5. P. B. MacCready, "Standardization of gustiness values from aircraft", *J. Appl. Meteorol.* **3**, 439 (1964).

6. R. M. Huffaker, Ed., NOAA Technical Memorandum ERL WPL-37, Feasibility study of satellite-borne lidar global wind monitoring system, (1978).
7. R. M. Hardesty, "Simultaneous measurements of range resolved species concentrations and wind velocity characteristics by pulsed coherent lidar", Digest of the 12th ILRC, Aix-en-Provence, France (1984).
8. G. Parry, "Speckle Patterns in Partially Coherent Light", in Laser Speckle and Related Phenomena, J. C. Dainty, Ed., Springer-Verlag, Berlin (1975).
9. H. Cummins, H. Swinney, "The theory of light beating spectroscopy", in Progress in Optics, Vol. VIII, E. Wolf, Ed., North-Holland Publishing Company, Amsterdam (1970).

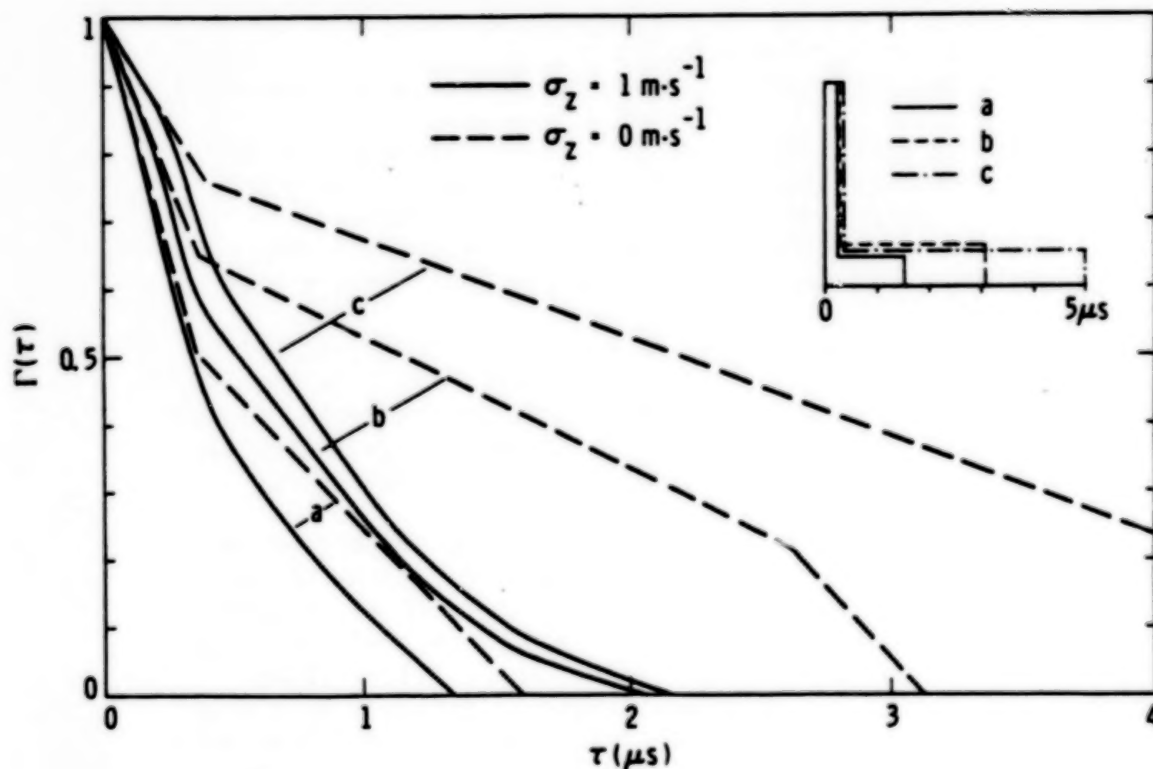


Fig. 1. Normalized temporal autocovariance function of aerosol returns versus time for three laser pulse shapes a, b, c.

N87

10364

UNCLAS

PULSED MONONODE DYE LASER DEVELOPED FOR A GEOPHYSICAL APPLICATION

J.P. Jegou, T. Pain and G. Mégie
Service d'Aéronomie du CNRS BP 3
91370 Verrières le Buisson (France)

Following the extension of the Lidar technique in the study of the atmosphere, the necessity of having a high power pulsed laser beam with a narrowed bandwidth and the possibility of selecting a particular wavelength within a certain spectral region arises.

We think of some possible experiments in the following fields :

- measurement of the temperature in the upper atmosphere by stimulation of the sodium layer present at the altitude of 90 kilometers
 - measurement of the pressure from ground level up to heights of 10-20 kilometers
 - measurement of the wind velocity by the Doppler shift detection of the backscattering emission
- In addition, new lab spectroscopic experiments can be envisaged.

With the collaboration of J.Y. Meyer (laboratoire de photophysique moléculaire ORSAY - FRANCE) we have developed a laser cavity using the multiwave Fizeau wedge (MMFW). Using the classical method of beam amplification with the aid of different stages, a new pulsed dye laser device has been designed.

The originality resides in the use of reflecting properties of the MMFW. Locally a plan wave coming with a particular angular incidence is reflected with a greater than unity coefficient ; this is the consequence of the wedge angle which doubles the participation of every ray in the interferometric process.

Taking into account the transmitting properties, we obtain a filter closing the laser cavity with a bandwidth better than that of a Fabry Perot interferometers (F P). Figure (1) shows the cavity design. It is defined by one MMFW (average thickness : 1,2 mm) and a mirror (MIR). An FP filter 10 mm thick is put in it. Tuning of wavelength is achieved by a step to step translation of the whole cavity (except the beam axis) with the consequent variation of the local thickness of the wedge. The accord of the mode length is realized by a piezo translator fixed at the back of the mirror. The control of the two parameters is performed by a micro computer.

A shortcoming of the Fizeau-cavity configuration results in both the dependence of the spectral response with location observation outside the cavity and with the transverse dimension of the beam. This difficulty is solved by placing a lens just

after the output mirror. It plays the role of a pinhole and improves the monomode character of the whole laser.

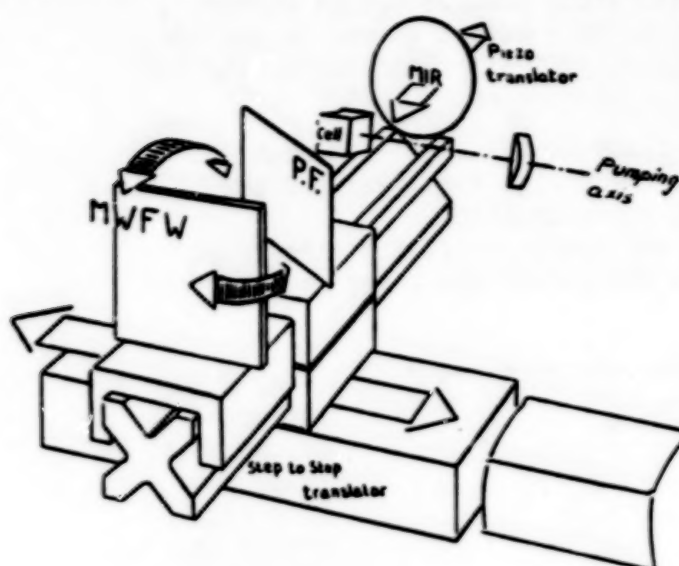


Fig. 1
Setup of the
Fizeau cavity
(the MIR + PF +
MFW elements
are mobile when
the wavelength
is tuned).

Despite of the weakness of the cavity signal, usually associated with a high super fluorescence in current pulsed lasers, one original set-up permits important gains in amplification and a large final spectral purity (Table 1).

Table 1 Characteristics of the laser device

	oscillator	Ampli 1	Ampli 2	Ampli 3
pump (mJ)	0,7 E-3	0,7 E-3	8 E-3	85 E-3
laser (mJ)	0,3 E-6	30 E-6	2 E-3	30 E-3
$\frac{ASE_o}{ASE + laser} (\%)^*$	no measurable	no measurable	5	35
spectral properties (nm)	/bandwidth	jitter	tunability	
	0,1 E-3	0,4 E-3	4	

* ASE + laser = amplified spontaneous emission + monomode emission

ASE o = amplified spontaneous emission + monomode emission

In our configuration high spectral purity is mainly achieved by combining different processes which decrease the backwards amplified spontaneous emission (ASE, propagating with

the opposite lens of laser beam) (fig. 2) :

- the cavity is partially disconnected from the amplifiers owing to the angle given to the Fizeau wedge used as output mirror. Consequently the reflected ASE on this output mirror is outside of the laser axis. The lens placed just after the cavity and the first amplifier accentuates this phenomenon.

The insertion of a $\lambda/4$ slide in the dye laser beam and the large distance between the third high amplifier and the others enable us to reduce the noise emission.

Mismatching of pumping and dye laser flux at the level of the different amplifiers is the second cause for degradation of the spectral purity.

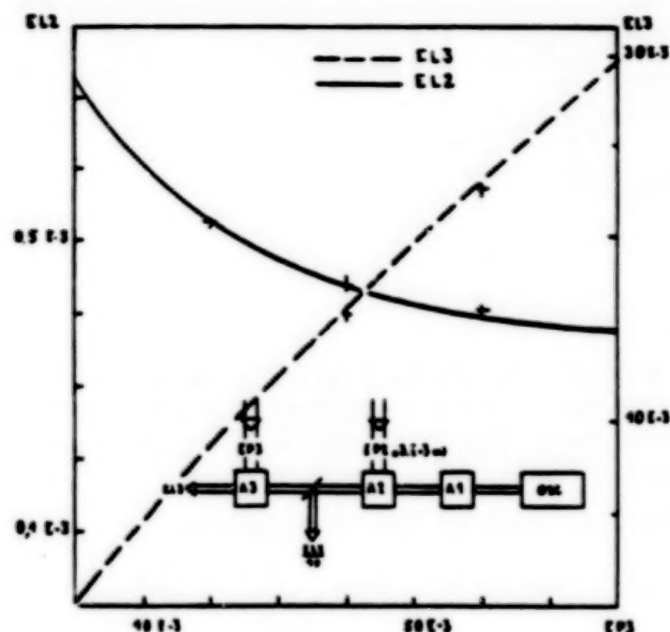


Fig. 2
Influence
of the third
stage pump-
ing flux
EP3 on the
dye laser
flux emitted
by the for-
mer stage
(EL2)

The feasibility of different geophysical applications envisageable with this laser is discussed.

N87

10365

UNCLAS

CALIBRATION AND ANALYSIS FOR A 0.53 μ m INCOHERENT DOPPLER LIDAR

J. Sroga and A. Rosenberg

RCA Astro-Electronics
P. O. Box 800
Princeton, NJ 08540I. Introduction

A ground based, prototype Doppler lidar is being developed to demonstrate the feasibility of an incoherent detection technique to remotely measure winds in the atmosphere. This prototype system consists of a narrow-band, single-frequency laser transmitter, a high-resolution, Fabry-Perot Interferometer (FPI) utilizing a multichannel Image Plane Detector (IPD) and a data acquisition system. A description of the prototype Doppler lidar hardware is given in Rosenberg and Sroga, 1985. This paper will describe the calibration and analysis procedures for this system. Preliminary results from data obtained with the system pointed vertically will be presented.

II. Instrument Calibration

The signal intensity measured in each channel of the FPI-IPD Doppler lidar is the convolution of the spectral distribution of the source (e.g. laser or atmospheric backscatter) with the instrument transmission function for that particular channel. The instrument functions, which contain information of the spectral broadening effects and the relative IPD channel sensitivities, are obtained by a wavelength scan of the instrument across a narrow-band, single-frequency source. Fig. 1 illustrates the transmission function of the 12-channel Doppler lidar FPI obtained by pressure scanning the etalon chamber while illuminating the FPI entrance aperture with diffuse light from a stabilized, single-frequency helium neon laser. The periodic nature of the FPI transmission function suggests that a Fourier series decomposition can be used to completely describe the instrumental broadening effects. Killeen and Hays, 1984 describe a procedure for calculating a Fourier series of such data and translating these Fourier coefficients computed at a calibration source wavelength to other operating wavelengths. Fig. 2 shows the magnitude of the channel #1 Fourier coefficients as a function of the harmonic term at the calibration source wavelength (a, 0.6328 μ m) and translated to the Doppler lidar operating wavelength (b, 0.532 μ m). The Fourier calibration coefficients for each FPI-IPD channel are calculated in a similar manner.



Fig. 1. Relative transmission function of the 12-channel FPI obtained during a pressure scan of the FPI etalon chamber using a stabilized, single-frequency helium neon laser as the calibration source.

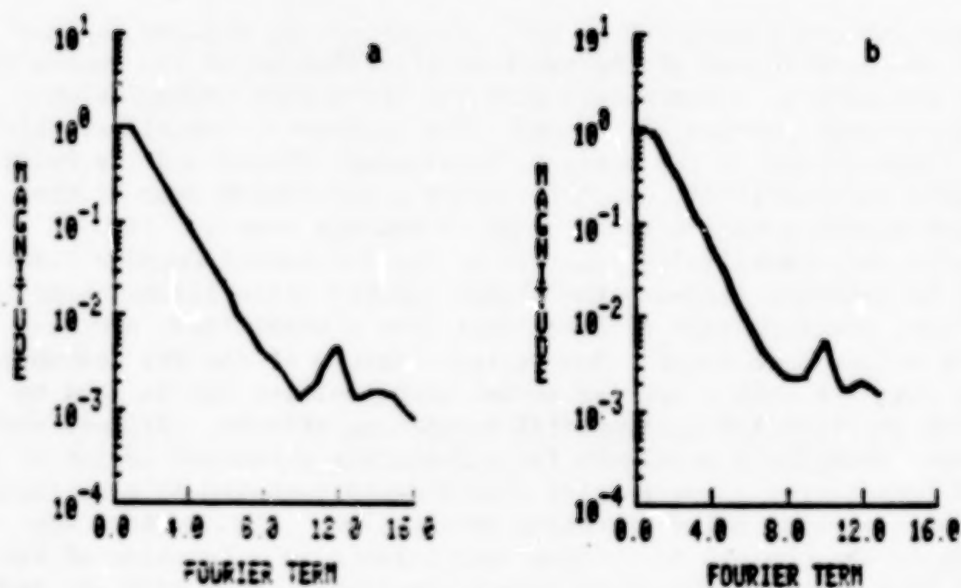


Fig. 2. Magnitude of the Fourier coefficients for channel #1 at the calibration source wavelength (a, 0.6328 μm) and translated to 0.532 μm (b).

III. Data Analysis

The Fourier calibration coefficients calculated from the above procedure are combined with an analytical description of the FPI and the atmospheric backscatter spectra to form a model of the Doppler lidar backscattered signals. This instrument model is a nonlinear function of the system design parameters and the Fourier calibration coefficients, which are the system constants, and variable parameters as the total aerosol and molecular backscatter intensities and the mean atmospheric Doppler shift velocity. A nonlinear regression technique (Draper and Smith, 1981), which is similar to the matrix technique of Killeen and Hays, 1984, is used to adjust these variable model parameters to yield a "best fit" of the model to the measured FPI-IPD intensities, and therefore optimum values for these parameters.

Preliminary atmospheric testing with the 0.53 μm Doppler lidar has been conducted to demonstrate the system capabilities. The calibration and analysis procedures have been applied to this data to derive the mean Doppler shift and separate the total aerosol and molecular backscatter contributions. Fig. 3a illustrates an example of data for a single shot obtained on 3 September, 1985 with the system pointing vertically. The sample labeled 1 is a measurement of the transmitted laser pulse spectrum and the subsequent samples represent the atmospheric backscatter spectra sampled at 300m intervals (2 = 300m, 3 = 600m). Fig. 3b shows the least-squares regression fit of the instrument model to this data. Fig. 4 is an average of approximately 10 shots along with the regression fit to this averaged data. A discussion of these results and error analysis will be presented.

References

- Draper, N. R., and H. Smith, 1981, Applied Regression Analysis, Second Edition, John Wiley and Sons, Inc., New York, NY, pp. 709.
- Killeen, T. L. and P. B. Hays, 1984, "Doppler Line Profile Analysis for a Multichannel Fabry-Perot Interferometer", Appl. Opt., V23, pp. 612-620.
- Rosenberg, A. and J. Sroga, 1985, "Development of a 0.5 μm Doppler Lidar for Space Applications" in Global Wind Measurements, W. E. Baker and R. J. Curran (Eds.), H. Deepak Publishing, Hampton, VA.

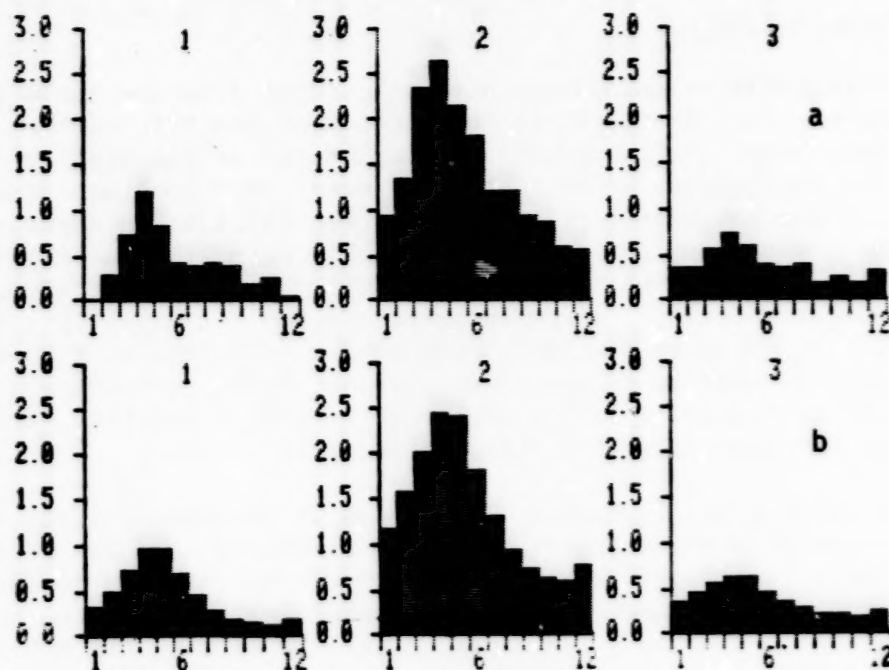


Fig. 3. Doppler lidar data obtained for a single laser pulse (a) and a regression fit of model to above data (b). See text for further description.

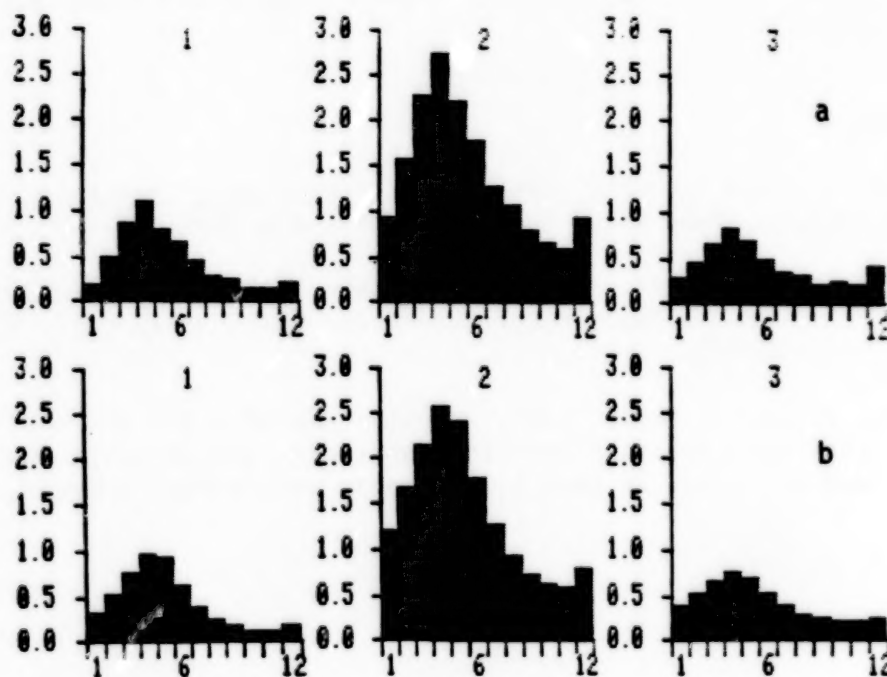


Fig. 4 Same as Fig. 3 except an average of ~ 10 shots.

N87

10366

UNCL

CO₂ LIDAR SYSTEM FOR ATMOSPHERIC STUDIES
 R. Barbini, A. Ghigo*, M. Giorgi, K.N. Iyer**,
 A. Palucci*, and S. Ribezzo
 ENEA, TIB, Divisione Fisica Applicata, P.O. Box
 65, 00044 Frascati (Rome), Italy

ABSTRACT

A Lidar facility using a TEA CO₂ laser source is being developed at the ENEA Laboratories for atmospheric studies. The different subsystems and the proposed experimental activities are described.

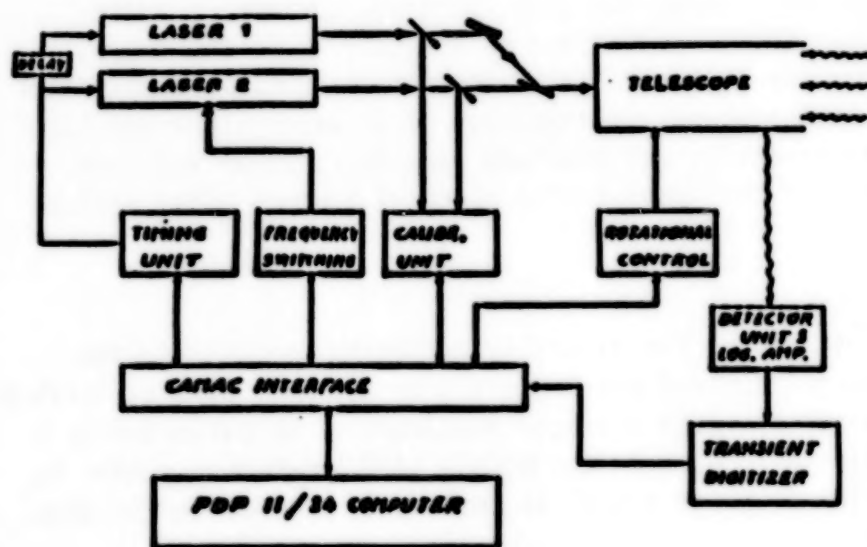
INTRODUCTION

The Lidar technique has been well recognized as a potential tool for atmospheric studies /1/. Among the various types of Lidar measurements, the DIAL technique is particularly suited for pollution monitoring and measurement of trace constituents because of its high sensitivity and long ranges /2/. The 9-12 μ m IR spectral region is rich with specific absorption signatures of many atmospheric pollutants, it is relatively eye safe and the atmospheric transmittance is high in this region. Coherent (Doppler) CO₂ Lidars also find unique application for precise wind measurements both from ground based and airborne platforms /3/.

LIDAR FACILITY

a) Lidar Transmitter

The Lidar system (Fig. 1) /4/ uses a tunable pulsed TEA CO₂ laser source in the 9-12 μ m



region as its transmitter. The transmitted beam should have low divergence to minimize the illuminated area. The beam should also have narrow pulse length to improve the range resolution. A laser source with these characteristics has been achieved using the Self Filtering Unstable Resonator (SFUR)/5/ concept. In this configuration (Fig. 2), a

Fig. 1 - Layout of the LIDAR/DIAL facility.

(*) ENEA Guest.

(**) ENEA Guest. Permanent address: Phys.Dept. Saurashtra University,
 360005 Rajkot (India).

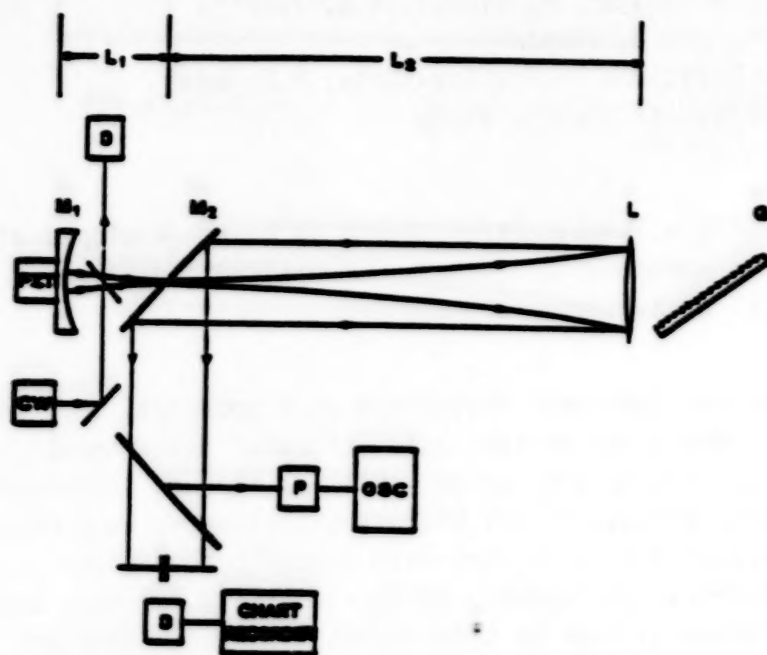


Fig. 2 - The CO₂ SFUR resonator: M₁, M₂ are mirrors; D = pyroelectric detector; P = photon drag detector; C.W. = CO₂ injection laser; PZT = piezo transducer; L = lens; G = grating.

plane mirror with a suitably chosen hole, placed at the confocal point of a negative branch unstable resonator, limits the output beam to single transverse mode with small divergence. Diffraction at the hole effectively counteracts the focusing action of the negative branch cavity thereby avoiding the hot spot and associated gas breakdown or damage to the optical components. The line tunability of the cavity can be achieved using a plane grating with a lens in front of

it (Fig. 2) which replaces one of the cavity mirrors. Alternatively a concave grating can also serve the same function. However, a major problem in this case is the appearance of astigmatism in the output beam: work is under way to correct this aberration. Single longitudinal mode locking has been achieved by injection of an external CW CO₂ laser. Insertion of an intra-cavity low pressure section is under way. The measured parameters of the laser source along with other Lidar system parameters are listed in Table I /6/.

b) The Receiving System

The signal backscattered by the naturally occurring aerosols in the atmosphere (for range resolved measurements) or returned by a calibrated or topographic target (in path averaged measurement) is collected by a telescope (Fig. 3) and focused on the HgCdTe (SBRC) detector cooled to 1N₂ temperature. The detected signal is amplified and fed to the data processing system.

c) Data Processing System

The analog signal from range resolved measurement is digitized by an 8 bit transient digitizer (Transiac) at a sampling rate of 100 MHz and stored in the computer (PDP 11/24) via CAMAC data acquisition system.

TABLE I - CO₂ LIDAR/DIAL SYSTEM

Laser source: TEA CO₂ grating tuned $\lambda = 9 + 11 \mu\text{m}$
 Pulse energy $E = 2.7 \text{ J TEM}_{00}$
 Pulse width $\tau = 80 \text{ ns}$
 Pulse repetition rate $f = 1 + 5 \text{ Hz}$
 Beam divergence $\theta = 0.65 \text{ mrad}$
 (half angle)

Receiver: Telescope

Newtonian $d = 33 \text{ cm}$
 $f \# = 3$
 FOV (adjustable) $\approx 1 \text{ mrad}$
 Detector: HgCdTe @ 77°K
 Area $1 \times 1 \text{ mm}^2$
 NEP (band $10^{-8} - 10^{-12} \text{ W}$
 integrated)

Data Acquisition System

Transient digitizer a) Tektronix mod. 7912
 Sampling rate 1 GHz
 b) Transiac
 Sampling rate 100 MHz
 Resolution 8 bit
 CAMAC interface with
 PDP 11/24 computer.

In the case of path averaged measurements using targets the return signal is digitized by Tektronix 7912 transient digitizer having a sampling rate of up to 1 GHz. The CAMAC system also controls the measurement cycle, telescope movements and other instrument settings.

d) **Calibration**

Since the Lidar system employs the backscattering from the aerosols to provide the return signal, precise knowledge of the aerosol backscattering coefficient β is necessary at the different CO₂ wavelengths. In order to obtain

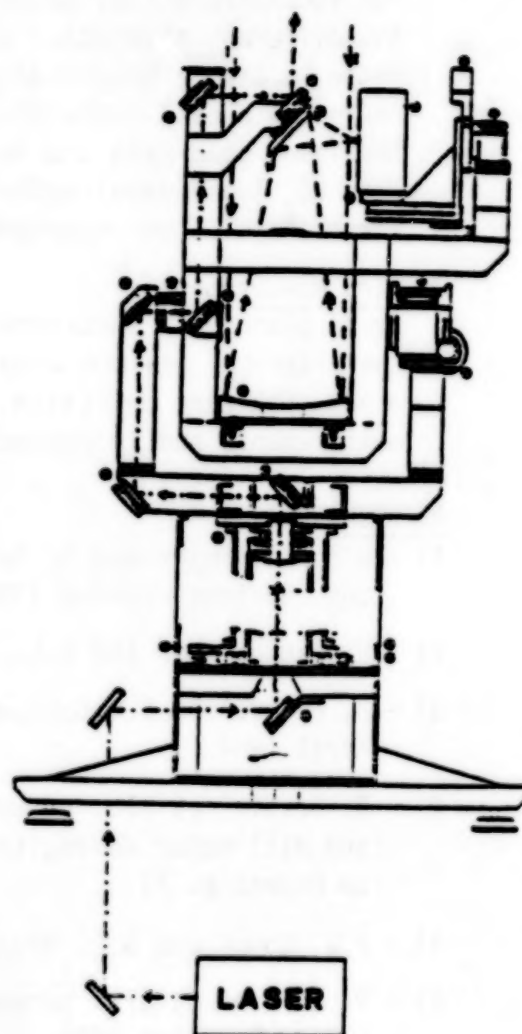


Fig. 3 - Telescope

this, the Lidar system has to be calibrated with targets of known reflectivity. We are planning to make measurements of the reflectivity ρ^* and its spectral and angular dependence with various targets, such as flame sprayed Aluminium, flowers of sulfur, Silicon Carbide sand paper which are expected to be Lambertian surfaces, in the 9-12 μm region.

The Lidar beam will be directed horizontally through the atmosphere to obtain backscatter coefficients of aerosols well below the boundary layer. Such measurements will also be used to study the amplitude and phase perturbations to the propagating beam introduced possibly by atmospheric turbulence using optical image processing techniques.

e) Absorption Measurements

For the Differential Absorption Lidar (DIAL) it is necessary to know the different absorption cross sections which depend on the laser line shape, pressure broadening effect and interference. An experiment to introduce a cell containing the desired gas at controlled pressure into the laser beam path and to measure the absorption coefficient at different CO_2 laser wavelengths is being set up. Preliminary measurements for ozone will be reported.

f) Wind Measurements

It is planned to incorporate heterodyne detection in the future whereby the Lidar can measure wind velocity to a precision of the order of a m/s. Coherent detection also improves the sensitivity of pollution measurements and increases the range.

REFERENCES

- 1) - D.K. Killinger and A. Mooradian: in "Optical and laser remote sensing" eds. Springer-Verlag (1983)
- 2) - R. Baumgartner and R.L. Byer: Opt.Lett. 2, 163 (1978)
- 3) - J. Bilbro et al.: Bull.of the American Meteorological Soc. 65, 4, April 1984
- 4) - R. Barbini et al.: paper presented at X Int.Conference on Infrared and Millimeter Waves, Lake Buena Vista (USA), December 1985, Conference Digest p. 71.
- 5) - P.G. Gobbi and G.C. Reali: Opt.Comm. 52, 195 (1984)
- 6) - R. Barbini et al.: paper presented at Lasers'85 Conference, Las Vegas (USA), December 1985

N87

10367

UNCLAS

GENERATION OF ATTENUATION CORRECTED IMAGES FROM LIDAR DATA

Edwin W. Eloranta and Daniel K. Forrest

Dept. of Meteorology
University of Wisconsin
Madison, WI

The interpretation of data generated by aerosol backscatter lidars is often facilitated by presentation of RHI and PPI images. These pictures are especially useful in studies of atmospheric boundary layer structure where convective elements, stratifications and aerosol laden plumes can be easily delineated. This paper describes procedures used at the University of Wisconsin to generate lidar images on a color enhanced raster scan display.

The generation of RHI and PPI images from lidar data presents several problems: 1) it is a computer intensive task because each image consists of 10^5 to 10^6 separate pixels, 2) data are acquired in polar coordinates (range, elevation angle) and thus do not map exactly onto the rectangular raster scan coordinates of the picture display, 3) attenuation corrections must be applied to produce a useful image, 4) even after attenuation and range-squared corrections the lidar return amplitudes often vary over a factor of 100 while image displays typically provide less than 32 distinguishable gray levels, 5) real-time display of lidar images is normally required to control data acquisition during experiments.

Different routines are used to form real-time and post-facto displays. Images prepared for publication or detailed analysis are generated using a more sophisticated correction for atmospheric attenuation than is used for the real-time pictures. Except for this difference, which is due to computation time constraints, the image forming routines are identical.

Real-time displays on the UW lidar are formed using the procedures described by Kunkel et al. (J. Applied Meteor., Vol. 16 #12). Each lidar profile is corrected for variations in the transmitted laser energy and for the inverse range-squared signal decrease. The logarithm of the lidar return is then displayed in an A-scope format. A pair of parallel straight lines are shown superimposed on the lidar return. The operator controls the vertical position, the separation and the slope of the displayed lines pairs. The lower line delineates the largest corrected return which will be displayed as black while the upper line indicates the smallest return which will saturate the displayed intensity. Before the lidar return is displayed signal values corresponding to the lower line are subtracted from the signal and the signal values are rescaled such that the distance between the enhancement lines corresponds to 64 levels. The rescaled signal is now used as an index to a color enhancement look-up table. Each element of

the table contains three values corresponding to the mixture of red, green and blue which is to be projected for each rescaled input value. A series of computer subroutines to load the color enhancement tables are available to the operator.

Changing the slope of the enhancement lines corresponds to providing a correction for a spatially invariant attenuation coefficient while changing the separation and the vertical position of the lines provides control of the displayed dynamic range.

The operator selects range and altitude boundaries of the displayed image. The program then computes the ranges at which the last two lidar profiles intersect the near edge of the display area. The lidar data points nearest in range to the intersection points are used to specify two pixels in the image. Any pixels which fall between these two pixels are filled in by linear interpolation. The program then computes the ranges at which the two profiles intersect the next vertical column of pixels and repeats the above process. This is continued until all pixels in the display memory which fall within the pie shaped sector between the last two lidar firing directions are specified.

This real-time display algorithm executes in well under one second per laser shot when run on a digital equipment PDP-11/40. While the pictures produced are excellent for real-time control of experiments and scanning of data tapes, careful examination of the images quickly reveals the limitations of the constant attenuation assumption. Images consisting of a well mixed hazy boundary layer under a much cleaner upper layer force the operator to choose between over-correcting for attenuation in the upper layer or under-correcting in the lower layer. Images containing dense plumes or strong swelling of hydrosopic aerosols at the top of convective cells occasionally show shadows resulting from variations in attenuation. An algorithm based on the Bernoulli solution to the lidar equation is used to improve the attenuation correction when preparing presentation quality pictures. In order to apply this solution, a functional relationship between the extinction cross section and the backscatter cross section must be provided: in addition the extinction cross section must be provided at one point in the data interval. The procedure proposed by Klett (Applied Optics, Vol. 20, #2), where the extinction cross section at large ranges is estimated, works only in the presence of substantial extinction. Because the extinction cross section is usually small in the fair weather boundary layer, the Klett approach is not applicable.

The RHI attenuation correction algorithm first estimates the extinction cross-section profile of the lowest elevation angle shot in the image. In the range interval between 1 and 7.5 kilometers, a least-squares linear fit is matched to the logarithm of the range-squared and energy corrected lidar profile.

The extinction at a data point just out of the overlap region is estimated, for each lidar return in the image, from:

$$BETA(R,J) = \frac{SIGNAL(R,J)}{LEAST-SQUARE FIT(R)} * SLOPE BETA * EXP(2*(TAU(J)-TAU(1)))$$

where:

BETA(R,J) = extinction at range, R, for J-th lidar return
 SIGNAL (R,J) = energy and range-square corrected lidar return
 TAU(J) = optical depth from lidar to range, R, for J-th return

and where: The value of the estimated optical depth, TAU(J), is set equal to TAU(1) unless it can be estimated from an immediately preceding image.

Equation 1 provides a first estimate of the extinction cross section at one point in each of the lidar profiles which make up the image. The Bernoulli solution to the lidar equation is then used to generate first guess values for the extinction at each point in all profiles. In the relatively uniform, small extinction conditions normally encountered in clear air boundary layer studies this procedure provides good initial values and therefore relatively good first estimates of the extinction field. However because of the well-known instability of the Bernoulli solutions small errors in the initial guesses will cause substantial errors at longer ranges. Images produced from these corrected profiles show unacceptable fluctuations between successive lidar shots.

The corrected data points are now grouped by altitude and a median filter is applied to each altitude group so as to provide a median profile of the extinction as a function of altitude. The median profile is very stable in the presence of errors in the Bernoulli solutions. The median vertical profile is then used as a guide to correct the initial guesses for each lidar shot. For each point along each lidar shot, we compute the correction to the initial guess which would place the point exactly on the median vertical profile. The initial guess is then adjusted by the median of the computed corrections for that shot and the Bernoulli solution is recomputed. This process is very stable in the presence of scattering inhomogeneities in the individual lidar return.

The recorrelated lidar profiles are once again used to compute a median vertical profile of extinction and the whole process is repeated until the maximum change in an initial guess of any of the returns in the picture is below an operator supplied threshold value. This procedure converges to produce an image from 50 lidar returns in ~ 30 seconds of computation time on the UW lidar VAX 751 computer and attached CSPI mini-map array processor.

The scattering cross section in the hazy mixed layer is occasionally as much as 100 times as large as it is in the clear stable layer immediately above. If the contrast range of the lidar display is adjusted to accommodate this large dynamic range, small fluctuations in scattering cross section are not visible in either layer and much interesting image detail is lost. Most of this detail is restored by displaying the difference of computed scattering cross section from a background level computed by fitting a smoothing spline to the median vertical profile of scattering cross section.

N87

10368

UNCLAS

GAS DISPERSION MEASUREMENTS USING A
MOBILE RAMAN LIDAR SYSTEM

J.D. Houston

Optech Inc., Downsview, Ontario, Canada M3J 2N6

D.R. Brown

British Gas Corporation, Midlands Research Station, U.K.

Over recent years, the exploitation of natural gas resources to supply energy demands has resulted in the need to engineer pipelines and plants capable of handling extremely high pressures and throughputs. This increase in scale of operation has meant that more attention has been directed to evaluating the consequences of releases of material whether accidental or deliberate in nature. These consequences must be understood in order to develop methods to define the engineering standards required to construct gas handling installations and pipework. An important aspect of assessing the consequences of a release is an understanding of how gas disperses in the atmosphere over a wide range of release and atmospheric conditions. The most cost effective way of providing such information is through the development and use of reliable theoretical prediction methods. Such theories must, however, be validated using experimental data obtained under conditions which not only address the critical physical processes occurring but also relate to the scale of likely full scale incidents. Experience has shown that it is not feasible to carry out sufficiently large scale experiments using conventional fixed probe measurement techniques. Therefore the need for some form of remote sensing device was identified. The various possibilities studied led to the conclusion that Light Detection And Ranging, LIDAR, offered the most suitable method.

This paper briefly describes the system designed and built for British Gas by Optech Inc. of Toronto, and discusses its recent use in monitoring operational ventings from a high pressure transmission system.

In measuring releases of natural gas, of prime importance are the flammable limits within which gas/air mixtures burn. For natural gas these limits are 15% and 5% by volume, the upper and lower flammable limits respectively. In terms of remote sensing, these concentrations are extremely large when compared to pollution problems which generally require the detection of parts per million (ppm) quantities. This high detection limit coupled with a modest range requirement ($\leq 1000\text{m}$) made it possible to consider the use of Raman scattering as the measurement technique.

The Raman technique provides a direct means of deriving absolute concentration values. A two-channel receiver is used to observe the Raman scattering from the nitrogen molecules in the atmosphere simultaneously with the Raman scattering from any methane gas. The ratio of the methane

and the nitrogen signals is then formed producing a self-referencing system. The relative intensity of the methane Raman signal can be converted directly to a concentration using the known concentration of nitrogen in the air. Information on the position or range of the gas cloud is obtained by measuring the time of flight of the transmitted laser pulse as it propagates through the atmosphere. Table 1 outlines the system specifications.

Table 1: LIDAR Specifications

Performance Specification for the Measurement of Methane

Methane concentration 2% - 20%

Distance range 100 - 1000m

Accuracy of Measurement 10%

Spatial Resolution

- transverse to line of sight, 0.05m at 100m range to 0.5m at 1000m range

- along line of sight, 1.4m

Background radiance conditions; clear daylight sky; visibility 13km

System Specification

Laser: xenon chloride excimer operating at 308nm

pulse width 4ns

average power typically 3-5W at 100 pps

Telescope Subsystem: 0.5m diameter f/10 Cassegrain reflecting mirror

Separate detection channels for nitrogen and methane

Data acquisition subsystem: 2 transient digitizers with 2 ns resolution
PDP 11 computer

Vehicle Specification

Ford Cargo Truck 10 tonne gross weight

Body size 2.5m wide 6.1m long

Onboard generator producing 12.5 KVA

Ratcliffe lifting table capable of lifting 1000 kg

The effectiveness of LIDAR as a field instrument is dependant equally on the optical engineering and the development of suitable software to control the system efficiently, collect data and to present this data in a usable format. In particular, for operations in the field, it is essential that the data collected are quickly fed back to the operator in a form which can be easily assimilated. A suite of programs has been developed to provide a rapid and interactive means of using the lidar system. Programs are available to check the system performance following alignment for a particular transceiver optical overlap configuration and to provide the necessary information to select proper settings on the data acquisition equipment. To optimize the collection of data in the minimum amount of time, software has been developed to assist in selecting the minimum number of shots along a line-of-sight for proper averaging and to display the matrix of maximum concentrations occurring along each line of sight. For a 10x10 matrix, this display can be obtained in about 1 minute

of acquiring the data. This rapid retrieval of data allows the scanning grid to be adjusted and optimized in order to remove lines of sight which are clearly well outside the gas plume. Subsequently, each line of sight can be displayed and the form and extent of the gas cloud can be studied.

Operational use of the Raman LIDAR will be illustrated with samples of measurements taken at a gas venting operation which took place on a part of the British Gas Corporation's transmission system. Examples will be presented of several presentation formats to illustrate the usefulness of LIDAR in mapping the form of the gas plume. These include data from measurements along an individual line-of-sight, lower flammability limit contours, contour slices and reconstructions of a 3-D picture of the plume contour made using a graphics software package.

The results demonstrate the operational capability of the BGC LIDAR to obtain concentration measurements at a transmission vent where no previous measurement method could be used. Improvements and developments in the software have enabled the system to be used interactively at such operations where time was critical. Use of the Raman LIDAR is continuing in an ongoing research program investigating the dispersion of natural gas plumes.

N87

10369

UNCLAS

SPECTROSCOPIC ASPECTS OF DIFFERENTIAL METHOD FOR
SOUNDING GAS COMPOSITION OF THE ATMOSPHERE

V.V.Zuev, I.I.Ippolitov, Yu.N.Ponomarev
The Institute of Atmospheric Optics, Siberian
Branch, USSR Academy of Sciences, Tomsk, 634055
U S S R

The remote sounding of atmospheric gases by the differential absorption method has been widely developed at present [1,2]. The extension of the method suggested in [3] allows one to measure both the concentration of an absorbing molecular component and the gas temperature. To realize the differential absorption method, one should analyze in detail not only the spectrum investigated but also the spectra of the other molecular components of air whose absorption lines are near the sounding-radiation frequencies. This is necessary for both determining the contribution from absorption by foreign gases to a lidar return and for choosing the sounding frequencies ν_1 and ν_2 . The optimal values ν_1 and ν_2 are found from the condition of maximum difference $\Delta\sigma = \sigma(\nu_1) - \sigma(\nu_2)$, where $\sigma(\nu_1)$ is the absorption cross section in the sounded gas line, $\sigma(\nu_2)$ out of the absorption line. The methods and techniques of sounding considered in [1-3] have been realized at radiation intensity not resulting in deviations of vibration-rotation level populations of the molecular medium from their equilibrium values and for successive sending of laser pulses at frequencies ν_1 and ν_2 into the investigated atmospheric volume. Paper [4] describes the possibility of utilizing the schemes and methods of double optical resonance spectroscopy when solving the problems on remote sounding. The method foresees the use of radiation at two frequencies simultaneously with the aim of primary population of the vibration-rotation transitions most convenient for sounding including those in hot bands.

The problems concerning the dynamics of populations of the sounded atmospheric-gas molecule levels taking into account the nonmonochromatic character of radiation (e.g. double frequency as in [4,5]), durations of exciting and sounding pulses, rates of relaxation of excited vibration-rotation states population along different channels (rotational, vibrational, and that of vibration-vibration exchange) in a natural multicomponent mixture of gases and air have been investigated in the paper.

The problems of spectroscopic software, completeness and accuracy of the initial spectroscopic information, information on channels and rates of relaxation from the viewpoint of developing specific schemes of sounding have been discussed. The values of deviations of vibration-rotation level populations of some atmospheric molecules (H_2O , CO_2 , O_2) from their equilibrium value at simultaneous action of double frequency radiation on the sounding path and the correspon-

05805 527
 ing dynamic variations of lidar-return amplitude have been estimated. The importance of nonlinear spectroscopic effects in the lidar return value variation at sounding radiation frequency equaling the resonance frequency of vibration-rotation transition in the problem on sounding the humidity profiles and concentrations of gaseous pollutants has also been estimated. The connection of the lidar-return characteristics at transmitting double-frequency laser radiation to the sounded volume with the values of meteorological parameters ρ and θ has been discussed, and the solution of the inverse problem on restituting these parameters has been considered.

References

1. Laser monitoring of the atmosphere. Ed. E.D.Hinkley. - Moscow, Mir, 1979, 416 p.
2. Spectroscopic methods for sounding the atmosphere. Ed. I.V.Samokhvalov. - Novosibirsk, Nauka, 1985, 140 p.
3. J.Mason. Lidar measurement of temperature: A new approach. - Appl.Opt., 1975, v.14, N1, p.76-78.
4. R.M.Measures. PROBE: a new technique for measuring the density profile of a specific constituent using counter-propagating laser pulses. - Appl.Opt., 1977, v.16, N11, pp. 3016-3026.
5. O.K.Voitsekhovskaya, K.A.Zamaraev, V.V.Zuev, I.I.Ippolitov. Microwave sounding of atmospheric gases: new approach. - Izv. VUZov, Radiofizika, 1986, N5(to be published).

N87

10370

UNCLAS

LINEWIDTH CHARACTERISTICS OF RAMAN-SHIFTED DYE LASER OUTPUT
AT 720 AND 940 nm

B. E. Grossmann^a, U. N. Singh^b, N. S. Higdon^c, L. J. Cotnoir^b,
T. D. Wilkerson^b, and E. V. Browell^c

Existing DIAL systems for water vapor measurements in the troposphere operate at wavelengths near 720 nm^{1,2}. The use of stronger water vapor absorption lines³ in the range 930-960 nm will significantly improve DIAL measurements in the upper troposphere and lower stratosphere where water vapor concentrations are low. The generation of light at 940 nm using a frequency doubled Nd:YAG pumped dye laser is inefficient due to the small absorption of infrared dyes at the pump wavelength. However, 940 nm generation utilizing stimulated Raman scattering (SRS) of dye lasers is attractive because of a potentially high conversion efficiency plus the possibility of retaining the narrow linewidth available from some dye lasers. In this paper, the Raman conversion efficiency and line broadening are presented for first Stokes operation at 720 and 940 nm using hydrogen and deuterium as the Raman media.

Figure 1 illustrates the present experimental setup. The laser source is a Nd:YAG pumped Quanta-Ray PDL-2 dye laser. With the grating alone as an intracavity element, the dye laser linewidth is 0.2 cm⁻¹ (FWHM), as recorded by a high finesse Fabry-Perot interferometer (Tropel Model 360) in combination with an Optical Multichannel Analyzer (Tracor-Northern OMA Model TN-1710). With hydrogen as the Raman medium, 940 and 720 nm were generated as first Stokes lines using pump wavelengths of 676 and 555 nm, respectively. The laser output energy was 50 mJ at 676 nm and 60 mJ at 555 nm. As observed by Byer⁴, conversion efficiency decreases with increasing wavelength. In our case, we first used hydrogen in a conventional SRS cell (Quanta Ray RS-1) and corrected for losses in the optics. At 400 psi the conversion efficiency for output at 720 and 940 nm was 40 and 20 percent, respectively, and at

^a Old Dominion University Research Foundation, Norfolk, VA, 23508. Working at the NASA Langley Research Center under NASA NCCI-32 while on leave from Electricité de France, Chatou, France

^b University of Maryland, Institute for Physical Science and Technology, College Park, MD, 20742

^c National Aeronautics and Space Administration, Langley Research Center, Hampton, VA, 23665.

200 psi the efficiency dropped to 20 and 10 percent, respectively. Figure 2 shows the first Stokes output energy as a function of hydrogen pressure in the SRS cell. In a second series of experiments, a waveguide Raman shifter (Lambda-Physik Model RS-4500D) was used with a 600- μm bore diameter for the fused silica capillary. First Stokes conversion efficiencies between 30 and 35 percent at 940 nm were observed for hydrogen pressures ranging from 150 to 350 psi. A reduction of the backward wave SRS as the pressure was lowered caused an increase in the net transmission of the waveguide. This led to a nearly constant overall conversion efficiency.

Inserting an etalon into the dye laser cavity, which narrows the laser linewidth to 0.02 cm^{-1} , we found the conversion efficiency to be the same as that measured for 0.2 cm^{-1} .

Particular emphasis was then put on the resulting SRS output linewidth, with the goal of obtaining lines as narrow as possible at 720 and 940 nm for lidar applications. Input linewidths at 555 and 676 nm and the output linewidth at 720 nm were measured with a Tropel Fabry-Perot interferometer using two sets of plates coated for these wavelengths. An additional interferometer (Tec-Optics Model FP-1) was used to measure the first Stokes linewidth at 940 nm. Fringe patterns for all wavelengths were recorded by an OMA. While the input laser linewidth at $\lambda = 555\text{ nm}$ was measured to be 0.020 cm^{-1} FWHM, the first Stokes ($\lambda = 720\text{ nm}$) linewidth varied from 0.029 to 0.050 cm^{-1} for hydrogen pressures ranging from 150 to 450 psi. Fringe patterns for the input laser linewidth and the first Stokes linewidth, using a hydrogen pressure of 350 psi, are shown in Figure 3(a) and (b), respectively. Similar results were obtained for the shift from 676 to 940 nm. This broadening is due to the pressure broadened Raman linewidth that is characteristic of the gas⁵. Assuming a Gaussian spectral distribution for the laser line shape and a Lorentzian profile for the Raman line shape, we calculated the resulting Raman linewidth by deconvolution. Because the Raman linewidth broadens with pressure, the measurement accuracy becomes better at higher pressure. Figure 4 shows the output linewidths measured at different pressures and the calculated pressure broadened Raman linewidth. From these measurements the hydrogen pressure broadening coefficient was determined to be $9.2 \pm 0.9 \times 10^{-5}\text{ cm}^{-1}/\text{psi}$, which is in agreement with previous measurements⁵. A pressure shift coefficient of approximately twice the value measured for the pressure broadened Raman linewidth could be observed, but the lack of high pressure data precluded any precise measurements.

In addition to hydrogen, deuterium was also used as a Raman medium. The conversion efficiency in a conventional single pass Raman shifter was too low to conduct good measurements. For this reason the waveguide Raman shifter was used instead. At a pressure of 350 psi, approximately 25 percent of the input energy was shifted to the first Stokes line at 720 nm. This number takes into account the large amount of backward wave SRS, which was significantly greater than for hydrogen. The linewidth at the first Stokes wavelength was measured to be 0.038 cm^{-1} at a pressure of 350 psi. This corresponds to a pressure broadening coefficient of $7.7 \times 10^{-5}\text{ cm}^{-1}/\text{psi}$. This agrees roughly with prior results⁵.

Using conventional cell and waveguide "Raman shifters", the shifting of dye lasers in hydrogen and deuterium was investigated. The linewidth at the first Stokes wavelength was found to be determined by pressure broadening in the Raman medium. The requirement for good conversion efficiency and narrow linewidth implies the use of a low pressure waveguide, or a low pressure Raman oscillator in combination with a high pressure amplifier. Further measurements will be made to identify the optimum technique for achieving high energy and narrow linewidth. Also, the Stokes beam spectral purity will be investigated to quantify the effect of the Raman process on the spectral quality of the input beam.

The authors wish to thank Neale Mayo, Barry Benson, and Kenneth Ritter for their excellent technical assistance on this experiment.

References

1. Browell, E. V., A. K. Goroch, T. D. Wilkerson, S. Ismail, and R. Markson, "Airborne DIAL water vapor measurements over the Gulf Stream." Conference Proceedings, Twelfth International Laser Radar Conference, Aix en Provence, France, August 13-17, 1984.
2. Cahen, C., G. Megie, and P. Flamant, "Lidar monitoring of the water vapor cycle in the troposphere." J. Applied Meteorology, 21, 2506 (1982).
3. Giver, L. P., B. Gentry, G. Schwemmer, and T. D. Wilkerson, "Water absorption lines, 931-961 nm: Selected intensities, N_2 collision-broadening coefficients, self-broadening coefficients, and pressure shifts in air." J. Quant. Spectrosc. Radiat. Transfer, 27, 423 (1982).
4. Byer, R. L., "Frequency conversion via stimulated Raman scattering." Electro-Optical Systems Design, (February 1980).
5. Murray, J. R., and A. Javan, "Effects of collisions on Raman line profiles of hydrogen and deuterium gas." J. of Molecular Spectroscopy, 42, 1 (1972).

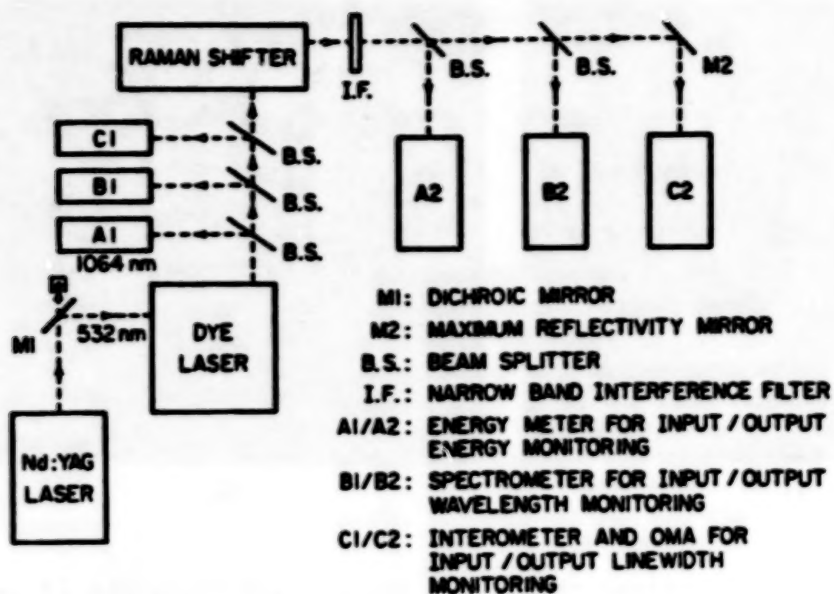


Figure 1: Experimental setup.

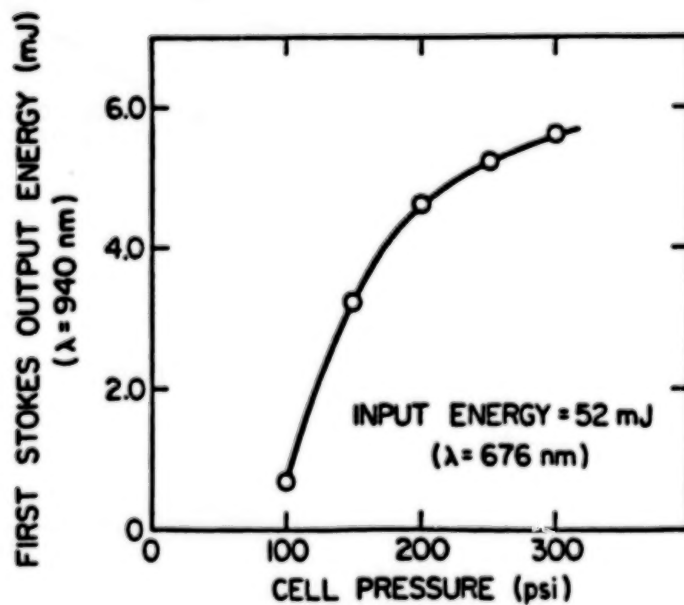


Figure 2: First Stokes output energy for SRS in H₂ pumped by 52 mJ at 676 nm versus gas pressure.

ORIGINAL PAGE IS
OF POOR QUALITY



Figure 3: Recorded fringe patterns of (a) the input laser linewidth (interferometer FSR = 0.25 cm^{-1}) and (b) the first Stokes linewidth (interferometer FSR = 0.20 cm^{-1}) at a hydrogen pressure of 350 psi.

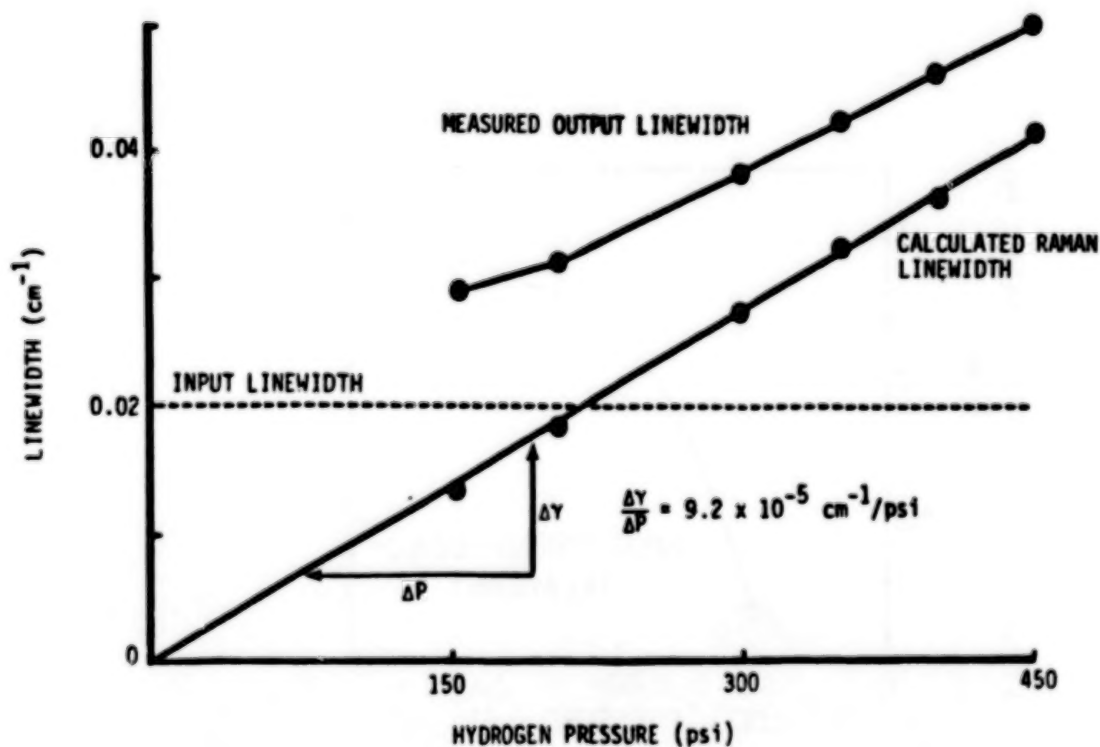


Figure 4: Output linewidth and Raman linewidth as a function of hydrogen pressure for 0.02 cm^{-1} input laser linewidth.

N87

10371

UNCLAS

THE GSFC GROUND-BASED LIDAR FOR THE MEASUREMENT OF STRATOSPHERIC OZONE

Thomas J. McGee, NASA Goddard Space Flight Center, Laboratory for Atmospheres, Greenbelt, Maryland, U.S.A.

Concern has risen over the last decade or so concerning the release of gases into the atmosphere which when photolyzed in the stratosphere can catalyze the destruction of ozone. Although the expected change in ozone column content is not that large (on the order of 5%), significant changes in the vertical profile are anticipated. Predictions at 40 km run as high as a 60% change in the next 50-100 years. Because of the importance of ozone in the thermal budget of the atmosphere, such a change will have a direct impact on the earth's climate. Long-term monitoring of stratospheric ozone is required to validate the predictions and Differential Absorption Lidar is particularly well suited to this measurement. GSFC is currently constructing a mobile lidar system based on a high-powered XeCl excimer laser. The system is expected to be operating by early Fall '86 and a campaign to compare the lidar results with a series of ROCOZ flights is planned.

The XeCl excimer laser will deliver either 0.5 J or 1 J pulses operating at a rep rate of 30 Hz or 80 Hz depending on linewidth. The free running system is expected to deliver 1 J @ 80 Hz, while a line narrowed injection-locked laser is spaced 500 mJ and 30 Hz. Simulations to be discussed indicate that with the 15 W laser and a 30" receiver scope a 4.5% measurement of ozone at 40 km can be made with the lidar stationed at sea level assuming a 2.5 km range cell. The same simulations show that moving the station to an elevation of 2 km reduces the estimated error to 3%. These errors are compatible with the quality of measurements required to make a determination of a long-term trend in ozone at 40 km.

N87

10372

UNCLAS

DEVELOPMENT OF A SIMULTANEOUS MULTI-WAVELENGTH
DYE LASER FOR DIFFERENTIAL ABSORPTION TECHNIQUE

Y.Saito, A.Nomura and T.Kano

Department of Information Engineering, Faculty of
Engineering, Shinshu University, Wakasato, Nagano,
Japan

A compact and simple simultaneous multi-wavelength dye laser cavity was developed for a differential absorption technique. Dielectric multilayer interference filters were inserted inside the cavities as tuning elements, and two types of a DIAL system were constructed by using the dye laser tuned with dielectric multilayer filters to measure NO₂ concentration. The usefulness of this dye laser was clarified for the differential absorption technique in outdoor experiments.

Some basic designs of the laser cavity with these filters to get simultaneously multi-wavelength output are summarized in Fig.1. When a filter is set outside a cavity, the linewidth of the output spectrum of the dye laser becomes wider than that at the incident angle 0° with an increasing of the angle. If the filter is inserted inside the cavity and dye solution is excited, it is expected that the linewidth of the output spectrum becomes narrower than that of the filter itself during round-trip times, and the output peak power increases at the wavelength tuned with the filter. It is easily possible to get desired wavelengths by changing tilt angle of the filter mechanically. In order to get the laser power simultaneously at the multi wavelengths, two or more filters should be used as tuning elements. If we use a cavity containing two dye cells as shown in Fig.1(b), it is easy to get simultaneously two laser beams separated spatially at the two wavelengths. A schematic diagram of simultaneous two-wavelength dye laser which emits the laser beam into the same optical path is shown in Fig.1(c). The light is reflected by the 1st filter F1 over almost the whole wavelength region except to the transmitted wavelength,

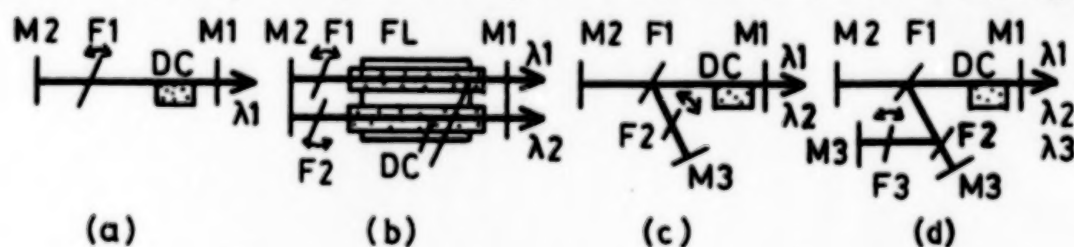


Figure 1. Schematic diagrams of the laser cavity with filters to get the simultaneous tunable multi-wavelength output. (a) Single wavelength¹⁾. (b) and (c) Two-wavelength²⁾³⁾. (d) Three-wavelength⁴⁾. (a), (c) and (d) are nitrogen laser pumped type. (b) is flashlamp pumped type. M; mirror, F; filter DC; dye cell, FL; flashlamp.

λ_1 , which is tuned by M1 and M2. The 2nd filter F2 is inserted into the 2nd cavity consisting of M1-F1-M3 which is tuned at the 2nd wavelength λ_2 . Each power of λ_1 and λ_2 is amplified in each cavity during roundtrip times. A simultaneous three-wavelength dye laser is constructed in the same manner as shown in Fig.1(d).

Many commercial filters with various characteristics were prepared and examined in experiments. Fig.2 shows typical examples of the simultaneous two- and three-wavelength spectra for a nitrogen laser pumped dye laser, where the linewidths of filters were 2nm at the incident angle 0° . Two wavelengths were tuned at the maximum (463.1nm) and minimum (465.8nm) absorption wavelength of NO_2 in the two-wavelength operation. Linewidths of the output were 0.4nm and the peak power was about 2.5 times of that obtained by the filter setting outside the cavity. The linewidth and the power were nearly constant and independent of the tilt angle of the filter. In the flashlamp pumped type, the linewidth and the power were halved and doubled, respectively, as compared with those obtained in a double prism tuning method. Also the linewidth obtained in the two-wavelength operation were one fourth of those obtained in the filter itself. In the nitrogen laser pumped type, fluctuations of the simultaneous three-wavelength operation were larger than those of the single- and simultaneous two-wavelength operation, in which the same pumping power was supplied.

In the filter tuning method, the high transmittance filter was better to get a good quality of the output spectrum, as the linewidth was narrowed during roundtrip times. When the

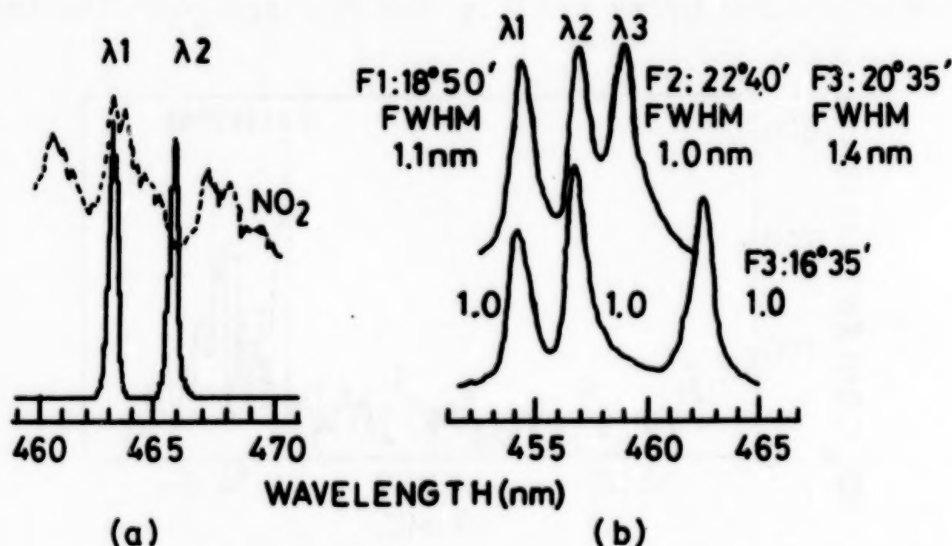


Figure 2. Output spectra of nitrogen laser pumped dye laser. (a) Two-wavelength³⁾; λ_1 and λ_2 are tuned NO_2 absorption spectrum (dashed line). (b) Three-wavelength⁴⁾; λ_3 shifts to shorter one with increasing the tilt angle of F3.

three wavelengths are tuned adequately, it is possible to measure simultaneously some molecules like NO_2 and SO_2 , and O_3 , NO_2 and aerosol density and so on.

Two types of DIAL systems, a long-path absorption type using a nitrogen pumped dye laser (5kW, 5ns, 10pps; Fig.1(c)), and range resolved type using a coaxial flashlamp pumped dye laser (5mJ, 300ns, 0.2pps; Fig.1(b)), were constructed and tested to confirm the feasibility in outdoor experiments. A two-wavelength beam was emitted to an atmosphere through a 10-power expander. In the receiving system, a telescope of the refracting type with a Fresnel lens of 50cm in diameter, two photomultipliers with two narrow band pass filters (0.35nm at FWHM), two wide band amplifiers (DC~50MHz) and a dual operation fast A/D converter (10ns/sample, 8bit) were used to detect simultaneously the signals at the two wavelengths and a micro-computer (16bit) was used as a processor.

A measurement of NO_2 concentration was made by the system in the stack which was set on a building located at the distance of 513m from the system. There was a national road in a heavy traffic along the building. In experiments, a concrete wall of this building at the back of the stack was selected as a topographic target. Fig.3 shows an example of results obtained in the long-path absorption DIAL system. The minimum detectable concentration of this system was about 20ppb at a total distance of 1.0km on a condition of shot noise. The peak concentration of NO_2 was 237ppb, which would correspond to the value of 24ppm.m if the plume passed the laser beam over 5m in length. Error bars of the experimental data were bigger than those when the plume was exhausted. This is caused from the NO_2 concentration being heavily changed and that the transmit-

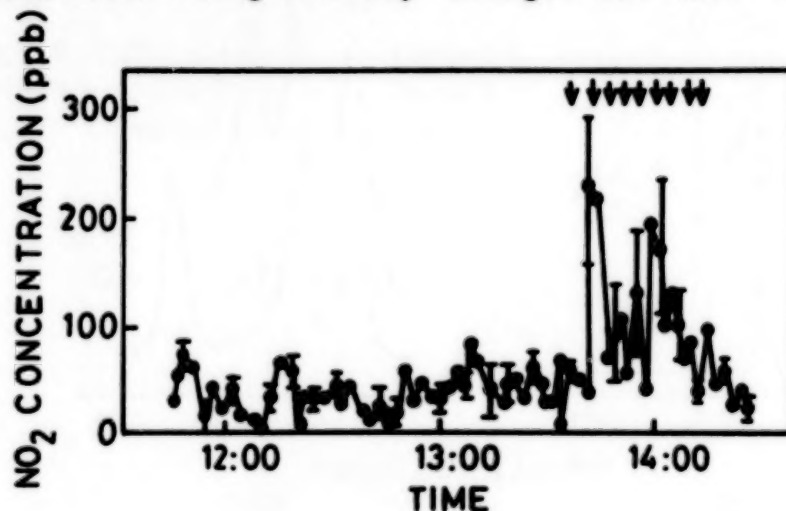


Figure 3. Time variations of NO_2 concentration in a stack plume at 513m from the DIAL system using a long-path absorption type by averaging 1000 signals. Arrows show the times when the plume could be observed by the naked eye⁵⁾.

tance of the plume was changed continuously because of the heavy changing of the density of the soot and smoke during the averaging time (90sec., 1000signals). Actually there was the case that the returned signal from the target could not have been obtained because of the large amount of absorption and scattering by the plume. This result implies that the numbers for averaging should be determined after the consideration about both the time variation of the concentration and the repetition rate of the laser pulse in order to get exactly the short time variation within a allowable error. This is an important thing in the measurement at the place where the concentration changes heavily and continuously like a stack plume or an intersecting point of a heavy traffic road. It may be assumed that many small variations out of the plume are caused from the traffic. In the range-resolved DIAL system, the NO₂ concentration was measured with 75m range resolution by averaging 50 signals (5 minutes) up to 300m, but the minimum concentration was comparatively large because the energy of the laser was not so large.

From these experimental results, the following things are concluded. A dielectric multilayer interference filter is a good tuning element if it is inserted into the laser cavity. A simultaneous tunable multi-wavelength dye laser can be made easily in combination with some filters. The dye laser with this filter tuning method is a useful apparatus in outdoor experiments when it is applied to the system like a DIAL system because of the simplicity of the cavity construction and the easiness of the tuning. It may be possible to measure some pollutions simultaneously using this simultaneous multi-wavelength dye laser and to apply it to many physical and chemical regions.

References

1. A.Nomura, Y.Shimomura, Y.Saito, and T.Kano, "Simple Tunable Dye Laser Using a Dielectric Multilayer Filter," Rev. Sci. Instrum. 53, 539 (1982).
2. Y.Saito, A.Nomura, R.Higuchi and T.Kano, "Development of Simultaneous Two-wavelength Dye Laser and its Application to DIAL System," The Review of Laser Engineering 13, 267 (1985), (in Japanese).
3. Y.Saito, T.Teramura, A. Nomura, and T.Kano, "Simultaneously Tunable Two-wavelength Dye Laser Using Two Dielectric Multilayer Filters," Appl. Opt. 22, 1799 (1983).
4. Y.Saito, T.Teramura, A.Nomura, and T.Kano, "Simultaneously Tunable Three-wavelength Dye Laser," Appl. Opt. 24, 2477 (1985).
5. Y.Saito, T.Fujimoto, A.Nomura, and T.Kano, "Simultaneous Two-wavelength Differential Absorption Laser Radar for NO₂ Measurement," Inst. Electron Commun. Eng. Jap. 85, OQE85-24 (1985), (in Japanese).

N87

10373

UNCLAS

ALEXANDRITE LASER SOURCE FOR ATMOSPHERIC
LIDAR MEASUREMENTS

J. Pelon*, C. Loth**, P. Flamant**, G. Mégie*

- * Service d'Aéronomie du CNRS BP 3
91370 Verrières le Buisson (France)
- ** Laboratoire de Météorologie Dynamique du CNRS
Ecole Polytechnique
91128 Palaiseau Cédex (France)

During the past years, there has been a marked increase in interest in the applications of vibronic solid-state lasers to meteorology and atmospheric physics. Two airborne lidar programs are now under development in France at CNRS and CNES, in addition to preliminary studies of future lidar applications from space platforms.

The differential absorption lidar (dial) method with vibronic solid-state lasers is very attractive for water vapor, temperature and pressure measurements (1), (2), (3). Alexandrite laser and titanium-sapphire are both suitable for these applications. However, only Alexandrite rods are commercially available to day.

The requirements on the laser source for airborne dial applications are two-fold : i) a restriction on laser linewidth and a requirement on stability and tunability with a good spectral purity ; ii) a requirement on the time separation between the two pulses. These constraints are summarized in table 1. In addition a laser energy of 50 to 100 mJ and a 5 to 10 Hz pulse repetition frequency are also required.

	H2O	p,T
emission wavelength	725-732 nm	760-770 nm
spectral width	1 pm	0.3 pm
spectral wavelength separation	70 pm	70 pm
temporal wavelength separation		100-400 μ s
spectral purity	99 % of the energy in 1 pm	

- Table 1 -

A dual wavelength double pulse oscillator is very attractive with respect to weight, electrical power and volume for future lidar emissions. Such a configuration is under development in our French laboratory and preliminary results have been obtained using a double Q switching with an acousto-optic device. We did demonstrate a broadband double-pulse operation of approximately 50 mJ in each pulse for a pulse separation of 100 μ s. The total energy of 100 mJ for 140 J is slightly lower than the 110 mJ for a single Q-switching after 250 μ s. The total energy extracted after 180 μ s is maximum for a 90 μ s delay between pulses (figure 1).

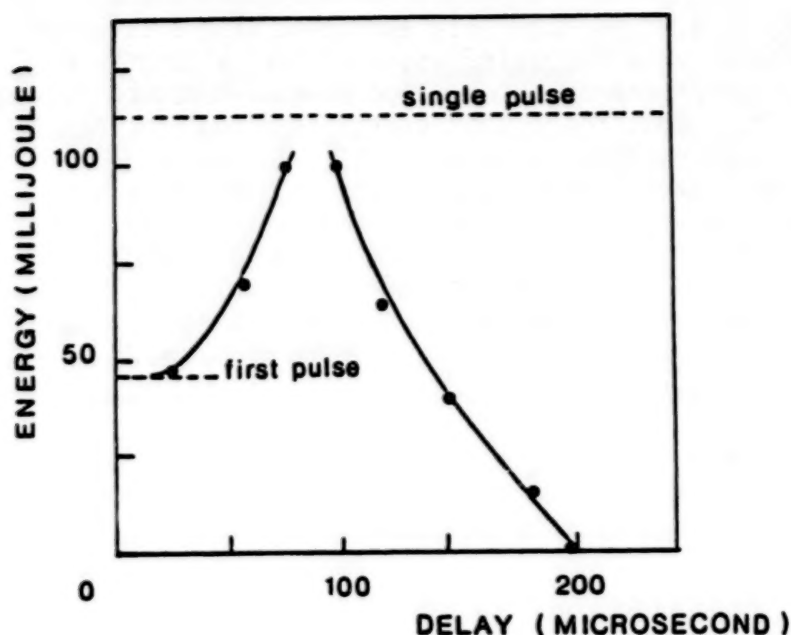


Figure 1 : Total output energy of the double pulse broadband oscillator as a function of the delay between the two emitted laser pulses.

In a separate work a narrow line single pulse emission has been obtained using a new cavity arrangement: the output coupler of the broadband cavity is replaced by an auxilliary cavity made of a diffraction grating G at grazing incidence in conjunction with two mirrors (figure 2).

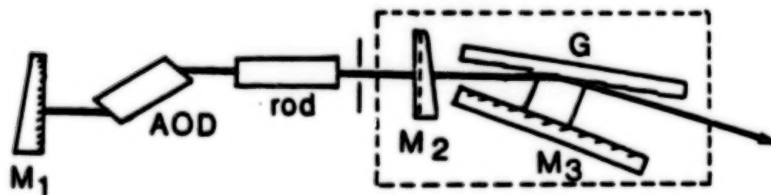


Figure 2 : Synoptic diagram of the narrow band Alexandrite oscillator.

A dual-mode laser emission (equivalent linewidth of 0,5 pm) is observed when the auxilliary cavity length is reduced to 9.3 cm total and when the grating is set at a grazing incidence angle of 88°. The laser mode separation recorded with the Fizeau

interferometer is 0.27 pm. It is in agreement with a value of 0.29 pm calculated from the main resonator cavity length. A strong modulation of the pulse envelope is also observed due to mode beating (fig. 3b). The output energy is 20 mJ (for an input of 180 J). We also observed a quasi-single mode emission (fig. 3c), with a smooth temporal envelop. In this case the observed mode linewidth is 0.14 pm (75 MHz) which corresponds to an experimental finesse of the Fizeau interferometer equal to 17. This value is in agreement with an apparatus function determined by a reflective finesse of 38, a defect finesse of approximately 25 and the number of successive reflections which reduces the experimental finesse at a value smaller than the expected theoretical limit.

Future works including a dual wavelength double pulse transmitter which is a follow-on of our previous developments on a laser pumped dye (4) will be discussed.

This work was supported by the Centre National d'Etudes Spatiales (France).

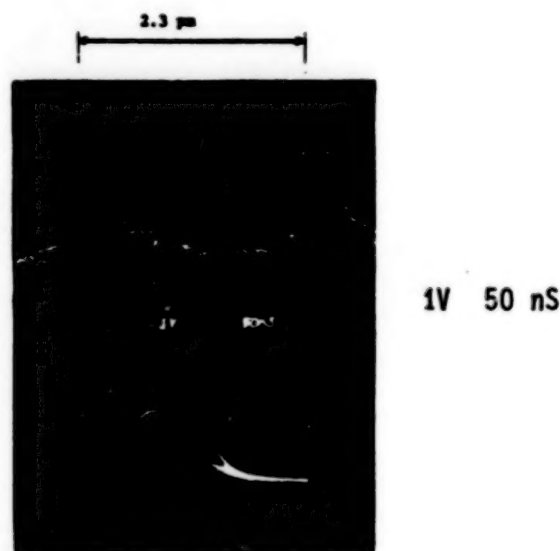


Figure 3 : Bimodal laser emission as recorded a) by a Fizeau interferometer with a 12 cm spacing between plates ($\delta\lambda = 2.3$ pm between consecutive orders) b) by a fast photodiode (temporal beating)

References

- (1) Cahen C., G. Mégie, P. Flamant, J. Appl. Meteor. 21, 1506, 1982.
- (2) Mégie G. Appl. Optics, 19, 34, 1980.

- (3) Korb C.L., C.Y. Weng. J. Appl. Meteor., 21, 1346, 1982.
- (4) Singh U., P.H. Flamant, C. Cahen, G. Mégie. Proceedings of the 12 ILRC, Aix en Provence, 1983.

N87

10374

UNCLAS

THE TFP AND A PULSED LD: NEW LIDAR COMPONENTS

Hiroshi Shimizu and Ichiro Matsui
National Institute for Environment Studies
Japan Environment Agency
Yatabe Tsukuba, Ibaraki, 305, Japan

Kazuhiro Asai
Tohoku Institute of Technology
Yagi-yama, Sendai 982, Japan

One of the large problems of lidar in practical use is that the price and the weight of a laser and a receiving telescope is too high. To solve this problem, many trials have been made.

In this paper, the system with the TFP (thin film paraboloid)¹⁾²⁾ for a receiving telescope and a pulsed LD (laser diode) for a laser source is proposed. Then, the lidar system will become very lightweight and inexpensive.

The TFP is made of an aluminum coated polyester film which is stretched across a circular ring and a pressure difference is created between the upper and lower surfaces. Due to the pressure difference, the surface of the film has a strain. The shape of the surface can be approximated by a paraboloid. When the ratio of focal length to the diameter of the TFP is almost 1, the effective diameter of the TFP where the surface is useful as a lidar receiver is about half of the actual diameter size of the TFP. The merits of the TFP are it is extremely lightweight and inexpensive. The thickness of the polyester film is only 100 μ m. The aluminum coated polyester film whose width is 1m is commercially available and the price is \$10/m². We made a 90 cm in diameter TFP from 1m² film. The top and the side view of the TFP are shown in Fig. 1.

Pulsed LDs are commercially available from M/A-Com Laser Diode, Inc. etc. The maximum output power of LDs are 1kW at the wavelength of 904 nm and 75 W at 850 nm. A pulsed output whose pulse width is 50 nsec and repetition rate is 500 Hz can be obtained by using a simple driver. The weight of the driver is only 1 kg and the weight of the LD is negligible. Although the output energy per pulse of a pulsed LD is very small compared with conventional pulsed laser sources, it can be used as a lidar energy source if it is combined with the large size TFP.

The schematic diagram and the specifications of the lidar system which was composed of the 90 cm in dia. TFP and a 75W peak power LD are shown in Fig. 2 and Table 1, respectively. In Fig. 2, the collected signal light is passed through an interference filter and received by a photomultiplier whose photocathode is made by GaAs. The output of the

photomultiplier is analog to digital converted by a transient recorder. The converted signal is summed up by an accumulator and stored by a magnetic disk.

The example of the received signal which is the vertical distribution of aerosol is shown in Fig. 3. Fig. 3 (a) is the A scope signal and (b) is the range corrected one. The observation time was 1 min (30000 pulses). From Fig. 3, it can be concluded that an aerosol distribution within 1.5 km can be obtained easily by using the system.

References

- 1) Hiroshi Shimizu, Nobuo Sugimoto and Yoshikazu Iikura, Conference abstract of lasers and electro-optics, Baltimore, U.S.A. 21-24 May 1985, p.264
- 2) Hiroshi Shimizu, To be presented in Applied Optics Vol. 25, No. 9

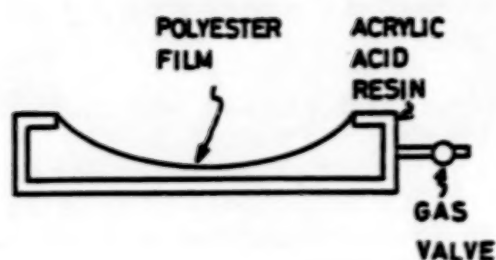


Fig. 1
Side and
top view
of the
90cm dia
TFP.

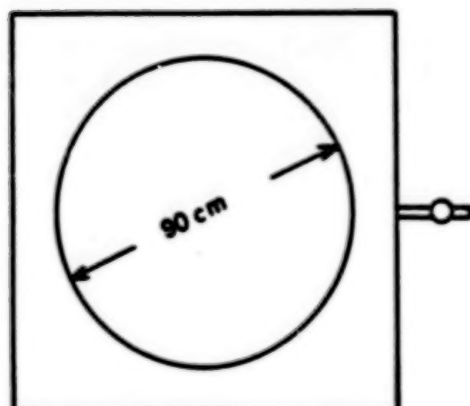


Fig. 2
Schematic
drawing
of the
TFP plus
LD lidar
system

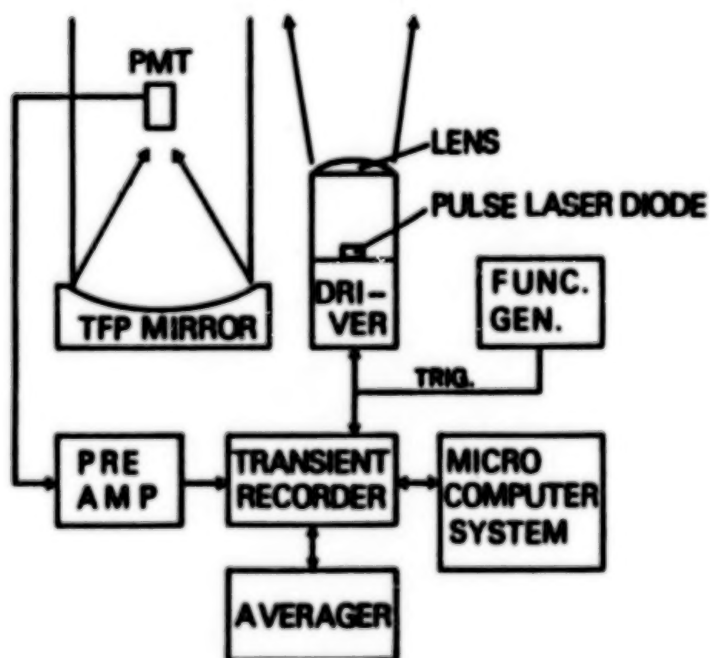


Table 1 Specifications of the TFP + LD lidar system

TFP		photo-multiplier	
diameter	90cm	maker & MODEL	Hamamatsu R636
focal length	150cm	transient recorder	
thickness of film	100 μ m	maker & model	Autnics S121
LD		min. sampling time	50nsec
maker	M/A-com LD	resolution	10bits
model	LA-167	accumulator	
max. power	75W	maker & model	Autnics F601
pulse width	75nsec	access time	1 μ sec
wavelength	858nm	micro computer	
		maker & model	Sord M343

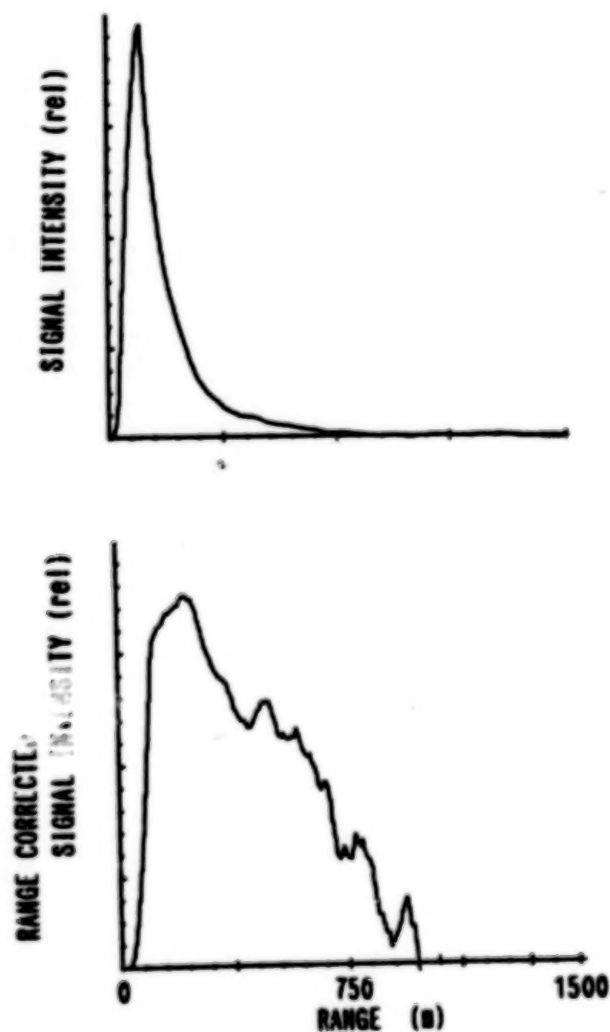


Fig. 3
Measured
lidar
signal

N87

10375

UNCLAS

CHEMICAL CONTAMINATION REMOTE SENSING

JOHN P. CARRICO
KIRKMAN R. PHELPS
ERNEST N. WEBB
RAYMOND A. MACKAY

U.S. ARMY CHEMICAL RESEARCH AND DEVELOPMENT CENTER

ABERDEEN PROVING GROUND, MARYLAND 21010-5423

E. R. Murray
SRI International
Menlo Park, California 94025

ABSTRACT

A ground mobile laser test bed system was assembled to assess the feasibility of detection of various types of chemical contamination using Differential Scattering (DISC) and Differential Absorption (DIAL) LIDAR techniques. Field experiments with the test bed system using chemical simulants were performed. Topographic reflection and range resolved DIAL detection of vapors as well as DISC detection of aerosols and surface contamination were achieved. Review of detection principles, design of the test bed system, and results of the experiments are discussed.

AUTHOR INDEX

The paper numbers are preceded by the capital letter designation of the session in which the papers were presented (see Contents). Page numbers are given in parentheses.

- Agert, S., D30 (155)
Akiyoshi, H., D22 (133)
Allario, F., A3 (3)
Amzajerian, F., E4 (181)
Ancellet, G.M., I4, (276)
Andreev, Yu. M., D11 (108)
Ansmann, A., C8 (70)
Arshinov, Yu. F., E7 (189)
Aruga, T., C4 (57)
Asai, K., C4 (57), I15 (314)
Averill, R.D., A5 (6)
- Baba, H., B10 (41)
Balin, Yu. S., B9 (38)
Banakh, V.A., D16 (122)
Barber, T.L., B3 (20)
Barbini, R., I7 (287)
Battistelli, E., D25 (139)
Beljaev, V.K., H7 (265)
Benard, J., C6 (61)
Bobrovnikov, S.M., E7 (189)
Boers, R., D9 (104), E11 (197)
Bogan, J.R., H5 (263)
Burris, J., D33 (167)
Bösenberg, J., C8 (70)
Braun, C., D8 (102)
Browell, E.V., A5 (6), B6 (28), C1 (49),
C7 (65), I11 (300)
Brown, D.R., I9 (295)
Bruscaglioni, P., D25 (139)
Burakov, S.D., D17 (125)
Butler, J., D33 (167)
- Cahen, C1., C6 (61)
Camagni, P., D32 (162)
Carnuth, W., F4 (208)
Carrico, J.P., I16 (318)
Carswell, A.I., B4 (22), D2 (85), D4 (92)
Cohen, A., D30 (155), E3 (180)
Colombo, G., D32 (162)
Cooney, J.A., E8 (192), E9 (193)
Cotnoir, L.J., C11 (80), I11 (300)
Curran, R.J., A2 (2)
Cutten, D., B2 (16)
Cvijin, P.V., I1 (266)
- Davies, J.E., B2 (16)
DeFoor, T., D21 (132)
Degnan, J.J., A5 (6)
DeLuisi, J.J., D21 (132)
Denisov, N.N., H7 (265)
Dombrowski, M., C2 (52), C3 (55),
D5 (94)
Draghi, S., H3 (259)
Dubinsky, R.N., D2 (8)
- Eberhard, W.L., D31 (158)
Edner, H., H2 (255)
Elliott, N., D26 (143)
Eloranta, E.W., I8 (291)
Endemann, M., A6 (10)
Evans, B.T.N., B8 (34)
- Farrington, M., F3 (207)
Fastig, S., E3 (180)
Ferdinandov, E., H7 (265)
Ferrario, A., D27 (146)
Firsov, K.M., D15 (119)
Flamant, P.H., C10 (76), I14 (310)
Forrest, D.K. I8 (291)
Fredriksson, K., H2 (255)
Fujiwara, M., D22 (133)
Fukunishi, H., D24 (135), F9 (219)
- Galle, B., D28 (148)
Galletti, E., H3 (258)
Garbi, M., H3 (258)
Gardner, C.S., F11 (226)
Gengchen, W., H4 (259)
Gerber, H., D1 (84)
Gerstl, S.A.W., D26 (143)
Ghigo, A., I7 (287)
Giorgi, M., I7 (287)
Glaznov, G.N., D14 (117)
Goad, J.H., A5 (6)
Gochelashvily, K.S., H7 (265)
Godin, S., F8 (215)
Godlevskii, A.P., D17 (125)
Granier, C., F10 (222)
Grant, W.B., H5 (263)
Gribenyukov, A.I., D11 (108)
Grossmann, B.E., I11 (300)
Gudimetla, V.S.R., E4 (181)

Hagard, A., B7 (32)
 Hall, F.F. Jr., E2 (176)
 Hall, W.M., A5 (6)
 Hardesty, R.M., E2 (176)
 Hart, W.D., G1 (230)
 Hayashida, S., F2 (203)
 Heaps, W.S., D20 (131), D33 (167)
 Higdon, N.S., I11 (300)
 Hinton, D.E., A5 (6)
 Hirasawa, T., D24 (135), F9 (219)
 Hoff, R.M., E10 (194)
 Hofmann, D.J., D19 (129)
 Holmes, J.F., E4 (181)
 Hooper, W.P., D1 (84)
 Houston, J.D., D4 (92), I9 (295)
 Huffaker, R.M., A4 (4), I2 (269)
 Hunt, J.M., E4 (181)

Igarashi, T., C4 (57)
 Igonin, G.M., D14 (117)
 Iikura, Y., F2 (203)
 Ilev, I.K., G2 (233)
 Inaba, H., H1 (251)
 Ippolitov, I.I., I10 (298)
 Ishikawa, N., B10 (41)
 Ishizu, M., C4 (57)
 Ismail, S., C7 (65)
 Itabe, T., C4 (57)
 Iwasaka, Y., D24 (135), F9 (219)
 Iyer, K.N., I7 (287)

Jager, H., D19 (129), F4 (208)
 Jain, S.L., H6 (264)
 Jegou, J.P., F10 (222), I5 (280)
 Jenkins, D.B., F3 (207), F7 (214)
 Jennings, S.G., G5 (244)
 Jindin, Z., D23 (134)
 Jinhuan, Q., D23 (134)
 Jinhui, S., D23 (134)

Kagann, R.H., C5 (59)
 Kano, T., F9 (219), I13 (306)
 Kapitanov, V.A., D11 (108)
 Kaprielov, B.K., G2, (233)
 Kastner, M., B5 (24)
 Kavaya, M.J., I2 (269)
 Kavryanov, S.I., B9 (38)
 Kawaguchi, S., F9 (219)
 Kent, G.S., F5 (210)
 Khmel'nitskii, G.S., D11 (108)
 Kleimann, M., D30 (155)
 Koepp, F., E5 (185)
 Koechler, G., D32 (162)
 Koga, R., D34 (168)
 Kolev, I.N., D13 (113), G2 (233)

Kopytin, Yu.D., D12 (111), D17 (125)
 Korb, C.L., C2 (52), C3 (55), D5 (94)
 Korol'kov, V.A., D12 (111)
 Kosaka, M., D34 (168)
 Kostin, B.S., D10 (105)
 Krekov, G.M., B9 (38)
 Krichbaumer, E5 (185)
 Kwon, K.H., F11 (226)

Larson, T.L., B3 (20)
 Lawrence, T.R., E2 (176)
 Lazarev, S.V., D17 (125)
 Lea, T.K., B11 (45)
 Lentz, W.J., G6 (248)
 Lesne, J.L., C6 (61)
 Levitskii, M.E., D12 (111)
 Lightsey, P.A., I3 (272)
 Littfass, M., D19 (129)
 Longenecker, D.U. D21 (132)
 Loth, C., I14 (310)
 Lutz, H., A1 (1)
 Lynch, M.J., B2 (16)

MacKay, R.A., I16 (318)
 Maeda, M., D6 (95), F6 (211)
 Makushkin, Yu.S., D15 (119)
 Manenkov, A.A., H7 (318)
 Matsui, I., F2 (203), I15 (314)
 Matvienko, G.G., D13 (113)
 McCormick, M.P. A7 (14), F1 (201)
 McGee, T.J., D33 (167), I12 (305)
 McNice, G.T., D31 (158)
 Measure, E.M., D3 (86)
 Megie, G., F8 (215), F10 (222),
 I5 (280), I14 (310)
 Melfi, S.H., D9 (104) E6 (188), E11 (197)
 Menzies, R.T., I4 (276)
 Milrod, J., C2 (52), D5 (94)
 Milton, M.J.T., C9 (73)
 Mironov, V.L., D16 (122)
 Mitev, V.L., H7 (265)
 Mitsel, A.A., D15 (119)
 Mitsev, TS.A., H7 (265)
 Murray, E.R., I16 (318)

Naats, I.E., D10 (105), D18 (126)
 Nadeev, A.I., E7 (189)
 Nakane, H., F2 (203)
 Nebol'sin, M.F., D12 (111)
 Nomura, A., D24 (135), F9 (219), I13, (306)

Omenetto, N., D32 (162)
 Ono, T., D24 (135)
 Ostanin, S.A., D17 (125)
 Otsuka, N., D22 (133)

- Pain, T., I5 (280)
 Pal, S.R., B4 (22) D2 (85)
 Palucci, A., I7 (287)
 Parvanon, O.P., G2 (233)
 Pedrini, A., D32 (162)
 Pelon, J., F8 (215) I14 (310)
 Petherman, J.C., C5 (59)
 Petri, K., E8 (192)
 Petrilla, R.L., G3 (237)
 Petroni, R., H3 (258)
 Phelps, K.R., I16 (318)
 Pili, P., D25 (139)
 Pizzolati, D27 (146)
 Ponomarev, Yu.N., D15 (119), I10 (298)
 Ponsardin, P., C6 (61)
 Poole, L.R., F5 (210)
 Popov, A.A., D18 (126)
 Post, M.J., E2 (175)
 Prochorov, A.M., H7 (265)
 P"rvanov, O.F. D13 (113)
- Qilin, X., D23 (134)
 Qinxin, K., H4 (259)
 Quenzel, H., A6 (10), B5 (24)
- Razenkov, I.A., B9 (38)
 Renger, W., A6 (10)
 Ribesso, S., I7 (287)
 Ritter, K.J., D7 (98)
 Roesler, F.L., F11 (226)
 Rosen, J.M., D19 (129)
 Rosenberg, A., C5 (59), I6 (283)
 Rossi, G., D32 (162)
 Rudenko, V.P., D15 (119)
- Saha, A.K., H6 (264)
 Saito, Y., I13 (306)
 Sakurai, K., B10 (41)
 Salik, A., E8 (192)
 Samokhvalov, I.V., D13 (113)
 Sano, H., D34 (168)
 Sasano, Y., B6 (28), F2 (203)
 Sassen, K., G3 (237)
 Schotland, R.M., B11 (45), I1 (266)
 Schwemmer, G.K., C2 (52), C3 (55),
 C11 (80), D5 (94)
 Schwiesow, R.L., I3 (273)
 Sechrist, C.F. Jr., F11 (226)
 Senft, D.C., F11 (226)
 Shams, M.Y., D35 (172)
 Sharin, P.P., D17 (125)
 Shelevoy, K.D., E7 (189)
 Shibata, T., D6 (95), F6 (211)
 Shimizu, H., I15 (314), F2 (203)
 Sidorov, B.G., D12 (111)
- Singh, U.N., C10 (76) C11 (80), I11 (300)
 Smith, R.B., D4 (92)
 Sugimoto, N., F2 (203)
 Soldatkin, N.P., D12 (111)
 Sosnin, A.V., D11 (108)
 Spinhirne, J.D., G1 (230)
 Sroga, J., I6 (283)
 Stoikova, E.V., H7 (265)
 Stokes, G.H. D26 (143)
 Stuchebrov, G.A., D11 (108)
 Stupin, D.M., D26 (143)
 Sunesson, A. H2 (255)
 Svanberg, S., H2 (255)
 Sztankay, Z.G., G4 (238)
- Taguchi, F., D29 (151)
 Takeuchi, N., B10 (41) F2 (203)
 Taylor, L.V., A3 (3)
 Thomas, L., F3 (207), F7 (214)
 Troxel, S.W., D31 (158)
- Uehara, K., D29 (151)
 Ueno, T., B10 (41)
 Ulitsky, A., D4 (92)
 Uneus, L., H2 (255)
 Unruh, W.P., D26 (143)
- Vaughan, G., F3 (207), F7 (214)
 Vaughan, J.M., E1 (174)
 Vaughan, W.R., A5 (6)
 Voelz, D.G., F11 (226)
 Voevodin, V.G., D11 (108)
- Walden, H., C2 (52), D5 (94)
 Wareing, D.P., F3 (207), F7 (214)
 Webb, E.N., I16 (318)
 Weinmann, J.A., D26 (143)
 Wells, J.G., A5 (6)
 Weng, C.Y., C3 (55)
 Werner, Ch., A6 (10)
 Wendt, W., D28 (148), H2 (255)
 Whiteman, D., E6 (188)
 Wilkerson, T.D., C11 (80), D7 (98),
 I11 (300)
 Woods, P.T. C1 (49), C9 (73)
- Young, S.A., B2 (16)
- Zaccanti, G., D25 (139)
 Zanzottera, E., D27 (146), H3 (258)
 Zardecki, A., D26 (143)
 Zhao, Y-Z., B11 (45) I1 (266)
 Zuev, V.E., B1 (15), D10 (105),
 D11 (108), D12 (111), D13 (113),
 D14 (117), D15 (119), D16 (122),
 D17 (125), D18 (126), E7 (189)
 Zuev, V.V., I10 (298)

Standard Bibliographic Page

1. Report No. NASA CP-2431	2. Government Accession No.	3. Recipient's Catalog No.	
4. Title and Subtitle THIRTEENTH INTERNATIONAL LASER RADAR CONFERENCE		5. Report Date August 1986	
		6. Performing Organization Code 618-32-33-07	
7. Author(s)		8. Performing Organization Report No. L-16201	
		10. Work Unit No.	
9. Performing Organization Name and Address NASA Langley Research Center Hampton, VA 23665-5225		11. Contract or Grant No.	
		13. Type of Report and Period Covered Conference Publication	
12. Sponsoring Agency Name and Address York University, Toronto, Canada Atmospheric Environment Service, Toronto, Canada National Aeronautics and Space Administration Washington, DC		14. Sponsoring Agency Code	
15. Supplementary Notes			
16. Abstract This publication contains extended abstracts of papers presented at the Thirteenth International Laser Radar Conference, held in Toronto, Ontario, Canada, August 11-15, 1986. One hundred fifteen papers were presented in both oral and poster sessions. The topics of the conference sessions were <ol style="list-style-type: none"> 1. Spaceborne Lidar/New Applications 2. Extinction/Visibility 3. Differential Absorption Lidar 4. Winds and Tropospheric Studies 5. Middle Atmosphere 6. Clouds and Multiple Scattering 7. Pollution Studies 8. New Systems This conference reflects the breadth of research activities being conducted in the lidar field. These abstracts address subjects from lidar-based atmospheric investigations to the development of new lidar systems and techniques.			
17. Key Words (Suggested by Authors(s)) Lidar Laser radar Remote sensing Atmospheric measurements		18. Distribution Statement Unclassified - Unlimited Subject Category 35	
19. Security Classif.(of this report) Unclassified	20. Security Classif.(of this page) Unclassified	21. No. of Pages 334	22. Price A15

END

DATE

FILMED

DEC 18 1986